

THE UNIVERSITY OF CHICAGO

THE OPTOELECTRONIC PROPERTIES OF NANOPARTICLES FROM FIRST
PRINCIPLES CALCULATIONS

A DISSERTATION SUBMITTED TO
THE FACULTY OF THE INSTITUTE FOR MOLECULAR ENGINEERING
IN CANDIDACY FOR THE DEGREE OF
DOCTOR OF PHILOSOPHY

BY
NICHOLAS PETER BRAWAND

CHICAGO, ILLINOIS

JUNE 2017

Copyright © 2017 by Nicholas Peter Brawand

All Rights Reserved

To my wife, Tabatha

TABLE OF CONTENTS

LIST OF FIGURES	vi
LIST OF TABLES	xii
ABSTRACT	xiv
1 INTRODUCTION	1
2 FIRST PRINCIPLES CALCULATIONS	4
2.1 Methodological Foundations	4
2.1.1 Density Functional Theory	4
2.1.2 Many Body Perturbation Theory	6
2.2 The Generalization of Dielectric Dependent Hybrid Functionals to Finite Sys- tems	8
2.2.1 Introduction	8
2.2.2 Theory	10
2.2.3 Results	12
2.3 Self-Consistency of the Screened Exchange Constant Functional	19
2.3.1 Introduction	19
2.3.2 Results	20
2.3.3 Effects of Self-Consistency	30
2.4 Constrained Density Functional Theory and the Self-Consistent Image Charge Method	35
2.4.1 Introduction	36
2.4.2 Methodology	39
2.4.3 Verification	42
2.4.4 Application to silicon quantum dots	52
3 OPTICAL PROPERTIES OF ISOLATED NANOPARTICLES	57
3.1 Nanoparticle Blinking	57
3.1.1 Introduction	57
3.1.2 Structural Models	60
3.1.3 Theory and Computational Methods	61
3.1.4 Results	64
3.1.5 Analysis of Blinking Processes	68
3.2 Tuning the Optical Properties of Nanoparticles: Experiment and Theory . .	70
3.2.1 Introduction	70
3.2.2 Results	72
4 CHARGE TRANSPORT PROPERTIES OF NANOPARTICLES	89
4.1 Defects and Charge Transfer in Nanoparticles	90
4.1.1 Introduction	90
4.1.2 Methods	92

4.1.3	Results	93
4.2	Improving Charge Transport Lead Chalcogenide Nanoparticles	106
4.2.1	Introduction	107
4.2.2	Methods	110
4.2.3	Results	112
5	CONCLUSIONS	126
5.1	Summary	129
5.1.1	List of Publications	129
5.1.2	Codes Released	130
5.1.3	Theoretical Methods Developed	130
	REFERENCES	131

LIST OF FIGURES

2.1	(Color online) Vertical ionization potentials (VIP) of the G2/97 subset consisting of 36 closed shell molecules computed as the highest occupied molecular orbital energy using the SX hybrid functional (SX), G_0W_0 starting from PBE wavefunctions ($G_0W_0@PBE$) [‡] and SX wavefunctions ($G_0W_0@SX$) and total energy differences ($\Delta SCF(PBE)$) [†] . [‡] data from Ref. [146] [†] data from Ref. [359]	14
2.2	(Color online) The fundamental gaps of several hydrogen passivated silicon nanostructures SiH_4 , $Si_{35}H_{36}$, $Si_{66}H_{64}$ and $Si_{87}H_{64}$ predicted using the SX hybrid functional (see text), G_0W_0 starting from PBE wavefunctions ($G_0W_0@PBE$) and SX wavefunctions ($G_0W_0@SX$). Fundamental gaps obtained from total energy differences ($\Delta SCF(PBE)$) are included for comparison.	17
2.3	(Color online) The first lowest optical singlet excitations predicted by the time dependent SX hybrid functional method (TDSX) compared to the revised best theoretical estimates (see text) of Thiel’s test set for 28 molecules. Values predicted for the same transitions by TDPBE0 (time dependent density functional calculations with the PBE0 functional) and BSE@ $G_0W_0@PBE0$ (results from the solution of the Bethe Salpeter Equation (BSE), starting from single-particle energies computed at the G_0W_0 level of theory, with DFT results obtained with the PBE0 functional) are taken from Ref. [181].	23
2.4	(Color online) Mean absolute errors (MAE) for (left to right): the ionization potentials (Photoemission) of Thiel’s test set (with the exception of propanamide due to lack of experimental data) predicted by the highest occupied molecular orbital energy computed using PBE0, $G_0W_0@PBE0$ and the screened exchange constant functional (SX); the lowest optical singlet transitions predicted by the SX functional (TDSX, i.e. time dependent density functional calculations using the SX functional, Eq. 2.17), TDPBE0 and PBE0 with many body perturbation theory corrections (BSE@ $G_0W_0@PBE0$) TDPBE0 and BSE@ $G_0W_0@PBE0$ are taken from Ref. [181].	24
2.5	Errors (eV) in the ionization energies of the molecules belonging to the GW 100 Test Set calculated with the screened exchange constant functional at the perturbative (SXP@PBE) and self-consistent (SX and ScSX) levels. We also report, CCSD(T) and experimental values [245, 213]. A <i>negative</i> error (see Equation 2.20) indicates an <i>underestimate</i> of the reference ionization potential.	25
2.6	Eigenvalues (λ_i) for Cu_2 of the symmetrized polarizability $\tilde{\chi}$ used to construct the inverse of the static dielectric function $\epsilon^{-1} = 1 + v_c^{1/2} \tilde{\chi} v_c^{-1/2}$ where v_c is the Coulomb interaction, computed using the screened exchange constant functional (SX) and the fully self-consistent screened exchange constant functional (ScSX). Inset: the highest occupied molecular orbital of Cu_2 predicted by the perturbative screened exchange constant method at PBE (SXP@PBE), SX and ScSX. Isosurfaces are evaluated at 10% of the maximum isovalue of the one obtained using ScSX.	31

2.7	The reduction of the SX error in the ionization potential (Δ) (Eqn. 2.22) as a function of the difference in the electronegativity of all molecules which contain only two atom types and exhibited a value of Δ greater than the average over the GW100 test set. The average absolute error with respect to CCSD(T) for these molecules is from 0.69 eV to 0.13 eV for SXP@PBE to SX respectively.	32
2.8	Difference in the screened exchange constant at different iterations of the self-consistency; iteration 1 (α^{SX}), iteration 2 and iteration 3 (α^{ScSX}) compared against the hybrid-GW crossing point ($\alpha^*_{\text{G}_0\text{W}_0}$) for the ionization potentials of the GW100 test set. A <i>negative</i> difference means the method <i>underestimates</i> $\alpha^*_{\text{G}_0\text{W}_0}$	35
2.9	Electronic coupling H_{AB} (eV) as a function of distance R (\AA) for hole transfer between two Zn atoms belonging to a Zn_2^+ cation, obtained with the generalized Mulliken-Hush method[73] (denoted GMH), constrained density functional theory using Becke weight partitioning (Wu and Van Voorhis)[27, 461], and in this work, using Hirshfeld partitioning[168] (see text). Calculated β decay rates are 2.55, 2.69, and 2.72 \AA^{-1} for the three methods, respectively.	43
2.10	Dependence of the energy and potential strength on the number of charges transferred $N = \int_{\Omega} w(\mathbf{r})\rho(\mathbf{r})d^3\mathbf{r}$ for Zn_2^+ at 5 \AA separation (The equilibrium distance of Zn_2^+ within PBE is 2.55 \AA).	44
2.11	Percent error in electronic coupling $\left(100\% \times \frac{H_{\text{AB}}(N) - H_{\text{AB}}(N_0)}{H_{\text{AB}}(N_0)}\right)$ versus the error in the number of charges transferred ($\Delta N = N - N_0$), relative to results obtained with N_0 for Zn_2^+ at 5 \AA separation (The equilibrium distance of Zn_2^+ within PBE is 2.55 \AA).	45
2.12	(Color online) Electronic couplings (H_{AB} , see Eq. 2.30) calculated using constrained density functional theory (CDFT) implemented in Quantum ESPRESSO (QE) versus values obtained with the CPMD code[11] (see Kubas, et al[219, 220]) for the HAB11 and HAB7 sets of π -conjugated molecules.	46
2.13	Semi-log plot of the electronic coupling for holes (top) and electrons (bottom) versus distance $R/\text{\AA}^{-1}$ between two $\text{Si}_{35}\text{H}_{36}$ QDs for configurations taken from 300K molecular dynamics trajectory. Electronic couplings are computed using the splitting in dimer (SID), anticrossing (AX), and constrained DFT (CDFT) methods (see text).	55
2.14	Isosurfaces of the highest occupied single particle molecular orbital (HOMO) of a $\text{Si}_{35}\text{H}_{36}$ dimer, as obtained using DFT and the PBE functional, for a configuration relaxed at T=0 and one extracted from an MD simulation performed at 300K. The separation between the nanoparticles is 3.75 \AA . White and yellow sphere represent hydrogen and silicon, respectively.	56

3.1	Model of a 1.3 nm silicon nanoparticle terminated by an oxide layer, as extracted from an amorphous matrix of SiO ₂ (see text). The three dangling bond defect geometries studied in this chapter, labeled P_b , P_{b0} and P_{b1} , are shown.[302, 340] The P_b defect, originally found at the (111) interface of bulk Si/SiO ₂ is back-bonded to three Si atoms. The P_{b0} and P_{b1} are both at the (100) interface. The P_{b0} is back-bonded to three Si atoms, while P_{b1} is back-bonded to two Si and one O atoms. The P_{b1} defect has been modeled using the geometry proposed by Poindexter et al.[340] Silicon, oxygen and hydrogen atoms are represented by yellow, red and white spheres, respectively. Each nanoparticle modeled in this chapter has a maximum of one dangling bond defect.	81
3.2	Charge transition levels for the P_b , P_{b1} and P_{b0} defects on the surface of strained oxidized 1.3 nm silicon NPs. The lowest and uppermost positions of the blue and red areas represent the negative of the ionization potential and electron affinity of the defectless oxidized 1.3 nm nanoparticle, respectively. Dashed lines are the charge transition levels computed for the same NP but in the absence of stress. The energy levels are all referenced to vacuum.	82
3.3	HOMO/LUMO gaps of the P_b and P_{b1} surface defect states in the presence of a strained oxide layer on the surface of three different Si nanoparticles. The insets represent the single particle energy levels and the corresponding gaps given by the colored arrows.	83
3.4	Configuration coordinate diagrams for the decay processes belonging to two separate spin channels. The notation $D^\alpha \rightarrow D^\beta$ denotes the transition of the dangling bond from charge state α to charge state β . See text for further description. . .	83
3.5	The logarithm of the ratio between radiative (k_r) and nonradiative (k_{nr}) decay rates for the four capture processes outlined in Figure 3.4, as a function of decreasing strain on the NP (see text), for a P_b defect at the surface of a 1.3 nm Si NP terminated by an oxide layer. The black horizontal line represents the boundary between radiative (white area) and nonradiative (gray area) recombination processes. Configurations representing different relaxation schemes around the defect (and hence different amount of strain) are shown on the x axis: r_{nn} (nearest neighbor), r_{np} (Si NP and first layer of oxygen) and r_∞ (all atoms in the system). Nonradiative rates given by Equation 3.7 and 3.3 are indicated by the dots and open circles respectively.	84
3.6	The model ligand/QD system utilized in this study. (a) Chemical structures, computed vacuum electronic dipoles, and labels used throughout this work of the molecules in our ligand library. 4-CN-CA ⁻ = 4-cyanocinnamate; 4-CF ₃ -CA ⁻ = 4-trifluoromethylcinnamate; 3,5-F-CA ⁻ = 3,5-difluorocinnamate; 4-H-CA ⁻ = cinnamate; 2,6-F-CA ⁻ = 2,6-difluorocinnamate; 4-OCH ₃ -CA ⁻ = 4-methoxycinnamate; 4-N(CH ₃) ₂ -CA ⁻ = 4-dimethylaminocinnamate. OA ⁻ = oleate (b) The X-type ligand exchange in which surface bound oleate is displaced by functionalized cinnamic acid molecules.	85

3.7	Surface analysis of PbS QDs before and after ligand exchange/PCR purification. (a) FT-IR spectra of neat ligand (lighter traces) and ligand/QD complex (darker traces) films. (b) ^1H NMR spectra in CDCl_3 of neat ligand (lighter traces) and ligand/QD complexes (darker traces). Both FT-IR and HNMR analysis suggests the efficient exchange of native OA^- ligands for R-CA^- and removal of excess R-CAH and OAH through PCR purification.	86
3.8	Photoelectron spectroscopy measurements of ligand/QD complexes. (a) Photoelectron cutoff region of XPS spectra used to determine ligand/QD film work function. (b) Valence band edge region of XPS spectra used to extract the ligand/QD film valence band maximum (VBM) with respect to the Fermi energy ($E_F - E_{VBM}$). The dashed black line represents the instrument equilibrated Fermi energy at an electron binding energy of 0 eV. (c) Band edge energies of films fabricated from OA^- and R-CA^- terminated 3.2 nm diameter PbS QDs; ionization energy (solid rectangles) and work function (dashed black lines). We also include the conduction band minimum (E_{CBM} , open rectangles) that is determined from summing the optical gap determined from absorbance measurements (opaque lines) and calculated exciton binding energy. The variation in the measurements made for duplicate samples was lower than the instrumental noise; therefore, the uncertainty of the ionization energy and work function values are represented as the width of the closed rectangle and surrounding light gray rectangle, respectively.	87
3.9	Band edge shifts of ligand/QD complexes . (a) Experimentally measured $\text{R-CA}^-/\text{QD}$ (solid squares) and $4\text{R-S}^-/\text{QD}$ (open circles) ionization energies as a function of calculated ligand dipole. The variation of ionization energy measurements made for duplicate samples was lower than the instrumental noise; therefore, the uncertainty of the data is less than the width of the data markers. The brown and gray open circles are data taken from Bent <i>et al.</i> [139] that correspond to $4\text{-NO}_2\text{-S}^-$ and 4-F-S^- capped PbS QDs, respectively. The blue dashed line is a fit to the data that includes the points associated with non-fluorinated ligands, and the red dashed line is a fit to the data that only includes the points associated with fluorinated ligands. (b) Calculated band edges renormalized by the number of ligands as computed for the three different isolated ligand/QD structural models with varying surface coverage as a function of the projected ligand dipole. (c) The energy of the highest occupied molecular orbital for isolated QDs (filled squares) and the square lattice of monolayer of QDs (open squares). The lines are guides to the eye and the larger data points represent the proposed physically accurate QD film environment - either isolated (closed squares) or inter-digitized monolayer (open squares) - for each $\text{R-CA}^-/\text{QD}$ sample based on inter-QD ligand shell electrostatic arguments as described in the text. (d) Side and (e) top view of a 3×3 repetition of the unit cell for an example $\text{R-CA}^-/\text{QD}$ monolayer. . . .	88
4.1	Energy levels for a series of silicon clusters, fully passivated by hydrogen (black lines), with one oxygen impurity at the surface (blue lines), and with a dangling bond (red lines). The abscissa shows the number of Si atoms in the cluster. . . .	94

4.2	(Color online) Semi-log plot of the calculated electron and hole coupling H_{AB}/meV between two $\text{Si}_{35}\text{H}_{36}$ nanoparticles (NPs) at 300K as a function of NP separation $R/\text{\AA}$	96
4.3	Isosurfaces of the spin-difference density of the $\text{Si}_{35}\text{H}_{36}$ - $\text{Si}_{35}\text{H}_{35}$ dimer with a dangling bond oriented away (\mathcal{A}) from the other dot. Red and blue isosurfaces represent the positive (spin up) and negative (spin down) portions of the spin-difference density respectively.	97
4.4	(Color online) Semi-log plot of computed electronic couplings H_{AB}/meV as a function of nanoparticle (NP) separation ($R/\text{\AA}$) for hole and electron transfer, when the dangling bonds (DB) are oriented either toward (\mathcal{T}) or away (\mathcal{A}) from the neighboring NP without a defect (See Figure 4.3). Results are shown for the $\text{Si}_{35}\text{H}_{36}$ - $\text{Si}_{35}\text{H}_{35}$ dimer.	98
4.5	(Color online) Semi-log plot of the computed electron and hole couplings H_{AB} between $\text{Si}_{35}\text{H}_{36}$ and $\text{Si}_{35}\text{OH}_{34}$ as a function of separation (R). The oxygen impurity is on the surface opposite of $\text{Si}_{35}\text{H}_{36}$	99
4.6	Calculated rates (k , see Eqn. 4.3) between two $\text{Si}_{35}\text{H}_{36}$ dots (Pa.), $\text{Si}_{35}\text{H}_{36}$ with $\text{Si}_{35}\text{H}_{35}$ (DB), and $\text{Si}_{35}\text{H}_{36}$ with $\text{Si}_{35}\text{H}_{34}\text{O}$ (O) separated by 3.75 \AA . Rates are presented as a function of the external reorganization energy, λ^{ext} , which is a parameter that describes the environmental response to the charge transfer process.	101
4.7	Top: Illustration of charge transfer between two NPs under the influence of image charges arising from the presence of a model electrode surface, represented by a black slab. Bottom: electronic coupling for holes (dashed) and electrons (solid) between fully passivated $\text{Si}_{35}\text{H}_{36}$ nanoparticles as a function of inter dot distance (R). Blue lines include the effects of image charges (Surface) and red lines are for isolated systems without image charges (Isolated).	104
4.8	(Color online) Ratio of charge hopping rates for fully passivated $\text{Si}_{35}\text{H}_{36}$ nanoparticles in the presence of image charges (k_{surf}) and without image charges (k_{iso}). Solid and dashed lines are for electron and hole transfer respectively. Transfer rates are computed for charges moving toward their images.	105
4.9	(a) Total energy of a H- $\text{Pb}_{28}\text{Se}_{28}$ nanoparticle, as a hydrogen atom is displaced from a Pb site (where it dopes the system p-type) to a Se site (where it dopes the system n-type), along a (100) surface facet. (b-c) Spin resolved projected density of electronic states (DOS) as a function of energy, for hydrogen at the Pb site and the Se site. The Fermi level is indicated by vertical dashed lines. The insets show the structural models of the NP: green, yellow and white spheres represent Pb, Se and H atoms, respectively.	113
4.10	Formation energy of a hydrogen atom adsorbed on the (100) facet of a $\text{Pb}_{28}\text{Se}_{28}$ NP in a positive (+1), neutral (0) and negative (-1) charge state, as a function of the Fermi energy (referred to the vacuum), for adsorption at Pb (H@Pb) and Se (H@Se) sites. Red, black and blue lines correspond to positive, neutral and negative charge states, respectively. The continuous (dashed) lines represent the most (least) stable configurations. Vertical lines represent charge transition levels. See Supplemental Information for the same diagram obtained for the (111) facet.	116

4.11	(a) Structural model (green, yellow, pink and white spheres represent lead, selenium, iodine and hydrogen atoms, respectively) and (b) Electronic density of states (DOS) for a $\text{Pb}_{55}\text{Se}_{38}\text{I}_{34}$ nanoparticle with one iodine ligand removed and one surface adsorbed hydrogen. The Fermi level is indicated by the vertical dashed line.	117
4.12	Formation energy (E_f) per number of hydrogen atoms (N_H) for a $\text{Pb}_{28}\text{Se}_{28}$ nanoparticle (NP) with several surface adsorbed hydrogen atoms. Black, red, and blue filled circles represent NPs undoped, hole doped and electron doped NPs, respectively.	119
4.13	(a) Structural model of the hydrogen-vacancy complex on the (100) facet of the $\text{Pb}_{28}\text{Se}_{28}$ nanoparticle (NP). Green, yellow, and white spheres represent lead, selenium, and hydrogen atoms, respectively. (b) Electronic density of states (DOS) of the charged vacancy ($(\text{V}_{\text{Se}})^{2+}$) and hydrogen-vacancy complex ($\text{H}_2\text{V}_{\text{Se}}$) compared to the DOS of the NP without any defect. See Supplemental Information for the same DOS obtained with the vacancy on the (111) facet.	122

LIST OF TABLES

2.1	Mean absolute error (MAE) in the vertical ionization potential of 36 closed shell molecules predicted by the highest occupied molecular orbital energy computed using the SX functional (SX) (see text), G_0W_0 starting from PBE0 wavefunctions ($G_0W_0@PBE0$), the SX hybrid functional ($G_0W_0@SX$) and PBE ($G_0W_0@PBE$). We also show the results for Hartree Fock with PBE correlation (EXXc), B3LYP[393], PBE0[326] and HSE06[218] for comparison.	15
2.2	Ionization energies (eV) for the molecules of the GW100 test set calculated with the screened exchange constant functional at the perturbative (SXP@PBE) and self-consistent (SX and ScSX) levels along with CCSD(T) and experimental values [245, 213].	26
2.3	Electronic couplings H_{AB} /meV calculated using CDFT for the HAB11[219] and HAB7[220] sets. QE, CPMD, and CP2K denote the Quantum ESPRESSO[137], CPMD[11], and CP2K[246, 172] codes, respectively. CP2K results were only available for the HAB11 set, and the molecules of the HAB7 set were not available (– above). TM and ONCV denote the Troullier-Martins[408] and optimized norm-conserving pseudopotentials[156, 366], respectively (see text). BW, BW+A, and FBB+A denote the Becke weight partitioning, Becke weight partitioning with atomic size adjustments, and fragment-based Becke weights with atomic size adjustments, respectively[172]). Two calculations carried out with QE and marked N/A did not converge without fractional occupations.	47
2.4	Mean error (ME)/meV, mean absolute error (MAE)/meV, root-mean-square deviation (RMSD)/meV, and mean absolute percent error (MAPE)/% for electronic couplings H_{AB} calculated using CDFT implemented in Quantum ESPRESSO (QE) for Troullier-Martins (QE/TM) and Optimized Norm-Conserving Pseudopotentials (QE/ONCV) and those obtained from the CPMD code[11] (see Kubas, et al[219, 220]) for the HAB11 and HAB7 sets.	49
2.5	Decay rates $(\beta)/\text{\AA}^{-1}$ for electronic couplings calculated using CDFT for the HAB11[219] and HAB7[220] sets of molecular dimers. β values were computed by fitting the results of Table 2.3 to the functional form $H_{AB} = A \exp^{-\beta R/2}$ on a log scale. QE, CPMD, and CP2K denote the codes Quantum ESPRESSO[137], CPMD[11], and CP2K[246], respectively. CP2K results were only available for the HAB11 set. TM and ONCV denote the Troullier-Martins[408] and optimized norm-conserving pseudopotentials[156, 366], respectively (see text). BW, BW+A, and FBB+A denote the Becke weight partitioning, Becke weight partitioning with atomic size adjustments, and fragment-based Becke weights with atomic size adjustments, respectively[172].	50

2.6	Mean error (ME)/ \AA^{-1} , mean absolute error (MAE)/ \AA^{-1} , root mean square deviation (RMSD)/ \AA^{-1} , and mean absolute percent error (MAPE)/% for decay rates $\beta/\text{\AA}^{-1}$ for electronic couplings calculated using CDFT implemented in Quantum ESPRESSO (QE) with Troullier-Martins (QE/TM) and Optimized Norm-Conserving Pseudopotentials (QE/ONCV) and those obtained from the CPMD code[11] (see Kubas, et al[219, 220]) for the HAB11 and HAB7 sets. β values were computed by fitting the results of Table 2.3 to the functional form $H_{AB} = A \exp^{-\beta R/2}$ on a log scale.	50
2.7	Root mean square deviation (meV) for electronic couplings H_{AB} between different implementations of constrained DFT for molecules of the HAB11 database[220]. QE, CPMD, and CP2K denote the codes Quantum ESPRESSO[137], CPMD[11], and CP2K[246, 172], respectively. TM and ONCV denote the Troullier-Martins[408] and optimized norm-conserving pseudopotentials[156, 366], respectively (see text). BW, BW+A, and FBB+A denote the Becke weight partitioning, Becke weight partitioning with atomic size adjustments, and fragment-based Becke weights with atomic size adjustments, respectively[172].	51
2.8	Mean absolute percent error (%) for electronic couplings H_{AB} between different implementations of constrained DFT for molecules of the HAB11 database[220]. QE, CPMD, and CP2K denote the codes Quantum ESPRESSO[137], CPMD[11], and CP2K[246, 172], respectively. TM and ONCV denote the Troullier-Martins[408] and optimized norm-conserving pseudopotentials[156, 366], respectively (see text). BW, BW+A, and FBB+A denote the Becke weight partitioning, Becke weight partitioning with atomic size adjustments, and fragment-based Becke weights with atomic size adjustments, respectively[172].	51
4.1	Decay constant $\beta/\text{\AA}^{-1}$ for hole and electron transfer reactions between Si nanoparticles, a $\text{Si}_{35}\text{H}_{36}$ passivated nanoparticle and one $\text{Si}_{35}\text{H}_{35}$ with the dangling bond oriented away (DB- \mathcal{A}) and towards (DB- \mathcal{T}) the neighboring $\text{Si}_{35}\text{H}_{36}$, and a $\text{Si}_{35}\text{H}_{36}$ passivated nanoparticle and one $\text{Si}_{35}\text{OH}_{34}$ with a doubly bonded oxygen oriented away (O- \mathcal{A}) from the neighboring $\text{Si}_{35}\text{H}_{36}$	99
4.2	Reorganization energies λ/eV for hole (left) and electron (right) transfer reactions. Donor and acceptor NPs are shown in rows and columns, respectively. See the Methods section for further details.	100
4.3	free energy differences $\Delta G/\text{eV}$ for hole (left) and electron (right) transfer reactions. Donor and acceptor NPs are shown in rows and columns, respectively. See the Methods section for further details.	100
4.4	The driving forces (ΔG), reorganization energies (λ), activation energies (E_{act}) and hopping rates (k_{CT} , see Eq. 4.10) at $T = 300\text{K}$ for hole transfer between NPs. Transitions are computed for NPs without a defect (NP), with a vacancy (NP+ V_{Se}) and with a vacancy passivated by hydrogen (NP+(H_2V_{Se})). $a \rightarrow b$ denotes the transition from NP a to NP b	124

ABSTRACT

The tunable optoelectronic properties of nanoparticles through the modification of their size, shape, and surface chemistry, make them promising platforms for numerous applications, including electronic and solar conversion devices. However, the rational design and optimization of nanostructured materials remain open challenges, e.g. due to difficulties in controlling and reproducing synthetic processes and in precise atomic-scale characterization. Hence, the need for accurate theoretical predictions, which can complement and help interpret experiments and provide insight into the underlying physical properties of nanostructured materials. This dissertation focuses on the development and application of first principles calculations to predict the optoelectronic properties of nanoparticles. Novel methods based on density functional theory are developed, implemented, and applied to predict both optical and charge transport properties.

In particular, the generalization of dielectric dependent hybrid functionals to finite systems is introduced and shown to yield highly accurate electronic structure properties of molecules and nanoparticles, including photoemission and absorption properties. In addition, an implementation of constrained density functional theory is discussed, for the calculation of hopping transport in nanoparticle systems. The implementation was verified against literature results and compared against other methods used to compute transport properties, showing that some methods used in the literature give unphysical results for thermally disordered systems. Furthermore, the constrained density functional theory implementation was coupled to the self-consistent image charge method, making it possible to include image charge effects self-consistently when predicting charge transport properties of nanoparticles near interfaces.

The methods developed in this dissertation were then applied to study the optoelectronic and transport properties of specific systems, in particular, silicon and lead chalcogenide nanoparticles. In the case of Si, blinking in oxidized Si nanoparticles was addressed. Si dangling bonds at the surface were found to introduce defect states which, depending on

their charge and local stress conditions, may give rise to ON and OFF states responsible for exponential blinking statistics. We also investigated, engineering of band edge positions of nanoparticles through post-synthetic surface chemistry modification, with a focus on lead chalcogenides. In collaboration with experiment, we demonstrated how band edge positions of lead sulfide nanoparticles can be tuned by over 2.0 eV. We established a clear relationship between ligand dipole moments and nanoparticle band edge shifts which can be used to engineer nanoparticles for optoelectronic applications.

Calculations of transport properties focused on charge transfer in silicon and lead chalcogenide nanoparticles. Si nanoparticles with deep defects and shallow impurities were investigated, showing that shallow defects may be more detrimental to charge transport than previously assumed. In the case of lead chalcogenide nanoparticles, hydrogen was found to form complexes with defects which can be used to remove potentially detrimental charge traps in nanoparticle solids. The methods and results presented in this dissertation are expected to help guide engineering of nanoparticles for future device applications.

CHAPTER 1

INTRODUCTION

One of the aims of molecular engineering is to design the microscopic properties of materials from the bottom up.

To achieve this goal, it is advantageous to have accurate and efficient computational methods to predict and optimize matter at the microscopic scale. By developing these methods and applying them to cutting edge nanoscience problems, in collaboration with experimentalists, results of scientific research can eventually be translated into design rules to optimize materials for device applications. Among methods for materials research from first principles, density functional theory (DFT)[205] is one of the most popular and versatile tools available for predicting structural, electronic and vibrational properties of broad classes of systems at the microscopic scale[72, 188]. Despite its success, the applicability of DFT to excited state phenomena such as carrier dynamics and optical properties has been limited[312, 14]. Extending and applying the DFT framework to optoelectronic properties of nanostructures and assemblies of nanostructured materials is the focus of this work, and it includes hybrid functional[28, 29, 221, 14] and constrained DFT method developments[104, 189].

A brief summary of the theoretical background on which this dissertation is based is given in Chapter 2 section 2.1 which focuses on density functional theory, and many body perturbation theory[357, 312, 335, 60] with an emphasis on the “GW approximation”[162]. Section 2.2 presents a functional developed in this dissertation called the screened exchange (SX) constant functional[47], for the accurate prediction of electronic and optical properties of finite systems based on density functional theory. We show that the proposed SX functional yields ionization potentials, fundamental and optical gaps of many, diverse systems in excellent agreement with experiments, including organic and inorganic molecules and semi-conducting nanoparticles and it predicts the correct alignment between energy levels of the exemplary TTF-TCNQ charge transfer system. A thorough analysis[50] of the SX functional is presented in section 2.3, where connections between hybrid density functional and many

body perturbation theory are presented. The functional described in section 2.2 is a useful tool to compute optoelectronic properties of nanostructures. However, in order to compute transport properties, additional methods need to be developed; here we focus on constrained DFT[104, 189]. An implementation[141] of constrained density functional theory including, self-consistently, the effect of contacts, is presented in section 2.4. We also present a verification of our results for sets of molecular systems and compare with other methods used in the literature. The CDFT method is then applied in Chapter 4 to study the effects of defect states on charge transport in nanoparticles[44, 422].

In Chapter 3, we present applications of the methods described in Chapter 2 to specific nanoscience problems. The first concerns nanoparticle blinking which is a ubiquitous problem and is detrimental to the performance of many nanoparticles applications[301, 55, 57, 86, 292, 420, 376, 54]. Section 3.1 focuses on blinking in oxidized Si nanoparticles and identifies the switching mechanism as the activation and deactivation of Si dangling bonds[328, 339, 341, 394, 338, 43, 340, 395, 197, 275, 192, 193, 441, 159, 30] at the surface[45]. Dangling bonds introduce defect states which, depending on their charge and local strain conditions, may give rise to ON and OFF states responsible for exponential blinking statistics. In section 3.2, we turn our attention to the engineering of nanoparticle band edges, with focus on lead chalcogenide nanoparticles[23, 68, 210, 467] which have been successfully used in solar cell devices[83, 223, 224, 249]. We show that the band edge positions of lead sulfide nanoparticles can be tuned by over 2.0 eV by surface chemistry modification[217]. Through collaboration with experiment, we established clear relationships between surface chemistry and the band edge positions. We found that in addition to ligand dipole, ligand interdigitization contributes to the band edge shifts.

In Chapter 4, we shift our attention from the optical properties of individual nanoparticles, to charge transfer and transport properties in an ensemble of nanoparticles[190]. Section 4.1 explores the effect of deep and shallow defect levels on transport, using constrained density functional theory and the self-consistent image charge method presented in section 2.4.

We show that shallow defects may be more detrimental to charge transport than deep ones, indicating the key importance of taking into account atomistic details when investigating transport properties[44]. In section 4.2, we focus on how charge transfer can be improved in lead chalcogenide nanostructured systems, by showing that hydrogen acts as an amphoteric impurity on PbSe nanoparticle surfaces and that post-synthesis hydrogen treatment of lead chalcogenide nanoparticle films is a viable approach to reduce electronic trap states or to dope well-passivated films[422]. Chapter 5 concludes the dissertation with a summary and future perspectives.

CHAPTER 2

FIRST PRINCIPLES CALCULATIONS

In this chapter, we discuss the theoretical background on which this dissertation is based, and present new method developments and codes to predict the optical and transport properties of nanoparticle systems. In section 2.1, we focus on density functional theory for ground state properties and then discuss many body perturbation theory for excited state properties. In section 2.2, we present a new method I developed called the screened exchange constant functional (SX) which is further analyzed in section 2.3 and applied to molecules and nanocrystals. Finally, in section 2.4, we discuss constrained density functional theory coupled to the self-consistent image charge method developed to take into account the effect of leads on the transport properties of materials.

2.1 Methodological Foundations

2.1.1 Density Functional Theory

Density functional theory (DFT) seeks to describe the ground state properties of a quantum mechanical system using the electron density $n(\mathbf{r})$. The first DFT for solids was proposed by L. H. Thomas [404] and E. Fermi [116] but it was the theorems by P. Hohenberg and W. Kohn [170] that gave modern DFT a firm theoretical foundation. The version of DFT that lead to modern electronic structure calculations was introduced by W. Kohn and L. Sham [206]. The Kohn-Sham single particle equations are:

$$\left(-\frac{1}{2}\nabla^2 + v_h(\mathbf{r}) + v_{xc}(\mathbf{r})\right)\phi_i(\mathbf{r}) = \epsilon_i\phi_i(\mathbf{r}) \quad (2.1)$$

where $n(\mathbf{r}) = \sum_i^{occ} |\phi_i(\mathbf{r})|^2$, is the electronic density; $v_h(\mathbf{r})$ is the Hartree potential defined as $\int d\mathbf{r}' \frac{n(\mathbf{r}')}{|\mathbf{r}-\mathbf{r}'|}$, ϵ_i is the single particle energy, $\phi_i(\mathbf{r})$ is the single particle wave function and $v_{xc}(\mathbf{r})$ is the exchange-correlation potential. The exact exchange-correlation potential is not

known and many local as well as non-local approximations to v_{xc} have been proposed in the literature [188].

The operator in Equation 2.1 depends on the density, and thus the Kohn-Sham equations need to be solved self-consistently. The single particle wave functions are then used to construct the ground state density which is used to compute the ground state properties of interacting electrons, such as the total energy.

Among the different approximations, proposed for the exchange-correlation potential, are the local[206] and semi-local functionals, e.g. the Perdew, Burke, and Enzerhof (PBE) generalized gradient approximation (GGA) [324], used in this dissertation. In addition, hybrid functionals [326, 218, 28, 462, 444, 209, 3, 305, 259, 332, 406, 75, 88, 437, 15, 180, 131, 392, 405] have been proposed which are orbital dependent and include the exact exchange self-energy;

$$\Sigma_X(\mathbf{r}, \mathbf{r}') = - \sum_j^N \phi_j(\mathbf{r}) \phi_j^*(\mathbf{r}') v(\mathbf{r}, \mathbf{r}'). \quad (2.2)$$

The hybrid potential entering the generalized Kohn-Sham formalism [370] is given by;

$$v_{xc}(\mathbf{r}, \mathbf{r}') = \alpha \Sigma_X(\mathbf{r}, \mathbf{r}') + (1 - \alpha) v_x(\mathbf{r}) + v_c(\mathbf{r}) \quad (2.3)$$

where the local exchange-correlation potential v_{xc} , of equation 2.1, has been split into two parts (v_x and v_c) and α is a constant to be chosen.

The choice of α is not straight forward. One successful example of hybrid functionals is the optimally tuned range separated hybrid [215], defined using parameters self consistently tuned to enforce the validity of Koopman's theorem [94] for molecules. However, the generalization of these functionals to solids is not a simple task [350]. Another interesting example is that of Koopmans-complaint functionals [40]. Motivated by the COHSEX approximation used within MBPT [162], an alternative class of hybrid functionals for solids referred to as dielectric dependent hybrid functionals, were introduced by equating the op-

timal mixing fraction of exact exchange with the inverse of the bulk dielectric constant. These hybrids have shown to be highly effective at determining band gaps and dielectric constants[375, 272, 5, 208, 385, 132, 386, 351].

Unfortunately, the generalization of dielectric hybrid functionals to finite systems is not straightforward, as there is no unique definition of an average dielectric constant for molecules or nanoparticles. In fact, the concept of dielectric constant of finite systems is ill defined, since the ratios of applied and induced fields differ, depending on the location and form of the probe. We note that several definitions of dielectric constants of nanoparticles have been proposed in the literature, many dependent on arbitrary volume definitions, yielding different results for the same system [109, 158] depending on the chosen definition of the volume. In Section 2.2, the generalization of dielectric dependent hybrid functionals to finite systems is presented. Before doing so, we briefly summarize many body perturbation theory, used throughout this dissertation.

2.1.2 Many Body Perturbation Theory

In this work, many body perturbation theory is used to compute quasiparticle corrections to Kohn-Sham eigenvalues. The quasiparticle equation is given by

$$H_{QP}\phi_i^{QP} = \epsilon_i^{QP}\phi_i^{QP} \quad (2.4)$$

where the quasiparticle Hamiltonian H_{QP} is obtained by replacing the exchange-correlation potential, v_{xc} in equation 2.1, with the self-energy operator;

$$\Sigma = iGW\tilde{\Gamma} \quad (2.5)$$

where G is the interacting one-particle Green's function, W is the screened coulomb interaction, and $\tilde{\Gamma}$ is the irreducible vertex given by, $\frac{\delta G^{-1}}{\delta V_{cl}}$ where V_{cl} is the total classical potential (external plus Hartree potential). Within the GW approximation, $\tilde{\Gamma}$ is equal to the identity

yielding:

$$\Sigma(\mathbf{r}, \mathbf{r}'; \omega) = i \int \frac{d\omega'}{2\pi} G(\mathbf{r}, \mathbf{r}'; \omega + \omega') W_{RPA}(\mathbf{r}, \mathbf{r}'; \omega') \quad (2.6)$$

where W_{RPA} is the screened Coulomb interaction obtained in the random phase approximation (RPA) and is defined as $W_{RPA}(\mathbf{r}', \mathbf{r}) = \int d\mathbf{r}'' \epsilon^{-1}(\mathbf{r}', \mathbf{r}'') v(\mathbf{r}'', \mathbf{r})$, where $\epsilon^{-1}(\mathbf{r}', \mathbf{r}'')$ is the static inverse dielectric matrix. $G(\mathbf{r}, \mathbf{r}', \tau)$ is the Green's function. Using the Kohn-Sham wavefunctions and eigenvalues, the Green's function can be written as:

$$G(\mathbf{r}, \mathbf{r}', \omega) = \sum_j \frac{\phi_j(\mathbf{r}) \phi_j^*(\mathbf{r}')}{\omega - \epsilon_j + i\eta \text{sign}(\epsilon_j - \epsilon_F)} \quad (2.7)$$

where η is a small positive quantity, ϵ_F is the Fermi energy, ϕ_j is the j th Kohn-Sham single-particle wavefunction, ϵ_j is the j th the Kohn-Sham eigenvalue. ϵ^{-1} may be evaluated at different levels of theory; here we used the random phase approximation [312], where $\epsilon^{-1} = 1 + v\chi$, where χ is the full polarizability. Within RPA, χ is given by $\chi = (1 - v\chi_o)^{-1} \chi_o$ where χ_o is the independent-particle polarizability given by:

$$\chi_o(\mathbf{r}, \mathbf{r}') = \sum_{i,j} \frac{f_i(1 - f_j)}{\epsilon_i - \epsilon_j} [\phi_i^*(\mathbf{r}) \phi_j(\mathbf{r}) \phi_j^*(\mathbf{r}') \phi_i(\mathbf{r}') + \text{c.c.}] \quad (2.8)$$

In practice, to obtain the quasiparticle corrections to the Kohn-Sham energy eigenvalues, the quasiparticle energies ϵ_i^{QP} are evaluated perturbatively as corrections to the Kohn-Sham energy eigenvalues:

$$\epsilon_i^{QP} = \epsilon_i + \langle \Sigma(\epsilon_i^{QP}) - v_{xc} \rangle \quad (2.9)$$

Both sides of the equation depend on ϵ_i^{QP} therefore the solution to equation 2.9 is normally obtained recursively using the secant method.

Once obtained, the quasiparticle energies are used to predict spectroscopic properties

such as the ionization potentials and electron affinities from experiment.

2.2 The Generalization of Dielectric Dependent Hybrid Functionals to Finite Systems

In this section, the generalization of dielectric dependent hybrid functionals to finite systems is introduced, where the definition of the mixing fraction of exact and semi-local exchange is physically motivated, nonempirical and system-dependent. We will compare this method against the results of the GW approximation, summarized in the previous section, and demonstrate that the proposed functional yields ionization potentials, fundamental and optical gaps of many, diverse molecular systems in excellent agreement with experiments, including organic and inorganic molecules and semiconducting nanoparticles. We will further demonstrate that this hybrid functional gives the correct alignment between energy levels of the exemplary TTF-TCNQ donor-acceptor system.

2.2.1 Introduction

Reprinted with permission from Nicholas P. Brawand, Márton Vörös, Marco Govoni, and Giulia Galli, *Physical Review X*, **6**, 041002 2016. Copyright (2016) by the American Physical Society.

As mentioned in the introduction, current first principles methods to predict the electronic and optical properties of solids and nanostructures are mainly based on density functional theory (DFT) [205, 72] and many body perturbation theory (MBPT) [357, 312, 335, 60]. In the case of molecules, methods adopted for their opto-electronic properties include ab initio quantum chemistry (QC) techniques [163, 18, 185, 123] and hybrid density functionals [28, 29, 221, 14]. While QC and MBPT methods have proven accurate for several classes of molecules and solids [39, 26], they remain computationally more demanding than DFT based techniques; they are limited to smaller sized systems and they have rarely been applied in

conjunction with ab initio molecular dynamics or Monte Carlo simulations.

While calculations of electronic excitation energies of solids rely mostly on single-particle energies, obtained within either DFT or MBPT, those for molecules encompass single-particle energies and total energy differences. A popular and rather accurate method, especially for small molecules, is the so-called delta self-consistent field method (Δ SCF) [273]; ionization potentials and electron affinities are obtained as total energy differences of the neutral and charged molecule, where an electron is either removed or added. Total energies may be obtained at different levels of theory, either with DFT or QC techniques. However, the Δ SCF method is limited to obtaining bound frontier orbital energies, and it cannot be easily generalized to solids [76]. In addition, it is not suitable for the calculation of energy level alignment between different molecules or nanoparticles in close proximity with each other, and hence to study charge transfer processes. Therefore, the search for density functionals yielding accurate electronic properties and in particular single-particle energies of broad classes of condensed and finite systems is an active field of research, impacting applications ranging from materials discovery to the interpretation of spectroscopic and transport measurements.

As mentioned previously, dielectric dependent hybrids are highly accurate for describing band gaps, dielectric constants and lattice constants of solids [375, 272, 5, 208, 385, 132, 386, 351]. Here, we present a generalization of dielectric dependent hybrid functionals to molecules and nanostructures, where we overcome the problem of introducing a dielectric constant of finite systems, by using a mixing fraction of exact and semi-local exchange defined as the ratio of the screened and unscreened exchange energies. Such ratio reduces to the inverse dielectric constant in the bulk limit. We show that the proposed functional yields ionization potentials, fundamental as well as optical gaps of molecular systems in excellent agreement with experiments, including organic and inorganic molecules and semiconducting nanoparticles. We further demonstrate that this hybrid functional yields the correct alignment between energy levels of the exemplary Tetrathiafulvalene-Tetracyanoquinodimethane (TTF-TCNQ) donor-acceptor system.

2.2.2 Theory

As mentioned above, the concept of a dielectric constant is ill defined for finite systems, and so is the volume. Hence in order to generalize dielectric dependent hybrid functionals to molecules, and in general to finite systems, we do not attempt to generalize the concept of dielectric constant used for condensed systems. Rather, we start from approximate forms of the self-energy obtained within MBPT, at the GW level [162] and we define a non empirical system dependent fraction of exact and semi-local exchange.

To obtain the mixing fraction of exact exchange, we approximate the quasiparticle GW self-energy, presented in the previous section, assuming that the screened Coulomb interaction W is static (i.e. frequency independent):

$$\Sigma_{GW}(\mathbf{r}, \mathbf{r}') \approx \frac{i}{2\pi} \int d\tau G(\mathbf{r}, \mathbf{r}', \tau) W(\mathbf{r}', \mathbf{r}) \delta(\tau + \gamma) e^{i\omega\tau} \quad (2.10)$$

Under the static approximation Eq. 2.10 becomes [59]:

$$\Sigma_{GW}(\mathbf{r}, \mathbf{r}') \approx \Sigma_{SX}(\mathbf{r}, \mathbf{r}') \quad (2.11)$$

where,

$$\Sigma_{SX}(\mathbf{r}, \mathbf{r}') = - \sum_j^N \phi_j(\mathbf{r}) \phi_j^*(\mathbf{r}') W(\mathbf{r}, \mathbf{r}'). \quad (2.12)$$

is the screened exchange self-energy; N is the the number of occupied electronic states. We then assume that the non-local screened exchange term is proportional to the Hartree-Fock exchange, as obtained using KS single-particles:

$$\Sigma_{SX}(\mathbf{r}, \mathbf{r}') = \alpha \Sigma_X(\mathbf{r}, \mathbf{r}') \quad (2.13)$$

where $\Sigma_X(\mathbf{r}, \mathbf{r}')$, repeated here for convenience, is given by:

$$\Sigma_X(\mathbf{r}, \mathbf{r}') = - \sum_j^N \phi_j(\mathbf{r}) \phi_j^*(\mathbf{r}') v(\mathbf{r}, \mathbf{r}'). \quad (2.14)$$

From Eq. 2.13 we define the state dependent screened exchange constant α_i^{SX} :

$$\alpha_i^{\text{SX}} = \frac{\langle \phi_i | \Sigma_{\text{SX}} | \phi_i \rangle}{\langle \phi_i | \Sigma_X | \phi_i \rangle} \quad (2.15)$$

Finally, we define the global screened exchange constant (SX) that will be used as the mixing fraction of exact exchange:

$$\alpha^{\text{SX}} = \frac{\sum_i^N \langle \phi_i | \Sigma_{\text{SX}} | \phi_i \rangle}{\sum_j^N \langle \phi_j | \Sigma_X | \phi_j \rangle}, \quad (2.16)$$

Note that, α^{SX} (Eq. 2.16), does not depend on any arbitrary volume definitions. The exchange correlation potential entering the generalized Kohn-Sham formalism [370] is obtained as:

$$v_{xc}(\mathbf{r}, \mathbf{r}') = \alpha^{\text{SX}} \Sigma_X(\mathbf{r}, \mathbf{r}') + (1 - \alpha^{\text{SX}}) v_x(\mathbf{r}) + v_c(\mathbf{r}) \quad (2.17)$$

where v_x and v_c are semi-local exchange correlation potentials, here chosen to be described within the PBE [325] approximation. Hereafter we refer to this functional as the SX hybrid functional. We note that Eq. 2.17 could be evaluated self-consistently, along the lines proposed in Ref. [385]. We also note that the use of Eq. 2.17 with the definition given in Eq. 2.16 is not size consistent. Size consistency will be addressed in future investigations.

In the case of condensed systems, if every element of the inverse dielectric matrix $\epsilon_{\mathbf{G}, \mathbf{G}'}^{-1}$ is replaced by the inverse of the macroscopic dielectric constant ϵ_∞^{-1} , the screened exchange constant reduces to the inverse of the macroscopic dielectric constant,

$$\alpha^{\text{SX}} = \epsilon_\infty^{-1} \quad (2.18)$$

and the SX functional reduces to the dielectric dependent hybrid functional.

2.2.3 Results

In this section we summarize the properties computed using the SX functional along with the computational details of our calculations. We report electronic properties corresponding to charged and neutral excitations, in particular vertical ionization potentials and fundamental gaps, typically measured in photoemission experiments, and absorption gaps and spectra. For both types of excitations, we first determined the ground state total energy and single-particle energies within DFT, at the PBE level of theory. The screened exchange constant (Eq. 2.15) was then evaluated for the highest occupied molecular orbital, and used to define the mixing fraction of exact exchange entering the global hybrid definition (Eq. 2.17).

Vertical ionization potentials and electron affinities of the G2 set and of TTF and TCNQ were computed using the single-particle energies obtained from the self-consistent solution of the Kohn-Sham equations with the global hybrid defined by Eq. 2.17. The fundamental gaps of the Si nanoparticles, and the vertical ionization potentials of Thiel’s test set were obtained in the same way. Absorption properties (i.e. optical gaps) of the Thiel’s test set were instead computed using time dependent density functional theory, as implemented in Quantum-Espresso in the the turboTDDFT code [130]. We used the latter code to solve the TDDFT equations in the adiabatic approximation, where the exchange-correlation potential was described by the functional of Eq. 2.17. We note that the evaluation of empty electronic states is not necessary in TDDFT calculations, when following the procedure of Ref. [130].

As mentioned previously, all results reported in this section were obtained using the mixing parameter from Eq. 2.15 where i is the index of the highest occupied molecular orbital (HOMO). The values of $\alpha_{i=\text{HOMO}}^{\text{SX}}$ and α^{SX} from Eq. 2.16 were found to be very similar for all the systems studied here; for example, we found a maximum difference ($\alpha_{i=\text{HOMO}}^{\text{SX}} - \alpha^{\text{SX}}$) of 0.06 for the G2/97 test set [93] described below, with an average difference of 0.02. In the case of silicon nanoparticles, the difference between $\alpha_{i=\text{HOMO}}^{\text{SX}}$ and α^{SX} decreases as the size

of the system increases, leading to $\alpha_{i=\text{HOMO}}^{\text{SX}} \approx \alpha^{\text{SX}}$ for $\text{Si}_{86}\text{H}_{76}$.

We note that the application of the SX functional consists of a single hybrid calculation for neutral systems, unlike the functionals of Ref. [215] and [94] which require multiple calculations of neutral and ionized systems. In addition, the use of SX is computationally less demanding than GW calculations, as frequency dependent dielectric matrices are not required. Once the screened exchange constant is obtained (using, e.g. the WEST code [146]), SX calculations of absorption and photoemission properties may be performed by any DFT code, where global hybrid functionals and TDDFT methods are available.

First we studied the ionization potentials and fundamental gaps of several molecules and nanoparticles and compared our results with those obtained with MBPT techniques and several other global hybrid methods. We then used Eq. 2.17 to compute optical properties within the framework of time dependent density functional theory, and we show below that remarkably the SX functional yields excellent results for both photoemission and optical gaps of a variety of molecules.

A common benchmark for GW calculations [60] is the evaluation of vertical ionization potentials of different subsets of the G2/97 data set [359, 62, 333]. Here we chose a subset consisting of 36 closed shell molecules [146]. The calculated vertical ionization potentials, i.e., the negative of the highest occupied molecular orbital energies obtained using Eq. 2.17 and the mean absolute error (MAE) with respect to the experimental values are presented in Fig. 2.1 and Table 2.1. All GW calculations were performed using the WEST code and the hybrid functional calculations using the Quantum Espresso software package [146, 134]; we employed norm-conserving pseudopotentials. A wavefunction energy cutoff of 85 Rydbergs was used for all molecular systems, except $\text{Si}_{35}\text{H}_{36}$, $\text{Si}_{66}\text{H}_{64}$ and $\text{Si}_{87}\text{H}_{64}$, for which we used 25 Rydbergs. Molecular geometries for the G2 test set and experimental vertical ionization potentials were taken from the NIST Computational Chemistry Comparison and Benchmark DataBase [304]. Molecular geometries for Thiel’s test set were taken from Ref. [369]. Single particle energies were referred to vacuum using the Makov-Payne correction scheme [264].

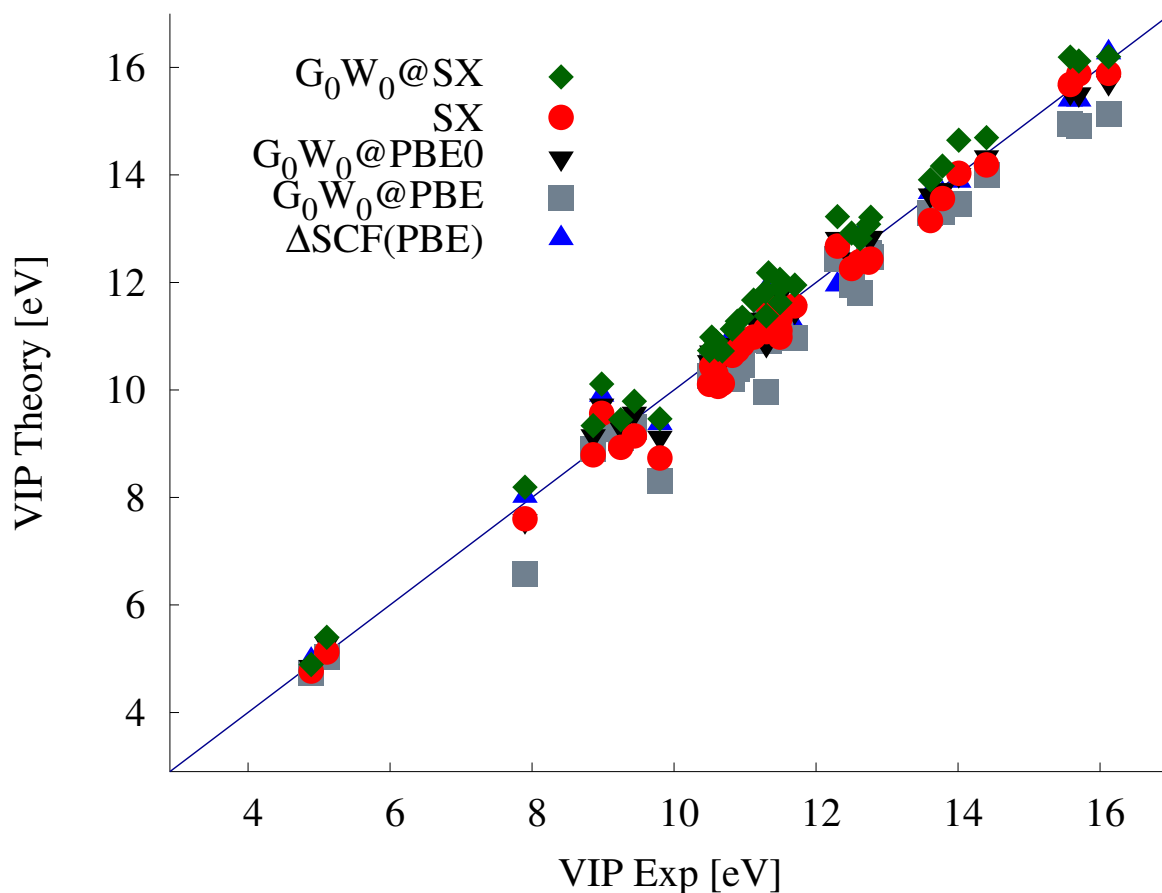


Figure 2.1: (Color online) Vertical ionization potentials (VIP) of the G2/97 subset consisting of 36 closed shell molecules computed as the highest occupied molecular orbital energy using the SX hybrid functional (SX), G_0W_0 starting from PBE wavefunctions ($G_0W_0@PBE$)[‡] and SX wavefunctions ($G_0W_0@SX$) and total energy differences ($\Delta SCF(PBE)$)[†]. [‡] data from Ref. [146] [†] data from Ref. [359]

In most cases, results obtained with the SX functional lie between those obtained at the G_0W_0 level of theory, with either PBE or SX wavefunctions, and they are in very good agreement with the experimental values and the $G_0W_0@PBE0$ results. In order to compare the results of the different levels of theory in a statistically meaningful way, we used a Wilcoxon signed-rank test [446] as implemented in the R package [346], and we compared the absolute errors of the SX functional and the popular $G_0W_0@PBE$ method; we found a p-value less than 0.043 and a 95% confidence interval of [0.01, 0.28] eV, indicating that the SX functional is more accurate than $G_0W_0@PBE$ on average for molecules which this subset

Method	MAE [eV]
$G_0W_0@PBE0^\ddagger$	0.19
SX	0.28
$G_0W_0@SX$	0.38
$G_0W_0@PBE^\ddagger$	0.44
$EXXc^\ddagger$	1.50
$B3LYP^\ddagger$	2.78
$PBE0^\ddagger$	2.87
$HSE06^\ddagger$	3.27
$PBE^\ddagger (\Delta SCF)^\dagger$	4.29 (0.24)
‡ data from Ref. [146]	
† data from Ref. [359]	

Table 2.1: Mean absolute error (MAE) in the vertical ionization potential of 36 closed shell molecules predicted by the highest occupied molecular orbital energy computed using the SX functional (SX) (see text), G_0W_0 starting from PBE0 wavefunctions ($G_0W_0@PBE0$), the SX hybrid functional ($G_0W_0@SX$) and PBE ($G_0W_0@PBE$). We also show the results for Hartree Fock with PBE correlation (EXXc), B3LYP[393], PBE0[326] and HSE06[218] for comparison.

is representative of. We note that popular hybrid functionals such as PBE0 and B3LYP, have fixed mixing fractions (α) below 0.50, rather different from the average value provided by Eq. 2.15 for the molecules studied here, i.e. $\alpha=0.72$ with a range of $\Delta\alpha=0.19$. This average mixing fraction is similar to the optimal mixing fraction reported in a previous study for the G3/99 test set [286]. In addition, Eq. 2.16 also yields similar mixing fractions as those of Ref. [12] and provides a physical justification to the results reported by Atalla et al. [12], which were obtained by self consistently fitting hybrid functional results to those of GW calculations.

A smaller fraction of exact exchange than given by Eq. 2.15, severely overestimates the amount of screening present in molecular systems, which in turn results in the poor performance, on this benchmark, of global hybrid functionals such as B3LYP, PBE0, as well as the range separated hybrid HSE06. However, we note that these and some semi-local functionals may yield more accurate predictions when total energy differences of neutral and ionized systems are considered [93, 359], instead of the eigenvalues of the neutral molecule; especially so for B3LYP, originally designed to yield total energies, not accurate response

properties from orbital energies. For example, Δ SCF calculations at the PBE level of theory yield a MAE of 0.24 eV for the G2 test set [359].

Small mixing fractions have also been shown to yield incorrect energy level alignments for several molecular systems. For example, it was found that functionals with $\alpha < 0.30$ predict spurious amounts of charge transfer for the TTF ($C_6H_4S_4$) and TCNQ ($C_{12}H_4N_4$) donor-acceptor system [12]. A correct charge transfer is obtained if the difference (Δ) between the lowest unoccupied molecular orbital (LUMO) of TCNQ and the HOMO of TTF is positive, in the limit of infinite separation between the two molecules. The mixing fractions predicted by Eq. 2.15 for TTF and TCNQ are 0.63 and 0.61 respectively. Evaluated at the average mixing fraction (0.62), the SX functional predicted $\Delta > 0$, with $\varepsilon_{LUMO}^{TCNQ} = -4.32$ and $\varepsilon_{HOMO}^{TTF} = -6.15$ eV. The mixing fraction which minimizes the deviation from straight line error was shown to be 0.70 for TCNQ and 0.8 for TTF [71, 13], not dissimilar from the values predicted by Eq. 2.15. Benzene is an additional example where a larger mixing fraction ($\alpha > 0.25$) was reported to be advantageous. In Ref. [362] a mixing fraction of $\alpha = 0.70$ for benzene was found to minimize the many-electron self-interaction error. Using Eq. 2.15, we found $\alpha_{i=HOMO}^{SX} = 0.67$.

We now turn to investigate how different levels of theory, including Eq. 2.17, perform as the size of the system is varied. In Fig. 2.2 we present the fundamental gaps of several hydrogen passivated silicon nanoparticles predicted using the SX functional. For most of the molecules in Fig. 2.1, the results obtained using Eq. 2.17 lie between those of $G_0W_0@PBE$ and $G_0W_0@SX$; these findings are similar to those of Fig. 2.2 with the addition that the quasiparticle corrections to the SX eigenvalues decrease as the size of the system increases. In contrast, we found the fundamental gaps predicted by Δ SCF(PBE) to fall consistently below those of $G_0W_0@PBE$ by an average value of 0.67 eV. Also provided in Fig. 2.2, are the mixing values predicted by Eq. 2.15, which increase as the size of the system decreases. This variation is related to the magnitude of electronic screening [149, 426] and of the quasiparticle corrections, consistent with predictions of previous works [355, 146, 107]; we note that the SX

hybrid proposed here, is the first global hybrid functional to yield such an a priori prediction of the magnitude of quasiparticle energy corrections as a function of system size.

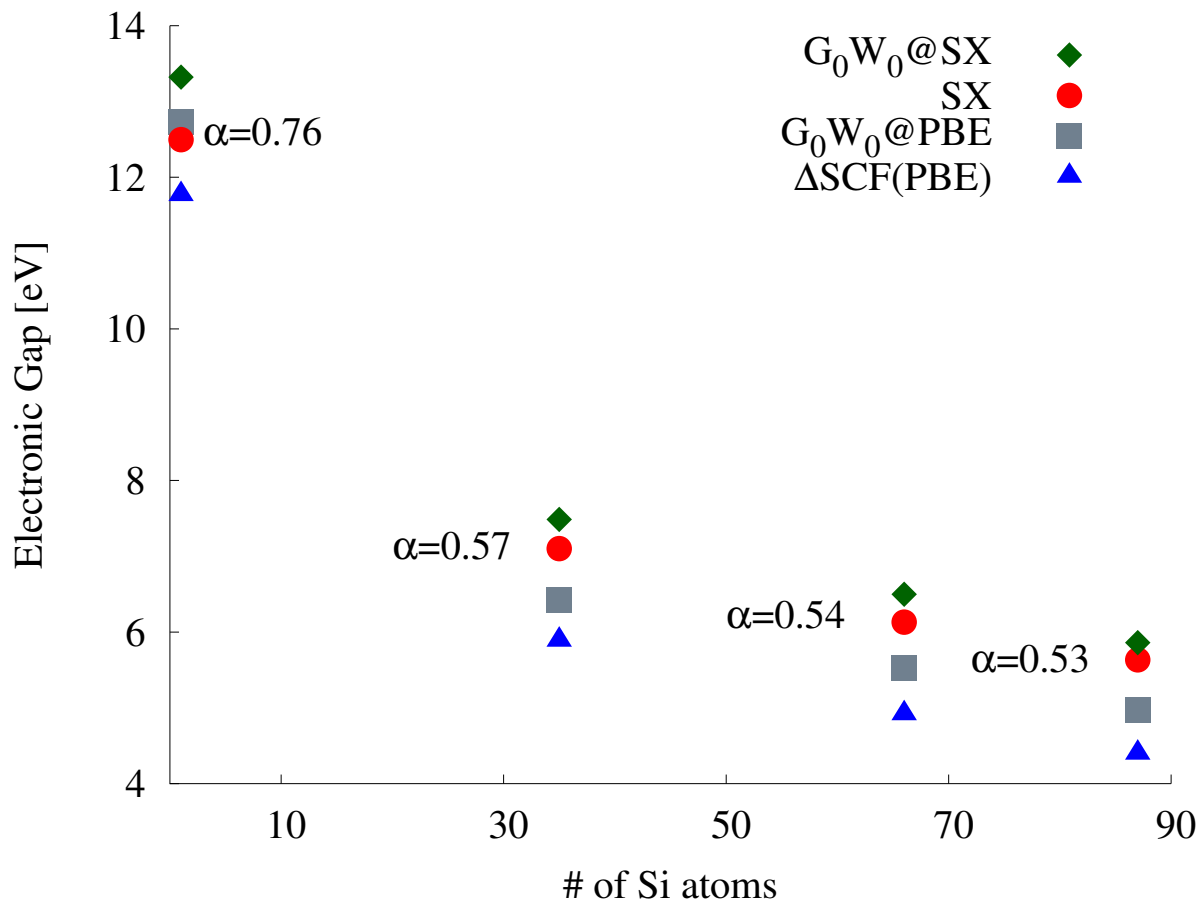


Figure 2.2: (Color online) The fundamental gaps of several hydrogen passivated silicon nanostructures SiH_4 , $Si_{35}H_{36}$, $Si_{66}H_{64}$ and $Si_{87}H_{64}$ predicted using the SX hybrid functional (see text), G_0W_0 starting from PBE wavefunctions ($G_0W_0@PBE$) and SX wavefunctions ($G_0W_0@SX$). Fundamental gaps obtained from total energy differences ($\Delta SCF(PBE)$) are included for comparison.

The improvement of the accuracy of adiabatic time dependent density functional theory is an area of active research in condensed matter physics and physical chemistry [117, 465, 125, 31, 352, 354, 130]; hence we explored the application of Eq. 2.17 to time dependent density functional theory (TDSX) and we show below that the SX functional can correctly reproduce not only ionization energies and fundamental gaps, but also optical gaps. In Fig. 2.3, we compare the first lowest optical singlet excitations predicted by TDSX with the revised best

theoretical estimates for the Thiel’s test set, as obtained from reference literature values and quantum chemistry calculations, e.g. coupled cluster [384]. Thiel’s test set consists of 28 molecules and was recently used for benchmarking state-of-the-art many body perturbation theory techniques based on the Bethe-Salpeter-Equation (BSE) and the GW approximation [181, 61]. [182] found TDPBE0 to be exceptionally accurate for this set with the lowest mean absolute error compared to 28 exchange correlation functionals. The mean absolute errors of the lowest optical singlet transitions predicted by TDSX are presented in Fig. 2.4, which shows that the SX functional performs almost as well as TDPBE0 for optical transitions. Also presented in Fig. 2.4 are the vertical ionization potentials (i.e. the highest occupied molecular orbital energies) for the same molecules. Importantly, the SX functional captures the physics of both quasiparticle and excitonic effects yielding accurate photoemission and optical properties.

A statistical analysis of the results for both the photoemission and absorption properties. Although TDPBE0 appears to outperform almost every other technique to describe optical excitations, the single-particle energies of the same functional (PBE0) fail to describe vertical ionization potentials as seen in the G2/97 and the Thiel’s test sets. This result suggests that TDPBE0 underestimates both quasiparticle and excitonic effects, resulting in a fortuitous cancellation of errors for these systems. We find $G_0W_0@PBE0$ is accurate for vertical ionization potentials, while the mean absolute error of optical excitations obtained from the solution of the Bethe Salpeter Equation (BSE) is larger than that of TDSX. Remarkably, the SX functional captures the physics of both quasiparticle and excitonic effects yielding accurate photoemission and optical properties.

In summary, in this section, we generalized the concept of dielectric dependent functionals to finite systems by defining a global hybrid functional (which we called the SX functional) with a mixing parameter between exact and local exchange that is non-empirical, and system dependent. We showed that the SX functional yields accurate results for both photoemission and optical properties of a variety of organic and inorganic molecules; in addition it yields the

most accurate combined results (charged and neutral excitations) compared to other global hybrid functionals and methods based on MBPT, while being computationally cost effective as compared to G_0W_0 calculations. We also demonstrated that the SX functional gives the correct alignment between energy levels of the exemplary TTF-TCNQ donor-acceptor system which many first principles or semi-empirical DFT based schemes proposed in the literature failed to reproduce. Finally, we presented a detailed statistical analysis of the data, in order to assess the accuracy of the proposed functional for molecules beyond the test sets investigated in this section.

2.3 Self-Consistency of the Screened Exchange Constant Functional

This section builds on the hybrid developments of the previous one. Here, we present an analysis of the performance of the screened exchange constant functional, defined section 2.2, at varying levels of self-consistency; no self-consistency, wave function self-consistency and screening self-consistency. We compare all three methods against CCSD(T) and experimental reference values and find them to be exceptionally accurate. We find that wave function self-consistency is especially important for ionic molecules. Lastly, we recast the SX self-consistent procedure in terms of a minimization problem and show that it converges to a mixing fraction of exact exchange which minimizes the starting point dependency of the G_0W_0 approximation.

2.3.1 Introduction

Reprinted with permission from Nicholas P. Brawand, Marco Govoni Márton Vörös, and Giulia Galli Unpublished. Copyright 2017 American Chemical Society.

As mentioned in the previous section, the mixing fraction of exact exchange of global DDH functionals is determined by the inverse dielectric constant. Such definition is well posed

for solids, but not for finite systems [47]. In the previous section, we generalized the DDHs to finite systems by defining the state dependent screened exchange constant. The screened exchange constant from Equation 2.15 was shown to yield accurate ionization potentials, fundamental gaps and optical gaps for a wide variety of molecules and nanoparticles[47]. We computed the average absolute difference between the state averaged screened exchange constant $\alpha = \frac{\sum_i \langle \phi_i | \Sigma_{\text{SEX}} | \phi_i \rangle}{\sum_j \langle \phi_j | \Sigma_{\text{X}} | \phi_j \rangle}$ and the one evaluated for the highest occupied orbital for the GW100 test set and we found it to be 0.03.

Here we analyze the performance of the functional defined in Equation 2.17 at different levels of self-consistency. In particular, we consider a perturbative approach (SXP) where, starting from PBE wave functions and eigenvalues, we obtain improved single particle energies as:

$$\epsilon_i^{\text{SXP@PBE}} = \epsilon_i^{\text{PBE}} + \alpha^{\text{SX}} \langle \phi_i | \Sigma_{\text{X}} - v_x^{\text{PBE}} | \phi_i \rangle \quad (2.19)$$

where ϵ_i^{PBE} and v_x^{PBE} are the PBE eigenvalues and exchange potential, respectively. This approach is reminiscent of the G_0W_0 perturbative method where quasiparticle energies are given by $\epsilon_i^{\text{GW}} = \epsilon_i^{\text{PBE}} + \langle \phi_i | \Sigma_{\text{GW}} - v_{xc}^{\text{PBE}} | \phi_i \rangle$ where Σ_{GW} is the GW self-energy[162]. We then consider two self-consistent approaches using the SX functional, which differ in the way α is computed: from PBE wavefunctions (SX) or fully self-consistently (ScSX).

2.3.2 Results

Calculations were performed using the Quantum-ESPRESSO software package[134] and Optimized Norm-Conserving Vanderbilt (ONCV) pseudopotentials.[157, 367] The screened exchange constant was computed with the WEST code.[146] Molecular geometries were taken from reference [[416]]. Energy cutoffs, were the same as those used to generate the GW100 data collection using the WEST code[145]; they were determined so that the energy of the highest occupied molecular orbital was converged to within 10 meV in a box size of 25 Å.

Single particle energies were referred to the vacuum level using the Makov-Payne[264] correction scheme. Eigenpotentials and eigenvalues (λ_i) of the dielectric matrix were calculated within the random phase approximation (RPA) using the projective dielectric eigendecomposition algorithm[447, 448, 293, 334] as implemented in the WEST code.[146] The number of eigenpotentials for each system was chosen to be 20 times the number of electrons. Many body perturbation theory and experimental[245] ionization potentials are from the WEST data collections[145]. CCSD(T) reference values were taken from reference [[213]].

We begin our analysis of the SX method with an overview of the overall performance compared to experiment and CCSD(T) on the GW100 test set. We then show that when achieving full self-consistency, the mixing fraction of ScSX converges to a value such that $\langle \phi_i | \Sigma_{\text{GW}} - v_{xc} | \phi_i \rangle \approx 0$ when v_{xc} is computed with wave functions obtained using ScSX. In other words the mixing fraction of ScSX converges to a value which corresponds to vanishing G_0W_0 quasiparticle corrections to the KS eigenvalues.

Here we excluded four molecules (boron nitride, copper cyanide, xenon, titanium tetrafluoride) from the GW100 set, for which experimental or CCSD(T) reference results are not available. We note that, many molecules in the GW100 test set do not have experimental reference values and CCSD(T) reference results available for the LUMO. For this reason, we focused only on the ionization potential. The accuracy of the SX functional to predict electron affinities, fundamental and optical gaps, has been considered in our previous work.[47]

We first present the error of perturbative and self-consistent SX for ionization potentials, with respect to CCSD(T). We then validate our results with experiments. These data are illustrated in Figure 2.5 and reported in Table 2.2. The error in the ionization potential is defined as:

$$\text{Error}_i = \text{IP}_i^{\text{F}} - \text{IP}_i^{\text{R}} \tag{2.20}$$

where IP_i^{R} and IP_i^{F} are the reference ionization potential (R), either CCSD(T) and exper-

iment, for the i -th molecule and and the same quantity computed with the functional (F), respectively. Using this definition, a negative error indicates an underestimate of the reference ionization potential. In addition to the error, we also provide the mean absolute error (MAE), the mean error (ME) and the standard deviation of the errors (STD). The MAE is given by

$$\text{MAE} = \frac{1}{N} \sum_i |\text{Error}_i| \quad (2.21)$$

where N is the total number of data included in the sum. Likewise the ME and STD are given by $\text{ME} = \frac{1}{N} \sum_i \text{Error}_i$ and $\text{STD} = \sqrt{\frac{1}{N} \sum_i (\text{Error}_i - \text{ME})^2}$ respectively. Lastly, we include $G_0W_0@PBE$ results[148] to provide a broader perspective on the accuracy of the SX functional.

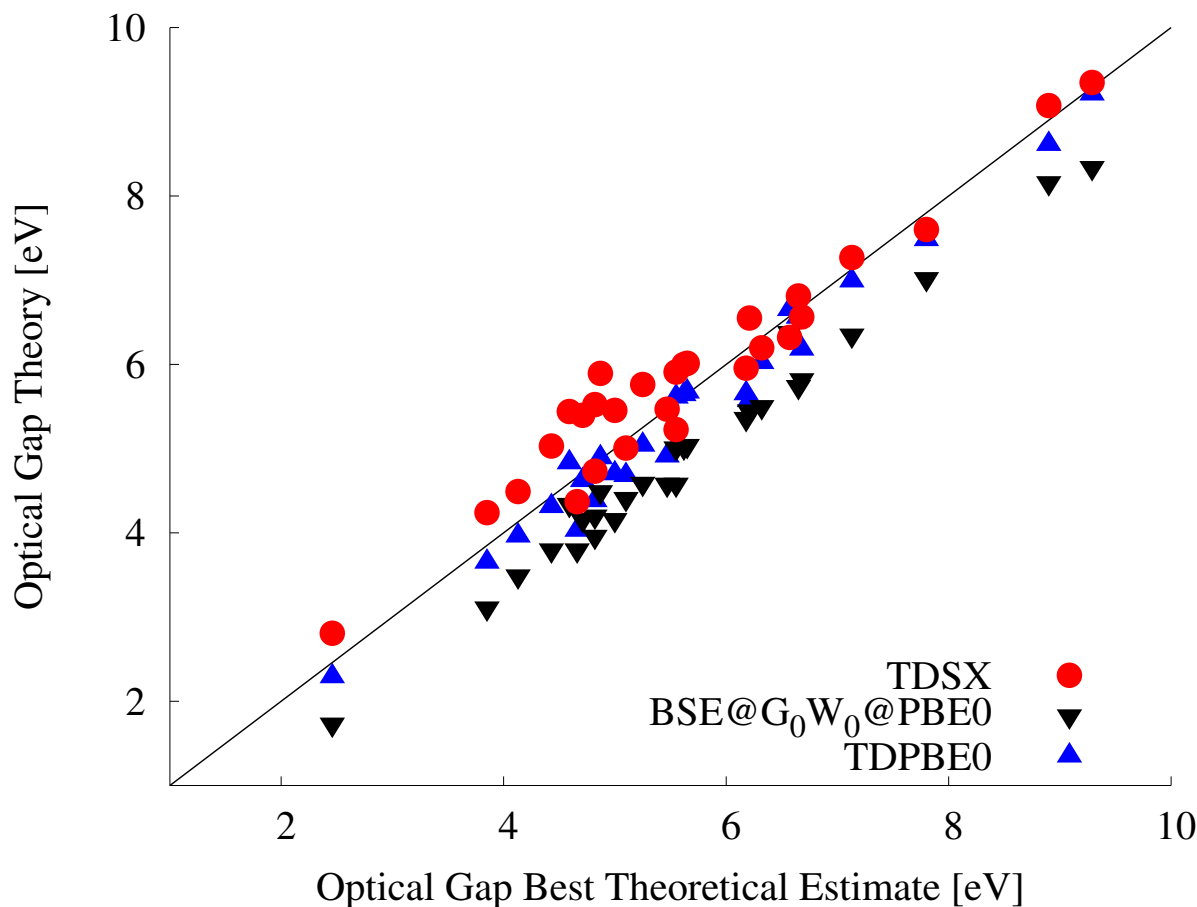


Figure 2.3: (Color online) The first lowest optical singlet excitations predicted by the time dependent SX hybrid functional method (TDSX) compared to the revised best theoretical estimates (see text) of Thiel’s test set for 28 molecules. Values predicted for the same transitions by TDPBE0 (time dependent density functional calculations with the PBE0 functional) and BSE@G₀W₀@PBE0 (results from the solution of the Bethe Salpeter Equation (BSE), starting from single-particle energies computed at the G₀W₀ level of theory, with DFT results obtained with the PBE0 functional) are taken from Ref. [181].

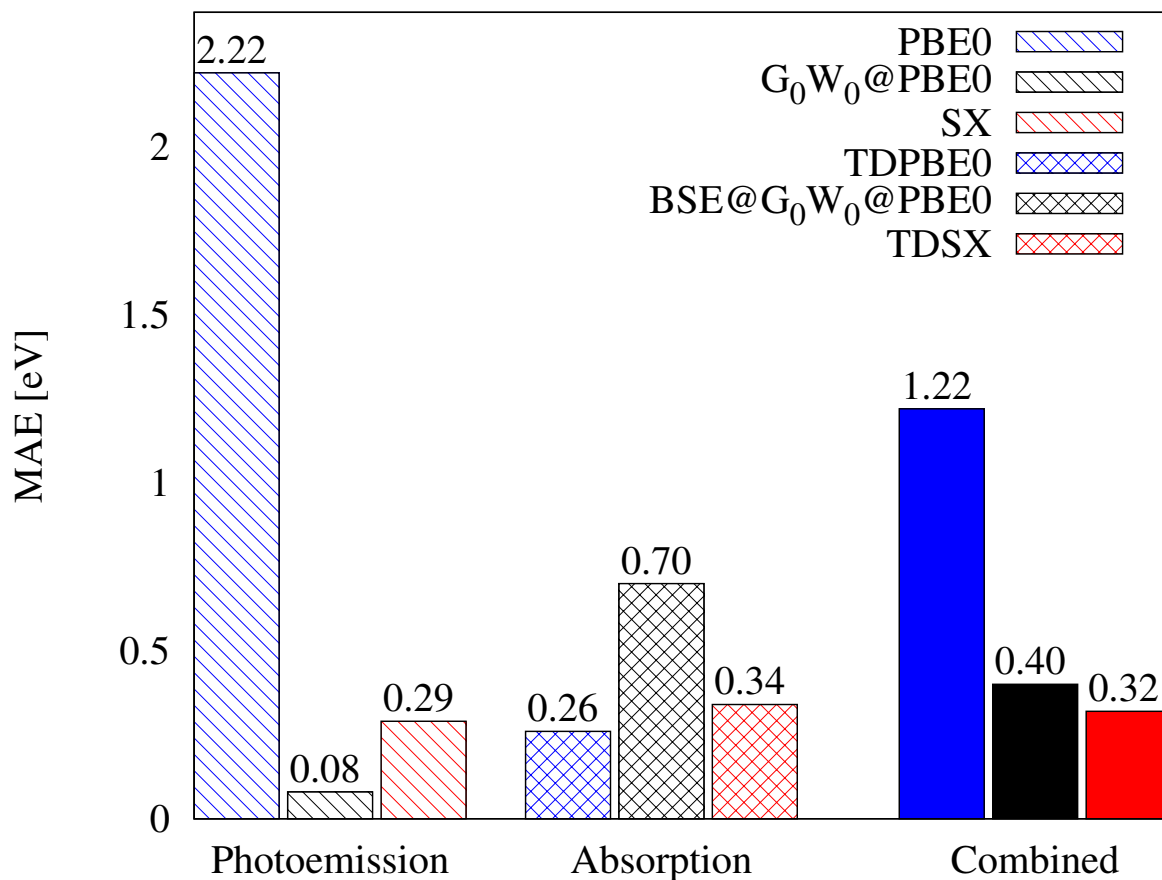


Figure 2.4: (Color online) Mean absolute errors (MAE) for (left to right): the ionization potentials (Photoemission) of Thiel’s test set (with the exception of propanamide due to lack of experimental data) predicted by the highest occupied molecular orbital energy computed using PBE0, $G_0W_0@PBE0$ and the screened exchange constant functional (SX); the lowest optical singlet transitions predicted by the SX functional (TDSX, i.e. time dependent density functional calculations using the SX functional, Eq. 2.17), TDPBE0 and PBE0 with many body perturbation theory corrections ($BSE@G_0W_0@PBE0$) TDPBE0 and $BSE@G_0W_0@PBE0$ are taken from Ref. [181].

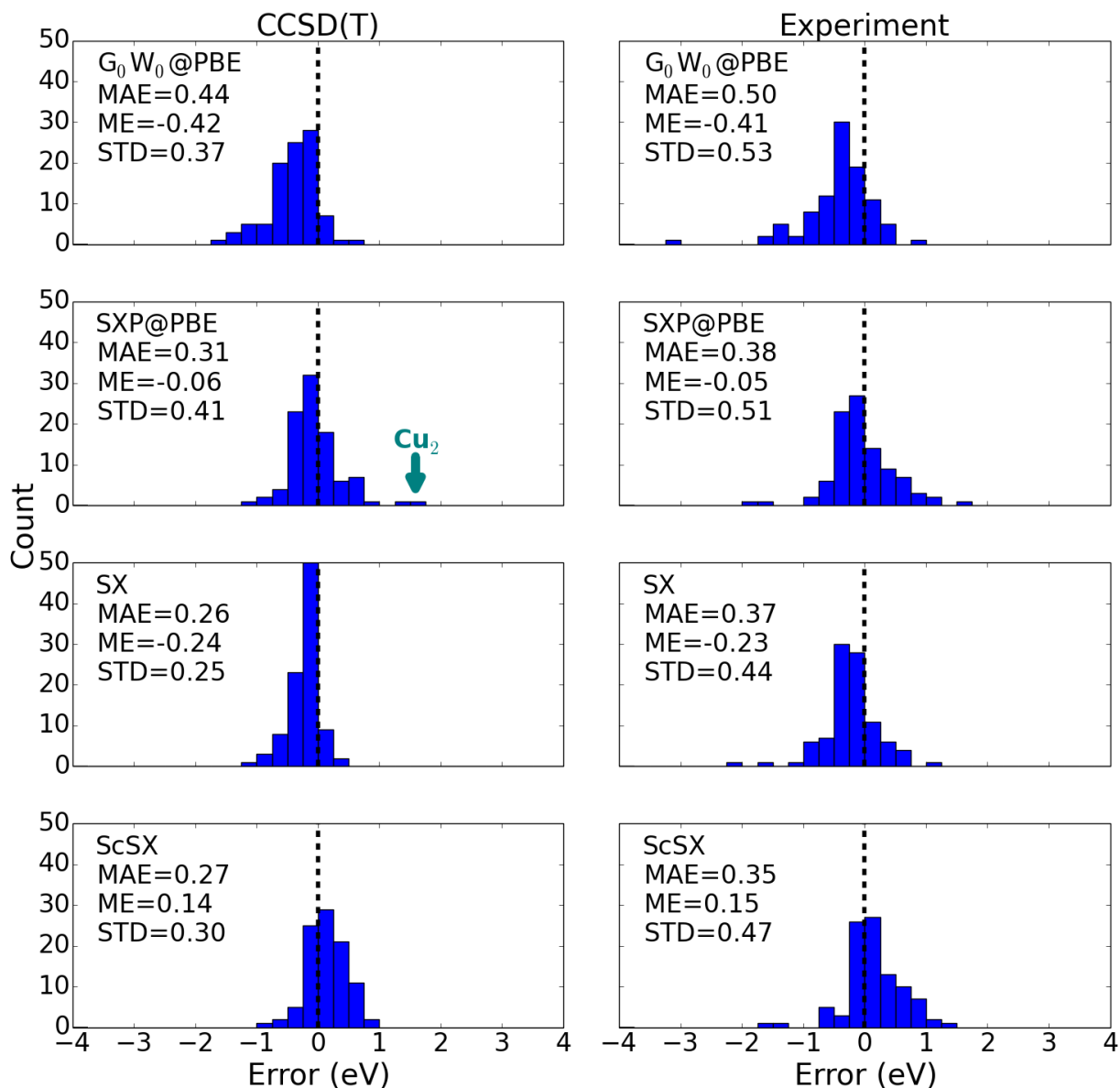


Figure 2.5: Errors (eV) in the ionization energies of the molecules belonging to the GW 100 Test Set calculated with the screened exchange constant functional at the perturbative (SXP@PBE) and self-consistent (SX and ScSX) levels. We also report, CCSD(T) and experimental values [245, 213]. A *negative* error (see Equation 2.20) indicates an *underestimate* of the reference ionization potential.

Table 2.2: Ionization energies (eV) for the molecules of the GW100 test set calculated with the screened exchange constant functional at the perturbative (SXP@PBE) and self-consistent (SX and ScSX) levels along with CCSD(T) and experimental values [245, 213].

Molecule	Experiment	CCSD(T)	SXP@PBE	SX	ScSX
ethylbenzene	8.77	8.85	8.55	8.53	8.8
ozone	12.73	12.55	12.62	12.51	12.98
boron nitride	NA	11.89	11.41	11.2	11.48
butane	11.09	11.57	11.61	11.66	12.03
toluene	8.82	8.9	8.58	8.56	8.82
phenol	8.75	8.7	8.52	8.37	8.69
pyridine	9.51	9.66	9.32	9.11	9.57
tetracarbon	12.54	11.26	10.79	10.83	11.17
phosphorus dimer	10.62	10.47	10.07	10.1	10.33
silver dimer	7.66	7.494	7.39	6.85	6.97
copper dimer	7.46	7.57	9.16	6.7	7.16
carbon dioxide	13.77	13.71	13.76	13.66	14.11
beryllium monoxide	10.1	9.94	10.48	9.59	10.01
magnesium monoxide	8.76	7.49	8.82	7.77	8.17
borane	12.03	13.28	13.16	13.11	13.47
hydrogen	15.43	16.4	16.03	15.97	16.28
boron monofluoride	11	11.09	10.59	10.66	11.02
lithium dimer	4.73	5.27	5.13	5.11	5.25
pentasilane	9.36	9.27	9.15	9.24	9.59
disilane	10.53	10.65	10.52	10.56	10.89
carbon oxyselenide	10.37	10.79	10.14	10.2	10.5
gallium monochloride	10.07	9.77	9.79	9.78	10.09
phosphorus mononitride	11.88	11.74	11.85	11.47	12.09
diborane	11.9	12.26	12.13	12.15	12.54
arsenic dimer	10	9.78	9.13	9.16	9.35
sodium dimer	4.89	4.95	4.77	4.78	4.87
potassium dimer	4.06	4.06	3.87	3.86	3.94

Table 2.2 continued

rubidium dimer	3.9	3.925	3.71	3.71	3.78
hydrazine	8.98	9.72	9.8	9.56	9.99
hexafluorobenzene	10.2	9.93	9.75	9.87	10.24
sodium tetramer	4.27	4.23	3.93	4.01	4.13
sodium hexamer	4.12	4.35	4.14	4.19	4.3
carbon oxysulfide	11.19	11.17	10.94	10.99	11.32
formaldehyde	10.89	10.84	11.05	10.76	11.23
tetraiodomethane	9.1	9.266	9.17	9.15	9.49
cyclopentadiene	8.53	8.68	8.2	8.19	8.47
copper cyanide	NA	10.85	11.96	10.67	11.21
tetrabromomethane	10.54	10.46	10.44	10.37	10.76
tetrachloromethane	11.69	11.56	11.56	11.48	11.91
urea	10.15	10.05	10.55	10.07	10.6
vinyl bromide	9.9	9.27	8.91	8.9	9.18
vinyl iodide	9.35	9.327	9.07	9.05	9.33
ethoxy ethane	9.61	9.82	10.25	9.88	10.4
aniline	8.05	7.99	7.79	7.67	8
cyclooctatetraene	8.43	8.35	7.92	7.98	8.27
carbon monoxide	14.01	14.21	13.94	14.22	14.67
ethanol	10.64	10.69	11.07	10.65	11.17
formic acid	11.5	11.42	11.72	11.45	11.96
thymine	9.2	9.08	8.85	8.91	9.3
uracil	9.68	10.13	9.27	9.19	9.73
methanol	10.96	11.04	11.4	10.99	11.49
cytosine	8.94	9.51	8.67	8.57	8.99
benzene	9.23	9.29	8.96	8.94	9.2
adenine	8.48	8.33	8.03	8	8.33
guanine	8.24	8.03	7.7	7.73	8.07
methane	14.35	14.37	14.27	14.18	14.54
ethane	12.2	13.04	12.59	12.52	12.88
ethylene	10.68	10.67	10.21	10.17	10.43

Table 2.2 continued

ethyn	11.49	11.42	10.98	10.97	11.25
hydrogen cyanide	13.61	13.87	13.25	13.2	13.52
propane	11.51	12.05	12.02	11.95	12.31
krypton	14	13.94	13.91	13.73	14.03
neon	21.56	21.32	21.56	21.18	21.62
argon	15.76	15.54	15.64	15.4	15.75
helium	24.59	24.51	24.11	23.94	24.38
xenon	12.13	NA	13.48	12.71	13.02
sulfur dioxide	12.5	13.49	12.34	12.28	12.74
vinyl chloride	10.2	10.09	9.75	9.74	10.05
vinyl fluoride	10.63	10.55	10.23	10.12	10.48
acetaldehyde	10.24	10.21	10.46	10.18	10.68
carbon disulfide	10.09	9.98	9.71	9.79	10.08
cyclopropane	10.54	10.87	10.8	10.73	11.05
tetrafluoromethane	16.2	16.3	16.91	16.56	17.19
iodine	9.36	9.509	9.41	9.39	9.66
lithium hydride	7.9	7.96	7.8	7.61	8.13
hydrogen chloride	12.79	12.59	12.56	12.37	12.7
sodium chloride	9.8	9.03	9.28	8.82	9.27
hydrogen fluoride	16.12	16.03	16.61	15.98	16.53
ammonia	10.82	10.81	10.9	10.65	11.08
potassium hydride	8	6.13	6.09	5.78	6.37
hydrogen peroxide	11.7	11.59	11.92	11.6	12.11
bromine	10.51	10.54	10.51	10.43	10.74
nitrogen	15.58	15.57	15.6	15.72	16.18
water	12.62	12.57	12.92	12.46	12.95
potassium bromide	8.82	8.13	8.32	7.93	8.32
fluorine	15.7	15.71	16.29	15.92	16.5
chlorine	11.49	11.41	11.38	11.29	11.64
germane	12.46	12.5	12.55	12.31	12.63
hydrazoic acid	10.72	10.68	10.27	10.33	10.66

Table 2.2 continued

hydrogen sulfide	10.5	10.31	10.22	10.1	10.41
magnesium fluoride	13.3	13.71	14.42	13.58	14.27
sulfur tetrafluoride	12	12.59	12.76	12.56	13.1
titanium tetrafluoride	NA	15.48	16.04	15.67	16.47
aluminum fluoride	15.45	15.46	16.02	15.38	16.04
aluminum iodide	9.66	9.815	9.68	9.63	9.97
arsine	10.58	10.4	10.2	10.22	10.48
magnesium chloride	11.8	11.67	11.72	11.45	11.88
lithium fluoride	11.3	11.32	12.09	11.2	11.86
phosphine	10.59	10.52	10.3	10.28	10.56
silane	12.82	12.8	12.67	12.66	13.05

Figure 2.5 shows that the relative order of the MAE’s for the perturbative and self-consistent results is the same when using experiment or CCSD(T) as a reference. However, it is clear that all comparisons against CCSD(T), the gold standard of quantum chemistry methods, have significantly smaller STD’s. Experimental data contain additional effects not included in any of the theories, arising from experimental conditions e.g., finite temperature and zero point motion effects. Hence we will focus on comparing our results with those of CCSD(T).

The performance of the perturbative and self-consistent SX functionals with respect to $G_0W_0@PBE$ are similar. We see a significant improvement in the MAE, ME and STD when some form of self-consistency is considered, using either SX or ScSX, as compared to SXP@PBE and $G_0W_0@PBE$ which are both perturbative approaches. The most notable improvement is in the STD when going from SXP@PBE results to SX and ScSX. We also estimated the MAE of GW@SX (0.29 eV) using a linear interpolation of GW corrections at different hybrid mixing fractions, yielding a slightly larger MAE error compared to SX and ScSX.

2.3.3 Effects of Self-Consistency

The outlier with the greatest error with respect to CCSD(T), in the case of the SXP@PBE results, is the copper dimer (Cu_2) which is labeled by the teal arrow in the second row, first column of Figure 2.5. Surprisingly, this outlier is absent in the SX and ScSX results. Upon examination of the G_0W_0 errors for Cu_2 against CCSD(T) (-0.23 eV, -0.67 eV, -0.55 eV, -0.36 eV, -0.15 eV) at various mixing fractions of exact exchange (0.0, 0.25, 0.5, 0.75, 1.0), we see the G_0W_0 errors are not-monotonic, with increasing amounts of exact exchange. This non-monotonic behavior is indicative of state reordering caused by exact exchange. Indeed the orbitals of Cu_2 are reordered after the Kohn-Sham eigenvalues are corrected by Equation 2.19; the highest occupied molecular orbital (HOMO) obtained with PBE is different from the one predicted by SXP@PBE. The electronic structure of copper clusters have been studied extensively in the literature[169, 247, 16, 296, 74, 322, 439]; the HOMO of Cu_2 is expected to be a σ_g bonding state formed by two copper s orbitals. The PBE functional predicts that the HOMO has odd symmetry while SXP@PBE, SX and ScSX all predict even symmetry. However, SXP@PBE predicted that the orbital is “d” like in character, as indicated by the blue isosurface plots shown in Figure 2.6.

Although using self-consistency greatly improves the results for the Cu_2 dimer, the accuracy of the SXP@PBE and SX results are similar overall, with the MAEs of the two data sets differing by 0.05 eV. We also found that the Cu dimer is an exception with regards to the qualitative change in the character of the wave function; the HOMO levels obtained with SXP@PBE and SX have the same symmetry for all the other outliers (defined as yielding errors greater than or equal to two standard deviations). The remaining outliers; lithium fluoride, aluminum fluoride, magnesium fluoride, magnesium monoxide, urea and hydrogen fluoride all contain ionic bonds. Charge transfer between species, such as in lithium fluoride [263], is poorly described by semi-local functionals and lead to poor MBPT predictions starting from KS states computed at the PBE level of theory[196, 470]. Inaccuracies in charge transfer predictions can be partially remedied by using hybrid functionals, as seen

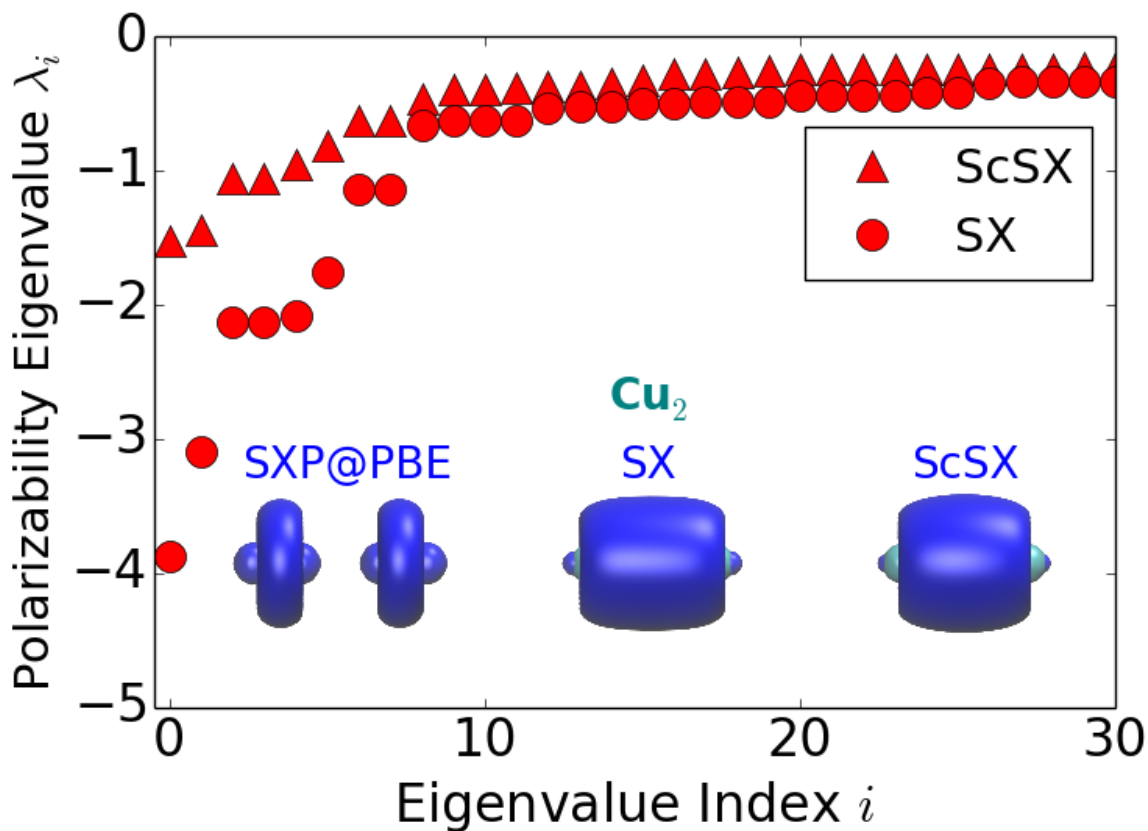


Figure 2.6: Eigenvalues (λ_i) for Cu_2 of the symmetrized polarizability $\tilde{\chi}$ used to construct the inverse of the static dielectric function $\epsilon^{-1} = 1 + v_c^{1/2} \tilde{\chi} v_c^{-1/2}$ where v_c is the Coulomb interaction, computed using the screened exchange constant functional (SX) and the fully self-consistent screened exchange constant functional (ScSX). Inset: the highest occupied molecular orbital of Cu_2 predicted by the perturbative screened exchange constant method at PBE (SXP@PBE), SX and ScSX. Isosurfaces are evaluated at 10% of the maximum isovalue of the one obtained using ScSX.

for example in the TTF-TCNQ donor-acceptor system[71, 47]. As a qualitative measure of the “ionicity” of each molecule, we calculated the difference in the Pauling electronegativity scale[449] of the atoms composing all diatomic molecules which contained only two atom types and that showed improvement above the MAE (see Figure 2.7). We define the reduction of the error in the ionization potential with respect to CCSD(T) reference values as the difference between the absolute SXP@PBE error ($|\text{Error}^{\text{SXP@PBE}}|$) and the absolute SX error ($|\text{Error}^{\text{SX}}|$):

$$\Delta = |\text{Error}^{\text{SXP@PBE}}| - |\text{Error}^{\text{SX}}| \quad (2.22)$$

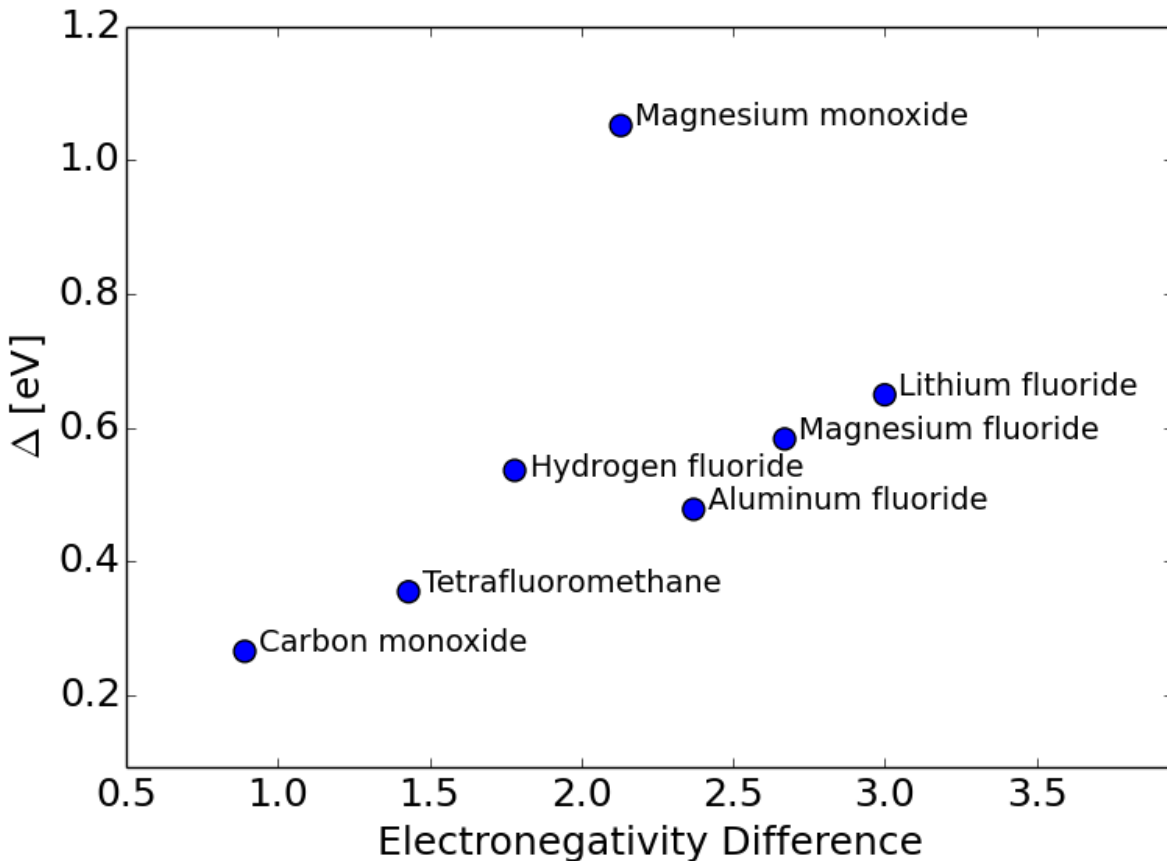


Figure 2.7: The reduction of the SX error in the ionization potential (Δ) (Eqn. 2.22) as a function of the difference in the electronegativity of all molecules which contain only two atom types and exhibited a value of Δ greater than the average over the GW100 test set. The average absolute error with respect to CCSD(T) for these molecules is from 0.69 eV to 0.13 eV for SXP@PBE to SX respectively.

Figure 2.7 shows a correlation between Δ and the difference in the atomic electronegativities. Furthermore, in each case we found that the dipole moment of all diatomic molecules increased at the SX level of theory compared to PBE, with an average increase of 15%, which is indicative of increased charge transfer at the SX level of theory, with respect to PBE. The largest increase in the dipole between SX and PBE, was found for the case of MgO which is the only molecule of this subset with a doubly charged anion. Hence we conclude that

wave function self-consistency appears to be most important in two distinct cases: for ionic molecules, where charge transfer needs to be correctly described and for molecules like Cu_2 , where the ordering of orbitals is different when using semilocal or hybrid functionals.

Figure 2.5 shows that the HOMO level computed with SX and ScSX are very similar. However, the eigenvalues (λ_i) of the symmetrized polarizability $\tilde{\chi}$ used to construct the inverse of the static dielectric function $\epsilon^{-1} = 1 + v_c^{1/2} \tilde{\chi} v_c^{-1/2}$ where v_c is the Coulomb interaction, obtained with SX and ScSX are very different. Figure 2.6 shows that λ_i 's are substantially larger in magnitude when using SX, and they converge to values differing by 10% with respect to those computed with ScSx. We observed that when solving Equation 2.17 self-consistently to obtain SX results, starting from PBE wavefunctions, the magnitude of the eigenvalues (λ_i) of $\tilde{\chi}$ are progressively reduced, thus leading to a reduction in the screening which results in an increase of the mixing fraction of exact exchange. The use of the RPA approximation when self-consistently evaluating the screening constant could be the cause of the slight overestimation of the ionization potentials by ScSX, which might be corrected by going beyond the RPA[410, 377, 63].

In a previous work Atalla et al.[12] proposed the following method for determining a system-dependent mixing fraction of exact exchange which removes the starting point dependence from the G_0W_0 method:

$$\alpha_{G_0W_0}^* = \arg_{\alpha} \min |\langle \psi(\alpha) | \Sigma(\alpha) - v_{xc}(\alpha) | \psi(\alpha) \rangle| \quad (2.23)$$

where Σ is the GW self-energy[12]. In practice $\alpha_{G_0W_0}^*$ can be found by evaluating the value of the energy level (e.g. the IP) using hybrid density functional theory and G_0W_0 for multiple values of α and evaluating the point where hybrid density functional and G_0W_0 results are the same (see the top left inset of Figure 2.8).

It was shown that $\alpha_{G_0W_0}^*$ minimizes both self-interaction errors and the G_0W_0 quasiparticle corrections to the KS eigenvalues and it also provides accurate quasi-particle energies[12]. It is interesting to investigate whether the α obtained using the ScSX functional is similar

to $\alpha_{G_0W_0}^*$ given by Equation 2.23. If we approximate Σ in Equation 2.23 by the v_{xc} defined in Equation 2.17, numerically we indeed found that α_{SX} and $\alpha_{G_0W_0}^*$ are very similar for the GW100 test set.

In Figure 2.8, we present the difference between the SX mixing fraction and $\alpha_{G_0W_0}^*$ (given by Equation 2.24) evaluated at different steps of the self-consistent cycle.

$$\Delta\alpha = \alpha - \alpha_{G_0W_0}^* \tag{2.24}$$

Upon comparison of the last two rows of Figure 2.8, we see that SX quickly converges within three steps. Furthermore, the MAE, or mean absolute difference in this case, of ScSX converges to within 0.05 of $\alpha_{G_0W_0}^*$ with a ME of -0.02. The results show that ScSX provides an excellent starting point for G_0W_0 calculations and further establishes the connection between hybrids and MBPT which can be used for future hybrid functional developments.

In summary, in this section, we analyzed the performance of the screened exchange constant functional[47] at different levels of self-consistency for the molecules of the GW100 set. We found excellent agreement for the computed values of the ionization potential with both CCSD(T) and experiment especially when wave function self-consistency is included. We found wave function self-consistency to be most important for ionic molecules and molecules where the character of the HOMO is highly dependent on the mixing fraction, as, e.g. for the Cu dimer. In addition, when using a mixing fraction (α^{SX}) determined self-consistently, within the random phase approximation (RPA), we found a slight overestimation of the IP reference values. Work is underway to evaluate the self-consistent screened exchange constants beyond the RPA. Finally, we found that the self-consistent process presented here, for evaluating the screened exchange constant, yields hybrid mixing fractions which greatly reduce the G_0W_0 quasiparticle corrections to the KS eigenvalues.

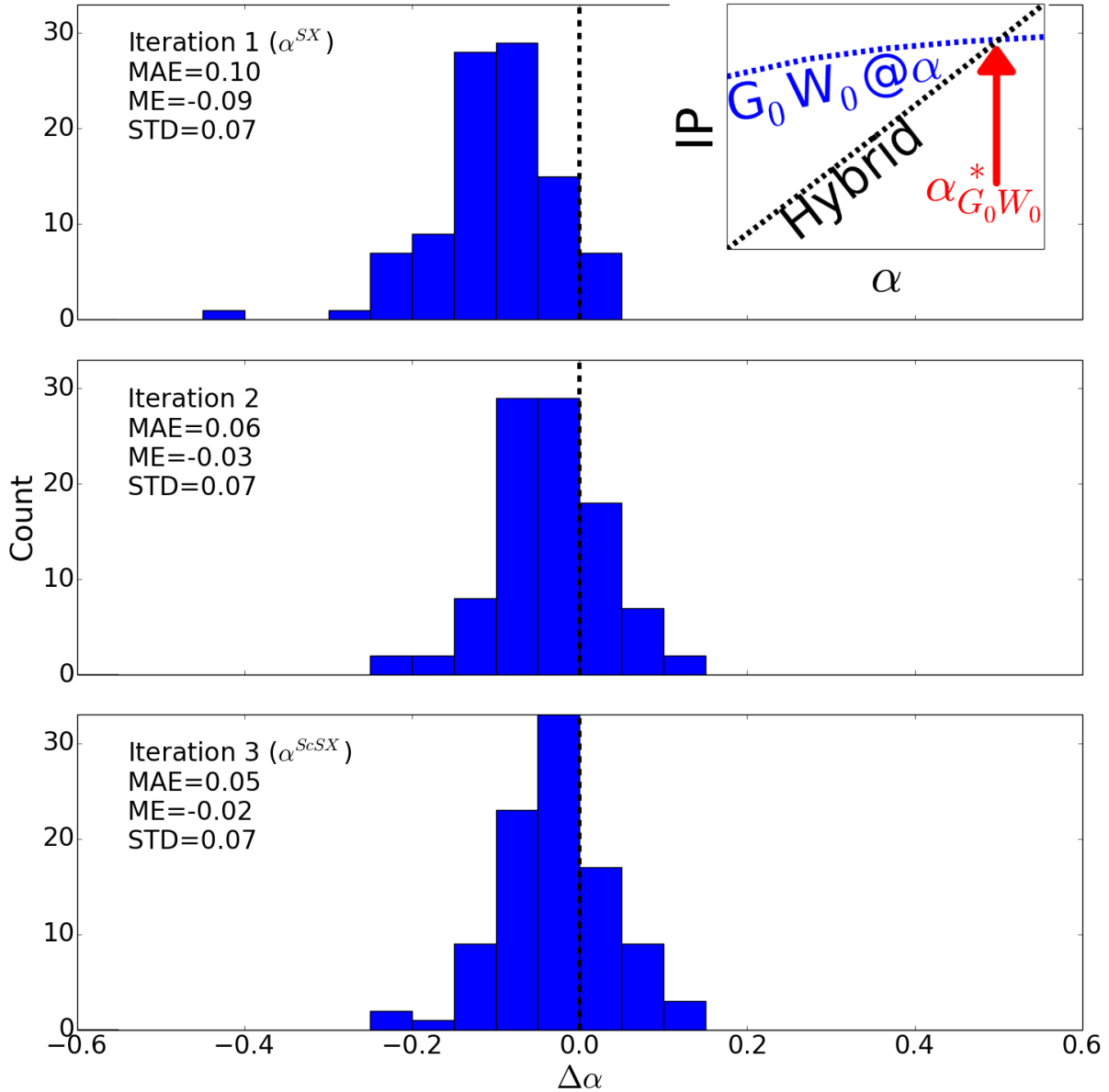


Figure 2.8: Difference in the screened exchange constant at different iterations of the self-consistency; iteration 1 (α^{SX}), iteration 2 and iteration 3 (α^{ScSX}) compared against the hybrid-GW crossing point ($\alpha_{G_0W_0}^*$) for the ionization potentials of the GW100 test set. A *negative* difference means the method *underestimates* $\alpha_{G_0W_0}^*$.

2.4 Constrained Density Functional Theory and the Self-Consistent Image Charge Method

In the previous section, we focused on the optoelectronic properties of materials. We now turn our attention to the development of methods to predict the transport properties of

materials. Here we present an implementation of constrained density functional theory (CDFT) for the calculation of charge transport in the hopping regime. The implementation is verified against literature results for molecular systems, and the dependence of results on numerical parameters is discussed. In addition, we compare the CDFT results against other methods which are typically used to compute transport properties in nanoparticle systems and demonstrate that some of these methods give unphysical results for thermally disordered systems. This analysis is important to illustrate the necessity for a robust approach such as CDFT to study transport properties.

2.4.1 Introduction

Reprinted with permission from Matthew B. Goldey, Nicholas P. Brawand, Márton Vörös, and Giulia Galli Unpublished. Copyright 2017 American Chemical Society.

Functional nanostructured systems have long been recognized as a promising platform for the development of materials with target properties, and they are an active area of theoretical and experimental research[211, 154, 390, 368, 191, 453, 79, 344]. Much progress has been made in recent years to predict structural and electronic properties of functional materials for energy conversion applications[256, 434, 243, 233, 356, 147, 44, 48, 198]; however, robust, *ab initio* methods for the description and optimization of electronic transport properties of nanostructured materials are not yet available, although several useful codes[287, 337, 261, 240, 342, 118, 396, 32, 19, 67] for electronic transport have been developed, based on various models and approximations. Much effort is still required, anchored within first principles theories, to describe electron and hole transport in materials for energy applications in order to define descriptors for the design of semiconductor nanostructures, e.g. with optimal solar and thermal energy conversion properties.

Here we focus on hopping transport and the efficient calculation of first principles parameters required either to compute transfer rates using Marcus theory[270] or to evaluate currents from Green's function approaches, e.g. using the Keldysh formalism[415, 285]. In

the framework of Marcus theory, charge transport rates (k) are expressed in terms of free energy differences (ΔG) between sites A and B involved in charge hopping, the electronic coupling between these sites (H_{AB}), and the reorganization energy (λ):

$$k_{AB} = \frac{2\pi}{\hbar} |H_{AB}|^2 \sqrt{\frac{1}{4k_B T \pi \lambda}} \exp \left[-\frac{(\Delta G + \lambda)^2 / 4\lambda}{k_B T} \right], \quad (2.25)$$

where k_B is the Boltzmann constant and T is the temperature. For the details of Marcus theory, we refer readers to existing reviews[270, 402, 315, 407, 20, 89].

In Eq. 2.25, sites A and B may represent two nanoparticles of an ensemble (e.g. a nanoparticle-based inorganic solar cell), or two different cages in a clathrate solid or a nanoparticle and a region of space in the surrounding matrix. Depending on the specific nanostructured system and problem and on the strength of the H_{AB} coupling, one may consider using transfer rate expressions derived from Landau-Zener theory[407] which include information about the phonon density of states of the nanoparticles, e.g.:

$$k = \left[1 - \exp \left(\frac{-2\pi^{\frac{3}{2}} H_{AB}^2}{\hbar \omega \sqrt{\lambda k_B T}} \right) \right] \frac{\omega}{2\pi} \exp \left(- \left(\frac{\lambda}{4} - |H_{AB}| \right) / k_B T \right) \quad (2.26)$$

where here ω is a representative molecular or nanoparticle phonon frequency.

In the cases of Marcus theory and the Landau-Zener formula, the electronic coupling can be obtained from first principles and in this manuscript we focus on constrained density functional theory (CDFT) to obtain this quantity. The use of CDFT to obtain couplings to evaluate rates within Marcus theory has been reviewed in previous works[189].

In addition to CDFT, many methods have been proposed for predicting the electronic coupling, such as the generalized Mulliken-Hush (GMH) method[73], excited state wavefunction methods[397], tight-binding approaches[314, 315, 262], anticrossing methods[373], and empirical quasiclassical approximations [77]. Many of these methods neglect polarization effects, and some of them do not contain any atomistic detail or orbital relaxation beyond the single particle picture[183], which may be important for materials with high densities of

states near the conduction band minimum or valence band maximum. Furthermore, none of these methods have been extended to include effects present in real devices arising from image charges within the surrounding electrodes and substrates.

CDFT, on the other hand, includes the effects of polarization and orbital relaxation through the evaluation of many-body wavefunctions describing localized charges. These wavefunctions may be obtained within density functional theory (DFT) by modifying the Kohn-Sham equations to include a spatially-dependent potential, whose strength is varied self-consistently to satisfy the constraint of the desired number of electrons localized on a given fragment or building block[104, 343, 458, 459, 461, 460, 36, 306, 307, 417, 133, 371, 189, 436, 388, 349, 260, 347, 172, 278]. The use of constrained DFT within the quantum chemistry and, since recently, the condensed matter physics community, is entering its fourth decade, since the first formulation in 1984 by Dederichs, et al.[104], and it is often employed within the formulation proposed by Qin Wu and Troy Van Voorhis. In addition to total energies for localized states and electronic couplings, CDFT may be used to obtain charge transfer energies and Heisenberg spin couplings[228, 189]. This method has been applied to molecules[127, 219, 220, 172], molecular solids[126, 308], oxides[35], organic photovoltaics[142], solvated ions in liquid water[36, 306], and defects in nanoparticle arrays[422, 44], as well as to provide corrections to results where hybrid DFT fails to compute total energy differences and geometries accurately[278].

The remainder of this section is organized as follows: we first present the details of our implementation of constrained DFT for periodic systems using plane wave basis sets. Second, we verify our implementation on molecular systems by comparing our results to existing literature data, and we include tests of the sensitivity of our implementation on numerical parameters. Finally, we present results for silicon quantum dots comparing constrained DFT against other commonly used methodologies for the calculation of electronic couplings, finding a robust performance for CDFT when other approaches lead to unphysical results for thermally disordered configurations.

2.4.2 Methodology

Within constrained DFT, an external potential is added to the self-consistent potential entering the Kohn-Sham equations, and its strength is varied self-consistently in order to localize a desired integer number of charges N_0 on a specified site[189, 458]. Specifically, one defines a free energy $F[\rho(\mathbf{r})](N)$, a functional of the density $\rho(\mathbf{r})$ and the total number of electrons, belonging to a volume Ω , which is minimized with respect to the total charge density of the system, under a constraint (expressed as a Lagrange multiplier) of charge localization:

$$F[\rho(\mathbf{r})](N) = E[\rho(\mathbf{r})] + V \left(\int_{\Omega} w(\mathbf{r})\rho(\mathbf{r})d^3\mathbf{r} - N_0 \right). \quad (2.27)$$

Here E is the Kohn-Sham total energy, ρ is the charge density, $w(\mathbf{r})$ is a spatially-dependent potential of strength V . Given a trial potential strength V , the solution of the Kohn-Sham equations yields a density ρ and a corresponding number of localized electrons $N = \int_{\Omega} w(\mathbf{r})\rho(\mathbf{r})d^3\mathbf{r}$. The potential strength V is then updated and the procedure repeated until the error in localized charges $\Delta N = N - N_0$ is within a chosen, small threshold.

CDFT charge transfer states give the correct 1/R distance dependence and the correct asymptotic limit[189]. These states can be correctly described even with semi-local functionals for which, for example, time-dependent DFT fails[110], since CDFT involves non-linear response of the density (the CDFT potential and the density are determined self-consistently). Perhaps more importantly, CDFT involves ground state total energies (which DFT describes much better than single particle virtual states) and describes charge transfer between ground states of a given system in the presence of a non-linear perturbation (the CDFT potential).

We implemented CDFT in Quantum-ESPRESSO[135], using Hirshfeld partitioning[168] of the electronic density to determine the real-space shape of the constraining potential. We chose Hirshfeld partitioning in order to compare directly with existing plane wave codes and,

most importantly, because such partitioning has been shown to be more reliable in defining fragments (e.g. in the presence of possibly delocalized anionic states) than schemes not based on the density such as Lowdin's and Mulliken's. The weighting function used in Hirshfeld partitioning is defined by the selection of atoms donating (D) and accepting (A) electrons,

$$w(\mathbf{r}) = \frac{\sum_i^D \rho_i(\mathbf{r}) - \sum_i^A \rho_i(\mathbf{r})}{\sum_i^{\text{all}} \rho_i(\mathbf{r})}, \quad (2.28)$$

and is generated from the square moduli (ρ_i) of pseudo-atomic wavefunctions, consistent with the chosen pseudopotentials. The sums in Eq. 2.28 run over pseudo-atomic densities belonging to donors (D), acceptors (A) or all atoms (all). These definitions are general and may be applied to both the total electronic density and the spin density.

After generating two diabatic states (e.g. corresponding to a charge (electron or hole) localized on two different quantum dots A and B), the coupling matrix H' is evaluated:

$$H'_{AB} = \frac{F_A + F_B}{2} S_{AB} - \langle \Phi_A | \frac{\hat{V}_A + \hat{V}_B}{2} | \Phi_B \rangle \quad (2.29)$$

Here F is the free energy defined in Eq. 2.27, S_{AB} is the overlap between the two Slater determinants ($\langle \Phi_A |$ and $\langle \Phi_B |$) constructed from the Kohn-Sham single particle energies from diabatic states A and B , $\hat{V} = Vw(\mathbf{r})$ (see Eq. 2.27).

The electronic coupling H_{AB} is obtained from Eq. 2.29 using Løwdin's orthogonalization [254]:

$$H = S^{-\frac{1}{2}} H' S^{-\frac{1}{2}}. \quad (2.30)$$

When investigating hopping transport in ensembles of quantum dots representing a given device, or in any other system of nanostructured building blocks, one is usually faced with the problem of including the effect of metallic leads and/or substrates. The derivation of

methods to calculate the renormalization of molecular electronic levels at metallic interfaces is an area of active research in condensed matter physics and physical chemistry[361, 389, 290]. Methods based on classical point charges neglect orbital relaxation, dipole interactions, and orbital reordering and are applied as *post hoc* corrections to orbital energies. Other methods require an atomistic simulation of the metallic surface or substrate and thus provide much greater detail; however, they are computationally demanding because they require that the surface be simulated along with the quantum dot or molecular ensemble being adsorbed [361, 389, 290]. In addition, these methods often require many body perturbation theory to accurately model the relative position of single particle energy levels, and hence their applicability has been limited to systems with a small number of atoms, for example a single benzene molecule adsorbed on graphite[290].

In order to include self-consistently image charge effects in CDFT calculations, we added an image charge potential $V_{\text{img.}}$ to the Kohn-Sham potential:

$$V_{\text{img.}}[\rho; \mathbf{r}] = -\frac{q_{\text{tot}}}{|\mathbf{r}|} - \frac{\vec{p}_{\text{tot}}[\rho] \cdot \mathbf{r}}{r^3} + \dots \quad (2.31)$$

where \mathbf{r} is centered on the site containing the constrained charged defined by CDFT, q_{tot} is the total charge of the system and \vec{p}_{tot} is the dipole moment of the system. $V_{\text{img.}}$ is a multipole expansion of the electrostatic potential of the image, which is added to the Kohn-Sham potential. In our procedure, the charge obtained at the end of each self-consistent Kohn-Sham iteration is used to update $V_{\text{img.}}[\rho; r]$ until the image interaction energy,

$$E_{\text{img.}} = \int_{\Omega} V_{\text{img.}}[\rho; \mathbf{r}] \rho(\mathbf{r}) d\mathbf{r} , \quad (2.32)$$

is converged within a predefined accuracy[44].

We now turn to presenting calculations carried out with the procedure outlined above. These calculations were performed with the Quantum Espresso package[135], using plane wave basis sets and optimized norm-conserving Vanderbilt (ONCV) pseudopotentials[156,

366] and Troullier-Martins pseudopotentials[408]. We used a wavefunction energy cutoff of 80 Ry, except for molecular dynamics and CDFT calculations of systems containing only Si and H, where a cutoff of 30 Ry was used. Our calculations employed the generalized gradient approximation with the PBE exchange-correlation functional[324]. The Martyna-Tuckerman correction[274] was applied to all CDFT calculations of molecular systems to remove any remaining fictitious electrostatic interactions between periodic images.

We first verified our results for simple molecules using literature reference data. We then compared our calculations on complex systems with those of other approaches commonly used at zero temperature, including quantum dots at finite temperature.

2.4.3 Verification

The consistent reproduction of benchmark values is necessary for confidence in any new code and is a sign of the technological maturity of computational methodologies[231]. In this section, we present first the electronic coupling for hole transfer in a simple dimer of Zn, and then we investigate the molecular data sets presented by Kubas et al[219, 220]. Results for Zn_2^+ are shown in Figure 2.9. We found excellent agreement with the results of Qin Wu and Troy Van Voorhis[461] in absolute magnitude of hole transfer couplings. Given the exponential decay of wavefunctions, the dependence of electronic couplings on distance is commonly parametrized to the form $H_{AB} \propto e^{-\beta R/2}$ to provide a characteristic decay rate for a charge transfer process.

Figures 2.10 and 2.11 present the total energy relative to the ground state energy of unmodified DFT and the applied potential strength as a function of the number of electrons transferred for Zn_2^+ at 5 Å of separation, as well as the error in the electronic coupling H_{AB} versus the error in the number of charges transferred Δ_N . The slope of the potential strength changes sharply in correspondence to an amount of charge transferred equal to one electron. A 1% deviation in the number of constrained electrons results in up to a 50 meV change in total energies. The same 1% deviation produces up to a 15% error in the

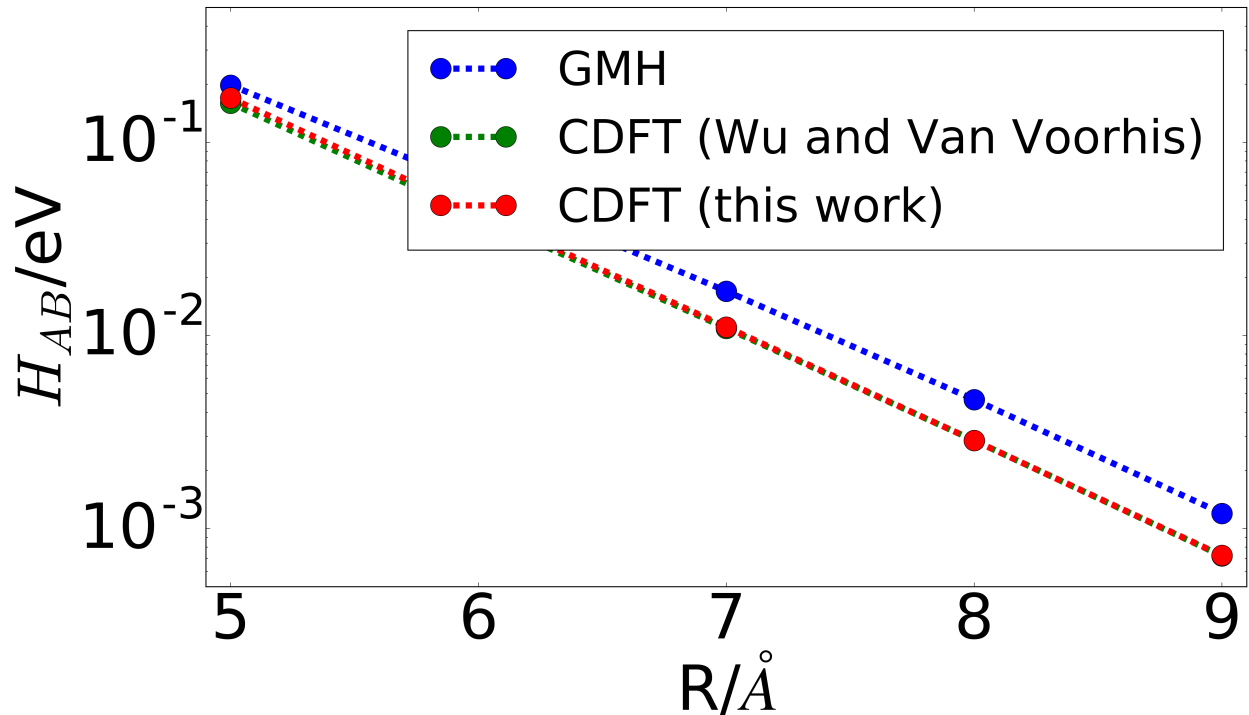


Figure 2.9: Electronic coupling H_{AB} (eV) as a function of distance R (Å) for hole transfer between two Zn atoms belonging to a Zn_2^+ cation, obtained with the generalized Mulliken-Hush method[73] (denoted GMH), constrained density functional theory using Becke weight partitioning (Wu and Van Voorhis)[27, 461], and in this work, using Hirshfeld partitioning[168] (see text). Calculated β decay rates are 2.55, 2.69, and 2.72 \AA^{-1} for the three methods, respectively.

calculated coupling, suggesting that tight convergence is necessary to achieve accurate CDFT couplings. Convergence within 1E-4 electrons yields errors in the estimated couplings within 1%. On the basis of these results, we recommend a precision of 5E-5 electrons for CDFT self-consistency, which we employ for our following calculations. Recent results employing a precision of 1E-2 electrons may need to be revisited.

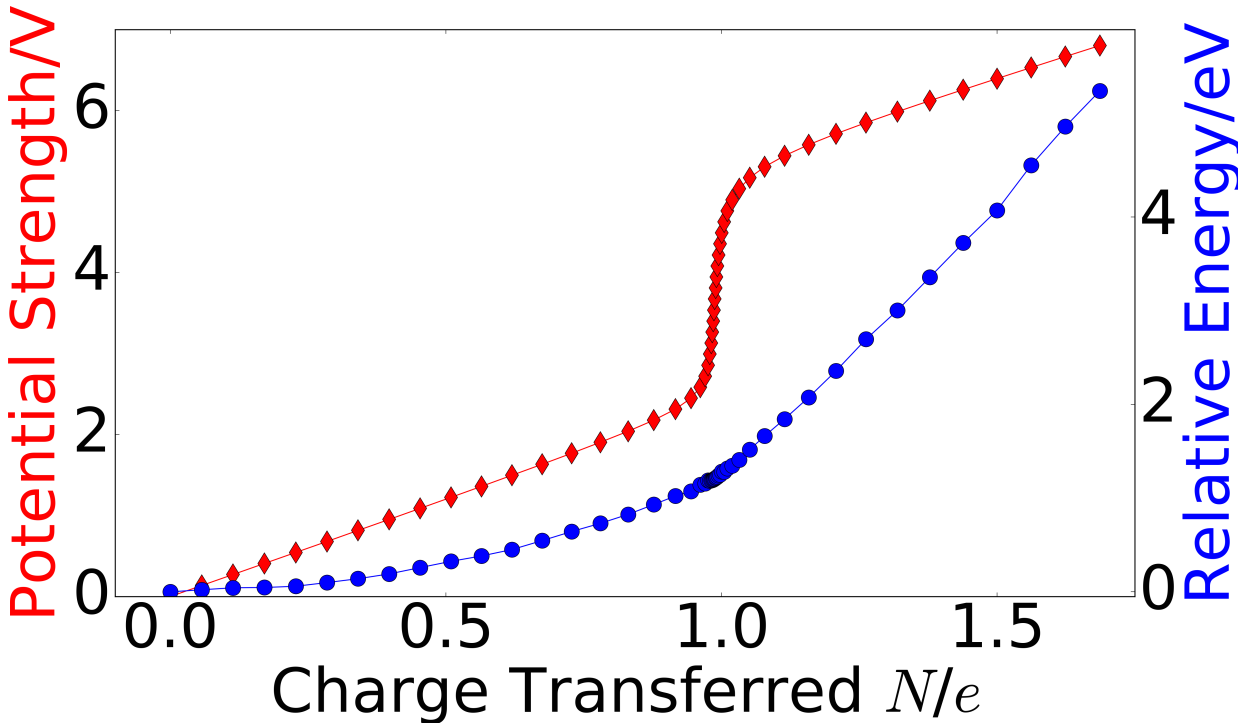


Figure 2.10: Dependence of the energy and potential strength on the number of charges transferred $N = \int_{\Omega} w(\mathbf{r})\rho(\mathbf{r})d^3\mathbf{r}$ for Zn_2^+ at 5 Å separation (The equilibrium distance of Zn_2^+ within PBE is 2.55 Å).

In Figure 2.12 and Table 2.3, we present results for literature datasets (HAB7 and HAB11 [219, 220]) of electronic couplings between identical molecular dimers. The sets consist of organic molecular dimers (varying in size from 8 to 80 atoms) at different separations (3.5, 4.0, 4.5, 5.0 Å). Molecular dimer geometries for the HAB11 and the HAB7 sets, composed of planar and π -conjugated molecules, were taken from the literature[219, 220]. Further details about these molecules are given by Kubas et al.[219, 220]. Comparisons between our results for Troullier-Martins (TM) pseudopotentials[408] and optimized norm-conserving (ONCV)

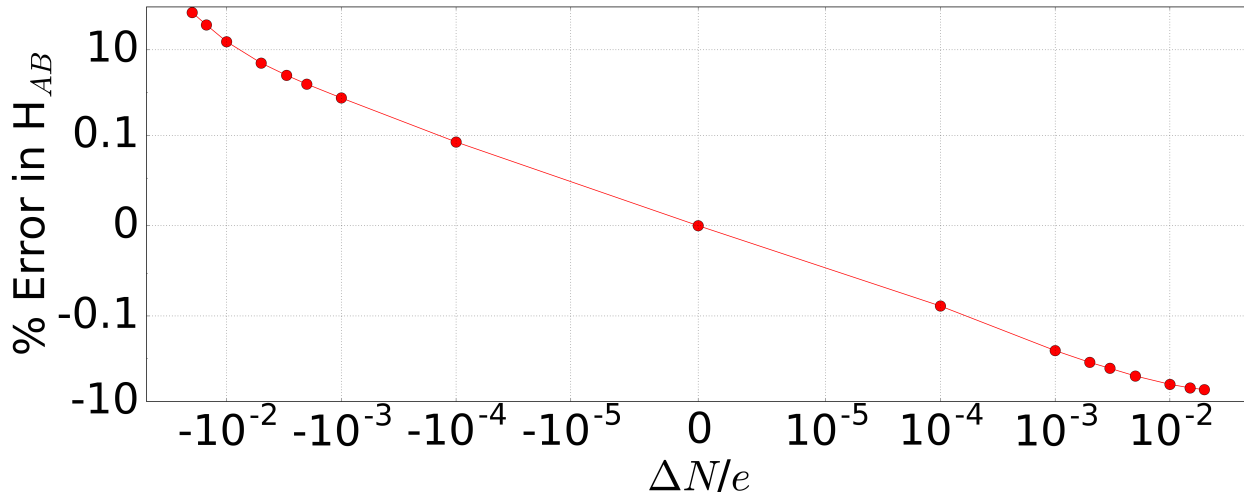


Figure 2.11: Percent error in electronic coupling $\left(100\% \times \frac{H_{AB}(N) - H_{AB}(N_0)}{H_{AB}(N_0)}\right)$ versus the error in the number of charges transferred ($\Delta N = N - N_0$), relative to results obtained with N_0 for Zn_2^+ at 5 Å separation (The equilibrium distance of Zn_2^+ within PBE is 2.55 Å).

pseudopotentials [156, 366], denoted QE/TM and QE/ONCV, are presented in Tables 2.4, 2.5, and 2.6 and compared with those obtained with the Car-Parrinello molecular dynamics code CPMD[11] and TM pseudopotentials by Kubas et al.[219, 220]. Tables 2.3 and 2.5 also contain calculated values for the HAB11[172], which were obtained using the CP2K code[246]. For a few systems (acetylene, benzene, and cyclobutadiene), direct comparison could not be made with CPMD since the electronic couplings were calculated between different orbitals.[219] Due to degeneracies in highly symmetric molecules, the charge-localized state can occupy one of several energetically equivalent orbitals, which have varying overlaps and electronic couplings with charge-localized states on neighboring molecules. This problem was addressed by Kubas et al., who chose the specific orbitals *a priori* in these cases. Since reading and reordering fragment-derived one-electron orbitals is not a routine procedure for Quantum ESPRESSO, we neglect these systems. As a result, these data points were excluded from Tables 2.4, 2.5, and 2.6 and Figure 2.12.

We found excellent agreement between the CPMD and Quantum ESPRESSO implementations; the mean absolute percent error (MAPE) in the couplings between the two codes is 2.7-3.5%, depending on the choice of pseudopotentials. We also found agreement for

the computed β values ($\text{ME} = 0.040 \text{ \AA}^{-1}$ and $= 0.029 \text{ \AA}^{-1}$ for TM and ONCV results, correspondingly). The different implementations of Hirshfeld partitioning, including intrinsic thresholds and cutoff radii for the atomic densities, are likely responsible for the small differences in the results obtained with these two codes.

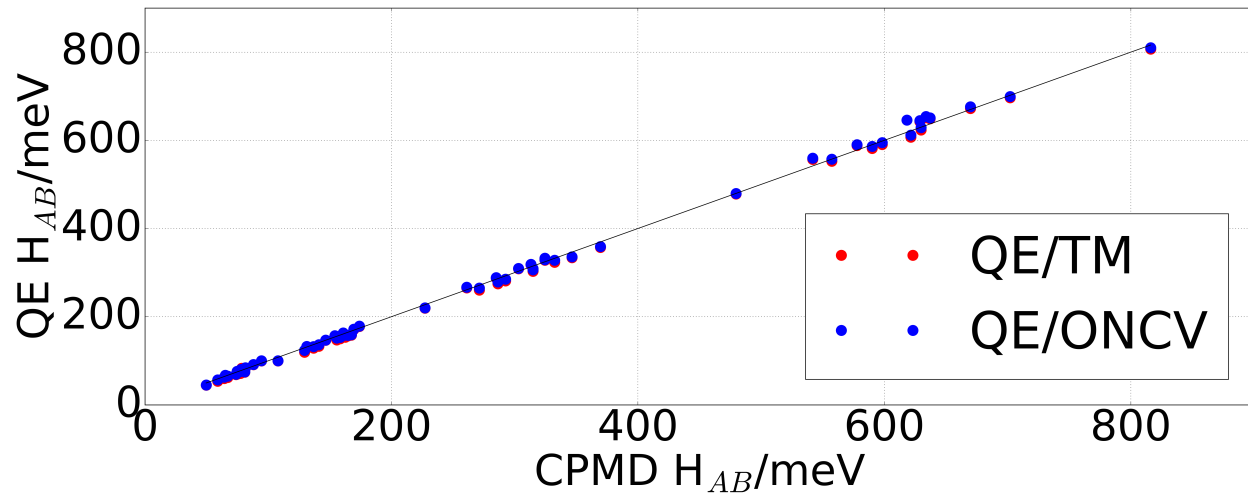


Figure 2.12: (Color online) Electronic couplings (H_{AB} , see Eq. 2.30) calculated using constrained density functional theory (CDFT) implemented in Quantum ESPRESSO (QE) versus values obtained with the CPMD code[11] (see Kubas, et al[219, 220]) for the HAB11 and HAB7 sets of π -conjugated molecules.

Table 2.3: Electronic couplings H_{AB} /meV calculated using CDFT for the HAB11[219] and HAB7[220] sets. QE, CPMD, and CP2K denote the Quantum ESPRESSO[137], CPMD[11], and CP2K[246, 172] codes, respectively. CP2K results were only available for the HAB11 set, and the molecules of the HAB7 set were not available (– above). TM and ONCV denote the Troullier-Martins[408] and optimized norm-conserving pseudopotentials[156, 366], respectively (see text). BW, BW+A, and FBB+A denote the Becke weight partitioning, Becke weight partitioning with atomic size adjustments, and fragment-based Becke weights with atomic size adjustments, respectively[172]). Two calculations carried out with QE and marked N/A did not converge without fractional occupations.

System	Separation/Å	QE/ONCV	QE/TM	CPMD	CP2K-BW	CP2K-BW+A	CP2K-FBB+A
Anthracene	3.50	651.07	648.78	637.00	–	–	–
Anthracene	4.00	329.15	327.96	324.50	–	–	–
Anthracene	4.50	171.49	170.80	169.40	–	–	–
Anthracene	5.00	91.60	90.98	87.90	–	–	–
Cyclopentadiene	3.50	699.45	696.57	702.10	653.07	647.63	745.59
Cyclopentadiene	4.00	335.82	334.03	346.40	304.77	299.33	386.40
Cyclopentadiene	4.50	159.32	158.06	167.40	138.78	136.06	190.48
Cyclopentadiene	5.00	75.03	74.04	80.90	65.31	65.31	92.52
Cyclopropene	3.50	810.11	806.87	816.10	772.80	770.08	900.70
Cyclopropene	4.00	358.90	357.16	369.60	334.70	331.98	440.82
Cyclopropene	4.50	157.57	156.58	164.80	146.94	146.94	209.53
Cyclopropene	5.00	69.42	68.87	73.90	68.03	68.03	92.52
Ethylene	3.50	611.67	607.08	621.50	598.65	601.37	702.05
Ethylene	4.00	306.29	302.77	314.80	304.77	304.77	361.91
Ethylene	4.50	153.01	150.12	158.30	152.38	152.38	174.15
Ethylene	5.00	N/A	82.97	78.40	73.47	73.47	78.91
Furane	3.50	594.68	590.53	598.20	–	–	–
Furane	4.00	285.25	281.40	292.50	–	–	–
Furane	4.50	136.33	132.82	141.00	–	–	–

Table 2.3 continued

Furane	5.00	65.36	62.23	67.00	–	–	–
Imidazole	3.50	586.23	581.57	590.10	541.51	541.51	636.75
Imidazole	4.00	278.88	274.77	286.30	247.62	247.62	318.37
Imidazole	4.50	132.22	128.69	136.80	117.01	117.01	152.38
Imidazole	5.00	63.01	59.99	64.30	54.42	54.42	68.03
Pentacene	3.50	645.97	N/A	618.30	–	–	–
Pentacene	4.00	309.60	308.54	303.00	–	–	–
Pentacene	4.50	156.82	156.12	154.00	–	–	–
Pentacene	5.00	80.19	79.74	77.70	–	–	–
Perfluoroanthracene	3.50	479.46	478.35	479.60	–	–	–
Perfluoroanthracene	4.00	219.90	219.41	227.20	–	–	–
Perfluoroanthracene	4.50	99.96	99.76	107.90	–	–	–
Perfluoroanthracene	5.00	45.01	44.76	49.60	–	–	–
Perylene	3.50	654.05	651.42	633.70	–	–	–
Perylene	4.00	332.83	331.43	324.50	–	–	–
Perylene	4.50	178.72	177.86	174.00	–	–	–
Perylene	5.00	100.26	99.59	94.40	–	–	–
Perylene diimide	3.50	559.38	557.01	541.80	–	–	–
Perylene diimide	4.00	266.88	265.55	261.00	–	–	–
Perylene diimide	4.50	132.64	131.94	131.20	–	–	–
Perylene diimide	5.00	67.30	66.83	65.10	–	–	–
Phenol	3.50	557.29	552.43	557.30	487.08	487.08	566.00
Phenol	4.00	264.94	260.46	271.30	217.69	214.97	280.28
Phenol	4.50	123.52	119.44	129.40	95.24	95.24	130.61
Phenol	5.00	56.87	53.55	58.90	43.54	43.54	59.87
Porphin	3.50	590.25	588.03	577.70	–	–	–
Porphin	4.00	288.54	287.50	285.00	–	–	–
Porphin	4.50	146.85	146.65	146.60	–	–	–
Porphin	5.00	76.17	75.71	74.70	–	–	–
Pyrrole	3.50	629.02	623.59	629.80	574.16	574.16	663.96
Pyrrole	4.00	309.13	304.20	314.80	272.11	269.39	340.14

Table 2.3 continued

Pyrrole	4.50	151.59	147.11	155.50	125.17	125.17	165.99
Pyrrole	5.00	74.56	70.59	75.70	57.14	57.14	76.19
Tetracene	3.50	644.67	642.28	628.80	–	–	–
Tetracene	4.00	318.79	317.65	313.10	–	–	–
Tetracene	4.50	163.00	162.24	160.80	–	–	–
Tetracene	5.00	84.36	83.84	81.50	–	–	–
Thiophene	3.50	676.13	672.15	669.90	609.54	612.26	699.33
Thiophene	4.00	328.24	323.50	332.30	280.28	277.56	353.75
Thiophene	4.50	158.10	153.35	162.40	127.89	127.89	165.99
Thiophene	5.00	75.61	71.45	77.40	59.87	59.87	73.47

Comparison	ME	MAE	RMSD	MAPE
QE/TM vs CPMD	-2.49	6.83	7.93	3.53
QE/ONCV vs CPMD	0.20	5.94	7.79	2.68
QE/ONCV vs QE/TM	2.34	2.34	2.84	1.30

Table 2.4: Mean error (ME)/meV, mean absolute error (MAE)/meV, root-mean-square deviation (RMSD)/meV, and mean absolute percent error (MAPE)/% for electronic couplings H_{AB} calculated using CDFT implemented in Quantum ESPRESSO (QE) for Troullier-Martins (QE/TM) and Optimized Norm-Conserving Pseudopotentials (QE/ONCV) and those obtained from the CPMD code[11] (see Kubas, et al[219, 220]) for the HAB11 and HAB7 sets.

In Tables 2.7 and 2.8, we present pairwise root-mean-square deviations (RMSDs) and mean absolute percent errors (MAPEs) for the molecules in the HAB11 database[219] as computed with our implementation, that of CPMD[11, 306], and the recent implementation in CP2K[246, 172]. Our and the CPMD results are within 10 meV in RMSD for this database,

System	QE/ONCV	QE/TM	CPMD	CP2K-BW	CP2K-BW+A	CP2K-FBB+A
Anthracene	2.618	2.614	2.637	–	–	–
Cyclopentadiene	2.989	2.977	2.884	3.078	3.068	2.787
Cyclopropene	3.283	3.278	3.205	3.245	3.238	3.028
Ethylene	2.669	2.771	2.759	2.795	2.800	2.915
Furane	3.001	2.945	2.919	–	–	–
Imidazole	3.029	2.975	2.955	3.057	3.057	2.978
Pentacene	2.706	2.776	2.760	–	–	–
Perfluoroanthracene	3.158	3.154	3.021	–	–	–
Perylene	2.503	2.499	2.534	–	–	–
Perylene diimide	2.824	2.821	2.818	–	–	–
Phenol	3.112	3.044	2.993	3.228	3.223	3.001
Porphin	2.729	2.727	2.721	–	–	–
Pyrrole	2.905	2.844	2.824	3.079	3.075	2.885
Tetracene	2.712	2.709	2.718	–	–	–
Thiophene	2.988	2.921	2.876	3.099	3.100	3.007

Table 2.5: Decay rates (β)/ \AA^{-1} for electronic couplings calculated using CDFT for the HAB11[219] and HAB7[220] sets of molecular dimers. β values were computed by fitting the results of Table 2.3 to the functional form $H_{AB} = A \exp^{-\beta R/2}$ on a log scale. QE, CPMD, and CP2K denote the codes Quantum ESPRESSO[137], CPMD[11], and CP2K[246], respectively. CP2K results were only available for the HAB11 set. TM and ONCV denote the Troullier-Martins[408] and optimized norm-conserving pseudopotentials[156, 366], respectively (see text). BW, BW+A, and FBB+A denote the Becke weight partitioning, Becke weight partitioning with atomic size adjustments, and fragment-based Becke weights with atomic size adjustments, respectively[172].

Comparison	ME	MAE	RMSD	MAPE
QE/TM vs CPMD	0.040	0.067	0.079	2.303
QE/ONCV vs CPMD	0.029	0.038	0.052	1.292
QE/ONCV vs QE/TM	-0.011	0.034	0.048	1.191

Table 2.6: Mean error (ME)/ \AA^{-1} , mean absolute error (MAE)/ \AA^{-1} , root mean square deviation (RMSD)/ \AA^{-1} , and mean absolute percent error (MAPE)/% for decay rates $\beta/\text{\AA}^{-1}$ for electronic couplings calculated using CDFT implemented in Quantum ESPRESSO (QE) with Troullier-Martins (QE/TM) and Optimized Norm-Conserving Pseudopotentials (QE/ONCV) and those obtained from the CPMD code[11] (see Kubas, et al[219, 220]) for the HAB11 and HAB7 sets. β values were computed by fitting the results of Table 2.3 to the functional form $H_{AB} = A \exp^{-\beta R/2}$ on a log scale.

	QE/TM	QE/ONCV	CPMD	CP2K-BW	CP2K-BW+A	CP2K-FBB+A
QE/TM	0.0	3.7	8.6	29.92	30.95	40.67
QE/ONCV	3.7	0.0	5.75	33.58	34.61	38.7
CPMD	8.6	5.75	0.0	36.43	37.52	33.53
CP2K-BW	29.92	33.58	36.43	0.0	2.04	64.83
CP2K-BW+A	30.95	34.61	37.52	2.04	0.0	65.9
CP2K-FBB+A	40.67	38.7	33.53	64.83	65.9	0.0

Table 2.7: Root mean square deviation (meV) for electronic couplings H_{AB} between different implementations of constrained DFT for molecules of the HAB11 database[220]. QE, CPMD, and CP2K denote the codes Quantum ESPRESSO[137], CPMD[11], and CP2K[246, 172], respectively. TM and ONCV denote the Troullier-Martins[408] and optimized norm-conserving pseudopotentials[156, 366], respectively (see text). BW, BW+A, and FBB+A denote the Becke weight partitioning, Becke weight partitioning with atomic size adjustments, and fragment-based Becke weights with atomic size adjustments, respectively[172].

	QE/TM	QE/ONCV	CPMD	CP2K-BW	CP2K-BW+A	CP2K-FBB+A
QE/TM	0.0	1.98	4.45	11.78	12.12	11.15
QE/ONCV	2.05	0.0	2.52	13.96	14.32	9.69
CPMD	4.7	2.61	0.0	16.57	16.92	7.4
CP2K-BW	10.24	11.78	13.7	0.0	0.36	19.98
CP2K-BW+A	10.5	12.05	13.96	0.36	0.0	20.22
CP2K-FBB+A	13.03	11.27	8.34	25.61	26.0	0.0

Table 2.8: Mean absolute percent error (%) for electronic couplings H_{AB} between different implementations of constrained DFT for molecules of the HAB11 database[220]. QE, CPMD, and CP2K denote the codes Quantum ESPRESSO[137], CPMD[11], and CP2K[246, 172], respectively. TM and ONCV denote the Troullier-Martins[408] and optimized norm-conserving pseudopotentials[156, 366], respectively (see text). BW, BW+A, and FBB+A denote the Becke weight partitioning, Becke weight partitioning with atomic size adjustments, and fragment-based Becke weights with atomic size adjustments, respectively[172].

while differing by 30-40 meV from those of the CP2K results. We note that the choice of constraining potentials may produce noticeable variations in the computed couplings, with MAPEs of 10-20% and RMSDs up to 66 meV between different localization approaches.

Having verified our methodology, we now turn to a case study of silicon quantum dots.

2.4.4 Application to silicon quantum dots

The electronic coupling as well as other electron transfer properties such as driving force and reorganization energy are paramount to understanding hopping transport in QD devices and yet few *ab initio* studies of QD solids focus on these properties and few address the effects of thermal disorder on the electronic coupling between QDs. For example, at 0 K a perfectly symmetric Si₃₅H₃₆ QD has degenerate HOMO and LUMO energy levels. These degeneracies are lifted by disorder at finite T or by the interaction with nearby QDs. Realistic simulation of charge transport in QD solids requires the inclusion of these effects.

In this section, we examine the effect of structural distortions induced by finite temperature on computed electronic couplings when using several different methods for estimating charge transfer parameters. Two methods often used for nanoscale materials are the splitting in dimer method and the anticrossing method. Within the splitting in dimer (SID) method, the electron (hole) transfer coupling is computed from the difference of the lowest unoccupied molecular orbital, or LUMO, (highest occupied molecular orbital, or HOMO) and the LUMO+1 (HOMO-1) one-electron energy levels:

$$H_{AB} = \frac{1}{2} \left[E_{\text{LUMO}+1(\text{HOMO})} - E_{\text{LUMO}(\text{HOMO}-1)} \right]. \quad (2.33)$$

The anticrossing (hereafter AX) method[373, 81] utilizes the response of one-electron wavefunctions to applied electric fields to estimate the electronic coupling. The applied electric field is varied to find the nearest approach of the HOMO (LUMO+1) and HOMO-1 (LUMO) energy levels for hole (electron) transfer processes, then the coupling is evaluated using the SID method. We refer interested readers to representative publications for more details[373, 81].

In Figure 2.13, we use the CDFT, SID, and AX methods to calculate the electron coupling between a dimer of Si₃₅H₃₆ QDs with a geometry taken from a 300K molecular dynamics trajectory. First, we consider the electronic couplings for hole transfer, on the left. While

CDFT electronic couplings for holes decrease exponentially ($\beta_{\text{CDFT}}^{\text{hole}} = 4.10 \text{ \AA}^{-1}$) for the disordered geometry, the SID and AX couplings behave unphysically, remaining either mostly constant ($\beta_{\text{SID}}^{\text{hole}} = 0.15 \text{ \AA}^{-1}$) or behaving erratically. For the electron transfer (see right hand side of Figure 2.13) the decay rates are 1.76, 0.97, and 1.35 \AA^{-1} for the CDFT, SID, and AX methods, possibly implying different physical mechanisms responsible for the decay in the three methods.

Two factors contribute to the failure of the SID and AX methods for the hole transfer: polarization effects from intermolecular interactions, as pointed out in the literature for the SID method[411, 89]; and disorder in the QD geometry leading to symmetry breaking. The single particle wavefunctions obtained for the relaxed configuration at $T=0$ and for a snapshot extracted from an MD system demonstrate this symmetry breaking, as shown in Figure 2.14. As expected, the HOMO wavefunction is delocalized across both sites in the relaxed configuration; however, the HOMO and HOMO-1 wavefunctions of the thermally disordered dot are localized on separate sites. As a result, the difference in the energy levels is largely independent of the inter-site distance. The example shown here indicates that CDFT is a more robust framework to compute electronic couplings, especially when thermally disordered configurations are involved.

In summary, in this section, we described a robust method for studying charge transport at the nanoscale using periodic constrained DFT. We compared our results to those found with other codes and localization potentials, showing minor differences coming from the use of different pseudopotentials and plane wave codes. Substantial differences were instead found for different localization potentials and for different convergence thresholds. Finally, our results for nanodots demonstrated key limitations of methods such as the energy splitting in dimer or the anticrossing methods. For silicon quantum dot dimers, constrained DFT predicts physical (i.e. exponential) decay rates for the electronic coupling of disordered geometries. By contrast, the energy splitting in dimer and anticrossing methods fail for hole transfers, resulting in an unphysical distance dependence of the electronic coupling. Work is

in progress to simulate more complex nanoscale materials using the methodology presented here.

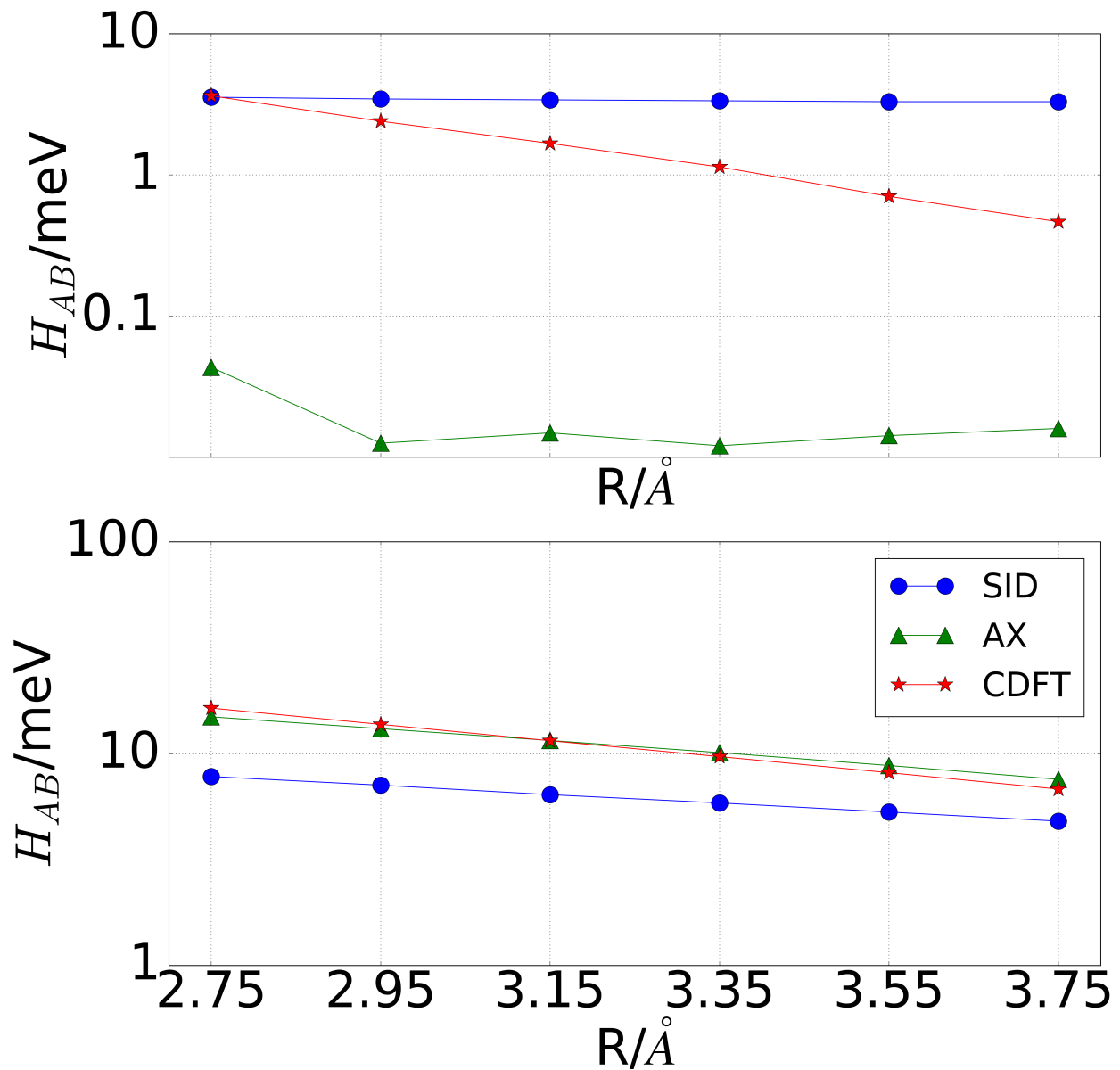


Figure 2.13: Semi-log plot of the electronic coupling for holes (top) and electrons (bottom) versus distance $R/\text{\AA}^{-1}$ between two $\text{Si}_{35}\text{H}_{36}$ QDs for configurations taken from 300K molecular dynamics trajectory. Electronic couplings are computed using the splitting in dimer (SID), anticrossing (AX), and constrained DFT (CDFT) methods (see text).

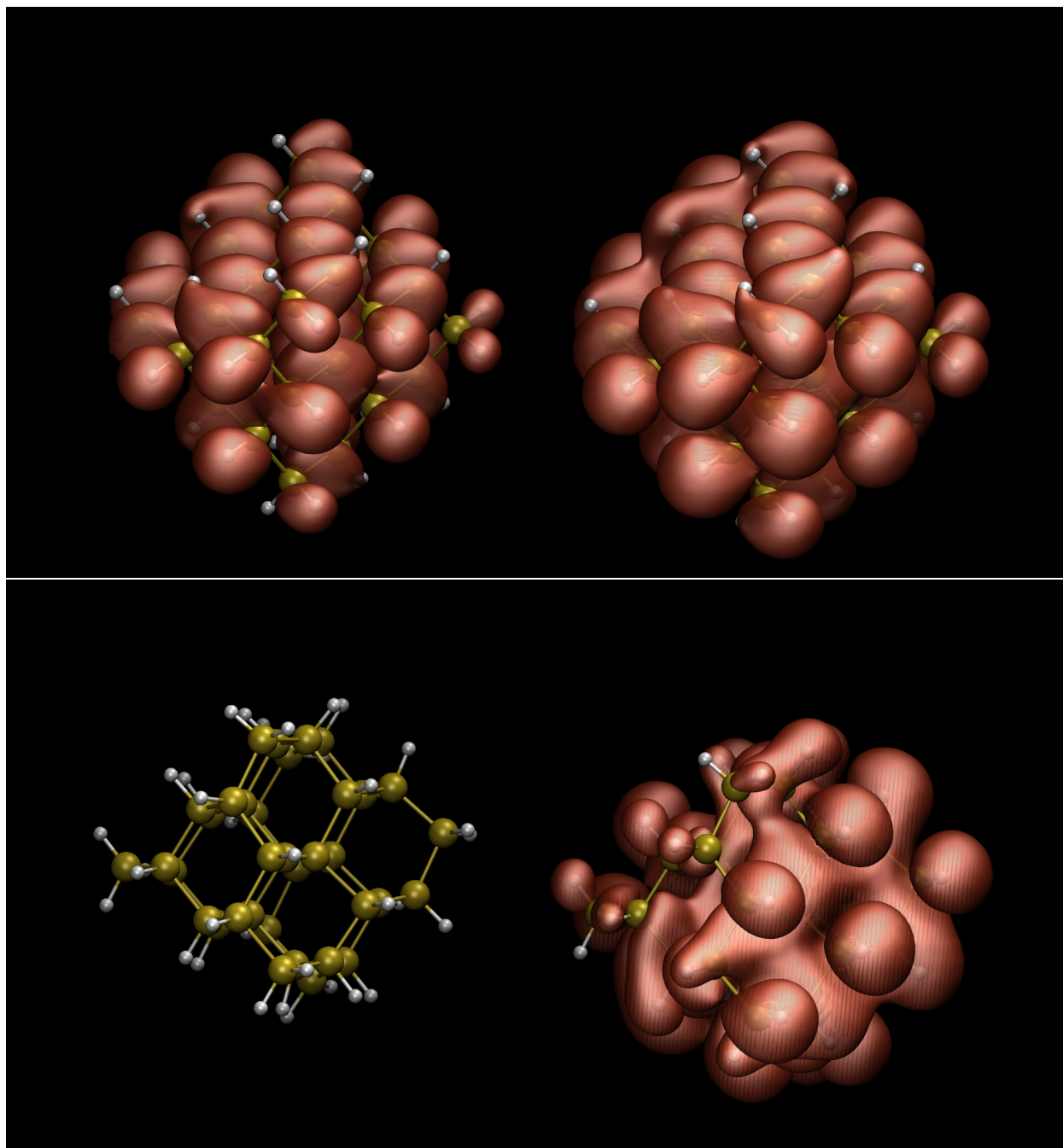


Figure 2.14: Isosurfaces of the highest occupied single particle molecular orbital (HOMO) of a Si₃₅H₃₆ dimer, as obtained using DFT and the PBE functional, for a configuration relaxed at T=0 and one extracted from an MD simulation performed at 300K. The separation between the nanoparticles is 3.75 Å. White and yellow sphere represent hydrogen and silicon, respectively.

CHAPTER 3

OPTICAL PROPERTIES OF ISOLATED NANOPARTICLES

In this chapter we turn our attention to the application of the methods discussed in chapter 2 to isolated nanoparticles. In section 3.1, we focus on oxidized silicon nanoparticles and addresses the ubiquitous problem of nanoparticle blinking which is detrimental to nanoparticle applications. Blinking is the switching between bright and dark states of nanoparticles under continuous excitation and was first reported two decades ago. A special type of blinking called “B-type” blinking is believed to be caused by nonradiative, recombination centers at the surface of nanoparticles. Recently B-type blinking has been observed in oxidized Si nanoparticles.[55, 57, 56] Here we show how Si dangling bonds at the surface of oxidized nanoparticles introduce defect states which, depending on their charge and local stress conditions, may give rise to B-type blinking.

In section 3.2, we discuss engineering band edge positions of nanoparticles through post-synthetic surface chemistry modification. Band edge positions of semiconductor nanoparticles determine their functionality in many optoelectronic applications. We show how band edge positions of lead sulfide (PbS) colloidal semiconductor nanoparticles, some of the most common types of nanoparticles, can be tuned by over 2.0 eV. We achieved this through ligand exchange of native ligands with functionalized cinnamate ligands. Our ab initio calculations and electrostatic models, together with experiment, establish a clear relationship between ligand dipole moments and nanoparticle band edge shifts which can be used to engineer nanoparticles for optoelectronic applications.

3.1 Nanoparticle Blinking

3.1.1 Introduction

Reproduced from Nicholas P. Brawand, Márton Vörös, and Giulia Galli *Nanoscale* 7, 3737 (2015) with permission from the Royal Society of Chemistry.

Fluorescence intermittency, also known as blinking, refers to the stochastic switching between bright (ON) and dark (OFF) states of molecular emitters under continuous excitation and can be found in a wide variety of systems, from single violamine molecules[353] to semiconductor nanoparticles (NPs).[301] Blinking may be a detrimental effect which decreases the quantum efficiency, brightness and overall performance of NPs in several applications such as single-molecule imaging, lasers and NP solar cells. Blinking of individual NPs was first reported in CdSe two decades ago and it has since been observed in CdS, CdTe, ZnS and Si. [301, 55, 57, 86, 292, 420, 376, 54] It is now believed that two types of blinking processes exist.[128] One, referred to as "A-type", is caused by photo-assisted Auger ionization. In the OFF state, all excited electron-hole (e-h) pairs recombine through nonradiative Auger recombination. The probabilities of the ON and OFF blinking times (t) follow a power law of the form $P(t) \propto t^{-\alpha}$ where $1 < \alpha < 2$ and several theoretical microscopic models were proposed to explain the switching mechanism. [376, 420, 112, 399, 222, 358, 336, 430, 144] We note that the power law distribution is ubiquitous in nature: earthquake magnitudes, solar flare intensities, wildfires sizes, the sizes of neuronal and sandpile avalanches all have a power law dependence and the origin of such dependence has been explained by the influential theory of self-organized criticality.[17, 271]

Another type of blinking, B-type, is believed to be caused by the charging and discharging of yet unidentified, electron-accepting, nonradiative, recombination centers at the surface of the NPs.[128] For example, blinking was observed in Si/SiO₂ nanoparticles, and it was suggested that the "simple opening and closing of an efficient nonradiative recombination center" could be a reasonable explanation for the observed linear dependence of the blinking frequency on excitation power; however the nonradiative center has remained so far unidentified.[55, 57, 56] Indeed, several types of native defects exist at the Si/SiO₂ interface and it is yet unclear which of them may cause blinking in NPSi/SiO₂ systems.[4, 381, 313, 318]

One of the most common defects at the Si/SiO₂ interface, both in the bulk and in

NPs, is the silicon dangling bond (DB), which has been the focus of several theoretical and experimental investigations.[328, 339, 341, 394, 338, 43, 340, 395, 197, 275, 192, 193, 441, 159, 30] At the bulk Si interface the isolated DB can exist in three different charge states: negative D^- , neutral D^0 and positive D^+ with two electronic transitions positioned 0.3 eV above the VBM and 0.25 eV below the CBM, respectively.[106, 187] After oxidation, the density of DB defects on a bulk Si surface may be of the order of 10^{12} cm^{-2} and even at these densities, DBs may be detrimental to the functionality of electronic devices.[197, 111] Though bulk silicon-silicon-oxide interfaces have been extensively studied, given their interest to the electronics industry, much less is known about the properties of DB defects on the surface of oxidized Si NPs.

In particular, all first principle studies of DBs at the surface of Si NPs were so far focused on hydrogen terminated samples in the absence of a host matrix[173, 234], which is however known to influence the electronic properties of the NPs.[153, 239] It is now known that quantum confinement leads to Si DB charge transition levels (CTLs) which are asymmetrically positioned within the electronic gap of fully hydrogen passivated Si NPs. Neutral DBs at the surface of hydrogenated Si NPs were predicted to be efficient nonradiative recombination centers responsible for low electron mobilities in organic-inorganic hybrid nanostructure materials[234]; recombination on charged DBs was instead found to be a radiative process for small Si crystallites with gap energies higher than 2.2 eV, at low temperatures.[227]

In this chapter, we used ab initio calculations to investigate the electronic properties and charge recombination dynamics in oxidized Si NPs containing surface DBs. We focused on the relative probability of radiative and nonradiative recombination processes[226, 6, 379, 248] as a function of stress at or close to the surface of the NP, where defects are present. From our results, we predicted that surface DBs introduce defect states which can cause blinking within oxidized Si NPs, and these DB states are responsible for the exponential blinking statistics observed experimentally in Si NP/oxide composites. Our study is the first to report ab initio calculations of recombination rates of defects at oxidized Si NP surfaces.

3.1.2 Structural Models

We considered three Si NPs; $\text{Si}_{77}\text{O}_{52}\text{H}_{76}$, $\text{Si}_{116}\text{O}_{72}\text{H}_{84}$ and $\text{Si}_{238}\text{O}_{119}\text{H}_{132}$ terminated with one oxidized layer, with diameters of 1.3, 1.6 and 1.9 nm respectively. These NPs were obtained in a previous study[239] through a coupled classical-ab initio molecular dynamics (MD) approach, by annealing Si NPs within an amorphous SiO_2 matrix consisting of 648 atoms.

After annealing, the NPs and their interfacial oxide layer shells were extracted from the host matrix and terminated by hydrogen atoms, so as to saturate all dangling bonds of the oxide. The projected density of states of the embedded and extracted NPs were compared, and found to be almost identical. We hence considered the extracted NPs with an oxide layer as representative of a Si NP under the stress conditions exerted by the matrix and, for computational simplicity, we studied the electronic properties of defects in the extracted NPs.

At the surface of the latter, we introduced three different types of DB defects, traditionally denoted: P_b , P_{b1} and P_{b0} ,¹ and we optimized the positions of nearest neighbor atoms under three different conditions, mimicking the presence of different stress fields on the surface of the nanoparticles. First, we simulated the presence of a highly constrained environment where only atoms that are nearest neighbors of the defect are allowed to relax (we denote this configuration by r_{nn}). We then considered the conditions under which only the outer most layer was held fixed and the interior atoms, including nearest neighbors of the defect, were allowed to relax (configuration r_{np}). Finally, we simulated a free standing NP where all atoms were allowed to relax (configuration r_∞). The final geometry of the smallest extracted model without any relaxation is presented in Figure 3.1.

1. The DB defect geometries are labeled P_b , P_{b0} and P_{b1} to indicate that the defects are Paramagnetic; they were first reported in Ref. [302]. The P_b defect is found at the bulk Si(111)/ SiO_2 interface while the P_{b1} and P_{b0} have been reported to exist at the Si(100)/ SiO_2 interface.[340]

3.1.3 Theory and Computational Methods

Usually, the presence of DBs introduce electronic defect states within the energy gap of the host semiconductor. Such states may become charged through different mechanisms, including (i) the exchange of electrons or holes with surrounding defects within the host matrix, (ii) the variation of the Fermi level by applying an electric field, or (iii) a change in the doping levels within the sample.

In order to study charge defects and compare their relative stability, it is useful to define charge transition levels. The value of the Fermi level ($\epsilon(q_1/q_2)$) at which two charge states, q_1 and q_2 , of the same defect have the same formation energy is called the charge transition level and is defined as:

$$\epsilon(q_1/q_2) = \frac{E^f(X^{q_1}; E_F = 0) - E^f(X^{q_2}; E_F = 0)}{q_2 - q_1} \quad (3.1)$$

where E_F is the Fermi level and $E^f(X^{q_1}; E_F = 0)$ is the formation energy of defect X in charge state q_1 . [120] In our calculations of E^f , atomic positions were allowed to relax within specific relaxation conditions (r_{nn} or r_∞), hence the transition levels reported in this chapter correspond to thermodynamic transition levels, as defined in Ref. [121].

To compute the nonradiative capture rates by a single DB we need to calculate the transition rate from a thermalized state manifold given by [276]:

$$k_{nr} = \sum_m f_m k_m \quad (3.2)$$

where m is the initial vibrational state manifold index, f_m is the quantum statistical equilibrium distribution and k_m is the transition rate of state m . In this chapter we treated the interaction to first order in the electron-phonon coupling and because the initial state is expected to decay to a manifold of final vibrational states, we may replace k_m in Equation 3.2 with Fermi's golden rule. Furthermore, we assumed the nonradiative transition processes to take place between two electronic states, along a single effective reaction coordinate, with

both states characterized by the same single vibrational frequency ω . The path of the effective parabolic vibrational mode was defined by $\{R_x\} = x\{R_f\} + (1-x)\{R_i\}$, where $\{R_i\}$ and $\{R_f\}$ are the optimized atomic coordinates of the system in the initial and final electronic states, respectively, as x is varied from 0 to 1. Under these conditions, Equation 3.2 gives the full quantum (FQ) transition rate:

$$k_{nr}^{FQ} = \sum_{m,n} f_m \frac{2\pi}{\hbar} |v|^2 |\langle \chi_{im} | Q - Q_i | \chi_{fn} \rangle|^2 \delta(E_o + m\hbar\omega - n\hbar\omega) \quad (3.3)$$

where E_o is the ionization energy of the defect defined as $E_o = E_i(\{R_i\}) - E_f(\{R_f\})$, $\chi_{i,m}$ is the harmonic wavefunction of the effective vibrational state with quantum number m , when the electron is in state i ; $Q - Q_i$ is the difference between the configuration coordinate of the reaction and the equilibrium configuration coordinate corresponding to an electron in the initial state i defined by $Q - Q_i = \sum_j \sqrt{M_j} (R_j - R_{i,j})$, where M_j is the mass of the j^{th} atom, R_j is the position of the j^{th} atom and $R_{i,j}$ is the equilibrium position of the j^{th} atom when the electron is in the initial state. f_m is the Bose-Einstein occupation of the vibrational state m and v is the electronic coupling computed within the static and linear coupling approximations[6, 226]:

$$v = (\epsilon_f - \epsilon_i) \langle \psi_i(r; \{R_i\}) | \frac{\partial \psi_f(r; \{R_i\})}{\partial Q} \rangle \quad (3.4)$$

where we assumed the many body electronic wavefunctions can be replaced by the single particle Kohn-Sham orbitals $\psi_i(r; \{R_i\})$ and $\psi_f(r; \{R_i\})$, i.e. the eigenfunctions of the electronic Hamiltonian at $\{R_i\}$; ϵ_i and ϵ_f are the respective eigenvalues.

In the high temperature limit $\hbar\omega \ll k_b T$ the ions can be treated classically and $f_m \approx \frac{\hbar\omega}{k_b T} e^{-\beta(E - E_i(\{R_i\}))}$, where $\beta = (k_b T)^{-1}$. Furthermore if v is small then k_m in Equation 3.2 can be replaced with $\frac{\omega}{\pi} P_{i \rightarrow f}$ where $P_{i \rightarrow f}$ is the probability that a transition $\psi_i \rightarrow \psi_f$ occurs, given by the Landau-Zener formula.[469] Under these conditions and making the substitution $\sum_m \rightarrow \int \frac{dE}{\hbar\omega}$, Equation 3.2 simplifies to the well known Marcus theory equation:[269, 226]

$$k_{nr}^{Marcus} = |V|^2 \sqrt{\frac{\pi\beta}{\hbar^2 E_{FC}}} e^{-\beta E_{act}} \quad (3.5)$$

where E_{FC} is the Franck-Condon shift and $V = v(Q - Q_i)$, when $Q - Q_i$ is evaluated at the crossing point. E_{act} is the activation energy given by:

$$E_{act} = \frac{(E_o - E_{FC})^2}{4E_{FC}}, \quad (3.6)$$

If we treat both the ions and the electron classically, then k_m can be replaced by $\frac{\omega}{\pi} \Theta(E - E_{act})$ so that the probability of the electron transition occurring is 1 if the energy of the system is greater than the activation energy. Under these conditions, Equation 3.2 gives the classical transition rate:

$$k_{nr}^C = \frac{\omega}{\pi} e^{-\beta E_{act}} \quad (3.7)$$

Equations 3.3, 3.5 and 3.7 serve as the basis for all nonradiative transition rate calculations considered in this chapter.

Radiative recombination rates were estimated using Fermi's golden rule and the dipole approximation and they are given by[66, 97]:

$$k_r = \frac{4n\alpha\omega^3}{3c^2} |\langle \psi_i(r; \{R_i\}) | \mathbf{r} | \psi_f(r; \{R_i\}) \rangle|^2 \quad (3.8)$$

where \hbar has been set to 1, c is the speed of light in vacuum and ω is the transition energy. Because the NP is mostly composed of Si atoms and we are only interested in the comparison of k_r and k_{nr} which, according to our results, differ by more than two orders of magnitude, the index of refraction (n) was approximated by that of bulk Si. We checked the strain dependence of the radiative lifetimes by calculating the decay rates of an excited electron in the fully relaxed and strained 1.3 nm NPs. We found both rates to be of the order of 10^6 s⁻¹, which is within the same order of magnitude of other theoretical predictions.[152, 78]

Geometry optimizations and all other results reported in this chapter were obtained using density functional theory (DFT) as implemented in the software package Quantum Espresso[135]. The generalized gradient corrected PBE functional[324] was used as an approximation for the exchange and correlation energy. Norm-conserving Rappe Rabe Kaxiras Joannopoulos (RRKJ)[348] pseudopotentials in separable (Kleinman-Bylander) form from the Quantum Espresso library[135] were adopted to describe the effective interaction between valence electrons and frozen ionic cores. The single particle Kohn-Sham (KS) orbitals were represented using a plane wave basis with a maximum energy cutoff of 80 Rydberg; energies and wavefunctions were considered converged after the estimated error on the electronic total energy was less than 10^{-8} Ry. Geometry optimizations were considered converged if all forces were less than 10^{-3} Ry/Bohr. Total energies of charged systems were obtained using the Makov-Payne correction (MPC) scheme.[267]

3.1.4 Results

In the following we discuss our results for the electronic properties of the neutral and charged dangling bond defects and for several radiative and nonradiative decay processes. By comparing computed values of k_r and k_{nr} as a function of the local stress in the NP, we show that decay channels are strongly dependent on strain and hence on the effect of the matrix on the NP. Finally we discuss blinking and its dependence on strain.

We first discuss our calculations of thermodynamic charge transition levels showing that the levels of P_b , P_{b1} and P_{b0} are stress dependent. The computed charge transition levels for the P_b , P_{b1} and P_{b0} defects on the surface of strained, oxidized 1.3 nm Si NPs are presented in Figure 3.2. They were obtained as total energy differences using Equation 3.1. All calculations represented by solid lines were carried out in the configuration characterized by the coordinate r_{nn} .

The dashed lines represent the CTLs of the fully relaxed NP with a single P_b defect in an unstrained configuration; the comparison with the solid line for the same system highlights

the effect of strain in determining the CTLs. In agreement with Ref. [173], we found that the CTL of the P_b defect is asymmetrically positioned within the gap of the defectless NP. This asymmetry is also present in the case of the P_{b1} and P_{b0} defects. Assuming the Fermi level can lie anywhere within the gap of the NP, then Figure 3.2 shows that the most likely charge state of the NP is the neutral charge state. Therefore, we now turn our attention to the single particle energy levels of the NP with a neutral DB defect, and verify that the defect states remain within the NP gap as its diameter is varied.

It is well known that DFT underestimates energy gaps, but it has nevertheless proven to be a useful tool to predict *trends* of energy gaps, e.g. as a function of NP size. In Figure 3.3 we present the HOMO/LUMO gaps of two DB defect geometries as a function of NP size. Not shown in Figure 3.3 are the P_{b0} gaps which were found to differ from those of the P_b defect by less than 0.05 eVs for the smallest NP. Our results predict that the defect energy levels remain within the gap of the oxidized NPs for all diameters.

The bulk model, "B" reported Figure 3.3, was simulated by a 215 Si atom supercell with a single dangling bond defect at the center. The neighboring atoms around the defect were passivated using an oxygen bridge and a hydrogen atom.

Having established that the single particle energy levels associated with the stable neutral defect are in the gap of the NPs, we now focus on the P_b defect on the surface of the 1.3 nm oxidized NP. We first discuss the potential energy surfaces corresponding to the electronic excitations displayed in Figure 3.3. Though the full PESs are not required to calculate k_{nr} , they help to visualize the decay processes. A qualitative description of the configuration coordinate is provided in Ref. [106]. The PESs were obtained by fitting parabolas to the total energy calculations required to obtain E_o and E_{FC} for the P_b defect on the surface of the 1.3 nm NP, within the r_{nn} relaxation condition. Two spin channels can be excited as shown in the two panels of Figure 3.4.

Though several atoms move along different paths during each of the reactions depicted in Figure 3.4, the configuration coordinate on the x-axis of Figure 3.4 represents, on average,

the position of a three-fold coordinated silicon surface atom along a radial direction of the NP, with the origin corresponding to the equilibrium position of the atom, and with the DB in the neutral charge state (D^0). The red curve corresponds to the DB in the neutral charge state (D^0) with an excited carrier in the conduction band. As the system relaxes the charge state of the DB changes. Depending on which spin channel the excited carrier occupies, the DB may transition to either the negative (D^-) or positive (D^+) charge state represented by the black curves in panels a) and b), respectively. During the transition from (D^0) to (D^-), the three-fold coordinated atom moves away from its nearest neighbors at equilibrium and from the NP center, in the positive radial direction. During the transition from (D^0) to (D^+), the three-fold coordinated surface atom moves in the negative radial direction towards the plane formed by its three nearest neighbors. When relaxation is completed, the DB returns to the neutral charge state (D^0).

The PESs of Figure 3.4 show that the nonradiative $D^+ \rightarrow D^0$ decay process is much slower than the other processes shown in Figure 3.4. However, the PESs may vary, depending on the amount of strain induced by the surrounding matrix. To elucidate the effect of strain on the character of recombination processes, we plotted in Figure 3.5 the $\ln(k_r/k_{nr})$ for the four decay processes outlined in Figure 3.4, as a function of decreasing strain.

Nonradiative recombination rates for the processes displayed in Figure 3.4 and the r_{nn} configurations were also calculated using Marcus theory (Equation 3.5). After comparing the two methods, Equations 3.5 and 3.7, we found the characters (radiative or nonradiative) of all the transitions within the r_{nn} configuration to be unchanged.

It is clear from Figure 3.5, that the nonradiative recombination rates are highly sensitive to the number of atoms that are permitted to relax around the defect, due to the exponential dependence of k_{nr} on E_{act} . The largest k_{nr}^{FQ} is of the order of $10^{12}s^{-1}$ which is the same order of magnitude as that predicted by H. Li, et al. for the charge recombination rate at a $Si_{147}H_{100}/P3HT$ interface in the presence of a dangling bond.[234] The nonradiative recombination rates were calculated for the three different configurations defined earlier (r_{nn} ,

r_{np} and r_{∞}). By holding some atoms fixed during relaxation we preserved the strain induced by the original surrounding matrix. Calculations allowing only nearest neighbor atoms to relax (r_{nn}) simulate a system where the matrix has a strong effect on the surface strain of the NP. Instead, the r_{∞} calculations simulate a free standing NP in the absence of the stress exerted by a host matrix. Our results show that the amount of strain – which was shown to be dependent on the density of the matrix and the size of the NP[239] – is a key factor in determining whether a recombination channel is radiative or nonradiative. For example, the $D^0 \rightarrow D^-$ process is predicted to be radiative in the r_{nn} configurations; however, the same process is predicted to be nonradiative for configuration r_{np} . Overall we found that the strain caused by the matrix increases the nonradiative recombination lifetimes with respect to that of unstrained NPs.

We also built an additional model of the P_b defect at a different location on the NP, indicated by the square in Figure 3.5. The qualitative behavior (whether a channel is radiative or nonradiative) of this model agrees with that reported in Figure 3.5 by the dots, except for the $D^0 \rightarrow D^-$ process which is predicted to be nonradiative for the r_{nn} geometry.

The nonradiative recombination rates also depend on the size of the NP, mostly through the dependence of the ionization energy on quantum confinement. As the size of the NP increases, the confinement energy decreases causing E_o to approach E_{FC} and thus decreasing the energy barrier (see Equation 3.6). While nonradiative recombination becomes more efficient as the size of the NP becomes larger, we expect the opposite trend for the radiative transitions, due to a reduction of the overlap between the HOMO/LUMO and the DB state, as well as the decrease in the energies of the transitions.[152] Hence, we predict there will be a crossing region where the $D^+ \rightarrow D^0$ process will become nonradiative. If we assume E_{FC} and k_r to be size independent, we predict that the $D^+ \rightarrow D^0$ process will become nonradiative for NPs larger than about 4 nm in diameter. Quasi-particle corrections to DFT single particle energies nearly cancel the exciton binding energy in Si NPs[108]; hence the values of computed DFT gaps are representative of measured optical gaps. In terms of

quasi-particle gaps our calculations are representative of NPs with larger radii.

Because the nonradiative lifetimes of the $D^+ \rightarrow D^0$ process is several orders of magnitude larger than the corresponding radiative one, if strain is present for both *Pb* models, we predict that the capture of an electron by a positively charged DB on the surface of an oxidized NP is most likely a radiative process for NPs smaller than about 4 nm in diameter. Instead, $D^- \rightarrow D^0$ is most likely nonradiative. These results differ from previous results obtained from empirical tight binding theory for hydrogen passivated NCs, which predicted both $D^- \rightarrow D^0$ and $D^+ \rightarrow D^0$ to be radiative processes.[227]

3.1.5 Analysis of Blinking Processes

Our calculations showed that there are strain conditions, represented by the coordinates r_{np} that, in the presence of DBs, may give rise to ON and OFF states in small oxidized Si nanoparticles. If a NP with a DB is excited while in the negatively charged state, the fastest recombination channels are all nonradiative, resulting in the OFF state. If the system is excited while in the positively or neutrally charged state, half of the recombination channels are radiative for both states but only the positively charged state is likely to emit photons with energies equal to the intrinsic gap of the NP. Hence, we label the positive charge state ON and the neutral state OFF. Therefore, the charge state of the DB can determine if the NP is in the ON or OFF state.

Switching between the OFF and ON state can occur if an electron from a neutral NP with a surface DB were to tunnel to the several possible defects that exist in the surrounding oxide.[4] Doing so would cause the NP/DB system to become positively charged (ON) until an electron transfer returns the system back to the neutral charge state (OFF). Hence our calculations provide an explanation for blinking processes observed in Si NPs.[55, 57, 86, 398, 412, 54] We note that recent experiments detecting blinking processes have been interpreted in terms of nonradiative recombination centers inside of or near CdSe/CdS/ZnS/InP NPs[358, 336] and Si NPs,[55, 57, 54] where the switching frequency between ON and OFF

states was found to depend linearly on the input power. This property suggests that the switching mechanism may indeed depend on single excitation processes, as our calculations suggest, rather than on more complex processes such as Auger recombination.

In summary, using ab initio calculations within density functional theory, we investigated the charge transition levels and recombination rates in Si NPs with oxidized surface layers and DB defects present at the surface. We showed that, depending on the charge state and strain conditions at the surface, DBs may act as nonradiative recombination centers. Based on these results, we predicted that surface dangling bonds introduce defect states at the surface of oxidized Si NPs that can cause ON and OFF blinking states. Switching between ON and OFF could be caused by charge transfer to other local defects or by temporary passivation of the DB state.

Hence our work provided a microscopic picture to explain how blinking may be achieved through surface DBs, which are highly sensitive to the local strain around each NP; however, as previously mentioned, blinking may also occur by photo-assisted Auger ionization. The coexistence of multiple mechanisms, with one being highly sensitive to strain, may explain the observed variation in the type of blinking exhibited by different NPs within the same sample.[57] Our results indicate that in a given sample, the number of NPs exhibiting exponential type blinking varies with size, strain and surface passivation. Hydrogen treatment[330, 229, 167] and annealing[295, 294, 167] may help reduce the density of dangling bands possibly reducing the amount of blinking. Deep level transient spectroscopy could be used to quantify the effects of strain by measuring charge transition levels and electron spin resonance experiments would be a good additional probe to validate our predictions.

Our results are the first reported ab initio calculations showing that dangling bonds on the surface of oxidized Si NPs can act as efficient nonradiative recombination centers or traps. Our findings thus also provide an *a priori* validation of the interpretation of the role that dangling bond defects play in several photonic and optoelectronic devices.[391, 321, 253, 327, 155]

3.2 Tuning the Optical Properties of Nanoparticles: Experiment and Theory

Band edge positions of semiconductors determine their functionality in many optoelectronic applications such as photovoltaics, photoelectrochemical cells, and light emitting diodes. We show here that band edge positions of lead sulfide (PbS) colloidal semiconductor nanocrystals, specifically quantum dots (QDs), can be tuned over 2.0 eV through surface chemistry modification. We achieved this remarkable control through the development of simple, robust, and scalable solution-phase ligand exchange methods, which completely replace native ligands with functionalized cinnamate ligands, allowing for well-defined, highly tunable chemical systems. By combining experiments and *ab initio* calculations, we establish clear relationships between QD surface chemistry and the band edge positions of ligand/QD hybrid systems. We find that in addition to ligand dipole, inter-QD ligand shell inter-digitization contributes to the band edge shifts. We expect that our established relationships and principles can help guide future optimization of functional organic/inorganic hybrid nanostructures for diverse optoelectronic applications.

3.2.1 Introduction

Reproduced from Daniel M. Kroupa, Márton Vörös, Nicholas P. Brawand, Brett W. McNichols, Elisa M. Miller, Jing Gu, Arthur J. Nozik, Alan Sellinger, Giulia Galli, Matthew C. Beard “Tuning Colloidal Quantum Dot Band Edge Positions through Solution-Phase Surface Chemistry Modification” Nature Communications (2017) with permission from the Nature Publishing Group.

Colloidal semiconductor nanocrystals, specifically quantum dots (QDs), are of interest to numerous scientific disciplines due to their highly tunable optical and electronic properties. The study of QDs has long been focused on the inorganic core; specifically, on quantum-confinement (*e.g.* size-dependent band gaps[64] and enhanced Auger-type processes[114]) or

increased surface-to-volume ratio effects (*e.g.* size-dependent phase transitions[2]). However, it has become increasingly clear that post synthetic surface chemistry modification, or ligand exchange, can critically influence QD optoelectronic properties, as well.[37, 207, 161, 464] Ligand exchanges are often performed in the solid-state, where films of QDs with long, aliphatic surface ligands are exposed to solutions of shorter alkyl-chain or atomic ligands for exchange. These types of ligand exchanges are convenient methods for constructing functional materials; however, establishing fundamental principles that govern the relationship between ligand/QD optoelectronic properties and the physicochemical nature of the surface is not straightforward, as many uncontrolled and ill-defined variables are introduced during QD processing including the extent of ligand exchange, QD core stoichiometry, facet-specific ligand coordination, and ligand denticity.

For the case of metal chalcogenide QDs, several research groups have studied the influence of surface chemistry on QD optoelectronic properties. Surface chemistry modification has long been used to effectively passivate surface states and electronically couple QDs through decreased inter-QD distance, thus leading to enhanced carrier transport in QD thin films and improved photoluminescence quantum yields.[250, 9] More recently, researchers have studied how ligand/QD optoelectronic properties are influenced by ligand functionalization through the variation of ligand coordination environment and/or ligand electron donating/withdrawing character.[138, 139, 34, 119] The Bawendi,[51, 84] Luther,[92] and Bent[364] groups found that surface chemistry modification using solid-state ligand exchange techniques can shift the ionization energy (IE) and work function (ϕ) of lead sulfide (PbS) QD thin films, thus allowing for the engineering of more efficient QD solar cells. All of these studies demonstrated that modifying the ligand/PbS QD interface produces quite distinct chemical systems, and some even suggested a link between QD band edge energy shifts and ligand dipole moment; however, due to the uncontrolled and ill-defined physicochemical nature of solid-state ligand exchanges, a clear and quantitative relationship has never been reported.

To this extent, we have developed a simple, robust, and scalable solution-phase X-type ligand exchange method for PbS QDs that replaces native surface ligands with functionalized cinnamate ligands, yielding highly tunable, well-defined organic/inorganic hybrid chemical systems. We explore a library of functionalized cinnamic acid molecules to systematically tune PbS QD surface chemistry, and find that thin films of fully ligand exchanged QDs exhibit remarkable band edge shifts: the band edge position of QDs can be tuned over 2.0 eV, the largest value reported to date. We use a combination of experiment and theory to directly establish the physical principles governing QD surface chemistry-induced band edge shifting, and find that ligand dipoles alone are insufficient to fully describe the observed band edge shifts. We propose that inter-QD ligand shell inter-digitization likely present in close packed QD thin films must be accounted for, and we report quantitative comparisons between theory and experiment.

3.2.2 Results

We identified seven functionalized cinnamic acid (R-CAH) ligands (3.2.2a) as candidates for solution-phase ligand exchanges at the oleate (OA^-) terminated, lead-rich surface of 3.2 nm diameter PbS QDs (QD synthesis, adapted from reference [164], is detailed in Methods). R-CAH molecules are ideal ligands for solution-phase exchange because i) the optoelectronic properties of the R-CAHs are widely tunable through functionalization of the aromatic ring of the ligand motif, ii) the vinyl linkage of R-CAH allows for electronic coupling of the dipole active portion of the ligand to the QD core, iii) the R-CA^- ligands impart long-term colloidal stability and prevents QD aggregation, iv) the carboxylate surface coordination environment of native oleate (OA^-) is conserved post-exchange, and v) the binding of R-CAHs induces broadband optical absorbance enhancement, which can be utilized to monitor the extent of exchange *in situ*. [138, 139, 216] We classify each R-CAH ligand by its functional group and whether it is protonated and free in solution or deprotonated and bound to the QD surface. Thus, 4-H-CAH denotes *trans*-cinnamic acid and 4-H-CA^- denotes *trans*-

cinnamate⁻. Of the ligands studied, only 4-CN-CAH was not commercially available and was synthesized in house. We found the calculated vacuum electronic dipole moment of the unbound, protonated R-CAHs to be readily tunable through functionalization of the aromatic ring of the cinnamic acid ligand motif (3.2.2a).

We developed a simple, robust, and scalable solution-phase ligand exchange method for the R-CAH ligands of interest in this work following the scheme described in 3.2.2b. Purification of the fully exchanged PbS QDs involved removal of the oleic acid (OAH) byproduct and residual R-CAH through multiple cycles of selective precipitation of the ligand exchanged QDs from solution using a nonpolar antisolvent (hexane), followed by centrifugation and re-dissolution in an appropriate solvent (PCR purification).

A combination of FT-IR (3.2.2a) and HNMR (3.2.2b) analysis provided direct evidence that OA⁻ is removed from the QD surface *via* an exchange with R-CA⁻. The FT-IR spectrum of OAH has a broad -OH feature from 2250-3250 cm⁻¹, alkane/alkene C-H stretches around 3000 cm⁻¹, and a distinct C=O stretch near 1680 cm⁻¹, while for the OA⁻/QD complex, the alkane/alkene C-H stretches are retained, but the broad -OH and sharp C=O stretches are no longer present. Instead, evidence of a bidentate carboxylate binding environment is observed with symmetric and asymmetric COO⁻ stretches at 1530 and 1408 cm⁻¹. For each ligand exchange we found comparable spectral changes between free R-CAHs and R-CA⁻/QDs, suggesting that the R-CA⁻ ligands coordinate the QD surface in a similar geometry as OA⁻ and no free R-CAH remains. Additionally, comparing the OA⁻/QD spectrum to the R-CA⁻/QD spectra, we observed a drastic decrease in the alkane/alkene C-H stretches (~3000 cm⁻¹), indicating efficient displacement of OA⁻ and removal of OAH. Additionally, the unique C≡N triple bond stretching can be clearly observed near 2250 cm⁻¹ for 4-CN-CA⁻/QD and 4-CN-CAH.

Furthermore, a comparison of the ¹H NMR spectra (3.2.2b) of free 4-H-CAH and 4-H-CA⁻/QD complex after purification showed distinct differences. The vinyl peak at 5.3 ppm is significantly broadened for the OA⁻/QD complex and shifted upfield due to dipolar

coupling.[166] The OA^-/QD spectrum showed a lack of the broad OAH acidic proton peak around 12 ppm, in agreement with OA^- chemical identity. Pure 4-H-CAH showed a doublet at 6.47 and 7.81 ppm from the alpha and beta vinyl protons, respectively, with a broad peak around 11.8 ppm from the acidic proton. The remaining peaks at 7.56, 7.40, and 7.42 ppm correspond to ortho, meta, and para aromatic protons, respectively. The 4-H- CA^-/QD spectrum showed drastically different features than those of the OA^-/QD complex and pure 4-H-CAH. The 4H- CA^-/QD aromatic and vinyl protons shift upfield and broaden significantly, accompanied by a concurrent loss of the carboxylic acid peak. Finally, the lack of the broad surface bound OA^- vinyl peak suggested there is very little residual OAH or OA^- in the ligand exchanged sample after PCR purification. The combination of FT-IR and HNMR analysis suggests the efficient and complete exchange of native OA^- ligands for R-CA^- followed by removal of excess R-CAH and OAH through PCR purification.

Using the library of completely exchanged $\text{R-CA}^-/\text{QDs}$ prepared following the method described in Section A, we cast films of QDs *via* a single deposition step on Au/glass substrates for X-ray photoelectron spectroscopy (XPS) measurements to extract the work function (ϕ) and valence band maximum (E_{VBM}) with respect to the Fermi level (E_F); ($E_F - E_{VBM}$), which can be summed to yield the ionization energy (IE) of the QD thin film. The raw XPS photoelectron cutoff and valence band region data sets are presented in 3.2.2a and 3.2.2b, respectively. We found that QD IE (3.2.2c, solid rectangles) is shifted across the $\text{R-CA}^-/\text{QD}$ library by 2.1 eV accompanied by a shift in ϕ (3.2.2c, black dashed) of 2.4 eV. As a guide, we also include the conduction band minimum (E_{CBM} , open rectangles) determined from summing the optical gap (opaque lines) and calculated exciton binding energy.[51] Each of the QD films exhibits a Fermi-level within the QD band gap indicative of n-type behavior (closer to the conduction band) that is consistent with the roughly constant Pb:S ratio measured from XPS analysis.[280] In accordance, the X-type ligand exchange does not involve the removal of surface Pb atoms. Note that for all of our ligand exchanges, the QDs are kept strictly air-free; once exposed to ambient conditions, we expect the degree

of oxidation to vary significantly across the ligand set, affecting the resulting Fermi-level position within the QD band gap.

Our analysis of the experimental band edge shifting data suggests that ligands containing fluorinated functional groups behave differently from those that do not – a phenomenon that has been previously reported for solid-state surface modification of ITO and ZnO with functionalized phosphonate molecules.[207] In particular, the 4-CN-CA⁻/QD complex has the most negative (electron withdrawing) projected ligand dipole, but its measured band edge is not as deep as either the 4-CF₃-CA⁻/QD or 3,5-F-CA⁻/QD complexes (3.2.2c and 4a). A linear least squares fit of the data that only includes the fluorinated ligand/QD complexes finds a best-fit slope of 0.45 eV/Debye (3.2.2a, red dashed line). In stark contrast, a best-fit line through the data that excludes the fluorinated ligand/QD complexes finds a much shallower slope, 0.12 eV/Debye (3.2.2a, blue dashed line). To confirm the generality of this observation, we tested a second class of ligands - functionalized benzenethiolates (4-R-S⁻), namely 4-H-S⁻ (3.2.2a, blue open circle) and 4-CH₃-S⁻ (3.2.2a red [solution-phase ligand exchange] and green [layer-by-layer ligand exchange] open circles). We found good agreement between the measured absolute IE versus ligand dipole with that of the cinnamate ligands, suggesting that the surface dipole at the ligand/QD interface is also similar for both classes of ligands. To extend the benzenethiolate library, we plot the IE versus calculated 4-R-S⁻ dipole taken from a separate data set collected by Bent *et al.*[364] (3.2.2a, brown and gray open circles) using a similar PbS 4-R-S⁻/QD material system, but using different techniques to measure film IE (ambient PES) and calculate ligand dipole. We note that while their measured IE for a 4-NO₂-S⁻/QD thin film (3.2.2a, open brown circle) finds good agreement with our non-fluorinated ligand data set (3.2.2a, blue dashed line), their measured IE for a 4-F-S⁻/QD thin film (3.2.2a, open gray circle) finds better agreement with our fluorinated ligand data set (3.2.2a, red dashed line). Therefore, we conclude that the observation of fluorinated ligands inducing deeper band edge shifts compared with non-fluorinated ligands is a general trend.

To understand the magnitude and direction of the experimental band edge shift measurements and how they relate to cinnamic acid ligand functionalization, we carried out first principles calculations using three different structural models of ligand/QD complexes with varying surface coverage. Ball-and-stick representations of the models can be found in the insert to 3.2.2b. Our calculations showed that the band edge shifts, δE , for the R-CA⁻/QD complexes are proportional to the ligand dipole calculated in vacuum for a given ligand/QD model, and that the models with higher ligand surface coverage exhibit stronger dependence on the ligand dipole. Furthermore, the calculated δE renormalized by the ligand surface coverage for each ligand/QD model all show a similar, roughly linear trend with the calculated ligand dipole (3.2.2b).

Since these ligand/QD complexes are smaller than those used in the experiments and are not fully ligated for computational reasons, we parameterized a simple electrostatic model[186] for better comparison with experiments. Assuming that the QD is spherical and its diameter is larger than the ligand/QD interface thickness where the surface dipole layer arises, δE is proportional to the number of ligands, N , and the effective surface dipole created by an adsorbed ligand, \tilde{p} , and it is inversely proportional to the surface area; $\delta E \propto N\tilde{p}/r^2$, where r is the QD radius. The effective surface dipole, \tilde{p} , is determined by both the intrinsic dipole of the free ligand, calculated in vacuum, and the induced dipole at the ligand/QD interface (surface dipole);[464, 51] we assumed that the former is proportional to the projected ligand dipole, p , and that the latter is the same for all of the R-CA⁻ ligands since the ligand binding environment (bidentate carboxylate) remains constant throughout the library. The computed band edge shifts were then fit with the linear equation $E = E_0 + \Delta E = E_0 + A(N/r^2)p$, where E_0 and $A(N/r^2)$ were considered as variables. Using the experimental QD diameter of 3.2 nm ($r = 1.6$ nm) and $N = 100$ ligands (determined *via* quantitative NMR), $A(N/r^2)$ varies between 0.255 and 0.355 eV/Debye across the various models, which are of the same order of magnitude as those determined experimentally.

Despite the good agreement between experiment and computation, in our computational

modeling we do not observe any significant deviation between fluorinated and non-fluorinated ligand/QD band edge data sets, which was clearly observed in our experimental measurements. To explain this deviation, we explored various surface-related phenomena. (1) It is conceivable that the number of ligands coordinating the QD surface may vary across the ligand set due to differences in steric-mediated packing densities. Recently, we utilized a combination of NMR spectroscopy and spectrophotometric absorption titration to monitor and characterize the solution-phase ligand exchange of native OA^- ligands for 2,6-F- CA^- ligands at PbS QD surfaces. We found that the total number of coordinating carboxylate ligands remains constant during these X-type ligand exchanges, demonstrating a stoichiometric (1:1), self-limiting exchange reaction that likely proceeds through a proton transfer between native OA^- and R-CAH free in solution.[216, 124] Here, we demonstrate that the ligand exchange is driven to completion, as evidenced by FT-IR and HNMR analyses; thus, each removed OAH is replaced by one R- CA^- . In agreement, XPS elemental analysis shows that the C:Pb ratio, once normalized for ligand stoichiometry, remains nominally constant between the OA^-/QDs and R- CA^-/QDs indicating the ligand-to-QD ratio remains constant. (2) Next we considered that, in the calculations, the ligands are oriented mostly perpendicular to the QD surface, while experimental configurations may vary, *e.g.* due to steric or cooperative packing at the surface. However, all three of our models with different ligand binding geometries/orientations showed similar behavior once renormalized for ligand surface coverage (3.2.2b).

Another possible explanation for the difference in behavior between the fluorinated and non-fluorinated R- CA^- ligands is variability in ligand/ligand electrostatic interaction. Strong intra-QD and inter-QD ligand interactions may result in reduced effective ligand dipole moment due to dipolar screening/depolarization fields.[53] (3) We modeled intra-QD ligand effects within a single QD ligand shell by re-calculating projected ligand dipoles taking into account ligand polarizability effects. We found that the absolute magnitude of the renormalized effective ligand dipoles as a function of ligand functional group changes substantially,

but the overall trend does not. Additionally, we performed slab simulations and, again, found that the effective dipole moment is reduced in close packed ligand monolayers, but the original trend is retained. We thus conclude that intra-QD ligand surface polarization is unlikely to be the effect responsible for the observed differences.

Finally, (4) we explored inter-QD ligand electrostatic effects by generating structural models of a QD film assembled from Model B by reducing the distance between periodic replicas in a simple cubic lattice in directions x and y (3.2.2d and 3.2.2e). The QD film IE was computed by measuring the HOMO of the monolayers relative to the average electrostatic potential in the middle of the vacuum region along the z direction. 3.2.2c shows the change in HOMO position when isolated QDs (closed squares) are brought together to form a monolayer of QDs with inter-digitized ligand shells (open squares). We expect that inter-digitization reduces the effective dipole moment felt by the QD core since the dipole moment of the ligands of neighbor QDs point in a direction opposing the ligands of the QD in question. Indeed, we find that inter-digitization reduces the magnitude of the band edge shift in the monolayer, and we expect that such ligand inter-digitization-dependent renormalization effects would be even more pronounced in three-dimensional films.

Ligand shell inter-digitization is commonly observed for QD films fabricated using aliphatic, monodentate ligands,[443, 442] and likely occurs with $R-CA^-$ ligands. However, we hypothesize that the extent of inter-QD ligand shell inter-digitization is mediated by the functional group on the aromatic ring. Specifically, QD ligand shells composed of fluorinated cinnamates likely do not inter-digitate due to dipolar fluorine-fluorine electrostatic interactions and, thus, will exhibit band edge positions closer to those of the isolated QDs (3.2.2c, closed squares). Fluorine is the most electronegative element on the periodic table, therefore, C-F bonds are highly dipolar leaving the fluorine (carbon) atom with a slight negative (positive) charge. Thus, the fluorine atoms of interacting ligand shells could repel one another and prevent inter-QD ligand shell inter-digitization. Using the principles of inter-QD ligand electrostatic effects mediating ligand shell inter-digitization, we find good agreement between the

computational predictions and the experimental trends (see the large square data markers in 3.2.2c, and compare to 3.2.2a). The fluorinated ligand/QD complexes are shifted to deeper IE s because their ligand shells remain isolated (3.2.2c, large, closed squares) compared to the non-fluorinated ligand/QD complexes, which undergo ligand shell inter-digitization induced dipole moment renormalization (3.2.2c, large, open squares).

In summary, through a combination of experiment and *ab initio* calculations, we established that ligand dipole is a critical parameter for predicting the overall direction and upper limit to the magnitude of band edge shifting in PbS QD thin films; however, ligand-ligand electrostatic effects that dictate inter-QD ligand inter-digitization and effectively screen the ligand shell dipole must also be considered. Controlling absolute band edge positions is an important design criterion for a large variety of potential solid-state and colloidal QD applications. We found that $IE(\phi)$ of our ligand/QD complex library ranges from 6.2 (5.4) eV for the 4-CF₃-CA⁻/QD complex to 4.1 (3.0) eV for the 4-N(CH₃)₂-CA⁻/QD complex. For comparison, we fabricated other PbS ligand/QD thin films that have been studied previously, following layer-by-layer film fabrication procedures as specified in the literature using a similar PbS QD system.[51, 92, 364] We found good agreement between the XPS band edge values we measured and those reported elsewhere, giving us confidence that our R-CA⁻/QD complex library induces the deepest and shallowest absolute band edges for PbS QD thin films, to date.

The procedures developed here are expected to translate to other R-CA⁻ ligands, of which there are greater than 500 known substitutional groups. In addition, we found similar trends of band edge shifts for a second class of ligands, functionalized benzenethiolates, including a similar deviation between theoretical and experimental ordering for fluorinated and non-fluorinated ligands. Our results can be extrapolated to larger QDs using an electrostatic model, showing that band edge shifts should be independent of QD diameter if the ligand surface coverage (ligands/nm²) remains constant as a function of size.

We also demonstrated a simple, robust, and scalable solution-phase ligand exchange

method that yielded well-defined, highly tunable chemical systems allowing us to cleanly and systematically correlate QD film band edge shifts with surface chemistry. Solution-phase ligand exchanges will benefit numerous synthetic processes. For example, conventional methods to fabricate QD thin films employ solid-state layer-by-layer, batch-processing fabrication techniques because the ligands most commonly employed do not impart QD colloidal stability. Here we deposited electronically coupled films *via* a single deposition step from low boiling point solvents. Single-step deposition from a colloidal QD “ink” allows for high-throughput, roll-to-roll processing where film thickness and morphology can be controlled through QD concentration and solvent composition.[297] Furthermore, single-step deposition techniques allow for QD superlattice formation, which holds the potential for highly conductive QD films through band-like transport.[463] The flexibility of employing organic ligands to produce functional inorganic/organic systems is very attractive for many emerging applications, and we expect the trends established here relating ligand properties with ligand/QD electronic properties to serve as a guide for further studies using *a-priori* approaches. While not the subject of the present work, we find that in addition to tuning band edge positions, all of the R-CA⁻ ligands induce broadband optical absorbance enhancement demonstrating that the beneficial band edge tuning does not come at the expense of degraded optical properties.

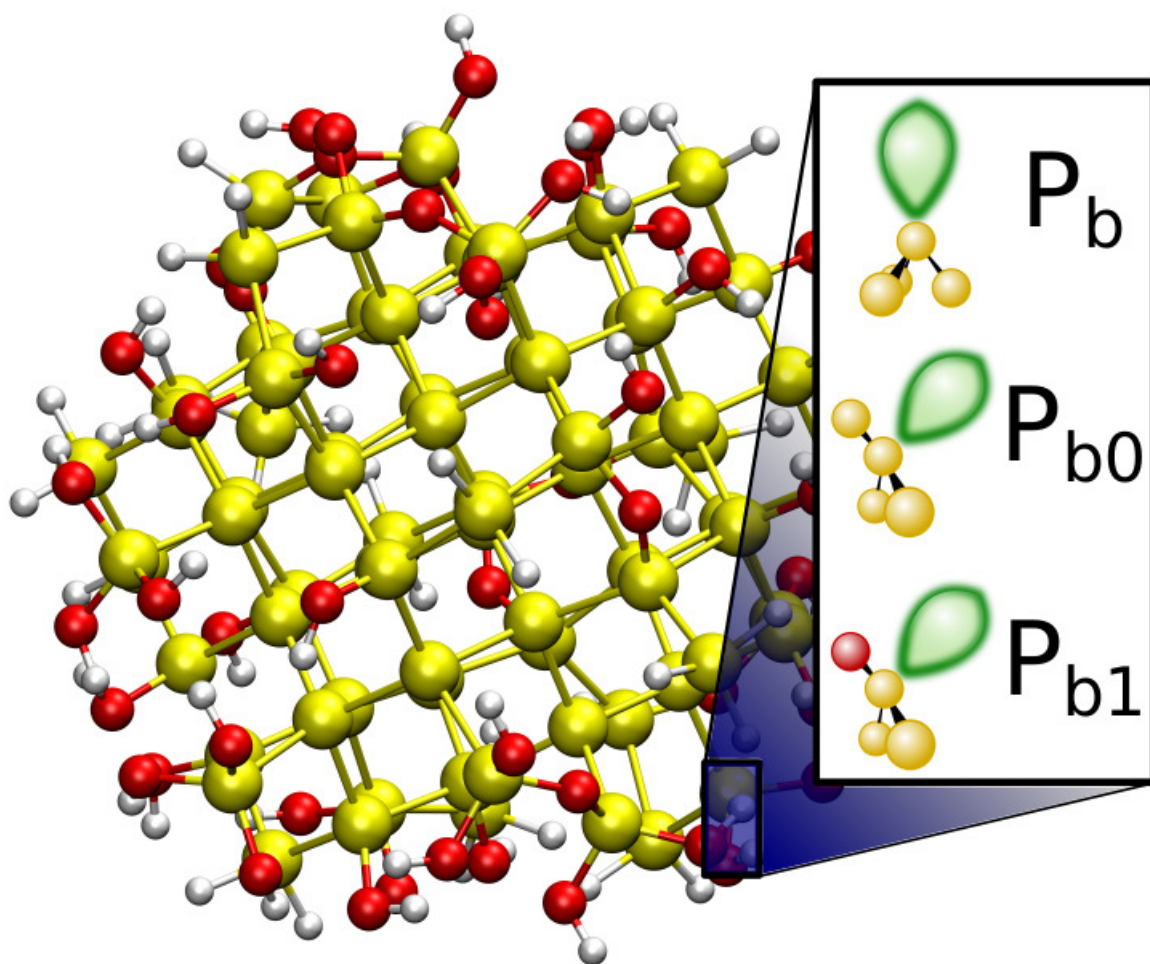


Figure 3.1: Model of a 1.3 nm silicon nanoparticle terminated by an oxide layer, as extracted from an amorphous matrix of SiO_2 (see text). The three dangling bond defect geometries studied in this chapter, labeled P_b , P_{b0} and P_{b1} , are shown.[302, 340] The P_b defect, originally found at the (111) interface of bulk Si/SiO_2 is back-bonded to three Si atoms. The P_{b0} and P_{b1} are both at the (100) interface. The P_{b0} is back-bonded to three Si atoms, while P_{b1} is back-bonded to two Si and one O atoms. The P_{b1} defect has been modeled using the geometry proposed by Poindexter et al.[340] Silicon, oxygen and hydrogen atoms are represented by yellow, red and white spheres, respectively. Each nanoparticle modeled in this chapter has a maximum of one dangling bond defect.

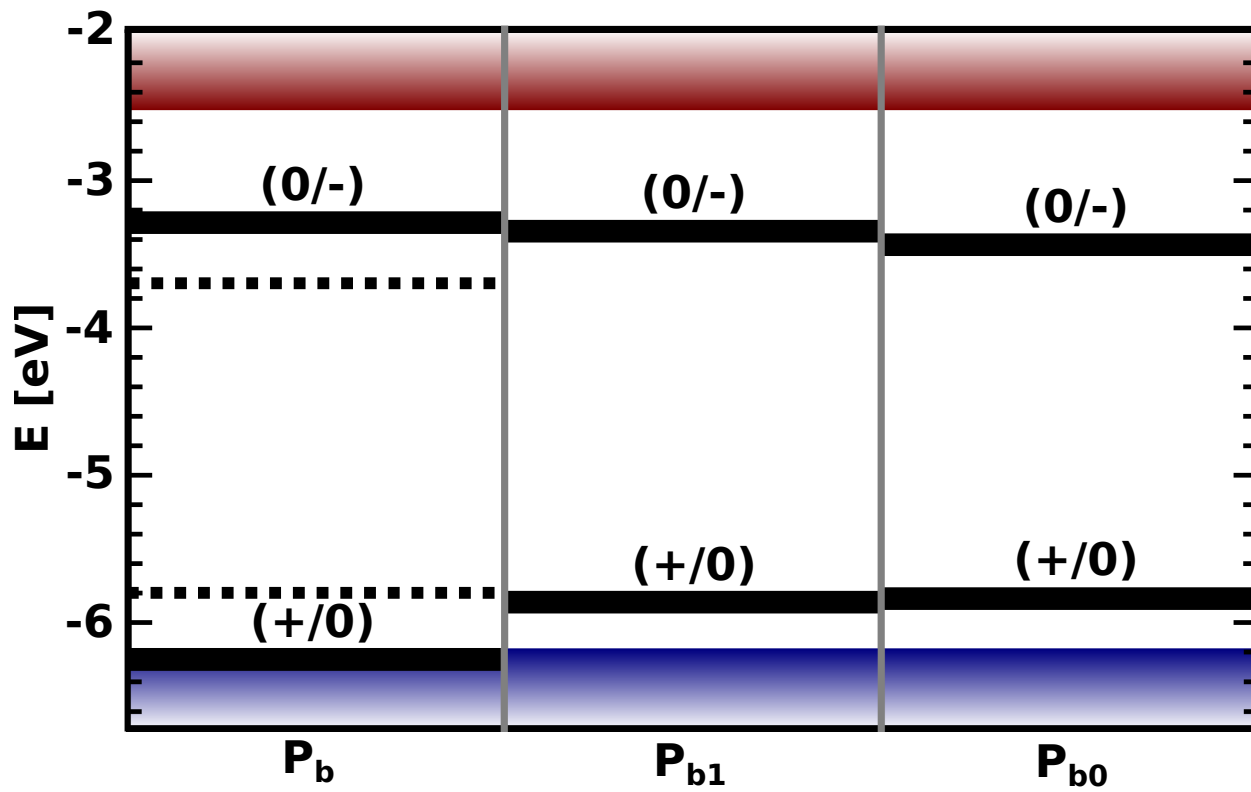


Figure 3.2: Charge transition levels for the P_b , P_{b1} and P_{b0} defects on the surface of strained oxidized 1.3 nm silicon NPs. The lowest and uppermost positions of the blue and red areas represent the negative of the ionization potential and electron affinity of the defectless oxidized 1.3 nm nanoparticle, respectively. Dashed lines are the charge transition levels computed for the same NP but in the absence of stress. The energy levels are all referenced to vacuum.

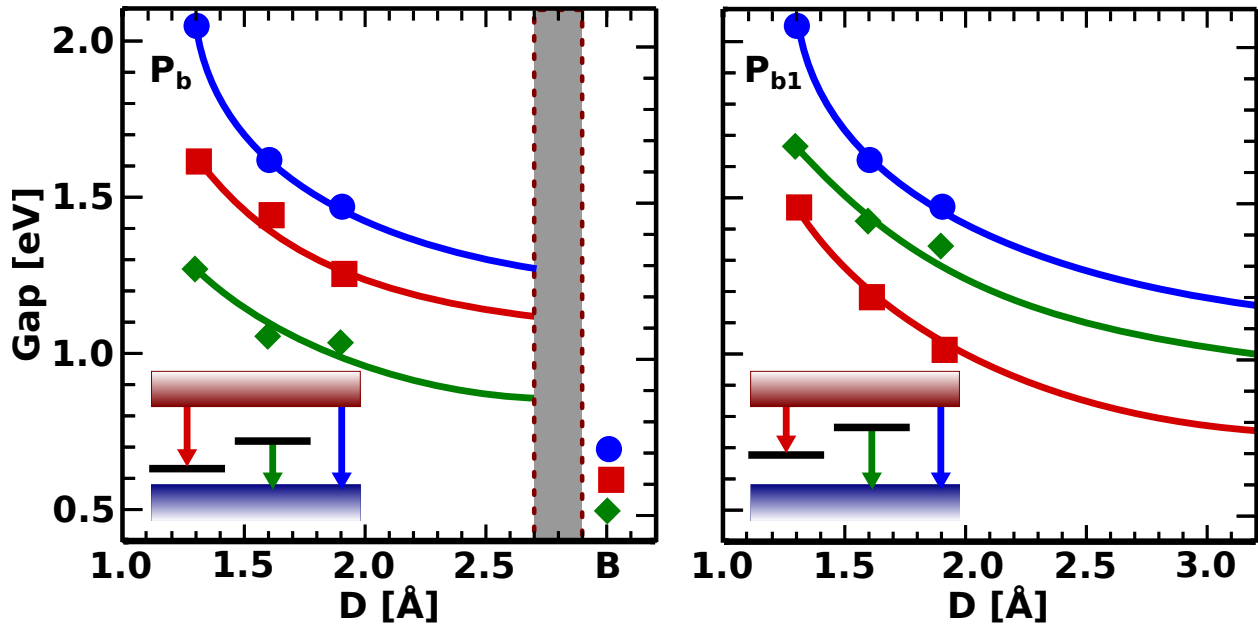


Figure 3.3: HOMO/LUMO gaps of the P_b and P_{b1} surface defect states in the presence of a strained oxide layer on the surface of three different Si nanoparticles. The insets represent the single particle energy levels and the corresponding gaps given by the colored arrows.

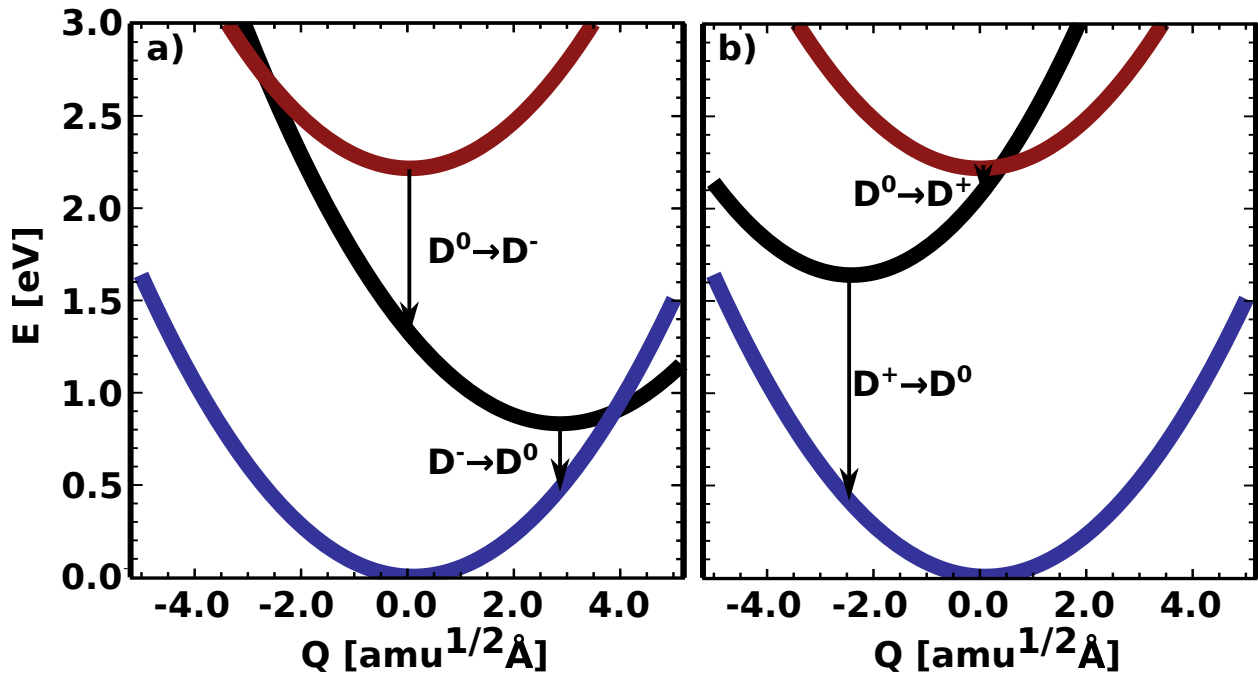


Figure 3.4: Configuration coordinate diagrams for the decay processes belonging to two separate spin channels. The notation $D^\alpha \rightarrow D^\beta$ denotes the transition of the dangling bond from charge state α to charge state β . See text for further description.

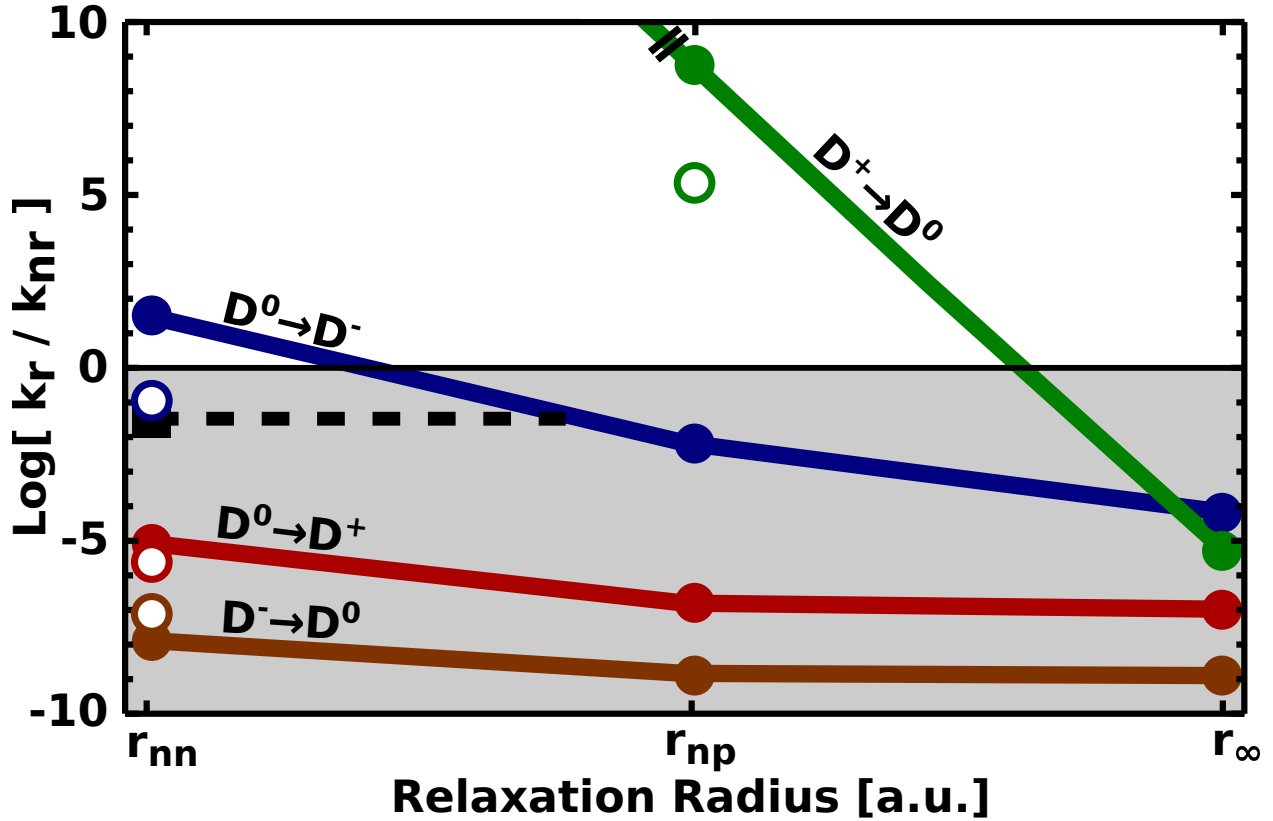


Figure 3.5: The logarithm of the ratio between radiative (k_r) and nonradiative (k_{nr}) decay rates for the four capture processes outlined in Figure 3.4, as a function of decreasing strain on the NP (see text), for a P_b defect at the surface of a 1.3 nm Si NP terminated by an oxide layer. The black horizontal line represents the boundary between radiative (white area) and nonradiative (gray area) recombination processes. Configurations representing different relaxation schemes around the defect (and hence different amount of strain) are shown on the x axis: r_{nn} (nearest neighbor), r_{np} (Si NP and first layer of oxygen) and r_{∞} (all atoms in the system). Nonradiative rates given by Equation 3.7 and 3.3 are indicated by the dots and open circles respectively.

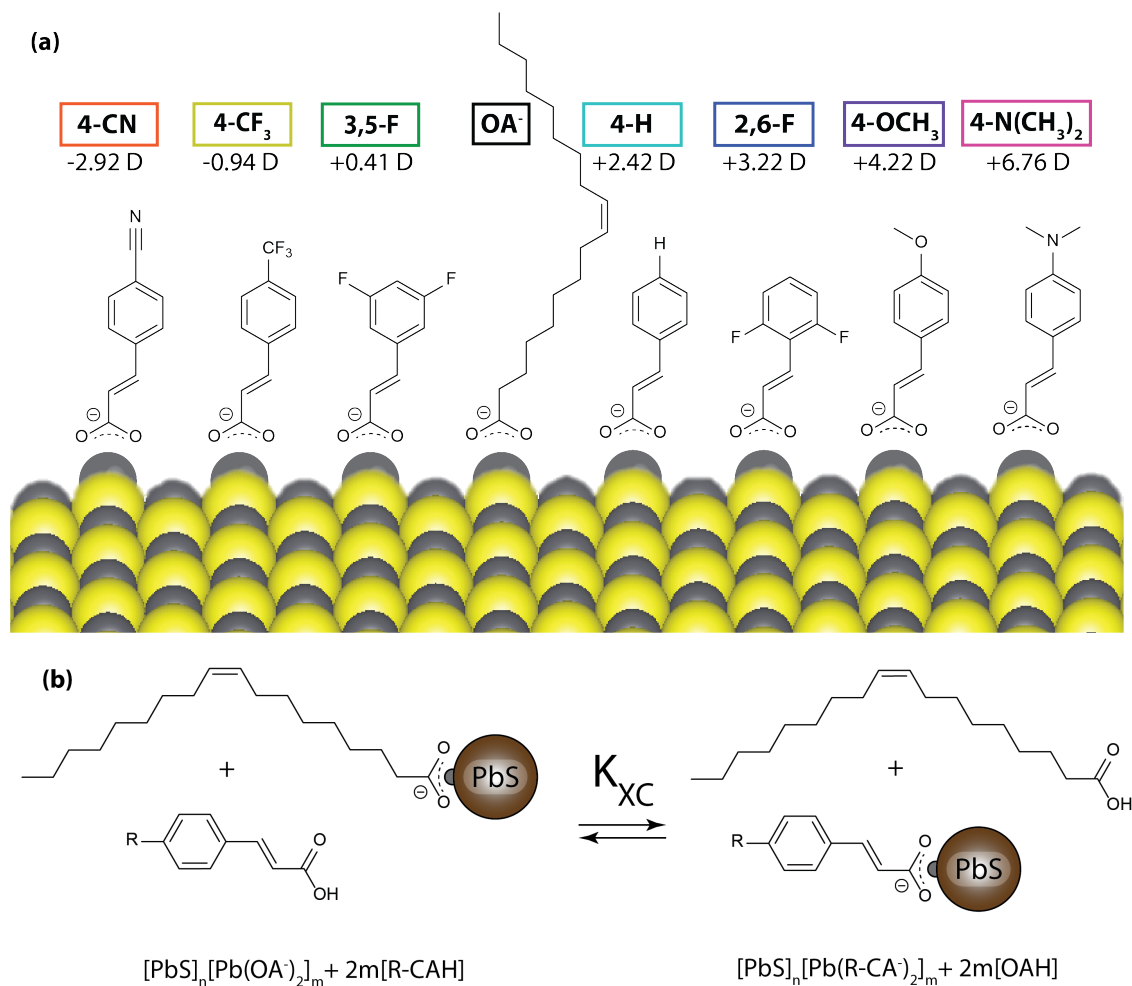


Figure 3.6: The model ligand/QD system utilized in this study. (a) Chemical structures, computed vacuum electronic dipoles, and labels used throughout this work of the molecules in our ligand library. 4-CN-CA⁻ = 4-cyanocinnamate; 4-CF₃-CA⁻ = 4-trifluoromethylcinnamate; 3,5-F-CA⁻ = 3,5-difluorocinnamate; 4-H-CA⁻ = cinnamate; 2,6-F-CA⁻ = 2,6-difluorocinnamate; 4-OCH₃-CA⁻ = 4-methoxycinnamate; 4-N(CH₃)₂-CA⁻ = 4-dimethylaminocinnamate. OA⁻ = oleate (b) The X-type ligand exchange in which surface bound oleate is displaced by functionalized cinnamic acid molecules.

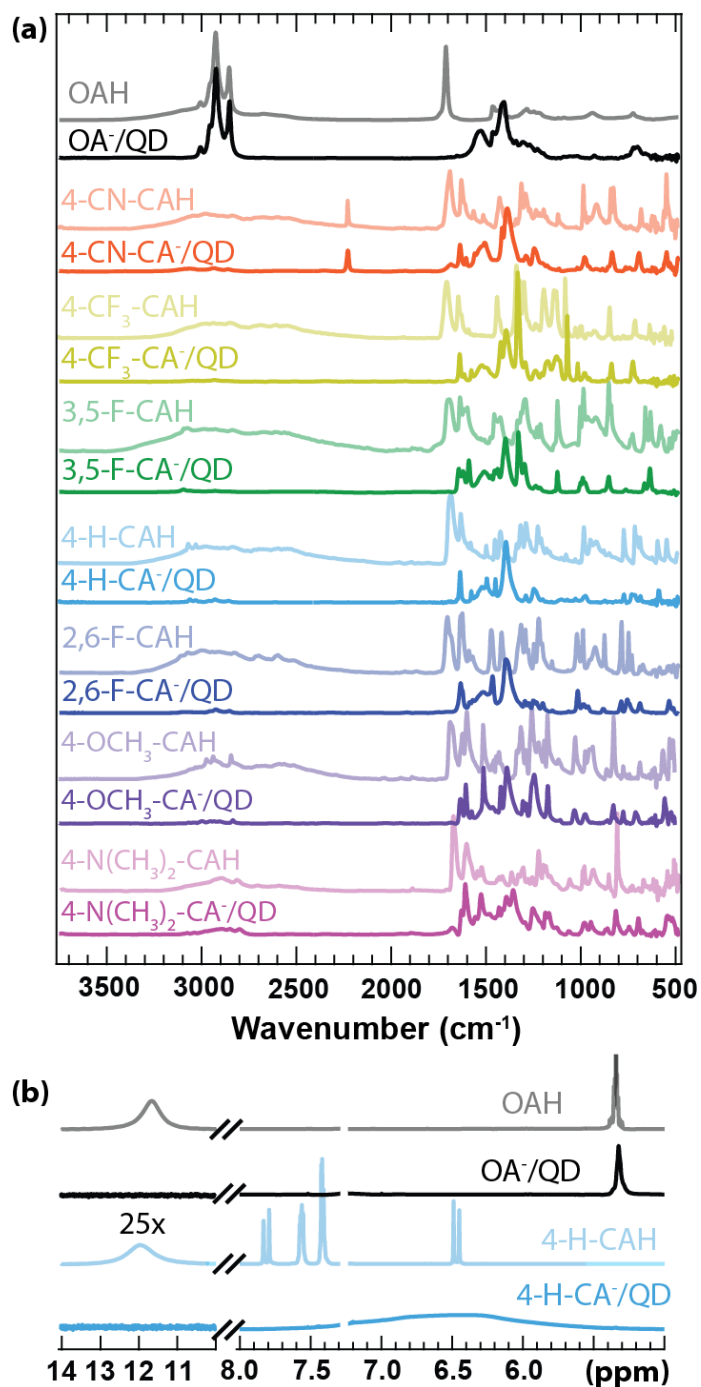


Figure 3.7: Surface analysis of PbS QDs before and after ligand exchange/PCR purification. (a) FT-IR spectra of neat ligand (lighter traces) and ligand/QD complex (darker traces) films. (b) ¹H NMR spectra in CDCl₃ of neat ligand (lighter traces) and ligand/QD complexes (darker traces). Both FT-IR and H NMR analysis suggests the efficient exchange of native OA⁻ ligands for R-CA⁻ and removal of excess R-CAH and OAH through PCR purification.

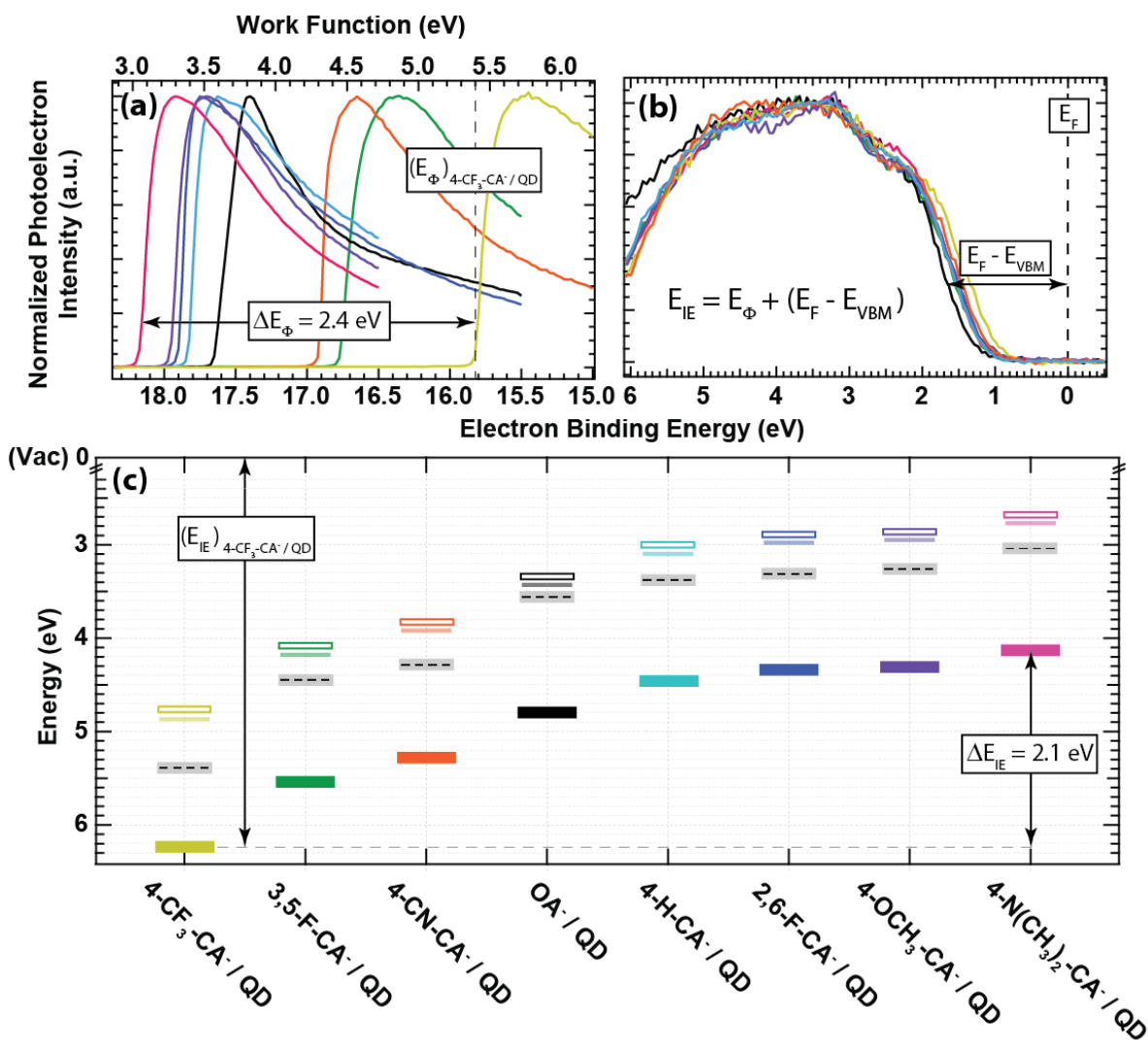


Figure 3.8: Photoelectron spectroscopy measurements of ligand/QD complexes. (a) Photoelectron cutoff region of XPS spectra used to determine ligand/QD film work function. (b) Valence band edge region of XPS spectra used to extract the ligand/QD film valence band maximum (VBM) with respect to the Fermi energy ($E_F - E_{VBM}$). The dashed black line represents the instrument equilibrated Fermi energy at an electron binding energy of 0 eV. (c) Band edge energies of films fabricated from OA^- and $R-CA^-$ terminated 3.2 nm diameter PbS QDs; ionization energy (solid rectangles) and work function (dashed black lines). We also include the conduction band minimum (E_{CBM} , open rectangles) that is determined from summing the optical gap determined from absorbance measurements (opaque lines) and calculated exciton binding energy. The variation in the measurements made for duplicate samples was lower than the instrumental noise; therefore, the uncertainty of the ionization energy and work function values are represented as the width of the closed rectangle and surrounding light gray rectangle, respectively.

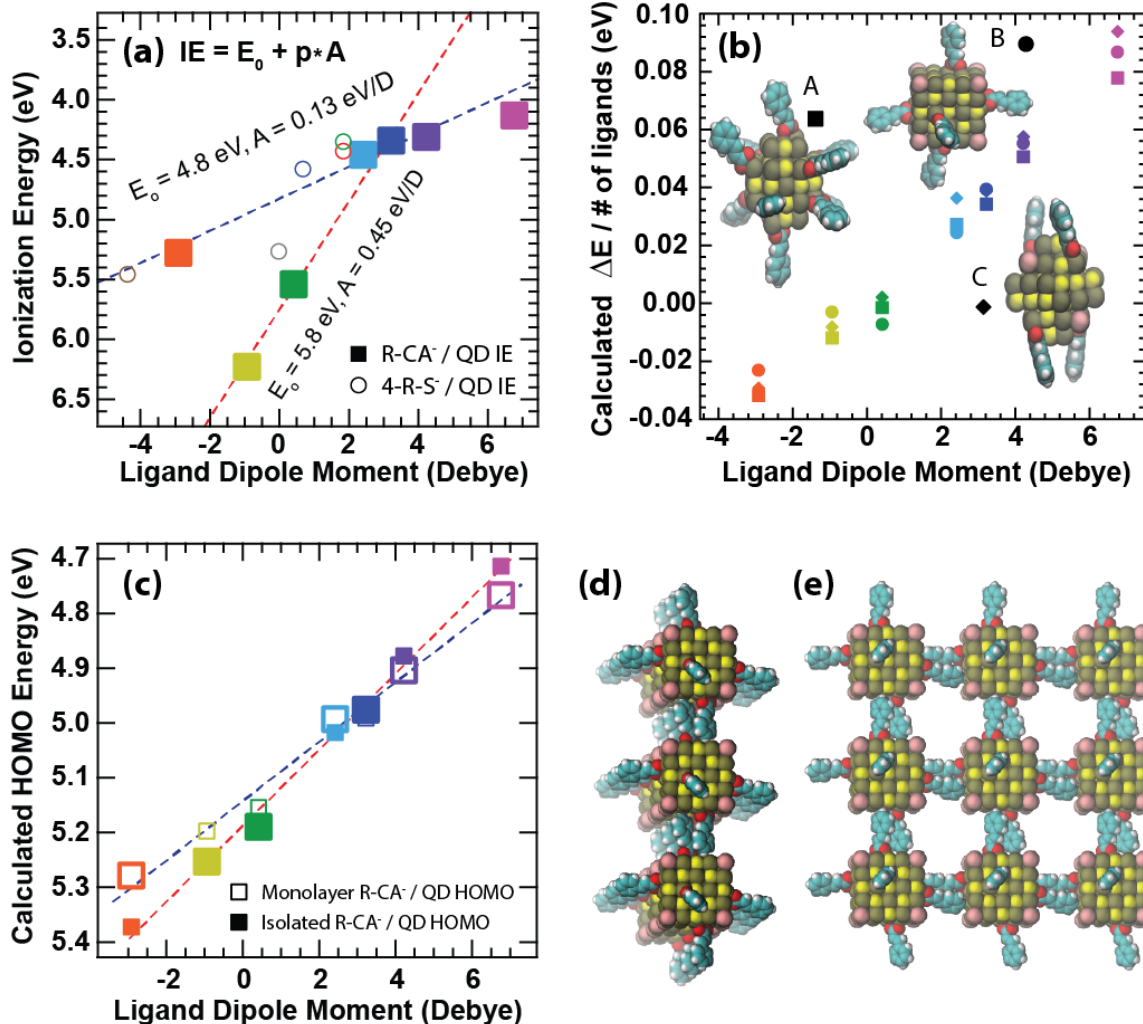


Figure 3.9: Band edge shifts of ligand/QD complexes . (a) Experimentally measured R-CA⁻/QD (solid squares) and 4R-S⁻/QD (open circles) ionization energies as a function of calculated ligand dipole. The variation of ionization energy measurements made for duplicate samples was lower than the instrumental noise; therefore, the uncertainty of the data is less than the width of the data markers. The brown and gray open circles are data taken from Bent *et al.*[139] that correspond to 4-NO₂-S⁻ and 4-F-S⁻ capped PbS QDs, respectively. The blue dashed line is a fit to the data that includes the points associated with non-fluorinated ligands, and the red dashed line is a fit to the data that only includes the points associated with fluorinated ligands. (b) Calculated band edges renormalized by the number of ligands as computed for the three different isolated ligand/QD structural models with varying surface coverage as a function of the projected ligand dipole. (c) The energy of the highest occupied molecular orbital for isolated QDs (filled squares) and the square lattice of monolayer of QDs (open squares). The lines are guides to the eye and the larger data points represent the proposed physically accurate QD film environment - either isolated (closed squares) or inter-digitized monolayer (open squares) - for each R-CA⁻/QD sample based on inter-QD ligand shell electrostatic arguments as described in the text. (d) Side and (e) top view of a 3x3 repetition of the unit cell for an example R-CA⁻/QD monolayer.

CHAPTER 4

CHARGE TRANSPORT PROPERTIES OF NANOPARTICLES

As we saw in the previous chapter defects at the surface of semiconducting nanoparticles (NP) give rise to electronic states within the gap, which can be detrimental to the optical properties of nanoparticles. This is also the case for charge transport in NP devices. In this chapter, we investigate charge transport in nanoparticles with deep and shallow defect levels, using the constrained density functional theory code presented in section 2.4.

In section 4.1, we study the effect of deep and shallow defects on charge transport. The atomistic details of how the presence of defects affect charge transport are still poorly understood and can lead to false assumptions. For example, we show that shallow defects can be more effective at capturing charges than deep defects. To demonstrate this concept, we study nanoparticles composed of silicon which is naturally abundant, non-toxic and technologically mature, containing dangling bonds and oxygen impurities. Dangling bonds are common and known to give rise to deep defects while oxygen defects give rise to shallow defects and are interesting because of the long-standing controversy surrounding their impact on the optical properties of silicon nanoparticles. The counter-intuitive results we find in section 4.1, challenge common assumptions and call for a reassessment of the role played by shallow defects in nanoparticle devices.

In section 4.2, we will turn our focus from the detrimental effects of trap states to the engineering of defect resistant nanoparticle devices. We will show how hydrogen can be used as a post processing treatment to dope and heal trap states to improve transport in lead chalcogenide nanoparticles. Lead chalcogenides are the most widely used nanoparticles because they are easy to synthesize and because of their favorable band gap. However, the mobility in these materials is still very poor. The results presented in section 4.2, suggest that post-synthesis hydrogen treatment of lead chalcogenide nanoparticle films is a viable approach to reduce electronic trap states and increase mobilities.

4.1 Defects and Charge Transfer in Nanoparticles

4.1.1 Introduction

Reprinted with permission from Nicholas P. Brawand, Matthew B. Goldey, Márton Vörös, and Giulia Galli *Chem. Mater.*, 2017, 29 (3), pp 12551262. Copyright 2017 American Chemical Society.

Advances in the synthesis of colloidal nanoparticles have led to the fabrication of monodisperse (size distribution <5%) and ordered nanoparticle solids, including superlattices,[212] which resulted in many applications such as field-effect transistors [171] and solar cells.[419] nanoparticle (NP) films have been shown to reach rather high photovoltaic performances, likely due to efficient charge transport between nanoparticles, achieved by precise control of size distribution, and of spacing by ligand engineering [258, 21, 374]. In addition, recent experiments have shown that electrode engineering is another effective means for controlling transport properties [191]. For example, in NP field effect transistors, majority carriers may be selected by manipulating the work function of the device contacts [191].

In spite of recent progress,[199] the rational design and the optimization of NP devices remain open challenges. Charge transport in films is affected by dopants, electrode surfaces, spacing between NPs, and defects (*e.g.* dangling bonds and the incorporation of extrinsic defects, *e.g.* oxygen in Si nanoparticles).[434, 300, 204, 191, 8, 179, 235, 298] However, the atomistic details of how the presence of electrodes and defects affect charge transport are still poorly understood.

From a theoretical standpoint, this lack of knowledge is largely due to the computational complexity and cost associated with simulating, from first principles, charge transport between arrays of defective nanoparticles in the presence of electrode surfaces. As a result, most theoretical investigations focused on idealized model systems, *i.e.*, isolated, identical nanoparticles with fully passivated surfaces. Methods used in the literature to model charge transport in NPs include, fragment-based approaches[320, 127, 438, 81, 474], the en-

ergy splitting in dimer method[203], and empirical quasiclassical approximations [77]. These methods neglect orbital relaxation beyond the single particle picture[183], the effect of polarization caused by localized charges, and environmental effects, such as image charges due to electrodes.

In this chapter, we focused on charge transport properties of silicon NPs, which are promising systems for photovoltaics[22, 452, 255, 450, 244, 427], LEDs[79], and optical labels for multiplexed imaging and drug delivery[80], due to the natural abundance of silicon, a non toxic material, and the widespread industrial expertise in its manufacturing. We carried out *ab initio* calculations within density functional theory (DFT), using constrained DFT (CDFT) which includes polarization and orbital relaxation effects. CDFT, though originally pioneered in 1984[104], has seen more extensive use in the modern formulation introduced by Wu and Van Voorhis[458, 461, 460, 459, 417, 189]. This methodology has been applied to the simulation of charge transport in a variety of materials, including molecules [127, 219, 220], molecular solids[126, 308], oxides[35], solvated ions[36, 306], and organic photovoltaic materials[142]. We studied NPs with intrinsic defects and impurities, and analyzed how deep and shallow defects may affect charge transport properties of NP films. We explicitly took into account the effect of image charges which may arise from electrodes or surfaces of substrates where films are deposited. Our results indicate that the common assumption that the ability of defects to trap charges is mainly dictated by their position in the energy gap of the film, is too simplistic and that the presence of shallow levels may be detrimental to charge transport.

We considered two of the most common defects in Si NPs, dangling bonds and oxygen impurities. Dangling bonds are known to give rise to deep defects, which have detrimental effects on charge transport in silicon devices [45, 328, 339, 341, 394, 338, 340, 395, 197, 275, 192, 193, 441, 159, 30]. As a representative shallow defect, we investigated doubly bonded oxygen (Si=O)[455, 345, 418] at the surface of the dot. Oxygen defects are interesting because of the long standing controversy surrounding their impact on the optical properties

of silicon NPs and Si=O is predicted to give rise to shallow defect states but its stability is a topic of debate [345, 418, 455, 256, 282, 78, 380, 323, 383, 382, 445, 7, 129, 98].

The rest of the paper is organized as follows; after giving a brief summary of our theoretical methods, we establish the relative energetic positions of Si dangling bonds and Si=O defect levels in the gap of silicon NPs. We then present charge hopping rates between NPs with and without defects, including the effect of image charges. Finally, we conclude by discussing the impact of defects on charge properties of Si NPs.

4.1.2 Methods

We carried out first principles calculations with the Quantum Espresso package [135], using plane wave basis sets and optimized norm-conserving Vanderbilt (ONCV) pseudopotentials[156, 366]. We used a wavefunction energy cutoff of 80 Ry, except for molecular dynamics and CDFT calculations of systems only containing Si and H, where a cutoff of 30 Ry was used. Our calculations were performed within the generalized gradient approximation with the PBE exchange-correlation functional[324]. The Martyna-Tuckerman correction[274] was applied in all CDFT calculations to correct for the fictitious electrostatic interactions between periodic images. Ionization potentials and electron affinities were computed using the Δ -SCF method at the neutral geometries and the Makov-Payne correction for total energies[265]. All calculations were performed with cell sizes ensuring a minimum distance of at least 14 Å between images. The internal reorganization energies (λ) and free energy differences (ΔG) were calculated using total energies of isolated donors (D) and acceptors (A):

$$\lambda = (D_i^f + A_i^f) - (D_f^f + A_f^f), \quad (4.1)$$

$$\Delta G = (D_f^f + A_f^f) - (D_i^i + A_i^i). \quad (4.2)$$

Here, D_x^y and A_x^y are the total energies of the donor and acceptor, respectively, in the x

atomic configuration and y electronic state. i and f denote initial and final states, respectively.

NP geometries were generated using the Nanocut software[409] and subsequent geometry relaxations were performed until all components of all forces were smaller than 0.001 Ry/Bohr. We generated a thermally disordered $\text{Si}_{35}\text{H}_{36}$ geometry using first-principles molecular dynamics (MD). After an initial ~ 3 -4 ps equilibration at 300K, the isolated NP was simulated for 1 ps and a time step of 0.97 fs in the NVT ensemble (with fixed particle number N , volume V , and temperature T) at 300K with the Berendsen thermostat with a time constant of 200 time steps. We note that these MD simulations were performed only to introduce thermal disorder rather than to gather statistical averages. While molecular crystals and dimers of organic molecules may exhibit high ordering due to van der Waals interactions[174, 454, 140], nanoparticle solids contain varying interdot distances. As such, we characterized the charge transport for nanoparticle dimers over a range of separations to increase the transferability of our results.

4.1.3 Results

Defect Energy Levels. Figure 4.1 presents the energy of the highest occupied molecular orbital (HOMO) and lowest unoccupied molecular orbital (LUMO) for a series of Si clusters, from the silane molecule to Si NPs composed of 35, 66, and 87 Si atoms.

They were computed by evaluating total energy differences (Δ -SCF) at the DFT/PBE[324] level of theory. We considered model systems with a dangling bond and doubly bonded oxygen defects. The position of the corresponding energy levels in the fundamental gap of NPs depends on the size of the nanoparticle; for example levels arising from oxygen double bonded to surface Si atoms are within the gaps of dots smaller than 2 nm in diameter, but resonant with the valence states for bigger dots. In the case of $\text{Si}_{35}\text{H}_{36}$, the presence of doubly-bonded oxygen atoms, results in both hole and electron traps, although the hole state is only 0.1 eV inside the gap, well within the tail distribution for the HOMO levels at

finite T (a distribution of HOMO levels is present at finite T, due to thermal disorder as verified by carrying out *ab initio* molecular dynamic simulations). Having established the relative energy positions of dangling bond and oxygen double bond states, we analyzed the effect of these defects on charge transport.

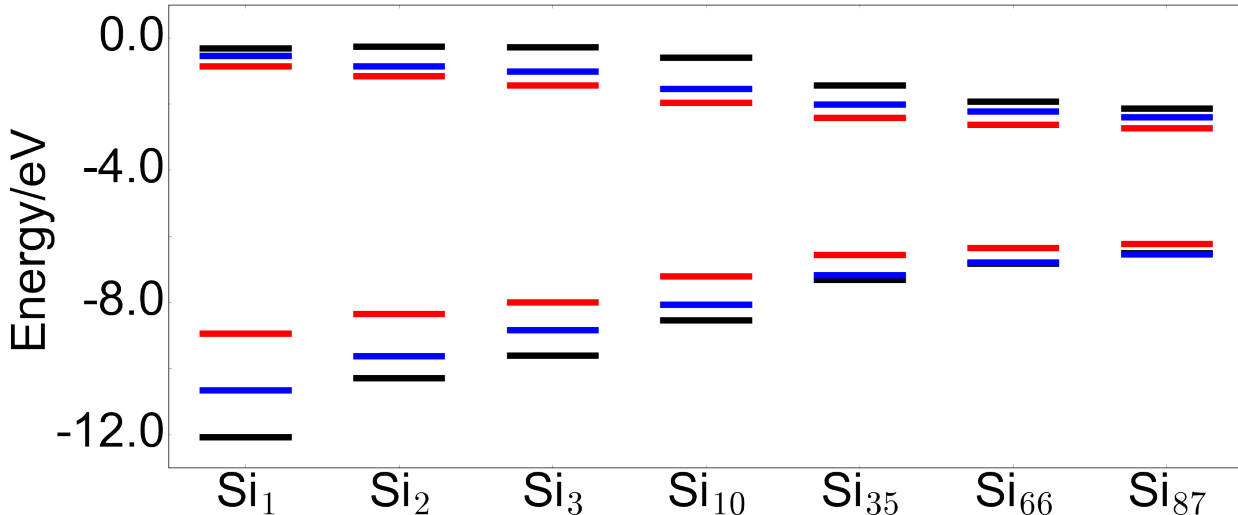


Figure 4.1: Energy levels for a series of silicon clusters, fully passivated by hydrogen (black lines), with one oxygen impurity at the surface (blue lines), and with a dangling bond (red lines). The abscissa shows the number of Si atoms in the cluster.

Charge Transfer Rates. If nanoparticles are well-separated in a film and exhibit minimal band dispersion, hopping is the dominant electron transport mechanism. In the absence of other charge carriers, which can promote Auger assisted electron transfer[478, 177, 311], hopping transport is accurately described by Marcus theory. [270, 268] Within Marcus theory, the rate of charge transfer k_{AB} between NPs A and B is given by:

$$k_{AB} = \frac{2\pi}{\hbar} |H_{AB}|^2 \sqrt{\frac{1}{4k_b T \pi \lambda}} \exp \left[-\frac{E_{act}}{k_b T} \right], \quad (4.3)$$

where H_{AB} is the electronic coupling between NPs, $\lambda = \lambda_{int.} + \lambda_{ext.}$ is the sum of internal (pertaining to the isolated system) and external (coming from the environment) reorganization energies and E_{act} is the activation energy defined as:

$$E_{act} = \frac{(\Delta G + \lambda)^2}{4\lambda}. \quad (4.4)$$

Here ΔG is the free energy difference and k_b is the Boltzmann constant and T is the temperature. Details pertaining to the computation of ΔG and λ are provided in Methods section.

The electronic coupling H_{AB} depends upon the overlap between diabatic wavefunctions representing localized charges. The square moduli of these wavefunctions depends exponentially ($e^{-\beta R}$) on the separation distance R , and so does H_{AB} which is $\propto e^{-\beta R/2}$, with a prefactor and decay rate β that are material dependent. Experimentally, β is inferred from measurements of the shift of the first excitonic peak as NPs are packed closer together in films [115].

The computed electronic couplings between fully passivated NPs are shown in Fig. 4.2. These values were evaluated using CDFT implemented within the Quantum ESPRESSO code. We observed a sharp decay of the hole transfer couplings, as expected due to the more localized nature of the HOMO with respect to that of the LUMO. The overall larger electron transfer couplings (red line in Figure 4.2), suggest that charge transfer is more efficient for electrons than holes in films of passivated Si NPs with the same size and structure ($\Delta G = 0$).

Next, we examined the effect of dangling bonds; we considered two silicon NPs, one of which has a dangling bond due to incomplete passivation, either pointing toward (\mathcal{T}) or away (\mathcal{A}) from the other nanoparticle. The \mathcal{A} configuration is shown in Figure 4.3 along with the isosurfaces of the spin-difference densities as computed by CDFT. These calculations yielded a localized spin up electron on the fully passivated nanoparticle and one spin down electron on the dangling bond site of the other nanoparticle. We computed the magnitude and the distance dependence of the electronic coupling for these configurations, as depicted in Figure 4.4. The hole coupling decays (β) differ depending on the orientation, with a β of 4.19 (1.83) \AA^{-1} for the \mathcal{T} (\mathcal{A}) configuration. Noticeably, the hole coupling (H_{AB}) is larger

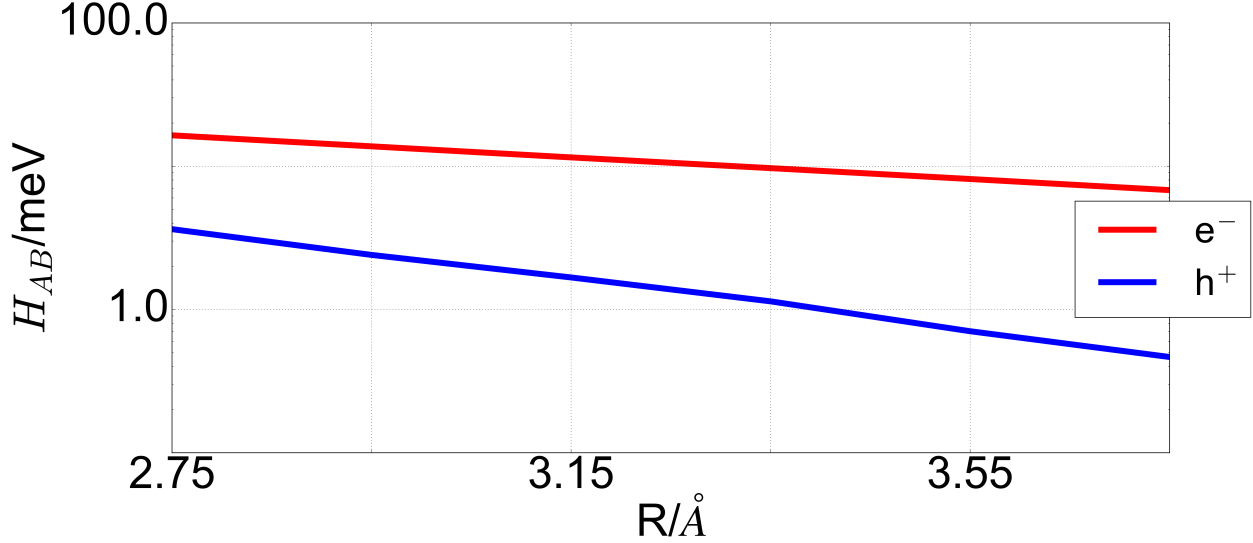


Figure 4.2: (Color online) Semi-log plot of the calculated electron and hole coupling H_{AB}/meV between two $\text{Si}_{35}\text{H}_{36}$ nanoparticles (NPs) at 300K as a function of NP separation $R/\text{\AA}$.

in magnitude for the \mathcal{A} configuration. Based on a simple single orbital picture, one may expect the coupling of the \mathcal{T} configuration to be larger than the \mathcal{A} configuration. However, the magnitude of the coupling is determined by a more complex and global rearrangement of the charge density and polarization in the dimer, which is not simply the overlap of the dangling bond state with the HOMO.

Unlike the hole couplings, those of the electrons are more sensitive to the orientation of the defect with respect to the neighboring NP. The \mathcal{T} configuration has a coupling decay β of 2.22\AA^{-1} ; the \mathcal{A} configuration exhibits instead deviation from the common exponential decay which is indicative of charge polarization effects. These calculations illustrate that the orientation of dangling bond defects can result in factors of 2 to 37-fold changes in electronic couplings, depending on the NP dimer separation.¹

These changes in couplings result in a 4 to 1000-fold variation in computed Marcus rates (assuming all other parameters entering Eq. 4.3 remain fixed). Our findings emphasize the

1. The largest separation considered here is 3.75\AA ; this maximum distance was chosen because at larger distances the computed hole couplings of the nanoparticles with doubly-bonded oxygen are smaller than the expected accuracy for our calculations. The same maximum distance was used for all systems investigated in this study.

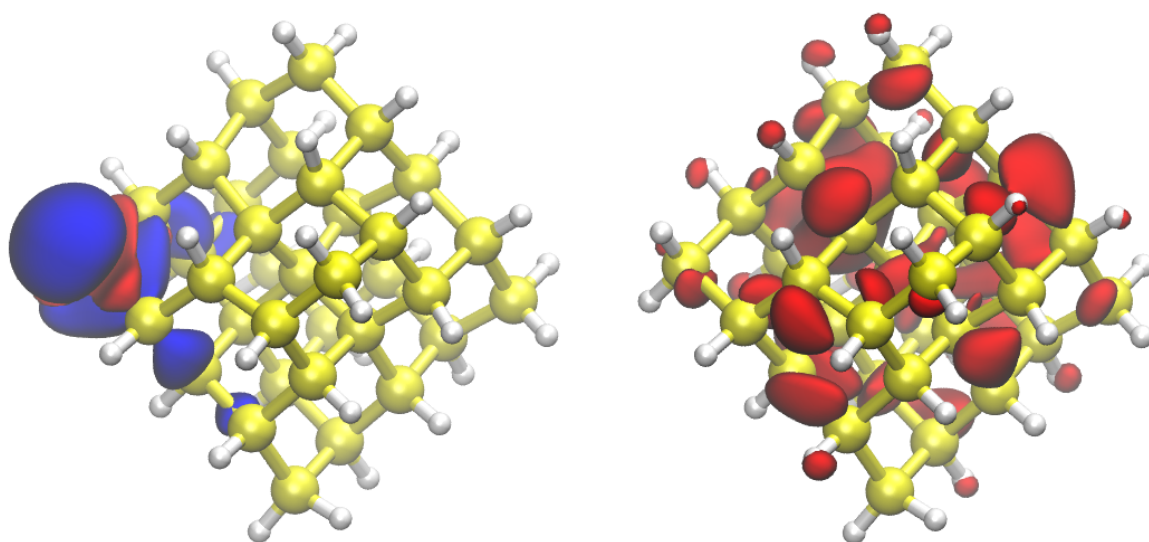


Figure 4.3: Isosurfaces of the spin-difference density of the $\text{Si}_{35}\text{H}_{36}$ - $\text{Si}_{35}\text{H}_{35}$ dimer with a dangling bond oriented away (\mathcal{A}) from the other dot. Red and blue isosurfaces represent the positive (spin up) and negative (spin down) portions of the spin-difference density respectively.

need to take into account atomistic details when predicting charge conduction pathways in NP films and superlattices.[424]

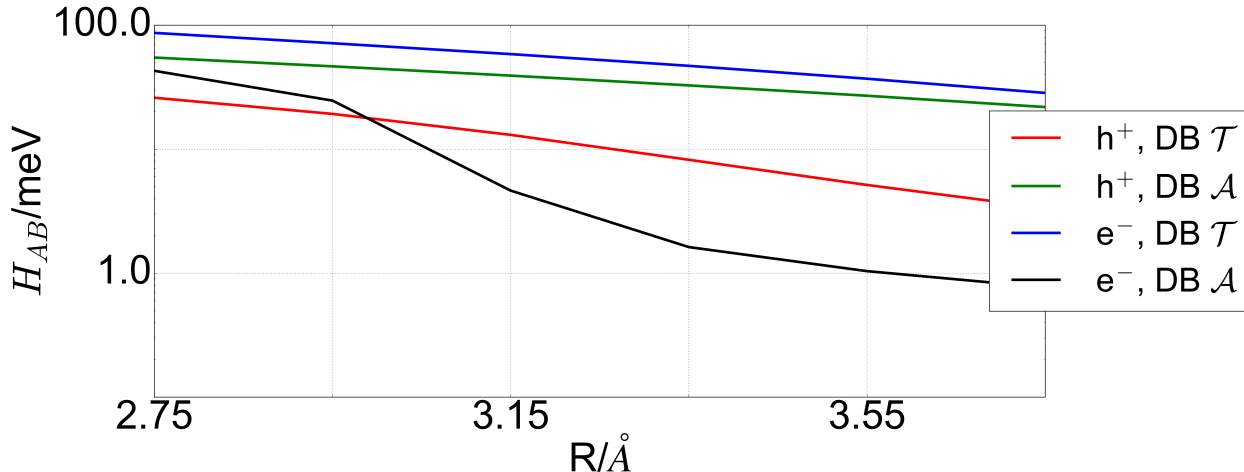


Figure 4.4: (Color online) Semi-log plot of computed electronic couplings H_{AB}/meV as a function of nanoparticle (NP) separation ($R/\text{\AA}$) for hole and electron transfer, when the dangling bonds (DB) are oriented either toward (\mathcal{T}) or away (\mathcal{A}) from the neighboring NP without a defect (See Figure 4.3). Results are shown for the $\text{Si}_{35}\text{H}_{36}\text{-Si}_{35}\text{H}_{35}$ dimer.

Figure 4.5 shows the electronic coupling versus distance for hole and electron transfers between a fully passivated silicon NP and one with a doubly bonded oxygen. These couplings display an exponential decay as a function of separation for both electron and hole transport. The hole transfer couplings are surprisingly small, (<1 meV) at the closest separation considered here, which supports the idea that oxygen is not a hole trap for these small NPs. We note that the coupling evaluated at 3.75 \AA is probably beyond our numerical accuracy (ca. 10^{-6} eV) which may explain the non-linear behavior of the last data point in Figure 4.5.

Table 4.1 displays the computed decay constant β for the different hole and electron transfers to/from defects. The hole transfer couplings decay most rapidly for the one with doubly bonded oxygen and least rapidly for the NP with a dangling bond oriented away from the dimer pair. The electron transfer couplings decay similarly for all systems except the NP with the dangling bond oriented away, which exhibits a more rapid decay.

Reorganization energies λ and free energy differences ΔG for the different electron transfer processes studied here are shown in Tables 4.2 and 4.3. These values were computed

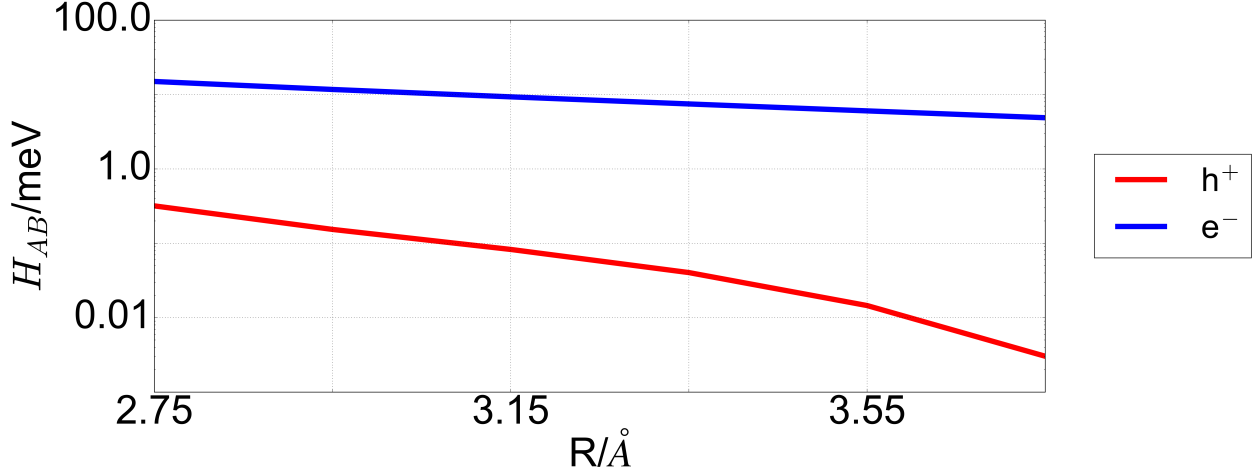


Figure 4.5: (Color online) Semi-log plot of the computed electron and hole couplings H_{AB} between $\text{Si}_{35}\text{H}_{36}$ and $\text{Si}_{35}\text{OH}_{34}$ as a function of separation (R). The oxygen impurity is on the surface opposite of $\text{Si}_{35}\text{H}_{36}$.

Charge	Passivated	DB- \mathcal{A}	DB- \mathcal{T}	O- \mathcal{A}
h^+	4.03	1.83	4.19	8.87
e^-	1.76	–	2.22	2.23

Table 4.1: Decay constant $\beta/\text{\AA}^{-1}$ for hole and electron transfer reactions between Si nanoparticles, a $\text{Si}_{35}\text{H}_{36}$ passivated nanoparticle and one $\text{Si}_{35}\text{H}_{35}$ with the dangling bond oriented away (DB- \mathcal{A}) and towards (DB- \mathcal{T}) the neighboring $\text{Si}_{35}\text{H}_{36}$, and a $\text{Si}_{35}\text{H}_{36}$ passivated nanoparticle and one $\text{Si}_{35}\text{OH}_{34}$ with a doubly bonded oxygen oriented away (O- \mathcal{A}) from the neighboring $\text{Si}_{35}\text{H}_{36}$.

using isolated NPs (consisting of 35 Si atoms) with fully relaxed geometries. Fully passivated nanoparticles show the smallest reorganization energies (less than 0.3 eV). Transfers to charge-localized defect states show larger reorganization energies (0.5-0.7 eV), consistent with more important structural reorganization upon charging. free energy differences are rather large (-0.8 to -1.5 eV) for electron and hole transfer to the defects, with the exception of hole transfer to the doubly bonded oxygen defect, which has a comparatively small free energy difference of -0.2 eV.

Comparison of Rates. Figure 4.6 presents rates computed from Eq. 4.3 for electron and hole transfer between NPs, with and without a defect (here oriented away), as a function of the external reorganization energy treated as a parameter. We focused on transfer rates

	Si ₃₅ H ₃₆	Si ₃₅ H ₃₅ DB	Si ₃₅ H ₃₄ O		Si ₃₅ H ₃₆	Si ₃₅ H ₃₅ DB	Si ₃₅ H ₃₄ O
Si ₃₅ H ₃₆	0.27	0.46	0.32	Si ₃₅ H ₃₆	0.17	0.70	0.67
Si ₃₅ H ₃₅ DB	0.64	0.83	0.69	Si ₃₅ H ₃₅ DB	0.64	1.17	1.14
Si ₃₅ H ₃₄ O	0.34	0.53	0.39	Si ₃₅ H ₃₄ O	0.35	0.89	0.85

Table 4.2: Reorganization energies λ /eV for hole (left) and electron (right) transfer reactions. Donor and acceptor NPs are shown in rows and columns, respectively. See the Methods section for further details.

	Si ₃₅ H ₃₆	Si ₃₅ H ₃₅ DB	Si ₃₅ H ₃₄ O		Si ₃₅ H ₃₆	Si ₃₅ H ₃₅ DB	Si ₃₅ H ₃₄ O
Si ₃₅ H ₃₆	0.00	-1.11	-0.19	Si ₃₅ H ₃₆	0.00	-1.47	-0.79
Si ₃₅ H ₃₅ DB	1.11	0.00	0.92	Si ₃₅ H ₃₅ DB	1.47	0.00	0.68
Si ₃₅ H ₃₄ O	0.19	-0.92	0.00	Si ₃₅ H ₃₄ O	0.79	-0.68	0.00

Table 4.3: free energy differences ΔG /eV for hole (left) and electron (right) transfer reactions. Donor and acceptor NPs are shown in rows and columns, respectively. See the Methods section for further details.

into these defect states due to the lifetimes of electrons in these traps, which are much longer than competing processes, such as recombination[45].

For NP dimers at a separation of 3.75 Å, electron transfer to oxygen defects occur 5 order of magnitude faster than those to dangling bond defects. The hopping rate to the shallower oxygen defect is faster than the one to the dangling bond for a wide range of reorganization energies. We find that the electron transfer rates for dangling bond defects increases with increasing reorganization energy. This surprising result shows that electron transfers to dangling bond defect states are in the so called inverted Marcus regime. Although these states are deep in energy as shown in Figure 4.1, doubly bonded oxygen defects are superior electron traps due to higher kinetic rates for electron capture. This is contrary to the general assumption that deep defects are better charge traps than shallow ones. In fact, the dangling bond state is in the inverted Marcus regime; electron transfer rates to this state decrease as its energy moves deeper into the gap of the NP.

The Effect of Electrodes. Image charges present in the surrounding electrodes may modify the charge hopping rates between nearby NPs computed above. While a simple electrostatic model could predict the qualitative changes in site-energies due to image charges,

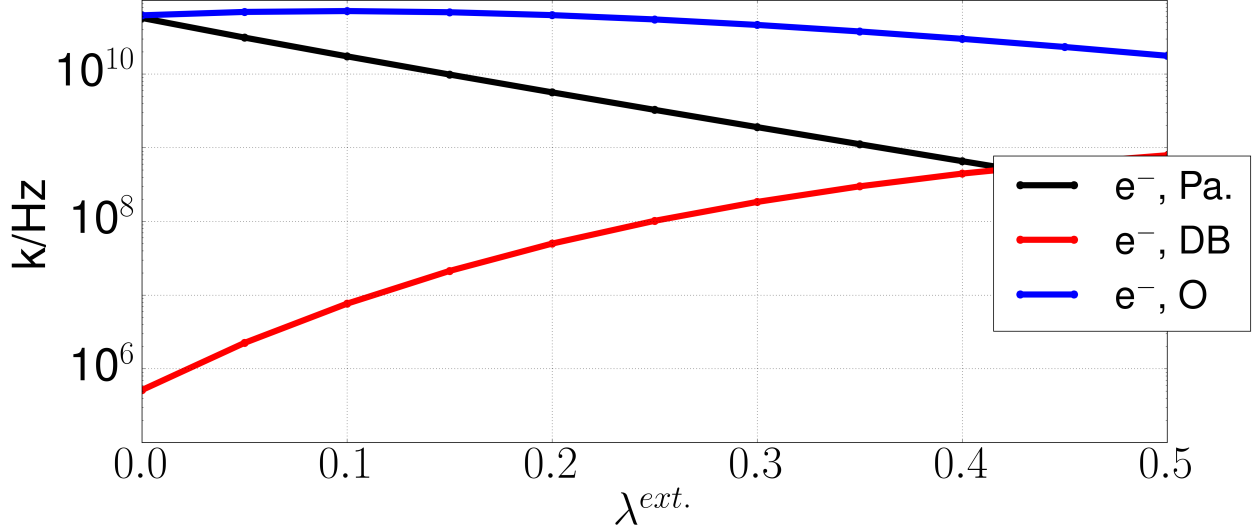


Figure 4.6: Calculated rates (k , see Eqn. 4.3) between two $\text{Si}_{35}\text{H}_{36}$ dots (Pa.), $\text{Si}_{35}\text{H}_{36}$ with $\text{Si}_{35}\text{H}_{35}$ (DB), and $\text{Si}_{35}\text{H}_{36}$ with $\text{Si}_{35}\text{H}_{34}\text{O}$ (O) separated by 3.75 Å. Rates are presented as a function of the external reorganization energy, λ^{ext} , which is a parameter that describes the environmental response to the charge transfer process.

it is difficult to include microscopic details such as the charge density localized at a defect or the change in the electronic coupling between NPs.

To include these effects, we added a density dependent potential to the Kohn-Sham (KS) equations. This additional potential describes image charges arising from the presence of a metallic surface, and is approximated with a multipole expansion (up to the dipole term). We then solved the KS equations self consistently in the presence of this density dependent potential together with the charge constraints from CDFT. We call this method the Self-consistent Image Charge Method (SICM).

In principle, we could include electrodes and substrates explicitly in the supercell used to describe NPs, but this is prohibitively expensive even for nanoparticles of moderate sizes. Furthermore, image charge effects are not fully captured by the usual approximations of DFT, such as LDA or PBE [290]. For example, reference [290] considered the effect of a graphene surface on the ionization potential and electron affinity of a single adsorbed benzene molecule. To include such an effect, they adopted many-body perturbation theory and the G_0W_0 approximation. This method, however, uses unperturbed wave functions,

and hence can not include the effect of the substrate on the electronic coupling. Wave function self-consistent GW methods are yet too expensive for even small dimers of NPs adsorbed on surfaces to be considered as viable approaches. Reference [252] used non-adiabatic molecular dynamics simulations to study charge transfer between a small PbSe cluster and TiO₂ surfaces. However, their method would require prohibitively long simulation times for dimers adsorbed on oxide surface.

To study the effects of image charges on the electronic coupling, we added a density dependent potential to the KS equations. This additional potential is a multipole expansion (considered up to the dipole term in this work) of the electrostatic potential due to the presence of the metallic surface:

$$V_{\text{img.}}[\rho](\mathbf{r}) = -\frac{q_{\text{tot}}}{|\mathbf{r} - 2\mathbf{z}_0|} - \frac{\vec{p}_{\text{tot}}[\rho] \cdot (\mathbf{r} - 2\mathbf{z}_0)}{(\mathbf{r} - 2\mathbf{z}_0)^3} + \dots \quad (4.5)$$

Here \mathbf{r} is the position operator defined within the supercell whose origin is the center of mass of the site containing the additional constrained charged defined by CDFT, \mathbf{z}_0 is the vector from the site containing the additional charge to the x-y mirror plane of the image charge, q_{tot} is the total charge of the system and \vec{p}_{tot} is the dipole moment of the isolated NP dimer system at the center of the supercell $\vec{p}_{\text{tot}}[\rho] = \int_{\Omega} \rho(\mathbf{r})\mathbf{r}d^3\mathbf{r}$.

The charge density ρ , obtained after each self consistent iteration of the KS equations, is used to update $V_{\text{img.}}[\rho](\mathbf{r})$ until the image interaction energy,

$$E_{\text{img.}} = \frac{1}{2} \int_{\Omega} V_{\text{img.}}[\rho](\mathbf{r})\rho(\mathbf{r})d^3\mathbf{r} , \quad (4.6)$$

is converged within a predefined accuracy. A similar method has been proposed in the past[58] but not applied in this context nor combined with CDFT.

Using the Si NP dimers from the previous section, we calculated the change in the electronic coupling in the presence of image charges using CDFT and the SICM. For example, with two NPs stacked perpendicular to the mirror plane just 5 Å away, we found that the

electronic coupling H_{AB} is insensitive to the presence of image charges. In Figure 4.7, we present the electron and hole couplings as functions of inter nanoparticle distance for fully passivated NPs with and without the presence of image charges. All the structural motifs examined here (including dangling bonds, oxygen defects and different orientations) were found to exhibit the same behavior as seen in Figure 4.7 for fully passivated NPs, with small changes (4-7%) in couplings.

Despite the surprising insensitivity of the electronic couplings to nearby metal surfaces, the hopping rates can still be impacted through the change in the free energy differences. Assuming the reorganization energies are constant, the activation barrier can be reduced for charges hopping toward their image charge. Using CDFT and SICM, we calculated the ratio of the hopping rates with image charges (k_{surf}) and without image charges (k_{iso}); the results are shown in Figure 4.8. We computed the change in the free energy difference by computing the interaction energy of the two diabatic states prepared by CDFT including the image charge field, described using SICM.

As expected, Figure 4.8 shows that the hopping rate toward image charges is increased. Therefore, in the absence of other external fields, the charges will hop toward the surface. This suggests that charge transport will predominantly take place along surfaces (*e.g.* at NP-substrate interfaces). Although we found the electronic coupling between nanoparticles to be insensitive to image charge fields, transport along an interface may differ from transport within the bulk region of NP solids. For example, the types of defects that occur at the NP-substrate interface may vary greatly from those found within the bulk, and these interface defects may require different means of passivation [4, 313, 423, 202]. These issues will be the focus of future theoretical investigations.

In summary, we used constrained density functional theory to study charge transfer between Si nanoparticles with deep dangling bonds defects and shallow oxygen impurities. We found that the widely held assumption that the ability of defects to trap charges is determined by the position of electronic energy levels within the intrinsic gap of the NP

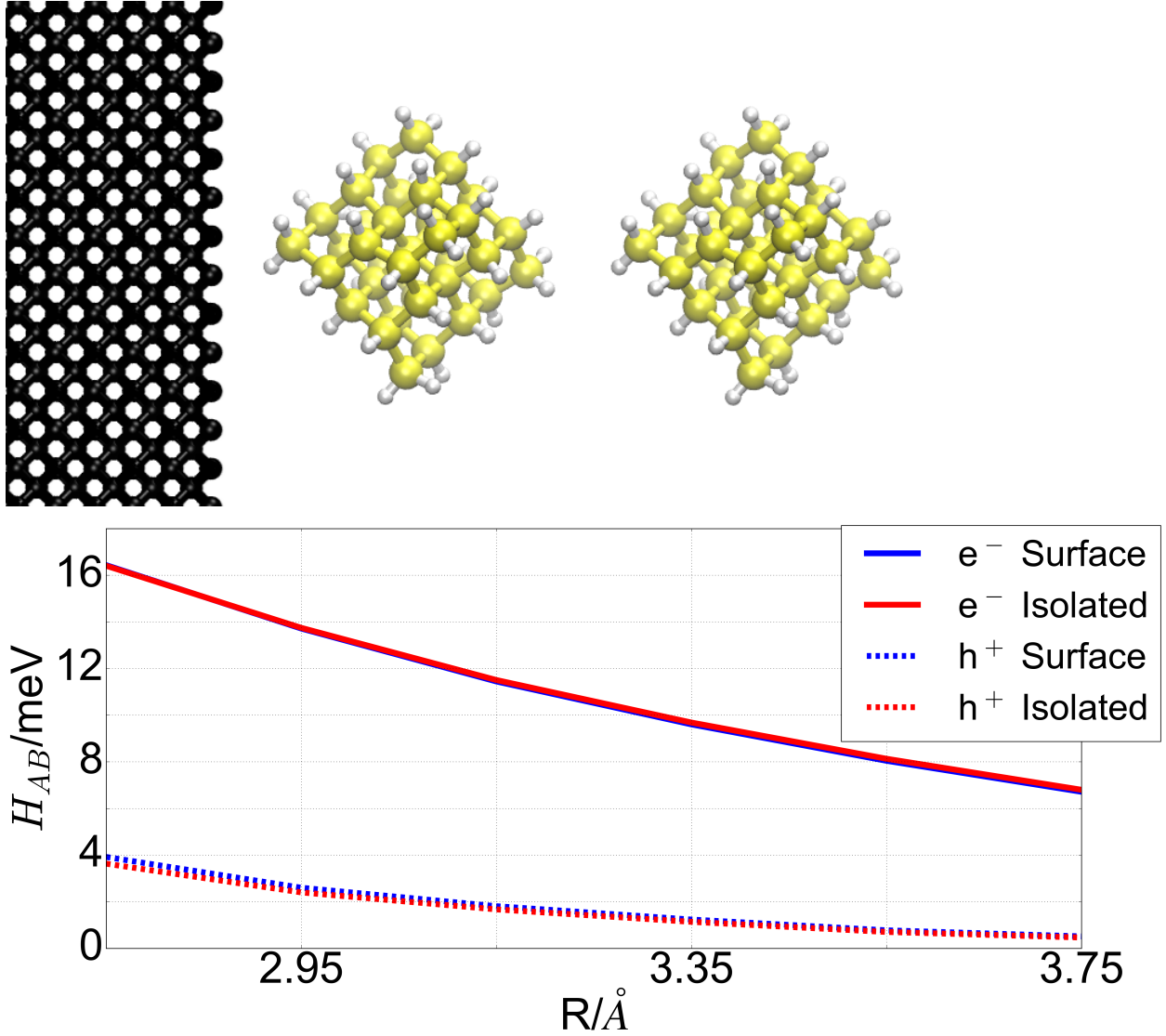


Figure 4.7: Top: Illustration of charge transfer between two NPs under the influence of image charges arising from the presence of a model electrode surface, represented by a black slab. Bottom: electronic coupling for holes (dashed) and electrons (solid) between fully passivated Si₃₅H₃₆ nanoparticles as a function of inter dot distance (R). Blue lines include the effects of image charges (Surface) and red lines are for isolated systems without image charges (Isolated).

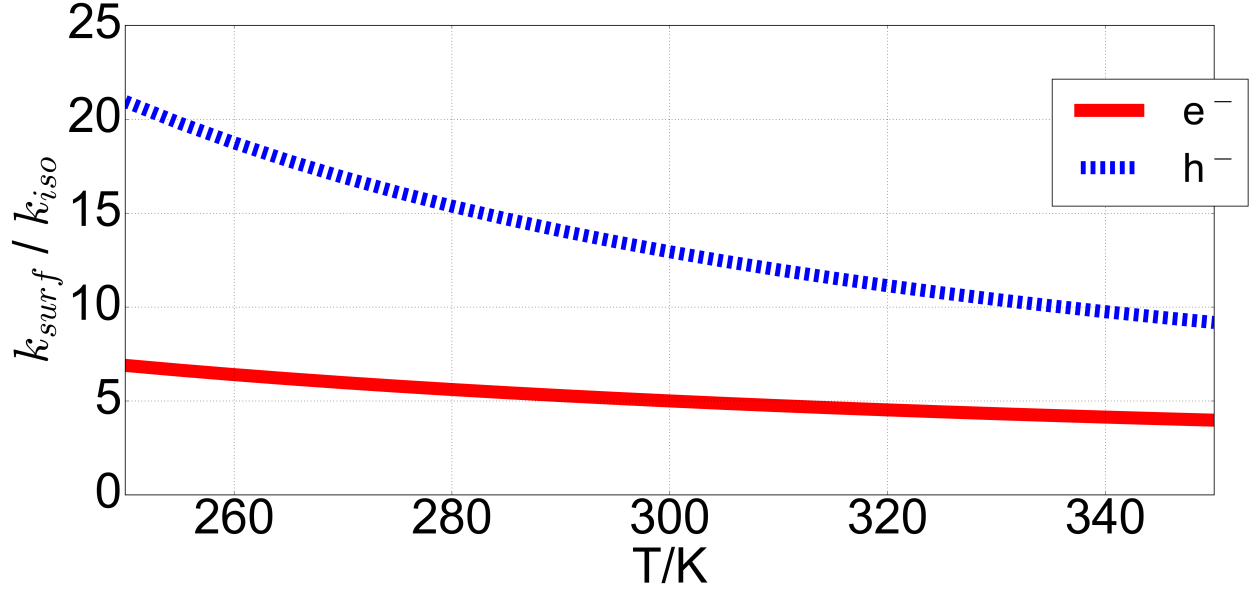


Figure 4.8: (Color online) Ratio of charge hopping rates for fully passivated $\text{Si}_{35}\text{H}_{36}$ nanoparticles in the presence of image charges (k_{surf}) and without image charges (k_{iso}). Solid and dashed lines are for electron and hole transfer respectively. Transfer rates are computed for charges moving toward their images.

is too simplistic. In fact, shallow defects, such as the Si=O bond at the surface, used here as an example, can be more detrimental to transport than deeper defects such as silicon dangling bonds, with trapping rates that differ by up to 5 orders of magnitude. This highlights the importance of including atomistic details, through *ab initio* calculations, in order to have a realistic and robust description of charge transport in complex nanostructured materials. We note that other models of charge transport, *e.g.* methods using Miller-Abrahams dynamics[279, 403, 67], that do not include reorganization energies arising from structural changes at the surface, lack the predictive power necessary to draw the conclusions reached in our study. We also found that electron and hole transfer rates for dangling bond defects depend strongly on orientation and spacing between the dots, which point at the importance of further studies of anisotropic charge transport pathways in NP arrays with individually engineered building blocks. We explored the effects of image charges on charge transfer between NPs located near electrode interfaces. We found the electronic coupling to be insensitive to the presence of images while the hopping rates are affected through changes

in the activation energy, which we computed by combining constrained density functional theory and the self-consistent image charge method.

Several reports showed that the presence of Si dangling bonds impact charge transport in Si NPs.[154, 391] For example, [154] reported the electrical conductivity of Si NPs embedded in SiO₂ matrices, and they found that hydrogen treatment increases the conductivities, which was attributed to the passivation of silicon dangling bonds at the surface of the dots. However, they also found that even after hydrogen treatment, transport was influenced by the presence of defects. Based on our results, we predict that the presence of shallow oxygen defects that cannot be passivated by hydrogen, may be responsible for the conductivity trends reported by [154].

We note that our results also shed light on the influence of NP size dispersion on charge transport properties, when transport is dominated by hopping. The position of frontier orbital energy levels of NPs depend on their diameter (due to quantum confinement); hence in films with dots of different sizes, isolated energy levels will form and be localized on specific NPs. Hopping transport through such an energy landscape may be analogous to transport across a film of monodispersed dots with shallow defects.[19] Since our results show that shallow defects can be just as, if not more, detrimental to transport than deep ones, achieving monodispersity may be more beneficial to transport than eliminating deep defects. Work is in progress to compute transport properties of disordered nanoparticle networks containing defects.

4.2 Improving Charge Transport Lead Chalcogenide Nanoparticles

Lead chalcogenide (PbX) nanoparticles are promising materials for solar energy conversion. However, the presence of trap states in their electronic gap limits their usability, and developing a universal strategy to remove trap states is a persistent challenge. Using calculations

based on density functional theory we show that hydrogen acts as an amphoteric impurity on PbX nanoparticle surfaces; hydrogen atoms may passivate defects arising from ligand imbalance or off-stoichiometric surface terminations, irrespective of whether they originate from cation or anion excess. We find that hydrogen adsorption on stoichiometric nanoparticles leads to electronic doping, preferentially n-type. Our findings suggest that post-synthesis hydrogen treatment of lead chalcogenide nanoparticle films is a viable approach to reduce electronic trap states or to dope well-passivated films.

4.2.1 Introduction

Reprinted with permission from Márton Vörös, Nicholas P. Brawand, and Giulia Galli *Chem. Mater.*, 2017, 29 (6), pp 24852493. Copyright 2017 American Chemical Society.

Third generation solar cells promise to overcome the Shockley-Queisser photo-conversion efficiency limit.[151, 378] An important class of third generation platforms are solar cells composed of colloidal semiconductor nanoparticles (NP).[23, 68, 210, 467] Several NPs were shown to exhibit efficient Multiple Exciton Generation (MEG), i.e. the generation of multiple electron-hole for one absorbed photon, thereby enhancing the photocurrent. An increased photocurrent translates into a theoretical maximum photo-conversion efficiency of up to 44.4%, without concentration, about 11% higher than the Shockley-Queisser limit.[201, 289, 24, 319, 372, 160, 428, 451, 429] Lead chalcogenides are the most widely used NPs because of their high MEG efficiency, in addition to their favorable band gap and ease of synthesis. Recently, MEG was also demonstrated in an actual lead chalcogenide NP solar cell device, paving the way to designing MEG enhanced solar cells.[25] However, the maximum photo-conversion efficiency reached so far in NP solar cells is 10.8%,[83, 223, 224, 249] rather far from the theoretical limit.

Many recent studies point at electronic defect states (or intra-gap states) as one of the main causes for the limited efficiency.[288, 41, 194, 176, 473, 477, 69, 432, 176] However, in spite of many intra-gap states being harmful for the operation of NP devices, not all of them

should be avoided. In fact, certain shallow defects states can be ionized at room temperature leading to electronic doping,[435, 310, 365, 390] which, in turn, may be used to control the conductivity of NP films, and exploited to build heterojunction solar cells. In contrast, states that are deep in the gap and are frequently well localized, can jeopardize charge transport by trapping carriers or by causing non-radiative recombination.[46] Although strategies to turn the presence of deep gap states into an advantage have been suggested[257, 99, 425], it is believed that deep states are overall harmful; for example, they are the cause for the observed low open circuit voltages of NP solar cells.[85]

In spite of several reports confirming the presence of trap states in films of lead chalcogenide nanoparticles [288, 41, 194, 176], their atomistic origin has remained elusive, but for few exceptions.[473, 477, 69, 432, 176] Ab initio calculations have suggested the presence of defect states in off-stoichiometric NPs and pointed out the possible use of ligands to achieve charge-orbital balance, in order to heal trap states.[435, 150, 200] Charge-orbital balance is defined by assuming that the formal charge state of all NP constituents, including the ligands, add up to zero, thus leading, in principle, to a gap without any defect states (or clean gap).[435, 387] However, recent calculations pointed out that even perfectly charge balanced NPs may have states in their gap.[477] For example, in the presence of charge balanced Se vacancies deep unoccupied states may be present in the electronic gap of PbS NPs.

Experimental strategies to remove trap states have concentrated mostly on ligand exchange techniques.[38, 317] The most efficient NP solar cells to date [83, 223, 224, 249] were synthesized by using short halogen based ligands. However, even with these short ligands, the open circuit voltage turned out to be low, suggesting that not all surface defects were healed. Efficient passivation of NP surfaces can also be achieved by shells grown over the cores of lead chalcogenide dots.[242, 101, 87, 468] Unfortunately, thick shells also confine the photoexcited carriers, making their extraction difficult. Thus, a surface passivation strategy that involves at most a monolayer of coverage is usually sought after.

Surface passivation of semiconductor NPs composed of elements other than Pb is better

understood. For example, dangling bonds are known to be the natural cause of trap states in silicon NPs [105, 46, 329] and they may be well passivated by hydrogen atoms.[230, 70] The latter are not only used as passivants. In ionic bulk semiconductors, atomic hydrogen dopants have been known to counteract the prevailing doping, for example, hydrogen neutralizes Mg acceptors in GaN.[291, 414, 102] Sometimes, hydrogen can enhance the conductivity of ionic compounds.[413, 414, 102] Indeed, early studies of bulk Pb chalcogenides showed that exposure of their surfaces to a hydrogen atmosphere turned p-type films into n-type ones. [100, 466, 113, 277]

Given the increasing amount of evidence that full surface passivation is not a requirement to heal trap states, and the success of hydrogen in passivating several NPs, it is interesting to explore whether hydrogen may be used to heal trap states in lead chalcogenide NPs.

In this Article, we used ab initio calculations to develop a strategy to heal electronic trap states in lead chalcogenides nanoparticles. We show that hydrogen acts as an amphoteric impurity on the surface of these nanoparticles, with the ability to adopt both positive and negative charge states. Hence, hydrogen may act as a charge bath for missing cations, anions, or ligands on the surface, and “clean” the gap of the NP. We predict that if hydrogen atoms are incorporated into well passivated nanoparticle films, they will likely induce doping with a preference towards turning the films into an n-type semiconductor. We suggest that, following the synthesis of films, hydrogen treatment of NP surfaces may be used as a post-processing step, and that by controlling the amount of hydrogen one may achieve either passivation or doping.

The rest of the paper is organized as follows: in the Methods section we describe our theoretical and computational approach; in the Results section we report our results on the effect of hydrogen treatment of PbSe NPs. Our conclusions are presented in the last section of the paper.

4.2.2 Methods

We carried out ab initio calculations using density functional theory as implemented in the QUANTUM-ESPRESSO (QE) code.[136] We built structural models of PbSe NPs by carving clusters of a given size out of a periodically repeated bulk PbSe lattice. According to experiments, the shape and size of the NPs can be controlled by the synthetic conditions, e.g. by precursors.[363, 457] The standard and most widely used oleic acid based synthesis leads to spherical PbSe NPs with exposed (100) and (111) facets.[476] Hence, we considered spherical-like NPs with (100) and (111) facets exposed (the former are non polar, while the latter are polar), and also smaller cubic ones, with (100) facets exposed. Since the spherical model was designed to be non-stoichiometric to mimic experimental conditions,[331, 95, 284, 283] we passivated its surface with one ligand used in several experiments, iodine.[91, 456, 225, 471, 299, 52, 224, 475] We obtained the following clusters: $\text{Pb}_{28}\text{Se}_{28}$ and $\text{Pb}_{55}\text{Se}_{38}\text{I}_{34}$, whose geometry is reported in the Supplemental Information.

We used plane wave basis sets and projector augmented wave pseudopotentials [33, 214] from the pslibrary, version 1.0.0[90, 232] and treated the following electrons as part of the valence partition: Pb: $5d^{10}6s^26p^2$ and Se: $4s^24p^4$. We used a wave function (charge density) energy cutoff of 60 (360) Ry. We verified that these cutoffs were sufficient to converge total energy differences (e.g. charge transition levels) within 0.02 eV. Most of our calculations were carried out using the generalized gradient approximation with the PBE exchange-correlation functional[324]; however, we also carried out some calculations using the hybrid functional PBE0, to assess the robustness of our results.[1] The PBE0 calculations were performed by using recently developed optimized norm-conserving Vanderbilt (ONCV) pseudopotentials with a wave function energy cutoff of 60 Ry.[157, 367, 232] We also tested the effect of spin-orbit coupling using the fully-relativistic version of the PAW pseudopotentials, as implemented in QE.[96]

The convergence of the total energy as a function of cell size for the charged isolated NPs was tested by increasing the NP–NP separation of $\text{Pb}_{28}\text{Se}_{28}$ from 10 Å to 15 Å and

by applying the Makov-Payne correction scheme[266]. Absolute single particle energies were computed with respect to the vacuum level, by determining the average electrostatic potential at the cell boundary.

Charge transfer rates between NPs were estimated using Marcus theory, following procedures reported in the literature[236, 400, 82, 238, 237] to estimate charge transport parameters of NPs. The electronic couplings entering Marcus theory were computed using constrained density functional theory (CDFT), which we implemented in QUANTUM-ESPRESSO in a version that will be soon contributed to the online package. The CDFT calculations were carried out on dimers of NPs separated by a minimum distance of two times the Pb-Se bond length, 6.54 Å. This NP-NP separation can be achieved experimentally with mono-atomic halogen ligands.[91] Each NP dimer was placed in the same tetragonal cell with dimensions of $a=23$ Å and $c=47$ Å. The CDFT field strength, which localizes the charge on either the donor or the acceptor NP, was optimised until the charge difference between two NPs was equal to one electron, within a tolerance of $10^{-6}e$. A smearing of 0.027 eV (1 mHa) was used to obtain diabatic states for charged systems with degenerate highest occupied molecular orbitals. The electronic coupling was then computed assuming integer occupation below the Fermi level.

Reorganization energies (λ) and driving forces (ΔG) were estimated using total energies of isolated donor and acceptor particles:

Here, \mathcal{D}_x^y and \mathcal{A}_x^y are the total energies of the donor and acceptor, respectively, in the x atomic configuration and y electronic state. The indices i and f denote initial and final states, respectively. The total energies entering Eq. 4.1 and 4.2 were obtained using the Makov-Payne correction [266] and a cubic cell with a lattice parameter of $a=23$ Å. All parameters were computed using a wave function energy cutoff of 60 Ry, ONCV pseudopotentials[157, 367, 232], the generalized gradient approximation with the PBE exchange-correlation functional[324].

4.2.3 Results

Although we focused on PbSe, due to a higher MEG efficiency than that of PbS, based on tests on selected systems we expect the general findings reported below to apply to PbS NPs as well.

We report below results for $\text{Pb}_{28}\text{Se}_{28}$ and $\text{Pb}_{55}\text{Se}_{38}\text{I}_{34}$, namely for relatively small nanoparticles of diameter 1.3 nm and 1.9 nm, respectively. However, we note that at the level of theory considered here (semi-local DFT), their electronic gaps are representative of those of experimental nanoparticles with diameter of 3 and 4 nm.[184, 281]

Doping of nanoparticles with a clean gap. We first discuss the effect of hydrogen on stoichiometric NPs without dangling bonds. Hydrogen was adsorbed on the surface of $\text{Pb}_{28}\text{Se}_{28}$, and its position was optimized on several different surface sites. We found that in the neutral charge state hydrogen preferably binds to Se sites, with a binding energy about 0.25 eV higher than on surface Pb sites. Se has a formal charge state of -2, thus hydrogen donates charge that fills the lowest unoccupied state of the NP. In other words, the formation of the bond between the anionic selenium and hydrogen concomitantly leads to a dangling bond in the cation, which is known to be positioned in close vicinity of the NP unoccupied states. At the Pb site, the opposite mechanism takes place: hydrogen accepts charge from the Pb ion, which has a formal charge state of +2. The compensating positive charge (hole) will thus occupy the highest occupied orbital. Although the energetics suggest that hydrogen prefers to be at the Se site, kinetic processes need to be considered as well. Therefore, we also computed the transition path of hydrogen atoms between the Pb and the Se sites using the climbing-image nudged elastic band (NEB) method.[165] The total energy along the transition path, as obtained from NEB, and the density of states at Pb and Se sites are shown in Figure 4.2.3. We found barriers of 0.3 eV and 0.55 eV for the Pb \rightarrow Se and Se \rightarrow Pb processes. We found similar energy barriers in the case of Pb \rightarrow Pb and Se \rightarrow Se H migration. In addition to barriers, vibrational frequencies are also required to estimate the diffusion coefficient of hydrogen.

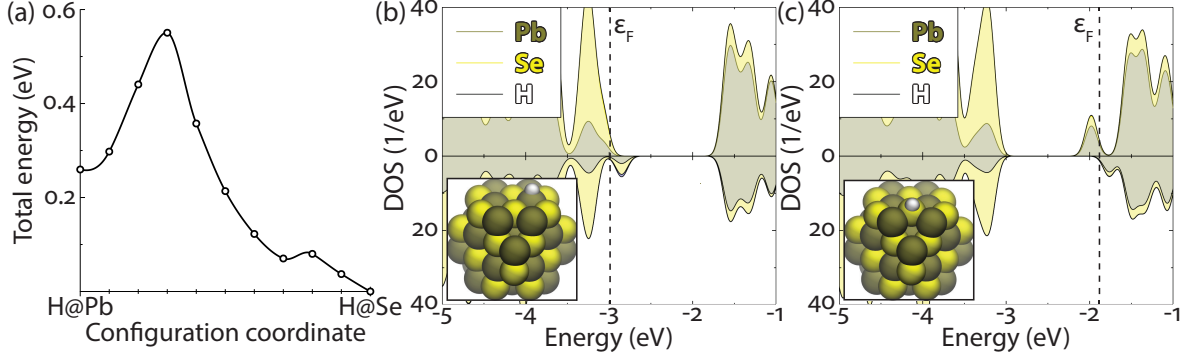


Figure 4.9: (a) Total energy of a H-Pb₂₈Se₂₈ nanoparticle, as a hydrogen atom is displaced from a Pb site (where it dopes the system p-type) to a Se site (where it dopes the system n-type), along a (100) surface facet. (b-c) Spin resolved projected density of electronic states (DOS) as a function of energy, for hydrogen at the Pb site and the Se site. The Fermi level is indicated by vertical dashed lines. The insets show the structural models of the NP: green, yellow and white spheres represent Pb, Se and H atoms, respectively.

Since we expect highly localized stretching modes on the NP surfaces, available measurements on small molecular systems containing Pb-H and Se-H bonds can be used to estimate the frequency of the surface vibrational modes. Recent measurements on lead hydrides reported Pb-H stretching mode frequencies at ≈ 1500 1/cm. [440] The high frequency modes of the Se-H bonds are estimated at ≈ 2350 1/cm, according to measurements of the IR-active modes of selenium hydride (SeH₂). [303]

We estimated the diffusion coefficient, D of hydrogen, using the approximation $D \approx n\nu^*a^2 \exp(-E_b/kT)$, where n is a dimensionality factor, ν^* is the frequency of an effective vibrational mode responsible for the diffusion, a is the hopping distance and E_b is the energy of the barrier.[421, 143] Using $n = 1/4$ for 2D diffusion, $\nu = 58$ THz (the average of the values extracted from the measurements discussed above), $a = 3.1\text{\AA}$, i.e. the Pb-Se nearest neighbor distance, and $E_b = 0.55$ eV, the rate-limiting Se \rightarrow Pb barrier energy, we found diffusion coefficients of $\approx 9 \times 10^{-12} \text{cm}^2/\text{s}$ at room temperature and $\approx 4 \times 10^{-7} \text{cm}^2/\text{s}$ at 600K. The latter are of the same order of magnitude as the diffusion coefficients of interstitial hydrogen in bulk silicon at room temperature.[42] This suggests that hydrogen may be mobile on the surface of the NPs at high temperature. We note that the diffusion coefficients obtained here

may be underestimated, since quantum tunneling effects, which were not taken into account, may lead to a reduction of the energy barrier E_b . [195]

In summary, our results show that if hydrogen is adsorbed on charge balanced, stoichiometric NPs, it preferentially leads to n-type doping. We note that since the presence of hydrogen is difficult to detect experimentally, the vibrational frequencies of surface modes discussed above might help in the identification of the adsorbed species. Surface sensitive infrared and Raman spectroscopic techniques, and in particular surface enhanced Raman spectroscopy on single NPs, combined with isotope effect studies could constitute good strategies to experimentally verify the presence of adsorbed hydrogen.

Charge compensation and ligand imbalance.

We now turn to the investigation of the effect of hydrogen when an extra charge or ligand imbalance are present. We used a grand canonical formulation, in which the formation energy of a defect (X) is expressed as: [122]

$$E_f^X(q, \epsilon_F) = E_{NP}^X(q) - E_{NP} - \sum_i \mu_i N_i + q\epsilon_F, \quad (4.7)$$

where $E_{NP}^X(q)$ is the total energy of the system with the defect in the charge state q , E_{NP} the total energy of the system without any defect in the neutral charge state, μ_i the chemical potential of the reservoirs, and ϵ_F the Fermi energy.

Negative values of E_f indicate that the formation of the defect state is a favorable process. However, positive values of E_f do not necessarily imply that the defect may not form. Indeed, the defect formation may result from an activated process, where the number of sites where hydrogen is present is given by:

$$c = c_0 \exp(-E_f^X(q, \epsilon_F)/kT), \quad (4.8)$$

and c_0 is the number of available adsorption sites.

Another useful concept when discussing defects is the charge transition level, defined as

the value of the Fermi energy at which the charge state of the defect changes. In the case of NP films, a Fermi level may be defined following charge equilibration processes between NPs. The charge transition level is expressed as:

$$\epsilon_F(q, q') = \frac{E_{NP}^X(q) - E_{NP}^X(q')}{q - q'}. \quad (4.9)$$

The total energies entering Eq. 4.7 and 4.9 are computed by optimizing the atomic geometry in each charged state. If $q' = q - 1$, then the charge transition level corresponds to the adiabatic ionization potential $\epsilon_F(q, q') = AIP$, while in the case of $q' = q + 1$, it corresponds to the adiabatic electron affinity: $\epsilon_F(q, q') = AEA$.

Figure 4.2.3 shows the formation energy as a function of the Fermi level of $\text{Pb}_{28}\text{Se}_{28}$ under the assumption that the NP film is in contact with a molecular hydrogen reservoir. The minimum and maximum of the Fermi level position correspond to the computed adiabatic ionization potential and electron affinity of the NP without any hydrogen, respectively. Our results show that the formation energy of hydrogen related defects is rather high (from about 0.1 eV to 1.25 eV, depending on the position of the Fermi level), suggesting that a molecular source of hydrogen is unlikely to dope the NPs. If, however, the hydrogen source contains atomic hydrogen then the defect formation energy is negative (for example, it is ≈ -1.1 eV for the neutral system at the PBE level of theory), e.g. hydrogen adsorption is favorable. These results are consistent with early experiments on bulk lead chalcogenides, which reported efficient doping of the solid when exposed to an atomic hydrogen atmosphere.[100, 466, 113, 277] In some of these experiments, atomic hydrogen was generated by converting H_2 to H using an electrically heated filament.[113]

More importantly, we found that in a negative (positive) charge state hydrogen is preferably located at a Pb (Se) site and that in both cases the electronic gap is clean, and hydrogen behaves as a charge compensator. It is also worth noting that there is a wide region (of about 1 eV), where neutral hydrogen is stable, which is a signature of positive U behavior. This is at variance with the most common behavior found in bulk materials, where neutral H

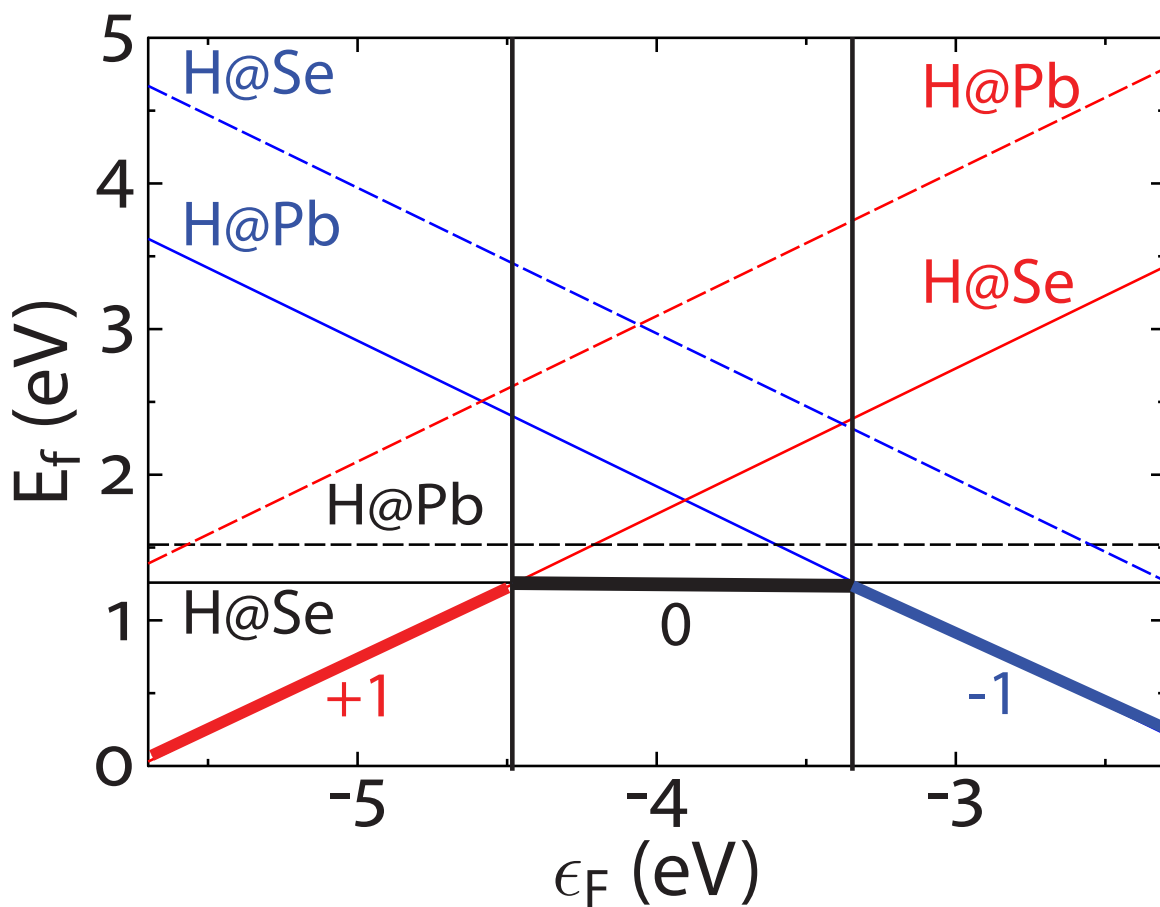


Figure 4.10: Formation energy of a hydrogen atom adsorbed on the (100) facet of a $\text{Pb}_{28}\text{Se}_{28}$ NP in a positive (+1), neutral (0) and negative (-1) charge state, as a function of the Fermi energy (referred to the vacuum), for adsorption at Pb (H@Pb) and Se (H@Se) sites. Red, black and blue lines correspond to positive, neutral and negative charge states, respectively. The continuous (dashed) lines represent the most (least) stable configurations. Vertical lines represent charge transition levels. See Supplemental Information for the same diagram obtained for the (111) facet.

(a)

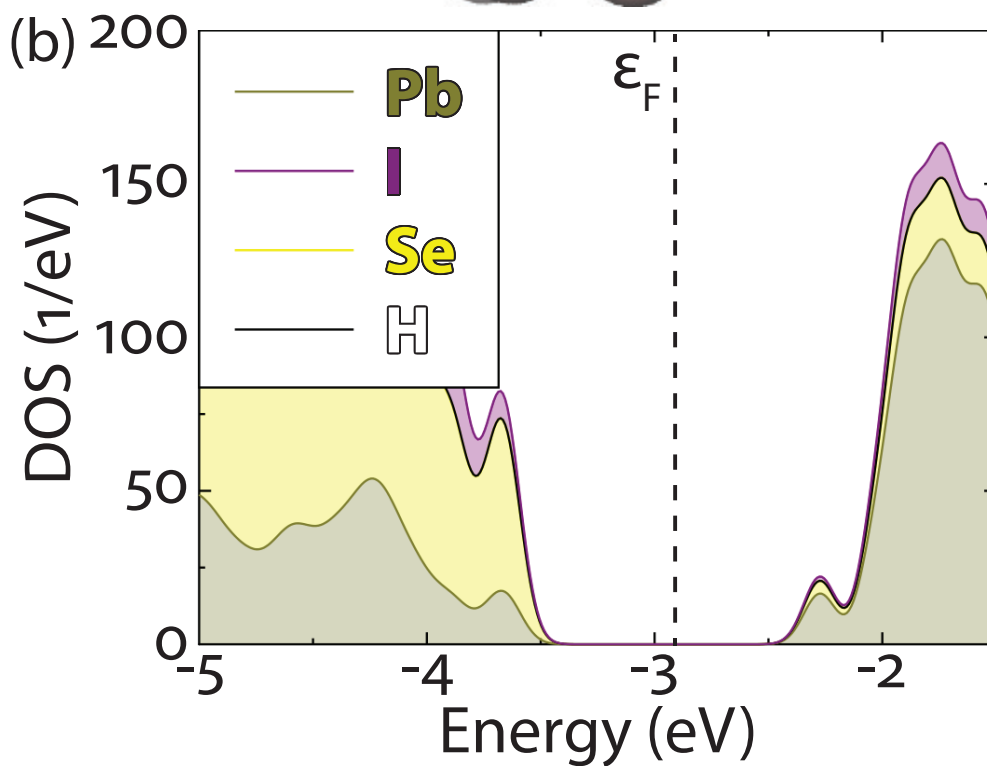
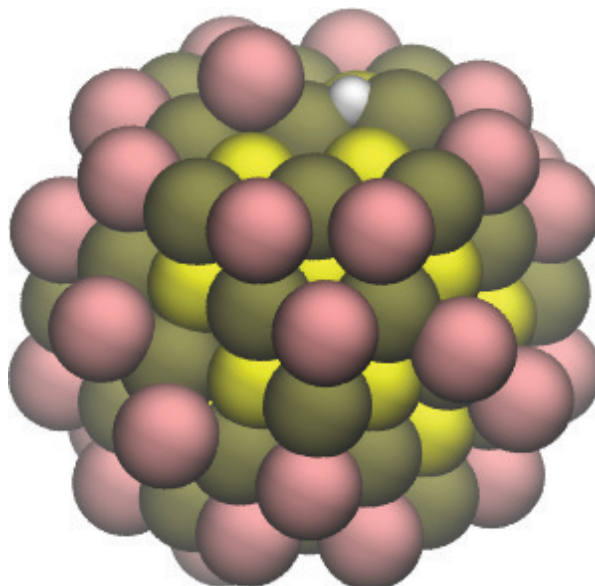


Figure 4.11: (a) Structural model (green, yellow, pink and white spheres represent lead, selenium, iodine and hydrogen atoms, respectively) and (b) Electronic density of states (DOS) for a $\text{Pb}_{55}\text{Se}_{38}\text{I}_{34}$ nanoparticle with one iodine ligand removed and one surface adsorbed hydrogen. The Fermi level is indicated by the vertical dashed line.

states are not stable and hydrogen always counteracts the existing doping of the system. We hypothesize that neutral H is stable in a wide energy region in NPs, because of the quantum confinement induced gap opening.

Next, we investigated whether hydrogen may provide an excess charge to counterbalance missing ligands. It is known that ligands may be stripped during, for example, ligand exchange processes,[10, 190] which are frequently used to replace native long ligands with shorter, sometimes mono-atomic ones, such as iodine.[91, 456, 225, 471, 299, 52, 224, 475] In our calculations, both large iodine terminated PbSe NP with one missing ligand and a hydrogen atom, and small stoichiometric clusters with an extra ligand and a hydrogen atom, turned out to have clean gaps, without intra-gap states (see Figure 4.2.3 for the density of states of the iodine terminated NP).

We further investigated whether multiple hydrogen atoms may be adsorbed on the surface of one single NP. Figure 4.2.3 shows the formation energy normalized by the number of hydrogen atoms (N_H) as a function of N_H on the surface. If the adsorption of subsequent hydrogens were independent of the existing ones, a flat line would be obtained. Instead, we found that it is energetically more favorable to adsorb second and subsequent hydrogen atoms when the adsorption takes place onto alternating Pb and Se sites.

We rationalized this behavior based on the Coulomb attraction of hydrogen atoms with opposite formal charges. This electrostatic energy varies with the distance between hydrogen atoms, which can be at most equal to the NP diameter; hence, the effects found here for $\text{Pb}_{28}\text{Se}_{28}$ will be less pronounced for larger NPs. Note that when an even number of hydrogen atoms is adsorbed, their charge can be mutually compensated, unlike the case of an odd number. We also note that even though the binding of additional hydrogen atoms is energetically favorable relative to the first one, the formation energy does increase, making it highly unlikely to adsorb multiple hydrogen atoms on one single NP.

Defect passivation by forming hydrogen complexes.

In addition to surface off-stoichiometry and ligand imbalance, another possible source of

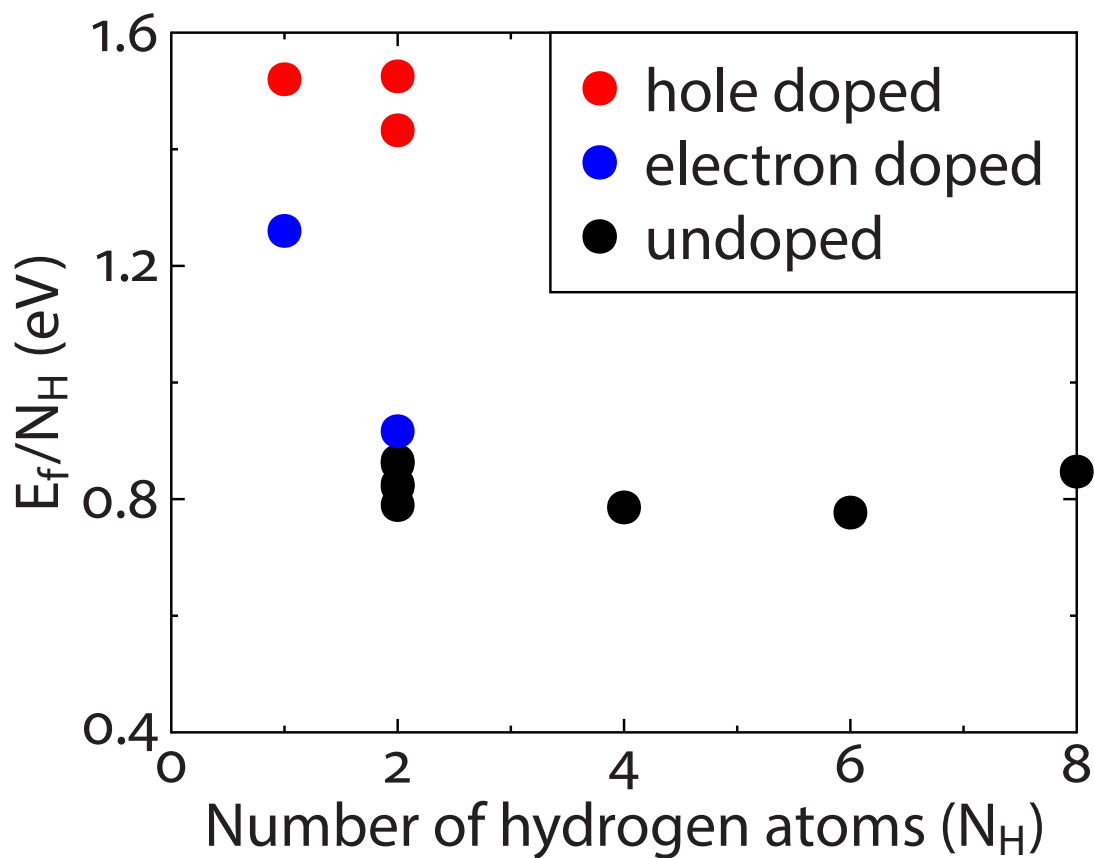


Figure 4.12: Formation energy (E_f) per number of hydrogen atoms (N_H) for a $\text{Pb}_{28}\text{Se}_{28}$ nanoparticle (NP) with several surface adsorbed hydrogen atoms. Black, red, and blue filled circles represent NPs undoped, hole doped and electron doped NPs, respectively.

trap states in PbSe NPs are intrinsic defects, such as vacancies.

Some calculations on bulk lead chalcogenides suggested that monovacancies and Schottky defects have the lowest formation energies, with Pb (Se) monovacancies giving rise to a shallow acceptor (deep donor) states, and Schottky defects creating donor-acceptor pairs inside the band gap.[241] In contrast, in PbS NPs, D. Zhrebetskyy et al. found that the charge-balanced S vacancy was the only defect giving rise to trap states among all the intrinsic defects they considered (Pb and S vacancies, surface Schottky defects).[477]

Since hydrogen is known for its ability to form complexes with electronically active defects,[102] we considered the case of hydrogen passivating Se vacancies by forming complexes with them. Our calculations confirmed the findings of D. Zhrebetskyy et al. on PbS NPs, i.e. that the trap states due to the anion vacancy may not be removed from the gap by making the vacancy charge-balanced. This result suggests that adsorbing two hydrogen atoms on the NP far away from the defect will not lead to a clean gap either, because charge transfer is not sufficient to remove the trap state. More importantly, we found that when hydrogen atoms approach a vacancy, they do form a complex: the formation energy of the hydrogen complex is 2.3 eV lower than that of hydrogen adsorption with no complex formation. Interestingly, only one hydrogen atom is sufficient to remove trap states from the gap, and the presence of a second one just ensures charge balance. Figure 4.2.3 shows the structural model and the density of states before and after forming the vacancy-hydrogen complex on the (100) facet of a $\text{Pb}_{28}\text{Se}_{28}$ NP (see Supplemental Information for the DOS obtained with a vacancy on the (111) facet). Since the use of the PBE functional may underestimate electronic gaps, which in turn could affect the energy position of defect levels,[103] we carried out several calculations to ensure the robustness of our results using the hybrid functional PBE0. The latter includes 25% exact exchange in the exchange correlation functional, which was shown to improve over gaps of finite systems obtained at the PBE level of theory.[360] We note that a recent study suggested that an even higher fraction of exact exchange may further improve results for finite systems.[49] We also computed the DOS by

including spin-orbit coupling (SOC), since it is known that states with strong Pb character may be substantially affected by SOC.[175] Although the absolute value of the gaps obtained at the PBE level increased by 1.2 eV when using PBE0, and decreased by 0.5 eV when including SOC, we reassuringly found that in the presence of a charged vacancy intra-gap states are still present, and that hydrogen atoms are responsible for the removal of these states. (See Supplemental Information for the DOS obtained with the PBE0 functional and with SOC.) Hence we concluded that our results are qualitatively robust and they show that a clean electronic gap may be obtained by adsorbing atomic hydrogen on the NP surfaces.

An additional interesting question is whether the introduction of hydrogen can also improve charge transfer between NPs. Enhancing charge transport in NP films is a major challenges in NP solar cells.[190, 251] Many theoretical studies assume that the presence of intra-gap states is a sufficient condition to trap charges, [200, 477] however only a few investigations addressed how charge transfer rates are affected by defects.[236] To address this problem, we computed the charge hopping rate from a NP without any defect to one with a defect (k_{CT}^{in}), and compared it with the hopping rate of the reverse process (k_{CT}^{out}). Hence, the efficacy of a NP with defect to trap charges can be quantified by the ratio k_{CT}^{in}/k_{CT}^{out} . If $k_{CT}^{in}/k_{CT}^{out} \gg 1$ then a defect is an effective charge trap which may jeopardize charge transport in films.

We computed the charge transfer rate (k_{CT}) ratio for several of our NP models using Marcus theory (see Table 4.4), where:

$$k_{CT} = |H_{ab}|^2 \sqrt{\frac{\pi\beta}{\hbar^2\lambda}} \exp^{-\beta E_{act}} . \quad (4.10)$$

Here H_{ab} is the electronic coupling between NP model a and NP model b , λ is the reorganization energy, E_{act} is the activation energy defined as:

$$E_{act} = \frac{(\Delta G + \lambda)^2}{4\lambda}, \quad (4.11)$$

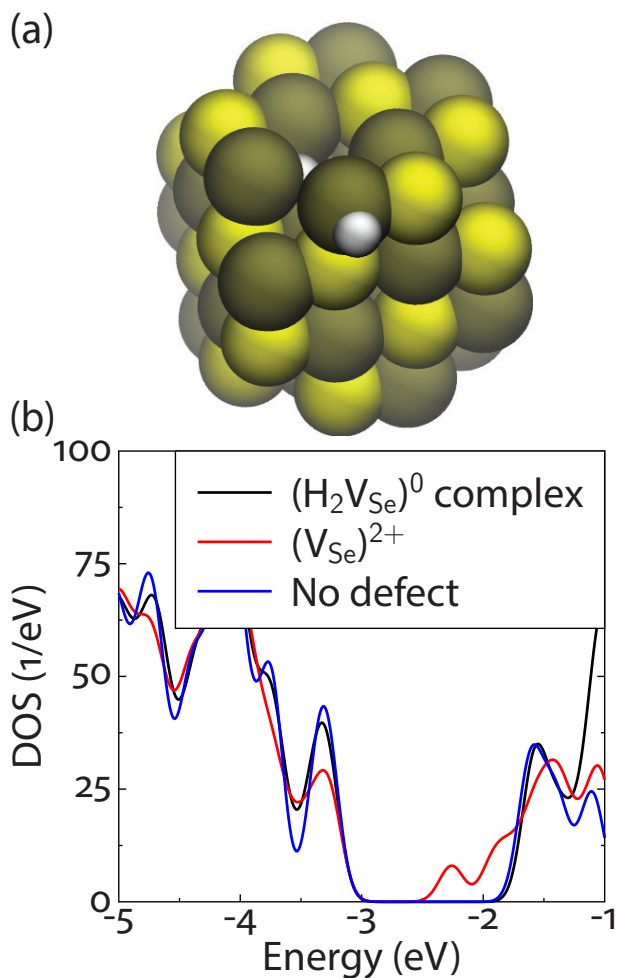


Figure 4.13: (a) Structural model of the hydrogen-vacancy complex on the (100) facet of the Pb₂₈Se₂₈ nanoparticle (NP). Green, yellow, and white spheres represent lead, selenium, and hydrogen atoms, respectively. (b) Electronic density of states (DOS) of the charged vacancy ((V_{Se})²⁺) and hydrogen-vacancy complex (H₂V_{Se}) compared to the DOS of the NP without any defect. See Supplemental Information for the same DOS obtained with the vacancy on the (111) facet.

where ΔG is the driving force and $\beta = \frac{1}{k_b T}$, k_b is the Boltzmann constant and T is the temperature. We computed the parameters entering Eqs. 4.10 and 4.11 as outlined in the Methods section.

We considered a NP without any defect, one with a Se vacancy, and one with a Se vacancy-H complex and computed all possible hole transfers between these models. Since a neutral Se vacancy introduces occupied states in the gap high in energy, this defect is expected to behave as a hole trap, i.e., $k_{CT}^{in}/k_{CT}^{out} \gg 1$.

Our results, shown in Table 4.4, indicate that indeed the V_{Se} defect behaves as a hole trap ($k_{CT}^{in}/k_{CT}^{out} \approx 10^6$). We found that the charge transfer rate of holes from a non-defective NP to one with a vacancy ($NP \rightarrow NP+V_{Se}$) is of the same order of magnitude as the transition between non-defective NPs ($NP \rightarrow NP$). In contrast, the charge transfer rate of escape from the NP with a vacancy to a non-defective one ($NP+V_{Se} \rightarrow NP$) is five orders of magnitude slower.

This trapping nature of vacancies can be ameliorated by the addition of hydrogen to form hydrogen-vacancy complexes (H_2V_{Se}). As shown in Table 4.4, despite an increase in the reorganization energy, the hopping rate of a hole from a non-defective NP to one with a hydrogen-vacancy complex ($NP \rightarrow NP+(H_2V_{Se})$) is comparable to that of pristine NPs. In addition, we find that the coupling (H_{ab}) is unaffected by the presence of hydrogen-vacancy complexes and, as indicated by the opposite transition ($NP+(H_2V_{Se}) \rightarrow NP$), the use of hydrogen increases the hopping rate of escape from vacancies by four orders of magnitude ($k_{CT}^{in}/k_{CT}^{out} \approx 1.2$). In summary, the presence of hydrogen atoms not only removes intra-gap states in defective NPs but it is also beneficial to charge transport in NP films.

To summarize, we used ab initio calculations to define a strategy to remove electronic gap states in lead chalcogenide films used in solar cell devices, hence suggesting ways to improve their efficiency. In particular, we proposed that hydrogen may be used as a post-processing agent to remove electronic trap states in already synthesized films. We found that hydrogen atoms absorbed at NP surfaces preferentially lead to n-type doping for stoichiometric NPs

Transition	$\Delta G(\text{meV})$	$\lambda(\text{meV})$	$E_{act}(\text{meV})$	$H_{ab}(\text{meV})$	$k_{CT}(\text{s}^{-1})$
NP \rightarrow NP	0	33	8	4	1.86e+14
NP \rightarrow NP+V $_{Se}$	-355	242	13	16	7.90e+14
NP \rightarrow NP+(H $_2$ V $_{Se}$)	-3	72	17	3	5.21e+13
NP+V $_{Se}$ \rightarrow NP	355	272	362	16	1.05e+09
NP+(H $_2$ V $_{Se}$) \rightarrow NP	3	79	21	3	4.24e+13

Table 4.4: The driving forces (ΔG), reorganization energies (λ), activation energies (E_{act}) and hopping rates (k_{CT} , see Eq. 4.10) at $T = 300\text{K}$ for hole transfer between NPs. Transitions are computed for NPs without a defect (NP), with a vacancy (NP+V $_{Se}$) and with a vacancy passivated by hydrogen (NP+(H $_2$ V $_{Se}$)). $a \rightarrow b$ denotes the transition from NP a to NP b .

and may charge balance off-stoichiometric ones; in addition, hydrogen can form complexes with defects, removing potentially detrimental charge traps with beneficial effects for charge transport dynamics as well. Our calculations suggested that atomic hydrogen maybe a more effective detergent of trap states than molecular hydrogen.

While we considered relatively small NPs, the results reported here are expected to hold qualitatively also for larger NPs. As mentioned in the Methods section, the DFT@PBE theoretical gaps of Pb $_{28}$ Se $_{28}$ (diameter of 1.3 nm, gap=1.65 eV) and Pb $_{55}$ Se $_{38}$ I $_{34}$ (diameter of 1.9 nm, gap=1.33 eV), correspond to those of experimental NPs with diameter of about 3 nm and 4 nm, respectively.[184, 281] In addition, our result of hydrogen n-type doping small stoichiometric NPs is consistent with experiments, which reported that hydrogen treatment may turn p-type bulk lead chalcogenides into n-type. Furthermore, the (+1/-1) charge transition level of interstitial hydrogen in bulk semiconductors was shown to behave universally, namely with energy close to -4.5 eV relative to the vacuum level.[414] We found the (+1/-1) charge transition levels at ≈ -4.0 eV for Pb $_{28}$ Se $_{28}$ (see Figure 4.2.3), close to the universal value for bulk systems. Since our results on small NPs seem to agree reasonably well with other calculations and measurements on bulk systems, our findings are expected to also apply to intermediate size regimes.

Although our study focused on the advantages of hydrogen treatment, the presence of hydrogen may also be related to possibly harmful effects, such as hysteresis or bias-stress effects, recently reported in the literature.[310, 316, 309] Hysteresis is here used to refer to

the history dependence of $I(V)$ curves, while the bias-stress effect is a related phenomenon in which the threshold voltage of transistors changes over time. Reference [472] ascribed the observed hysteretic behavior of NP field effect transistors (FET) to small ion diffusion, although dynamic surface reconstruction[432, 431] and ligand diffusion[433] may be possible causes as well. It is plausible that hydrogen may diffuse within the NP, especially at elevated temperatures and large applied voltages, thus possibly contributing to hysteresis and bias-stress effects. However, we note that despite being a drawback for example in FETs, this hysteretic behavior could be utilized to build memory devices [65]. Furthermore, atomic layer deposition techniques, that infill the space between NPs, might be able to lock in hydrogen atoms and prevent their diffusion.[251, 401]

Work is in progress to study the finite temperature behavior of isolated NPs and NP solids and the effect of applied bias.

CHAPTER 5

CONCLUSIONS

This dissertation focused on the study of optoelectronic properties of nanostructured materials including the development, implementation, and application of first principles methods.

In particular, in order to study electronic properties, we generalized dielectric dependent hybrid functionals[375, 272, 5, 208, 386, 385, 132, 351] to finite systems by introducing methods to compute the average screening of exchange interactions in molecules and nanoparticles, without invoking arbitrary volume definitions[47]. We constructed a new hybrid functional, called the screened exchange constant functional and demonstrated that it is extremely accurate for describing both photoemission and absorption properties of finite systems, and predicting correct energy level alignments. We also analyzed the screened exchange constant functional at varying levels of self-consistency and found that self-consistency is particularly important for ionic molecules and molecules where the character of the HOMO is highly dependent on the mixing fraction of exact exchange included in the functional[50]. The development of the screened exchange constant functional enabled highly accurate calculations of the optoelectronic properties of molecules and nanoparticles.

In terms of transport property calculations, we presented an implementation of constrained density functional theory (CDFT)[104, 189] for the calculation of charge transport in the hopping regime[141]. The implementation was verified against literature results and the dependence of results on numerical parameters was investigated. In addition, we compared with other methodologies which are used to compute transport properties in nanoparticle systems and we demonstrated that some of these methods give unphysical results for thermally disordered systems. In order to study transport in nanoparticles near interfaces, we coupled the self-consistent image charge method with constrained density functional theory. The methods for electronic transport properties briefly summarized above, were applied to silicon and lead chalcogenide nanoparticles.

Starting with isolated nanoparticles, we demonstrated that Si dangling bonds[328, 339,

341, 394, 338, 43, 340, 395, 197, 275, 192, 193, 441, 159, 30] at the surface of oxidized nanoparticles introduce defect states which, depending on their charge and local stress conditions, may give rise to ON and OFF states responsible for exponential blinking statistics[45]. These results provided a microscopic picture of how blinking may be achieved through surface dangling bonds, which are highly sensitive to the local strain around each nanoparticle. As a consequence, we were able to determine that the number of nanoparticles in a given sample, exhibiting exponential type blinking should vary with size, strain and surface passivation. Both hydrogen treatment[330, 229, 167] and annealing[295, 294, 167] may reduce the amount of blinking and deep level transient spectroscopy, along with electron spin resonance experiments could be used to validate these predictions.

In collaboration with experimentalists at the National Renewable Energy Laboratory in Golden, Colorado (M. C. Beard et al.) we demonstrated how the band edges of nanoparticles can be engineered through surface chemistry modification[217]. We showed that the band edge positions of lead chalcogenide nanoparticles[23, 68, 210, 467], can be tuned by over 2.0 eV through surface chemistry modification. We achieved such control by replacing native ligands with functionalized cinnamate ligands with increasing dipole moments. Our results established clear relationships between nanoparticle surface chemistry and the band edge positions of ligand/nanoparticle hybrid systems. We also found that the band edges of nanoparticles with fluorinated ligands, according to experiment, do not have the same dependency on ligand dipole as the nanoparticles with non-fluorinated ligands. In most cases we found good agreement between theory and experiment, however, the properties of fluorinated ligands were not yet reproduced by the theoretical calculations. We believe that in addition to ligand dipole, the inter-nanoparticle ligand shell inter-digitization contributes to the band edge shifts and we expect that our established relationships and principles can help guide future optimization of nanoparticle applications. In addition to optical properties, we also studied charge transport in nanostructured systems, by using CDFT. We investigated charge transfer between Si nanoparticles with deep dangling bonds defects and shallow oxy-

gen impurities[455, 345, 418] and we found that shallow defects may be more detrimental to charge transport than deep ones because charge transfer to deep trap states may be slowed down due to the presence of the inverted Marcus regime[44, 270, 268]. This effect is missed by simpler models of charge transport, such as Miller-Abrahams dynamics[279, 403] that do not include reorganization energies arising from structural changes at the surface. We found that electron and hole transfer rates for dangling bond defects depend strongly on the orientation of nanoparticles, which points to the importance of further studies of anisotropic charge transport in nanoparticle arrays with individually engineered building blocks. We also explored the effects of image charges[178, 290] on charge transfer between nanoparticles located near electrode interfaces. Surprisingly, we found the electronic coupling to be mostly insensitive to the presence of images charges. However, as expected, hopping rates were still affected by changes in the activation energy, which we computed by combining constrained density functional theory and the self-consistent image charge method.

Finally, we showed how hydrogen can be used to improve charge transfer between nanoparticles by removing trap states[422]. We found that hydrogen atoms absorbed at lead chalcogenide nanoparticles surfaces, preferentially lead to n-type doping of stoichiometric nanoparticles and may charge balance of off-stoichiometric ones. In addition, we predicted that hydrogen can form complexes with defects, removing potentially detrimental charge traps with beneficial effects for charge transport dynamics as well, however, the presence of hydrogen may also be related to possibly harmful effects, such as hysteresis or bias-stress effects[310, 316, 309]. Overall, these investigations highlighted the key importance of taking into account the atomistic properties, of nanoparticles when investigating optical and transport properties and were made possible by the methods presented and developed in this dissertation.

5.1 Summary

5.1.1 List of Publications

1. **Nicholas P. Brawand** , Marco Govoni, Márton Vörös, and Giulia Galli Performance and self-consistency of the screened exchange constant functional submitted (2017)
2. Matthew B. Goldey, **Nicholas P. Brawand** , Márton Vörös, and Giulia Galli Charge Transport in Nanostructured Materials: Implementation and Verification of Constrained Density Functional Theory submitted (2017)
3. **Nicholas P. Brawand**, Matthew Goldey, Márton Vörös, and Giulia Galli Defect states and charge transport in quantum dot solids *Chem. Mater.*, 29 (3), pp. 1255-1262 (2017)
4. Daniel M. Kroupa, Márton Vörös, **Nicholas P. Brawand**, Brett W. McNichols et al. Tuning Colloidal Quantum Dot Band Edge Positions through Solution-Phase Surface Chemistry Modification *Nat. Commun.* Accepted (2017)
5. Lili Wang, **Nicholas P. Brawand**, Márton Vörös, Peter D. Dahlberg et al. Excitations partition into two distinct populations in bulk single-domain-single-crystal $\text{CH}_3\text{NH}_3\text{PbBr}_3$ perovskites due to polaron formation submitted (2016)
6. Márton Vörös, **Nicholas P. Brawand**, and Giulia Galli Hydrogen treatment as a detergent of electronic trap states in lead chalcogenide nanoparticles *Chem. Mater.* 29 (6), pp. 2485-2493 (2017)
7. **Nicholas P. Brawand**, Márton Vörös, M. Govoni, and G. Galli Generalization of dielectric dependent hybrid functionals to finite systems *Phys. Rev. X* 6, 041002 (2016)
8. **Nicholas P. Brawand**, Márton Vörös, and Giulia Galli Surface Dangling Bonds Are a Cause of Type-II Blinking in Si Nanoparticles *Nanoscale* 7, 3737 (2015)

9. **Nicholas P. Brawand**, Mark T. Lusk Silicon Clathrate Quantum Dots and the Anisotropic Dependence of Quantum Confinement J. Phys. Chem. C 118 (46), pp 27091-27096 (2014)

5.1.2 Codes Released

1. The screened exchange constant plugin for WEST[145] - evaluates the screened exchange constant.
2. Constrained density functional theory and the self-consistent image charge method - evaluate transport properties implemented in Quantum-ESPRESSO.

5.1.3 Theoretical Methods Developed

1. The screened exchange constant functional - the generalization of dielectric dependent hybrids to finite systems.
2. The self consistent image charge method - coupled with constrained density functional theory, yields transport properties near metallic interfaces.

REFERENCES

- [1] Carlo Adamo and Vincenzo Barone. Toward reliable density functional methods without adjustable parameters: The pbe0 model. *The Journal of Chemical Physics*, 110(13):6158–6170, 1999.
- [2] A. P. Alivisatos. Perspectives on the physical chemistry of semiconductor nanocrystals. *The Journal of Physical Chemistry*, 100(31):13226–13239, 1996.
- [3] Audrius Alkauskas, Peter Broqvist, and Alfredo Pasquarello. Defect energy levels in density functional calculations: Alignment and band gap problem. *Phys. Rev. Lett.*, 101:046405, Jul 2008.
- [4] Audrius Alkauskas, Peter Broqvist, and Alfredo Pasquarello. Alignment of defect energy levels at sisio2 interface from hybrid density functional calculations. *AIP Conf. Proc.*, 1199(1):79–80, 2010.
- [5] Audrius Alkauskas, Peter Broqvist, and Alfredo Pasquarello. Defect levels through hybrid density functionals: Insights and applications. *Phys. Status Solidi B*, 248(4):775–789, 2011.
- [6] Audrius Alkauskas, Qimin Yan, and Chris G. Van de Walle. First-principles theory of nonradiative carrier capture via multiphonon emission. *Phys. Rev. B*, 90:075202, Aug 2014.
- [7] G. Allan, C. Delerue, and M. Lannoo. Nature of luminescent surface states of semiconductor nanocrystallites. *Phys. Rev. Lett.*, 76:2961–2964, Apr 1996.
- [8] Antonio J. Almeida, Ayaskanta Sahu, Andreas Riedinger, David J. Norris, Martin S. Brandt, Martin Stutzmann, and Rui N. Pereira. Charge trapping defects in cdse nanocrystal quantum dots. *J. Phys. Chem. C*, 120(25):13763–13770, 2016.
- [9] Nicholas C. Anderson, Mark P. Hendricks, Joshua J. Choi, and Jonathan S. Owen. Ligand exchange and the stoichiometry of metal chalcogenide nanocrystals: Spectroscopic observation of facile metal-carboxylate displacement and binding. *Journal of the American Chemical Society*, 135(49):18536–18548, 2013. PMID: 24199846.
- [10] Nicholas C. Anderson, Mark P. Hendricks, Joshua J. Choi, and Jonathan S. Owen. Ligand exchange and the stoichiometry of metal chalcogenide nanocrystals: Spectroscopic observation of facile metal-carboxylate displacement and binding. *Journal of the American Chemical Society*, 135(49):18536–18548, 2013.
- [11] Wanda Andreoni and Alessandro Curioni. New advances in chemistry and material science with cpmd and parallel computing. *Parallel Computing*, 26:819–842, 2000.
- [12] Viktor Atalla, Mina Yoon, Fabio Caruso, Patrick Rinke, and Matthias Scheffler. Hybrid density functional theory meets quasiparticle calculations: A consistent electronic structure approach. *Phys. Rev. B*, 88:165122, Oct 2013.

- [13] Viktor Atalla, Igor Ying Zhang, Oliver T. Hofmann, Xinguo Ren, Patrick Rinke, and Matthias Scheffler. Enforcing the linear behavior of the total energy with hybrid functionals: Implications for charge transfer, interaction energies, and the random-phase approximation. *Phys. Rev. B*, 94:035140, Jul 2016.
- [14] Roi Baer, Ester Livshits, and Ulrike Salzner. Tuned range-separated hybrids in density functional theory. *Annu. Rev. Phys. Chem.*, 61(1):85–109, 2010.
- [15] Roi Baer and Daniel Neuhauser. Density functional theory with correct long-range asymptotic behavior. *Phys. Rev. Lett.*, 94:043002, Feb 2005.
- [16] Kopinjol Baishya, Juan C. Idrobo, Serdar Ogut, Serdar, Mingli Yang, Koblar A. Jackson, and Julius Jellinek. First-principles absorption spectra of Cu_n ($n = 2-20$) clusters. *Phys. Rev. B*, 83:245402, Jun 2011.
- [17] Per Bak, Chao Tang, and Kurt Wiesenfeld. Self-organized criticality: An explanation of the $1/f$ noise. *Phys. Rev. Lett.*, 59:381, Jul 1987.
- [18] Rodney J. Bartlett and Monika Musial. Coupled-cluster theory in quantum chemistry. *Rev. Mod. Phys.*, 79:291–352, Feb 2007.
- [19] H. Bässler. Charge transport in disordered organic photoconductors a monte carlo simulation study. *Phys. Status Solidi B*, 175(1):15–56, 1993.
- [20] Heinz Bässler and Anna Köhler. Charge transport in organic semiconductors. *Top. Curr. Chem.*, 312:1–65, 2012.
- [21] William J Baumgardner, Kevin Whitham, and Tobias Hanrath. Confined-But-Connected Quantum Solids via Controlled Ligand Displacement. *Nano Lett.*, 13(7):3225–3231, jul 2013.
- [22] Matthew C. Beard, Kelly P. Knutsen, Pingrong Yu, Joseph M. Luther, Qing Song, Wyatt K. Metzger, Randy J. Ellingson, and Arthur J. Nozik. Multiple exciton generation in colloidal silicon nanocrystals. *Nano Lett.*, 7(8):2506–2512, 2007.
- [23] Matthew C Beard, Joseph M Luther, and Arthur J Nozik. The promise and challenge of nanostructured solar cells. *Nature nanotechnology*, 9(12):951–954, 2014.
- [24] Matthew C. Beard, Joseph M. Luther, Octavi E. Semonin, and Arthur J. Nozik. Third generation photovoltaics based on multiple exciton generation in quantum confined semiconductors. *Accounts of Chemical Research*, 46(6):1252–1260, 2013.
- [25] Matthew C. Beard, Joseph M. Luther, Octavi E. Semonin, and Arthur J. Nozik. Third generation photovoltaics based on multiple exciton generation in quantum confined semiconductors. *Accounts of Chemical Research*, 46(6):1252–1260, 2013.
- [26] F. Bechstedt. *Many-Body Approach to Electronic Excitations: Concepts and Applications*. Springer Series in Solid-State Sciences. Springer Berlin Heidelberg, 2014.

- [27] A D Becke. A Multicenter Numerical Integration Scheme for Polyatomic Molecules. *J. Chem. Phys.*, 88(4):2547, 1988.
- [28] Axel D. Becke. Densityfunctional thermochemistry. iii. the role of exact exchange. *J. Chem. Phys.*, 98(7):5648–5652, 1993.
- [29] Axel D. Becke. Perspective: Fifty years of density-functional theory in chemical physics. *J. Chem. Phys.*, 140(18), 2014.
- [30] M.R. Beltrán. A model of interface defect states at si/sio2 amorphous (non-periodic) interfaces. *J. Non-Cryst. Solids*, 163(2):148 – 161, 1993.
- [31] J. A. Berger. Fully parameter-free calculation of optical spectra for insulators, semiconductors, and metals from a simple polarization functional. *Phys. Rev. Lett.*, 115:137402, Sep 2015.
- [32] Marco Bernardi. First-principles dynamics of electrons and phonons*. *The European Physical Journal B*, 89(11):239, 2016.
- [33] P. E. Blöchl. Projector augmented-wave method. *Phys. Rev. B*, 50:17953–17979, Dec 1994.
- [34] Brian P. Bloom, Liu-Bin Zhao, Yang Wang, David H. Waldeck, Ruibin Liu, Peng Zhang, and David N. Beratan. Ligand-induced changes in the characteristic size-dependent electronic energies of cdse nanocrystals. *The Journal of Physical Chemistry C*, 117(43):22401–22411, 2013.
- [35] Jochen Blumberger and Keith P McKenna. Constrained Density Functional Theory Applied to Electron Tunnelling Between Defects in MgO. *Phys. Chem. Chem. Phys.*, 15(1):2184–96, 2013.
- [36] Jochen Blumberger, Ivano Tavernelli, Michael L. Klein, and Michiel Sprik. Diabatic Free Energy Curves and Coordination Fluctuations for the Aqueous Ag + Ag 2+ Redox Couple: A Biased Born-Oppenheimer Molecular Dynamics Investigation. *J. Chem. Phys.*, 124(2006), 2006.
- [37] Michael A. Boles, Daishun Ling, Taeghwan Hyeon, and Dmitri V. Talapin. The surface science of nanocrystals. *Nat Mater*, 15(2):141–153, Feb 2016. Review.
- [38] Michael A Boles, Daishun Ling, Taeghwan Hyeon, and Dmitri V Talapin. The surface science of nanocrystals. *Nature materials*, 15(2):141–153, 2016.
- [39] George H. Booth, Andreas Gruneis, Georg Kresse, and Ali Alavi. Towards an exact description of electronic wavefunctions in real solids. *Nature*, 493(7432):365–370, January 2013.
- [40] Giovanni Borghi, Andrea Ferretti, Ngoc Linh Nguyen, Ismaila Dabo, and Nicola Marzari. Koopmans-compliant functionals and their performance against reference molecular data. *Phys. Rev. B*, 90:075135, Aug 2014.

- [41] Deniz Bozyigit, Sebastian Volk, Olesya Yarema, and Vanessa Wood. Quantification of deep traps in nanocrystal solids, their electronic properties, and their influence on device behavior. *Nano Letters*, 13(11):5284–5288, November 2013.
- [42] Hartmut Bracht. Diffusion mechanisms and intrinsic point-defect properties in silicon. *MRS Bulletin*, 25(6):2227, Jan 2011.
- [43] V. Ya Bratus, V. A. Yukhimchuk, L. I. Berezhinsky, M. Ya Valakh, I. P. Vorona, I. Z. Indutnyi, T. T. Petrenko, P. E. Shepeliavyi, and I. B. Yanchuk. Structural transformations and silicon nanocrystallite formation in SiO_x films. *Semiconductors*, 35(7):821–826, July 2001.
- [44] Nicholas P. Brawand, Matthew B. Goldey, Márton Vörös, and Giulia Galli. Defect states and charge transport in quantum dot solids. *Chemistry of Materials*, 0(0):null, 0.
- [45] Nicholas P Brawand, Marton Voros, and Giulia Galli. Surface Dangling Bonds Are a Cause of B-Type Blinking in Si Nanoparticles. *Nanoscale*, 7:3737–3744, 2015.
- [46] Nicholas P. Brawand, Marton Vörös, and Giulia Galli. Surface dangling bonds are a cause of b-type blinking in si nanoparticles. *Nanoscale*, 7:3737–3744, 2015.
- [47] Nicholas P. Brawand, Márton Vörös, Marco Govoni, and Giulia Galli. Generalization of dielectric-dependent hybrid functionals to finite systems. *Phys. Rev. X*, 6:041002, Oct 2016.
- [48] Nicholas P. Brawand, Márton Vörös, Marco Govoni, and Giulia Galli. Generalization of dielectric-dependent hybrid functionals to finite systems. *Phys. Rev. X*, 6:041002, Oct 2016.
- [49] Nicholas P. Brawand, Márton Vörös, Marco Govoni, and Giulia Galli. Generalization of dielectric-dependent hybrid functionals to finite systems. *Phys. Rev. X*, 6:041002, Oct 2016.
- [50] Nicholas P. Brawand, Márton Vörös, Marco Govoni, and Giulia Galli. Performance and self-consistency of the screened exchange constant functional, 2017. submitted.
- [51] Patrick R. Brown, Donghun Kim, Richard R. Lunt, Ni Zhao, Mounqi G. Bawendi, Jeffrey C. Grossman, and Vladimir Bulovi. Energy level modification in lead sulfide quantum dot thin films through ligand exchange. *ACS Nano*, 8(6):5863–5872, 2014. PMID: 24824726.
- [52] Patrick R. Brown, Donghun Kim, Richard R. Lunt, Ni Zhao, Mounqi G. Bawendi, Jeffrey C. Grossman, and Vladimir Bulovi. Energy level modification in lead sulfide quantum dot thin films through ligand exchange. *ACS Nano*, 8(6):5863–5872, 2014.
- [53] Merlin Bruening, Ellen Moons, Dana Yaron-Marcovich, David Cahen, Jacqueline Libman, and Abraham Shanzer. Polar ligand adsorption controls semiconductor surface potentials. *Journal of the American Chemical Society*, 116(7):2972–2977, 1994.

- [54] Benjamin Bruhn, Fatjon Qejvanaj, Tom Gregorkiewicz, and Jan Linnros. Temporal correlation of blinking events in cdse/zns and si/sio2 nanocrystals. *Physica B*, 453(0):63–67, 2014. Low-Dimensional Semiconductor Structures - A part of the {XXII} International Material Research Congress (IMRC 2013).
- [55] Benjamin Bruhn, Fatjon Qejvanaj, Ilya Sychugov, and Jan Linnros. Blinking statistics and excitation-dependent luminescence yield in si and cdse nanocrystals. *J. Phys. Chem. C*, 118(4):2202–2208, 2014.
- [56] Benjamin Bruhn, Fatemeh Sangghaleh, and Jan Linnros. Fabricating single silicon quantum rods for repeatable single dot photoluminescence measurements. *Phys. Status Solidi A*, 208(3):631–634, 2011.
- [57] Benjamin Bruhn, Jan Valenta, Fatemeh Sangghaleh, and Jan Linnros. Blinking statistics of silicon quantum dots. *Nano Lett.*, 11(12):5574–5580, 2011.
- [58] Thomas Brumme, Matteo Calandra, and Francesco Mauri. Electrochemical doping of few-layer zrnc1 from first principles: Electronic and structural properties in field-effect configuration. *Phys. Rev. B*, 89:245406, Jun 2014.
- [59] Fabien Bruneval. *Exchange and Correlation in the Electronic Structure of Solids, from Silicon to Cuprous Oxide: GW Approximation and beyond*. PhD thesis, Ecole Polytechnique, 2005.
- [60] Fabien Bruneval and Matteo Gatti. Quasiparticle self-consistent gw method for the spectral properties of complex materials. In Cristiana Di Valentin, Silvana Botti, and Matteo Cococcioni, editors, *First Principles Approaches to Spectroscopic Properties of Complex Materials*, volume 347 of *Topics in Current Chemistry*, pages 99–135. Springer Berlin Heidelberg, 2014.
- [61] Fabien Bruneval, Samia M. Hamed, and Jeffrey B. Neaton. A systematic benchmark of the ab initio bethe-salpeter equation approach for low-lying optical excitations of small organic molecules. *J. Chem. Phys.*, 142(24):244101, 2015.
- [62] Fabien Bruneval and Miguel A. L. Marques. Benchmarking the starting points of the gw approximation for molecules. *J. Chem. Theory Comput.*, 9(1):324–329, 2013.
- [63] Fabien Bruneval, Francesco Sottile, Valerio Olevano, Rodolfo Del Sole, and Lucia Reining. Many-body perturbation theory using the density-functional concept: Beyond the gw approximation. *Phys. Rev. Lett.*, 94:186402, May 2005.
- [64] L. E. Brus. Electronelectron and electronhole interactions in small semiconductor crystallites: The size dependence of the lowest excited electronic state. *The Journal of Chemical Physics*, 80(9):4403–4409, 1984.
- [65] Christoph Busche, Laia Vila-Nadal, Jun Yan, Haralampos N. Miras, De-Liang Long, Vihar P. Georgiev, Asen Asenov, Rasmus H. Pedersen, Nikolaj Gadegaard, Muhammad M. Mirza, Douglas J. Paul, Josep M. Poblet, and Leroy Cronin. Design and

- fabrication of memory devices based on nanoscale polyoxometalate clusters. *Nature*, 515(7528):545–549, November 2014.
- [66] Marco Califano, Alberto Franceschetti, and Alex Zunger. Lifetime and polarization of the radiative decay of excitons, biexcitons, and trions in cdse nanocrystal quantum dots. *Phys. Rev. B*, 75:115401, Mar 2007.
- [67] I. Carbone, S. A. Carter, and G. T. Zimanyi. Monte carlo modeling of transport in pbse nanocrystal films. *J. Appl. Phys.*, 114(19):193709, 2013.
- [68] Graham H. Carey, Ahmed L. Abdelhady, Zhijun Ning, Susanna M. Thon, Osman M. Bakr, and Edward H. Sargent. Colloidal quantum dot solar cells. *Chemical Reviews*, 115(23):12732–12763, 2015.
- [69] Graham H. Carey, Illan J. Kramer, Pongsakorn Kanjanaboos, Gabriel Moreno-Bautista, Oleksandr Voznyy, Lisa Rollny, Joel A. Tang, Sjoerd Hoogland, and Edward H. Sargent. Electronically active impurities in colloidal quantum dot solids. *ACS Nano*, 8(11):11763–11769, 2014.
- [70] E. Cartier, J. H. Stathis, and D. A. Buchanan. Passivation and depassivation of silicon dangling bonds at the si/sio₂ interface by atomic hydrogen. *Applied Physics Letters*, 63(11):1510–1512, 1993.
- [71] Fabio Caruso, Viktor Atalla, Xinguo Ren, Angel Rubio, Matthias Scheffler, and Patrick Rinke. First-principles description of charge transfer in donor-acceptor compounds from self-consistent many-body perturbation theory. *Phys. Rev. B*, 90:085141, Aug 2014.
- [72] M.E. Casida and M. Huix-Rotllant. Progress in time-dependent density-functional theory. *Annu. Rev. Phys. Chem.*, 63(1):287–323, 2012.
- [73] Robert J. Cave and Marshall D. Newton. Calculation of Electronic Coupling Matrix Elements for Ground and Excited State Electron Transfer Reactions: Comparison of the Generalized MullikenHush and Block Diagonalization Methods. *J. Chem. Phys.*, 106(1997):9213, 1997.
- [74] Chia-Yen Cha, G. Gantefor, and W. Eberhardt. Photoelectron spectroscopy of cu_n clusters: Comparison with jellium model predictions. *The Journal of Chemical Physics*, 99(9):6308–6312, 1993.
- [75] Jeng Da Chai and Martin Head-Gordon. Systematic optimization of long-range corrected hybrid density functionals. *J. Chem. Phys.*, 128(8), 2008.
- [76] M. K. Y. Chan and G. Ceder. Efficient band gap prediction for solids. *Phys. Rev. Lett.*, 105:196403, Nov 2010.
- [77] Ting Chen, K. V. Reich, Nicolaas J. Kramer, Han Fu, Uwe R. Kortshagen, and B. I. Shklovskii. Metal-insulator transition in films of doped semiconductor nanocrystals. *Nat. Mater.*, 15(3):299–303, March 2016.

- [78] Xiaobo Chen, Xiaodong Pi, and Deren Yang. Bonding of oxygen at the oxide/nanocrystal interface of oxidized silicon nanocrystals: An ab initio study. *J. Phys. Chem. C*, 114(19):8774–8781, 2010.
- [79] Kai-Yuan Cheng, Rebecca Anthony, Uwe R. Kortshagen, and Russell J. Holmes. Hybrid silicon nanocrystalorganic light-emitting devices for infrared electroluminescence. *Nano Lett.*, 10(4):1154–1157, 2010.
- [80] Shanmugavel Chinnathambi, Song Chen, Singaravelu Ganesan, and Nobutaka Hanagata. Silicon quantum dots for biological applications. *Adv Healthc Mater*, 3(1):10–29, 2014.
- [81] Iek-Heng Chu, Marina Radulaski, Nenad Vukmirovic, Hai-Ping Cheng, and Lin-Wang Wang. Charge Transport in a Quantum Dot Supercrystal. *J. Phys. Chem. C*, 115:21409–21415, 2011.
- [82] Iek-Heng Chu, Marina Radulaski, Nenad Vukmirovic, Hai-Ping Cheng, and Lin-Wang Wang. Charge transport in a quantum dot supercrystal. *The Journal of Physical Chemistry C*, 115(43):21409–21415, 2011.
- [83] Chia-Hao M. Chuang, Patrick R. Brown, Vladimir Bulović, and Mounqi G. Bawendi. Improved performance and stability in quantum dot solar cells through band alignment engineering. *Nat Mater*, 13:796801, 2014.
- [84] Chia-Hao M. Chuang, Patrick R. Brown, Vladimir Bulovic, and Mounqi G. Bawendi. Improved performance and stability in quantum?dot solar cells through band alignment engineering. *Nat Mater*, 13(8):796–801, 2014. Letter.
- [85] Chia-Hao Marcus Chuang, Andrea Maurano, Riley E. Brandt, Gyu Weon Hwang, Joel Jean, Tonio Buonassisi, Vladimir Bulovi, and Mounqi G. Bawendi. Open-circuit voltage deficit, radiative sub-bandgap states, and prospects in quantum dot solar cells. *Nano Letters*, 15(5):3286–3294, 2015.
- [86] Frank Cichos, Jörg Martin, and Christian von Borczyskowski. Emission intermittency in silicon nanocrystals. *Phys. Rev. B*, 70:115314, Sep 2004.
- [87] Claudiu M Cirloganu, Lazaro A Padilha, Qianglu Lin, Nikolay S Makarov, Kirill A Velizhanin, Hongmei Luo, Istvan Robel, Jeffrey M Pietryga, and Victor I Klimov. Enhanced carrier multiplication in engineered quasi-type-ii quantum dots. *Nature communications*, 5:4148, 2014.
- [88] Aron J. Cohen, Paula Mori-Sanchez, and Weitao Yang. Development of exchange-correlation functionals with minimal many-electron self-interaction error. *J. Chem. Phys.*, 126(19), 2007.
- [89] Veaceslav Coropceanu, J Cornil, Demetrio A. da Silva Filho, Yoann Olivier, Robert Silbey, , and Jean-Luc Brédas. Charge transport in organic semiconductors. *Chem. Rev.*, 107(4):926–952, 2007.

- [90] Andrea Dal Corso. Pseudopotentials periodic table: From h to pu. *Computational Materials Science*, 95:337 – 350, 2014.
- [91] RW Crisp, DM Kroupa, AR Marshall, EM Miller, J Zhang, MC Beard, and JM Luther. Metal halide solid-state surface treatment for high efficiency pbs and pbse qd solar cells. *Scientific reports*, 5:9945–9945, 2014.
- [92] Ryan W. Crisp, Daniel M. Kroupa, Ashley R. Marshall, Elisa M. Miller, Jianbing Zhang, Matthew C. Beard, and Joseph M. Luther. Metal halide solid-state surface treatment for high efficiency pbs and pbse qd solar cells. *Scientific Reports*, 5:9945 EP –, Apr 2015. Article.
- [93] Larry A. Curtiss, Paul C. Redfern, Krishnan Raghavachari, and John A. Pople. Assessment of gaussian-2 and density functional theories for the computation of ionization potentials and electron affinities. *J. Chem. Phys.*, 109(1):42–55, 1998.
- [94] Ismaila Dabo, Andrea Ferretti, Nicolas Poilvert, Yanli Li, Nicola Marzari, and Matteo Cococcioni. Koopmans’ condition for density-functional theory. *Phys. Rev. B*, 82:115121, Sep 2010.
- [95] Quanqin Dai, Yingnan Wang, Xinbi Li, Yu Zhang, Donald J. Pellegrino, Muxun Zhao, Bo Zou, JaeTae Seo, Yiding Wang, and William W. Yu. Size-dependent composition and molar extinction coefficient of pbse semiconductor nanocrystals. *ACS Nano*, 3(6):1518–1524, 2009.
- [96] Andrea Dal Corso. Projector augmented wave method with spin-orbit coupling: Applications to simple solids and zincblende-type semiconductors. *Phys. Rev. B*, 86:085135, Aug 2012.
- [97] L. D. Dal Negro, J. H. Yi, J. Michel, L. C. Kimerling, S. Hamel, A Williamson, and G. Galli. Light-emitting silicon nanocrystals and photonic structures in silicon nitride. *IEEE J. Quant. Electron*, 12(6):1628–1635, Nov 2006.
- [98] Mita Dasog, Zhenyu Yang, Sarah Regli, Tonya M. Atkins, Angelique Faramus, Mani P. Singh, Elayaraja Muthuswamy, Susan M. Kauzlarich, Richard D. Tilley, and Jonathan G. C. Veinot. Chemical insight into the origin of red and blue photoluminescence arising from freestanding silicon nanocrystals. *ACS Nano*, 7(3):2676–2685, 2013. PMID: 23394574.
- [99] A. Datas, E. López, I. Ramiro, E. Antolín, A. Martí, A. Luque, R. Tamaki, Y. Shoji, T. Sogabe, and Y. Okada. Intermediate band solar cell with extreme broadband spectrum quantum efficiency. *Phys. Rev. Lett.*, 114:157701, Apr 2015.
- [100] A.L. Dawar, Partap Kumar, S.K. Paradkar, and B.K. Sachar. The effects of hydrogen in stabilizing the electrical properties of n-pb0.8sn0.2te thin films. *Infrared Physics*, 23(1):19 – 22, 1983.
- [101] Luca De Trizio and Liberato Manna. Forging colloidal nanostructures via cation exchange reactions. *Chemical Reviews*, 116(18):10852–10887, 2016.

- [102] Chris G. Van de Walle and Jrg Neugebauer. Hydrogen in semiconductors. *Annual Review of Materials Research*, 36(1):179–198, 2006.
- [103] Peter Deák, Bálint Aradi, Thomas Frauenheim, Erik Janzén, and Adam Gali. Accurate defect levels obtained from the hse06 range-separated hybrid functional. *Phys. Rev. B*, 81:153203, Apr 2010.
- [104] P. H. Dederichs, S. Blügel, R. Zeller, and H. Akai. Ground states of constrained systems: Application to cerium impurities. *Phys. Rev. Lett.*, 53:2512–2515, Dec 1984.
- [105] C. Delerue, G. Allan, and M. Lannoo. Theoretical aspects of the luminescence of porous silicon. *Phys. Rev. B*, 48:11024–11036, Oct 1993.
- [106] C. Delerue and M. Lannoo. *Nanostructures: Theory and Modeling*. Springer, Verlag Berlin Heidelberg, 2004.
- [107] C. Delerue, M. Lannoo, and G. Allan. Excitonic and quasiparticle gaps in si nanocrystals. *Phys. Rev. Lett.*, 84:2457–2460, Mar 2000.
- [108] C. Delerue, M. Lannoo, and G. Allan. Excitonic and quasiparticle gaps in si nanocrystals. *Phys. Rev. Lett.*, 84:2457–2460, Mar 2000.
- [109] C. Delerue, M. Lannoo, and G. Allan. Concept of dielectric constant for nanosized systems. *Phys. Rev. B*, 68:115411, Sep 2003.
- [110] Andreas Dreuw and Martin Head-Gordon. Failure of Time-Dependent Density Functional Theory for Long-Range Charge-Transfer Excited States: The Zincbacteriochlorin-Bacteriochlorin and Bacteriochlorophyll-Spheroidene Complexes. *J. Am. Chem. Soc.*, 126(12):4007–4016, mar 2004.
- [111] Arthur H. Edwards. Interaction of h and h₂ with the silicon dangling orbital at the (111) si/sio₂ interface. *Phys. Rev. B*, 44:1832, Jul 1991.
- [112] Al. L. Efros and M. Rosen. Random telegraph signal in the photoluminescence intensity of a single quantum dot. *Phys. Rev. Lett.*, 78:1110, Feb 1997.
- [113] R.F. Egerton and A.J. Crocker. The electrical effect of atomic hydrogen on lead telluride. *Surface Science*, 27(1):117 – 124, 1971.
- [114] Randy J. Ellingson, Matthew C. Beard, Justin C. Johnson, Pingrong Yu, Olga I. Micic, Arthur J. Nozik, Andrew Shabaev, and Alexander L. Efros. Highly efficient multiple exciton generation in colloidal pbse and pbs quantum dots. *Nano Letters*, 5(5):865–871, 2005. PMID: 15884885.
- [115] Aaron T. Fafarman, Weon-kyu Koh, Benjamin T. Diroll, David K. Kim, Dong-Kyun Ko, Soong Ju Oh, Xingchen Ye, Vicky Doan-Nguyen, Michael R. Crump, Danielle C. Reifsnyder, Christopher B. Murray, and Cherie R. Kagan. Thiocyanate-capped nanocrystal colloids: Vibrational reporter of surface chemistry and solution-based route to enhanced coupling in nanocrystal solids. *J. Am. Chem. Soc.*, 133(39):15753–15761, 2011. PMID: 21848336.

- [116] E. Fermi. Eine statistische methode zur bestimmung einiger eigenschaften des atoms und ihre anwendung auf die theorie des periodischen systems der elemente. *Zeitschrift fur Physik*, 48(1):73–79, 1928.
- [117] Anna Maria Ferrari, Roberto Orlando, and Michel Rrat. Ab initio calculation of the ultravioletvisible (uv-vis) absorption spectrum, electron-loss function, and reflectivity of solids. *J. Chem. Theory Comput.*, 11(7):3245–3258, 2015.
- [118] Jaime Ferrer, Colin J Lambert, Víctor Manuel García-Suárez, D Zs Manrique, D Vissontai, L Oroszlany, Rubén Rodríguez-Ferradás, Iain Grace, SWD Bailey, K Gillemot, et al. Gollum: a next-generation simulation tool for electron, thermal and spin transport. *New Journal of Physics*, 16(9):093029, 2014.
- [119] Matthew T. Frederick and Emily A. Weiss. Relaxation of exciton confinement in cdse quantum dots by modification with a conjugated dithiocarbamate ligand. *ACS Nano*, 4(6):3195–3200, 2010. PMID: 20503978.
- [120] Christoph Freysoldt, Blazej Grabowski, Tilmann Hickel, Jörg Neugebauer, Georg Kresse, Anderson Janotti, and Chris G. Van de Walle. First-principles calculations for point defects in solids. *Rev. Mod. Phys.*, 86:253–305, Mar 2014.
- [121] Christoph Freysoldt, Blazej Grabowski, Tilmann Hickel, Jörg Neugebauer, Georg Kresse, Anderson Janotti, and Chris G. Van de Walle. First-principles calculations for point defects in solids. *Rev. Mod. Phys.*, 86:253–305, Mar 2014.
- [122] Christoph Freysoldt, Blazej Grabowski, Tilmann Hickel, Jörg Neugebauer, Georg Kresse, Anderson Janotti, and Chris G. Van de Walle. First-principles calculations for point defects in solids. *Rev. Mod. Phys.*, 86:253–305, Mar 2014.
- [123] Richard A. Friesner. Ab initio quantum chemistry: Methodology and applications. *Proceedings of the National Academy of Sciences of the United States of America*, 102(19):6648–6653, 2005.
- [124] Bernd Fritzing, Richard K. Capek, Karel Lambert, Jos C. Martins, and Zeger Hens. Utilizing self-exchange to address the binding of carboxylic acid ligands to cdse quantum dots. *Journal of the American Chemical Society*, 132(29):10195–10201, 2010. PMID: 20608680.
- [125] Alex P. Gaiduk, Dzmitry S. Firaha, and Viktor N. Staroverov. Improved electronic excitation energies from shape-corrected semilocal kohn-sham potentials. *Phys. Rev. Lett.*, 108:253005, Jun 2012.
- [126] Fruzsina Gajdos, Harald Oberhofer, Michel Dupuis, and Jochen Blumberger. On the Inapplicability of Electron-Hopping Models for the Organic Semiconductor Phenyl-C61-Butyric Acid Methyl Ester (PCBM). *J. Phys. Chem. Lett.*, 4(6):1012–1017, mar 2013.

- [127] Fruzsina Gajdos, Siim Valner, Felix Hoffmann, Jacob Spencer, Marian Breuer, Adam Kubas, Michel Dupuis, and Jochen Blumberger. Ultrafast Estimation of Electronic Couplings for Electron Transfer Between Π -Conjugated Organic Molecules. *J. Chem. Theor. Comput.*, 10(10):4653–4660, 2014.
- [128] Christophe Galland, Yagnaseni Ghosh, Andrea Steinbrück, Milan Sykora, Jennifer A. Hollingsworth, Victor I. Klimov, and Han Htoon. Two types of luminescence blinking revealed by spectroelectrochemistry of single quantum dots. *Nature*, 479(7372):203–207, November 2011.
- [129] C. Garcia, B. Garrido, P. Pellegrino, R. Ferre, J. A. Moreno, J. R. Morante, L. Pavesi, and M. Cazzanelli. Size dependence of lifetime and absorption cross section of si nanocrystals embedded in sio₂. *Appl. Phys. Lett.*, 82(10):1595–1597, 2003.
- [130] Xiaochuan Ge, Simon J. Binnie, Dario Rocca, Ralph Gebauer, and Stefano Baroni. turbotddft 2.0 hybrid functionals and new algorithms within time-dependent density-functional perturbation theory. *Comput. Phys. Commun.*, 185(7):2080 – 2089, 2014.
- [131] Matteo Gerosa, Carlo Enrico Bottani, Lucia Caramella, Giovanni Onida, Cristiana Di Valentin, and Gianfranco Pacchioni. Electronic structure and phase stability of oxide semiconductors: Performance of dielectric-dependent hybrid functional dft, benchmarked against *gw* band structure calculations and experiments. *Phys. Rev. B*, 91:155201, Apr 2015.
- [132] Matteo Gerosa, Carlo Enrico Bottani, Lucia Caramella, Giovanni Onida, Cristiana Di Valentin, and Gianfranco Pacchioni. Electronic structure and phase stability of oxide semiconductors: Performance of dielectric-dependent hybrid functional dft, benchmarked against *gw* band structure calculations and experiments. *Phys. Rev. B*, 91:155201, Apr 2015.
- [133] Prasenjit Ghosh and Ralph Gebauer. Computational approaches to charge transfer excitations in a zinc tetraphenylporphyrin and c70 complex. *The Journal of Chemical Physics*, 132(10):104102, 2010.
- [134] Paolo Giannozzi, Stefano Baroni, Nicola Bonini, Matteo Calandra, Roberto Car, Carlo Cavazzoni, Davide Ceresoli, Guido L Chiarotti, Matteo Cococcioni, Ismaila Dabo, Andrea Dal Corso, Stefano de Gironcoli, Stefano Fabris, Guido Fratesi, Ralph Gebauer, Uwe Gerstmann, Christos Gougoussis, Anton Kokalj, Michele Lazzeri, Layla Martin-Samos, Nicola Marzari, Francesco Mauri, Riccardo Mazzarello, Stefano Paolini, Alfredo Pasquarello, Lorenzo Paulatto, Carlo Sbraccia, Sandro Scandolo, Gabriele Sclauzero, Ari P Seitsonen, Alexander Smogunov, Paolo Umari, and Renata M Wentzcovitch. Quantum espresso: a modular and open-source software project for quantum simulations of materials. *J. Phys.: Condens. Matter*, 21(39):395502, 2009.
- [135] Paolo Giannozzi, Stefano Baroni, Nicola Bonini, Matteo Calandra, Roberto Car, Carlo Cavazzoni, Davide Ceresoli, Guido L Chiarotti, Matteo Cococcioni, Ismaila Dabo, Andrea Dal Corso, Stefano de Gironcoli, Stefano Fabris, Guido Fratesi, Ralph Gebauer,

- Uwe Gerstmann, Christos Gougoussis, Anton Kokalj, Michele Lazzeri, Layla Martin-Samos, Nicola Marzari, Francesco Mauri, Riccardo Mazzarello, Stefano Paolini, Alfredo Pasquarello, Lorenzo Paulatto, Carlo Sbraccia, Sandro Scandolo, Gabriele Scлаuzero, Ari P Seitsonen, Alexander Smogunov, Paolo Umari, and Renata M Wentzcovitch. Quantum espresso: A modular and open-source software project for quantum simulations of materials. *J. Phys: Condens. Matter*, 21(39):395502–395521, 2009.
- [136] Paolo Giannozzi, Stefano Baroni, Nicola Bonini, Matteo Calandra, Roberto Car, Carlo Cavazzoni, Davide Ceresoli, Guido L Chiarotti, Matteo Cococcioni, Ismaila Dabo, Andrea Dal Corso, Stefano de Gironcoli, Stefano Fabris, Guido Fratesi, Ralph Gebauer, Uwe Gerstmann, Christos Gougoussis, Anton Kokalj, Michele Lazzeri, Layla Martin-Samos, Nicola Marzari, Francesco Mauri, Riccardo Mazzarello, Stefano Paolini, Alfredo Pasquarello, Lorenzo Paulatto, Carlo Sbraccia, Sandro Scandolo, Gabriele Scлаuzero, Ari P Seitsonen, Alexander Smogunov, Paolo Umari, and Renata M Wentzcovitch. Quantum espresso: a modular and open-source software project for quantum simulations of materials. *J. Phys.: Condens. Matter*, 21(39):395502, 2009.
- [137] Paolo Giannozzi, Stefano Baroni, Nicola Bonini, Matteo Calandra, Roberto Car, Carlo Cavazzoni, Davide Ceresoli, Guido L Chiarotti, Matteo Cococcioni, Ismaila Dabo, Andrea Dal Corso, Stefano de Gironcoli, Stefano Fabris, Guido Fratesi, Ralph Gebauer, Uwe Gerstmann, Christos Gougoussis, Anton Kokalj, Michele Lazzeri, Layla Martin-Samos, Nicola Marzari, Francesco Mauri, Riccardo Mazzarello, Stefano Paolini, Alfredo Pasquarello, Lorenzo Paulatto, Carlo Sbraccia, Sandro Scandolo, Gabriele Scлаuzero, Ari P Seitsonen, Alexander Smogunov, Paolo Umari, and Renata M Wentzcovitch. Quantum espresso: a modular and open-source software project for quantum simulations of materials. *J. Phys.-Condens. Mat.*, 21(39):395502, 2009.
- [138] Carlo Giansante, Luigi Carbone, Cinzia Giannini, Davide Altamura, Zoobia Ameer, Giuseppe Maruccio, Anna Loiudice, Maria R. Belviso, P. Davide Cozzoli, Aurora Rizzo, and Giuseppe Gigli. Colloidal arenethiolate-capped pbs quantum dots: Optoelectronic properties, self-assembly, and application in solution-cast photovoltaics. *The Journal of Physical Chemistry C*, 117(25):13305–13317, 2013.
- [139] Carlo Giansante, Ivan Infante, Eduardo Fabiano, Roberto Grisorio, Gian Paolo Suranna, and Giuseppe Gigli. Darker-than-black pbs quantum dots: Enhancing optical absorption of colloidal semiconductor nanocrystals via short conjugated ligands. *Journal of the American Chemical Society*, 137(5):1875–1886, 2015. PMID: 25574692.
- [140] Matthew B. Goldey, Bastien Belzunces, and Martin Head-Gordon. Attenuated MP2 with a Long-Range Dispersion Correction for Treating Nonbonded Interactions. *J. Chem. Theory Comput.*, 11(9):4159–4168, 2015.
- [141] Matthew B. Goldey, Nicholas P. Brawand, Mrton Vrs, and Giulia Galli. Charge transport in nanostructured materials: Implementation and verification of constrained density functional theory, 2017. submitted.

- [142] Matthew B. Goldey, Daniel Reid, Juan de Pablo, and Giulia Galli. Planarity and multiple components promote organic photovoltaic efficiency by improving electronic transport. *Phys. Chem. Chem. Phys.*, 18:31388–31399, 2016.
- [143] R Gomer. Diffusion of adsorbates on metal surfaces. *Reports on Progress in Physics*, 53(7):917, 1990.
- [144] Francisco M. Gómez-Campos and Marco Califano. Hole surface trapping in cdse nanocrystals: Dynamics, rate fluctuations, and implications for blinking. *Nano Lett.*, 12(9):4508–4517, 2012. PMID: 22849432.
- [145] Marco Govoni. west-code.org, 2017. [Online; accessed 2017-1-26].
- [146] Marco Govoni and Giulia Galli. Large scale gw calculations. *J. Chem. Theory Comput.*, 11(6):2680–2696, 2015.
- [147] Marco Govoni and Giulia Galli. Large scale gw calculations. *Journal of Chemical Theory and Computation*, 11(6):2680–2696, 2015.
- [148] Marco Govoni and Giulia Galli. Manuscript in preparation, 2017.
- [149] Marco Govoni, Ivan Marri, and Stefano Ossicini. Carrier multiplication between interacting nanocrystals for fostering silicon-based photovoltaics. *Nature Photonics*, 6(10):672–679, 2012.
- [150] Fabio Grassi, Mario Argeri, Leonardo Marchese, and Maurizio Cossi. First principle study of capping energies and electronic states in stoichiometric and nonstoichiometric pbse nanoclusters. *The Journal of Physical Chemistry C*, 117(49):26396–26404, 2013.
- [151] M.A. Green. *Third generation photovoltaics: advanced solar energy conversion*. Springer series in photonics. Springer, 2006.
- [152] Roberto Guerra and Stefano Ossicini. High luminescence in small Si/sio₂ nanocrystals: A theoretical study. *Phys. Rev. B*, 81:245307, Jun 2010.
- [153] Roberto Guerra and Stefano Ossicini. Role of strain in interacting silicon nanoclusters. *Phys. Rev. B*, 87:165441, Apr 2013.
- [154] S. Gutsch, J. Laube, A. M. Hartel, D. Hiller, N. Zakharov, P. Werner, and M. Zacharias. Charge transport in si nanocrystal/sio₂ superlattices. *J. Appl. Phys.*, 113(13), 2013.
- [155] S. Gutsch, J. Laube, A. M. Hartel, D. Hiller, N. Zakharov, P. Werner, and M. Zacharias. Charge transport in si nanocrystal/sio₂ superlattices. *J. Appl. Phys.*, 113(13):133703–133712, 2013.
- [156] D. R. Hamann. Optimized Norm-Conserving Vanderbilt Pseudopotentials. *Phys. Rev. B - Condens. Matter Mater. Phys.*, 88(8):1–10, 2013.
- [157] D. R. Hamann. Optimized norm-conserving vanderbilt pseudopotentials. *Phys. Rev. B*, 88:085117, Aug 2013.

- [158] S. Hamel, A. J. Williamson, H. F. Wilson, F. Gygi, G. Galli, E. Ratner, and D. Wack. First-principles calculations of the dielectric properties of silicon nanostructures. *Appl. Phys. Lett.*, 92(4):043115, 2008.
- [159] Masami Hane, Yoshiyuki Miyamoto, and Atsushi Oshiyama. Atomic and electronic structures of an interface between silicon and beta cristobalite. *Phys. Rev. B*, 41:12637, Jun 1990.
- [160] M. C. Hanna and A. J. Nozik. Solar conversion efficiency of photovoltaic and photoelectrolysis cells with carrier multiplication absorbers. *Journal of Applied Physics*, 100(7):074510, 2006.
- [161] Rachel D. Harris, Stephanie Bettis Homan, Mohamad Kodaimati, Chen He, Alexander B. Nepomnyashchii, Nathaniel K. Swenson, Shichen Lian, Raul Calzada, and Emily A. Weiss. Electronic processes within quantum dot-molecule complexes. *Chemical Reviews*, 116(21):12865–12919, 2016. PMID: 27499491.
- [162] Lars Hedin. New method for calculating the one-particle green’s function with application to the electron-gas problem. *Phys. Rev.*, 139:A796–A823, Aug 1965.
- [163] Trygve Helgaker, Sonia Coriani, Poul Jrgensen, Kasper Kristensen, Jeppe Olsen, and Kenneth Ruud. Recent advances in wave function-based methods of molecular-property calculations. *Chem. Rev.*, 112(1):543–631, 2012.
- [164] Mark P. Hendricks, Michael P. Campos, Gregory T. Cleveland, Ilan Jen-La Plante, and Jonathan S. Owen. A tunable library of substituted thiourea precursors to metal sulfide nanocrystals. *Science*, 348(6240):1226–1230, 2015.
- [165] Graeme Henkelman, Blas P. Uberuaga, and Hannes Jansson. A climbing image nudged elastic band method for finding saddle points and minimum energy paths. *The Journal of Chemical Physics*, 113(22):9901–9904, 2000.
- [166] Zeger Hens and Jos C. Martins. A solution nmr toolbox for characterizing the surface chemistry of colloidal nanocrystals. *Chemistry of Materials*, 25(8):1211–1221, 2013.
- [167] Daniel Hiller, Sebastian Gutsch, Andreas M. Hartel, Philipp Lper, Thoralf Gebel, and Margit Zacharias. A low thermal impact annealing process for sio2-embedded si nanocrystals with optimized interface quality. *J. Appl. Phys.*, 115(13):134311–134319, 2014.
- [168] F L Hirshfeld. Bonded-Atom Fragments for Describing Molecular Charge Densities. *Theor. Chem. Accounts Theory, Comput. Model. (Theoretica Chim. Acta)*, 44(2):129–138, 1977.
- [169] Joe Ho, Kent M. Ervin, and W. C. Lineberger. Photoelectron spectroscopy of metal cluster anions: Cun, agn, and aun. *The Journal of Chemical Physics*, 93(10):6987–7002, 1990.

- [170] P. Hohenberg and W. Kohn. Inhomogeneous electron gas. *Phys. Rev.*, 136:B864–B871, 1964.
- [171] Zachary C. Holman, Chin Yi Liu, and Uwe R. Kortshagen. Germanium and Silicon Nanocrystal Thin-Film Field-Effect Transistors From Solution. *Nano Lett.*, 10(7):2661–2666, 2010.
- [172] Nico Holmberg and Kari Laasonen. Efficient constrained density functional theory implementation for simulation of condensed phase electron transfer reactions. *Journal of Chemical Theory and Computation*, 0(0):null, 0. PMID: 28009515.
- [173] Ki-Ha Hong, Jongseob Kim, Jung Hoon Lee, Jaikwang Shin, and U-In Chung. Asymmetric doping in silicon nanostructures: The impact of surface dangling bonds. *Nano Lett.*, 10(5):1671–1676, 2010.
- [174] Yuanhang Huang, Matthew B. Goldey, Martin Head-Gordon, and Gregory Beran. Achieving High-Accuracy Intermolecular Interactions By Combining Coulomb-Attenuated Second-Order Møller-Plesset Perturbation Theory With a Long-Range Dispersion Correction. *J. Chem. Theory Comput.*, 10:2054, 2014.
- [175] Kerstin Hummer, Andreas Grüneis, and Georg Kresse. Structural and electronic properties of lead chalcogenides from first principles. *Phys. Rev. B*, 75:195211, May 2007.
- [176] Gyu Weon Hwang, Donghun Kim, Jose M. Cordero, Mark W. B. Wilson, Chia-Hao M. Chuang, Jeffrey C. Grossman, and Mounqi G. Bawendi. Identifying and eliminating emissive sub-bandgap states in thin films of pbs nanocrystals. *Advanced Materials*, 27(30):4481–4486, 2015.
- [177] Kim Hyeon-Deuk, Joonghan Kim, and Oleg V. Prezhdo. Ab initio analysis of auger-assisted electron transfer. *The Journal of Physical Chemistry Letters*, 6(2):244–249, 2015. PMID: 26263457.
- [178] J. C. Inkson. Many-body effect at metal-semiconductor junctions. ii. the self energy and band structure distortion. *Journal of Physics C: Solid State Physics*, 6(8):1350, 1973.
- [179] Alexander H. Ip, Susanna M. Thon, Sjoerd Hoogland, Oleksandr Voznyy, David Zhitomirsky, Ratan Debnath, Larissa Levina, Lisa R. Rollny, Graham H. Carey, Armin Fischer, Kyle W. Kemp, Illan J. Kramer, Zhijun Ning, André J. Labelle, Kang Wei Chou, Aram Amassian, and Edward H. Sargent. Hybrid Passivated Colloidal Quantum Dot Solids. *Nat. Nanotechnol.*, 7(9):577–582, 2012.
- [180] Viktor Ivády, Rickard Armiento, Krisztián Szász, Erik Janzén, Adam Gali, and Igor A. Abrikosov. Theoretical unification of hybrid-dft and DFT+ u methods for the treatment of localized orbitals. *Phys. Rev. B*, 90:035146, Jul 2014.
- [181] Denis Jacquemin, Ivan Duchemin, and Xavier Blase. Benchmarking the bethesalpeter formalism on a standard organic molecular set. *J. Chem. Theory Comput.*, 11(7):3290–3304, 2015.

- [182] Denis Jacquemin, Valrie Wathélet, Eric A. Perpète, and Carlo Adamo. Extensive tddft benchmark: Singlet-excited states of organic molecules. *J. Chem. Theory Comput.*, 5(9):2420–2435, 2009.
- [183] J.F. Janak. Proof That $dE/dn_i = E_i$ in Density-Functional Theory. *Phys. Rev. B*, 18(2):7165–7168, 1978.
- [184] Jacek Jasieniak, Marco Califano, and Scott E. Watkins. Size-dependent valence and conduction band-edge energies of semiconductor nanocrystals. *ACS Nano*, 5(7):5888–5902, 2011.
- [185] Frank Jensen. *Introduction to Computational Chemistry*. John Wiley & Sons, 2006.
- [186] Kwang Seob Jeong, Zhiyou Deng, Sean Keuleyan, Heng Liu, and Philippe Guyot-Sionnest. Air-stable n-doped colloidal hgs quantum dots. *The Journal of Physical Chemistry Letters*, 5(7):1139–1143, 2014. PMID: 26274461.
- [187] N. M. Johnson, D. K. Biegelsen, M. D. Moyer, S. T. Chang, E. H. Poindexter, and P. J. Caplan. Characteristic electronic defects at the sio₂ interface. *Appl. Phys. Lett.*, 43(6):563–565, 1983.
- [188] R. O. Jones. Density functional theory: Its origins, rise to prominence, and future. *Rev. Mod. Phys.*, 87:897–923, Aug 2015.
- [189] Benjamin Kaduk, Tim Kowalczyk, Troy Van Voorhis, and Troy Van Voorhis. Constrained Density Functional Theory. *Chem. Rev.*, 112(1):321–70, jan 2012.
- [190] Cherie R. Kagan and Christopher B. Murray. Charge transport in strongly coupled quantum dot solids. *Nature Nanotechnology*, 10(12):1013–1026, November 2015.
- [191] Cherie R Kagan and Christopher B Murray. Charge Transport in Strongly Coupled Quantum Dot Solids. *Nat. Nanotechnol.*, 10(12):1013–1026, 2015.
- [192] H. Kageshima and K. Shiraishi. Microscopic mechanism for sio₂si interface passivation: Sio double bond formation. *Surf. Sci.*, 380(1):61 – 65, 1997.
- [193] Hiroyuki Kageshima and Kenji Shiraishi. Theoretical study of the band offset at silicon-oxide/silicon interfaces with interfacial defects. *Surf. Sci.*, 407(13):133 – 139, 1998.
- [194] Khabiboulakh Katsiev, Alexander H. Ip, Armin Fischer, Iori Tanabe, Xin Zhang, Ahmad R. Kirmani, Oleksandr Voznyy, Lisa R. Rollny, Kang Wei Chou, Susanna M. Thon, Graham H. Carey, Xiaoyu Cui, Aram Amassian, Peter Dowben, Edward H. Sargent, and Osman M. Bakr. The complete in-gap electronic structure of colloidal quantum dot solids and its correlation with electronic transport and photovoltaic performance. *Advanced Materials*, 26(6):937–942, February 2014.
- [195] L. Katz, M. Guinan, and R. J. Borg. Diffusion of h₂, d₂, and t₂ in single-crystal ni and cu. *Phys. Rev. B*, 4:330–341, Jul 1971.

- [196] Amandeep Kaur, Erik R. Ylvisaker, Deyu Lu, Tuan Anh Pham, Giulia Galli, and Warren E. Pickett. Spectral representation analysis of dielectric screening in solids and molecules. *Phys. Rev. B*, 87:155144, Apr 2013.
- [197] K. Keunen, A. Stesmans, and V. V. Afanas'ev. Inherent si dangling bond defects at the thermal (110)si/sio₂ interface. *Phys. Rev. B*, 84:085329, Aug 2011.
- [198] Svetlana V. Kilina, Patrick K. Tamukong, and Dmitri S. Kilin. Surface chemistry of semiconducting quantum dots: Theoretical perspectives. *Accounts of Chemical Research*, 49(10):2127–2135, 2016.
- [199] Svetlana V. Kilina, Patrick K. Tamukong, and Dmitri S. Kilin. Surface chemistry of semiconducting quantum dots: Theoretical perspectives. *Acc. Chem. Res.*, 49(10):2127–2135, 2016. PMID: 27669357.
- [200] Donghun Kim, Dong-Ho Kim, Joo-Hyoung Lee, and Jeffrey C. Grossman. Impact of stoichiometry on the electronic structure of PbS quantum dots. *Physical Review Letters*, 110(19):196802, May 2013.
- [201] Victor I. Klimov. Multicarrier interactions in semiconductor nanocrystals in relation to the phenomena of auger recombination and carrier multiplication. *Annual Review of Condensed Matter Physics*, 5(1):285–316, 2014.
- [202] Jan M. Knaup, Marton Voros, Peter Deak, Adam Gali, Thomas Frauenheim, and Efthimios Kaxiras. Annealing simulations to determine the matrix interface structure of sic quantum dots embedded in sio₂. *Phys. Status Solidi C*, 7(2):407–410, 2010.
- [203] Sharon E. Koh, Chad Risko, Demetrio A. Da Silva Filho, Ohyun Kwon, Antonio Facchetti, Jean Luc Brédas, Tobin J. Marks, and Mark A. Ratner. Modeling Electron and Hole Transport in Fluoroarene-Oligothiopene Semiconductors: Investigation of Geometric and Electronic Structure Properties. *Adv. Funct. Mater.*, 18(2):332–340, 2008.
- [204] W K Koh, A Y Kuposov, J T Stewart, B N Pal, I Robel, J M Pietryga, and V I Klimov. Heavily Doped N-Type PbSe and PbS Nanocrystals Using Ground-State Charge Transfer From Cobaltocene. *Sci Rep*, 3:2004, 2013.
- [205] W. Kohn and L. J. Sham. Self-consistent equations including exchange and correlation effects. *Phys. Rev.*, 140:A1133–A1138, Nov 1965.
- [206] W. Kohn and L. J. Sham. Self-consistent equations including exchange and correlation effects. *Phys. Rev.*, 140:A1133–A1138, 1965.
- [207] Unsal Koldemir, Jennifer L. Braid, Amanda Morgenstern, Mark Eberhart, Reuben T. Collins, Dana C. Olson, and Alan Sellinger. Molecular design for tuning work functions of transparent conducting electrodes. *The Journal of Physical Chemistry Letters*, 6(12):2269–2276, 2015. PMID: 26266603.

- [208] David Koller, Peter Blaha, and Fabien Tran. Hybrid functionals for solids with an optimized hartreefock mixing parameter. *J. Phys.: Condens. Matter*, 25(43):435503, 2013.
- [209] Hannu-Pekka Komsa and Alfredo Pasquarello. Assessing the accuracy of hybrid functionals in the determination of defect levels: Application to the as antisite in gaas. *Phys. Rev. B*, 84:075207, Aug 2011.
- [210] Maksym V. Kovalenko, Liberato Manna, Andreu Cabot, Zeger Hens, Dmitri V. Talapin, Cherie R. Kagan, Victor I. Klimov, Andrey L. Rogach, Peter Reiss, Delia J. Milliron, Philippe Guyot-Sionnest, Gerasimos Konstantatos, Wolfgang J. Parak, Taeghwan Hyeon, Brian A. Korgel, Christopher B. Murray, and Wolfgang Heiss. Prospects of nanoscience with nanocrystals. *ACS Nano*, 9(2):1012–1057, 2015.
- [211] Maksym V. Kovalenko, Liberato Manna, Andreu Cabot, Zeger Hens, Dmitri V. Talapin, Cherie R. Kagan, Victor I. Klimov, Andrey L. Rogach, Peter Reiss, Delia J. Milliron, Philippe Guyot-Sionnest, Gerasimos Konstantatos, Wolfgang J. Parak, Taeghwan Hyeon, Brian A. Korgel, Christopher B. Murray, and Wolfgang Heiss. Prospects of nanoscience with nanocrystals. *ACS Nano*, 9(2):1012–1057, 2015.
- [212] Maksym V Kovalenko, Liberato Manna, Andreu Cabot, Zeger Hens, Dmitri V Talapin, Cherie R Kagan, Victor I. Klimov, Andrey L Rogach, Peter Reiss, Delia J Milliron, Philippe Guyot-Sionnest, Gerasimos Konstantatos, Wolfgang J Parak, Taeghwan Hyeon, Brian A Korgel, Christopher B Murray, and Wolfgang Heiss. Prospects of Nanoscience With Nanocrystals. *ACS Nano*, 9(2):1012–1057, feb 2015.
- [213] Katharina Krause, Michael E. Harding, and Wim Klopper. Coupled-cluster reference values for the gw27 and gw100 test sets for the assessment of gw methods. *Molecular Physics*, 113(13-14):1952–1960, 2015.
- [214] G. Kresse and D. Joubert. From ultrasoft pseudopotentials to the projector augmented-wave method. *Phys. Rev. B*, 59:1758–1775, Jan 1999.
- [215] Leeor Kronik, Tamar Stein, Sivan Refaely-Abramson, and Roi Baer. Excitation gaps of finite-sized systems from optimally tuned range-separated hybrid functionals. *J. Chem. Theory Comput.*, 8(5):1515–1531, 2012.
- [216] D. M. Kroupa, N. C. Anderson, C. V. Castaneda, A. J. Nozik, and M. C. Beard. In situ spectroscopic characterization of a solution-phase x-type ligand exchange at colloidal lead sulphide quantum dot surfaces. *Chem. Commun.*, 52:13893–13896, 2016.
- [217] Daniel M. Kroupa, Marton Voros, Nicholas P. Brawand, Brett W. McNichols, and et al. Tuning colloidal quantum dot band edge positions through solution-phase surface chemistry modification, 2017. accepted.
- [218] Aliaksandr V. Krukau, Oleg A. Vydrov, Artur F. Izmaylov, and Gustavo E. Scuseria. Influence of the exchange screening parameter on the performance of screened hybrid functionals. *J. Chem. Phys.*, 125(22), 2006.

- [219] Adam Kubas, Felix Hoffmann, Alexander Heck, Harald Oberhofer, Marcus Elstner, and Jochen Blumberger. Electronic Couplings for Molecular Charge Transfer: Benchmarking CDFT, FODFT, and FODFTB Against High-Level Ab Initio Calculations. *J. Chem. Phys.*, 140(10):104105, mar 2014.
- [220] Adam Kubas, Felix Hoffmann, Alexander Heck, Harald Oberhofer, Marcus Elstner, and Jochen Blumberger. Electronic Couplings for Molecular Charge Transfer: Benchmarking CDFT, FODFT, and FODFTB Against High-Level Ab Initio Calculations. II. *PCCP*, 17:14342–14354, dec 2014.
- [221] Stephan Kümmel and Leeor Kronik. Orbital-dependent density functionals: Theory and applications. *Rev. Mod. Phys.*, 80:3–60, Jan 2008.
- [222] M. Kuno, D. P. Fromm, S. T. Johnson, A. Gallagher, and D. J. Nesbitt. Modeling distributed kinetics in isolated semiconductor quantum dots. *Phys. Rev. B*, 67:125304, Mar 2003.
- [223] Andr J. Labelle, Susanna M. Thon, Silvia Masala, Michael M. Adachi, Haopeng Dong, Maryam Farahani, Alexander H. Ip, Andrea Fratolocchi, and Edward H. Sargent. Colloidal quantum dot solar cells exploiting hierarchical structuring. *Nano Letters*, 15(2):1101–1108, 2015.
- [224] Xinzheng Lan, Oleksandr Voznyy, F. Pelayo Garca de Arquer, Mengxia Liu, Jixian Xu, Andrew H. Proppe, Grant Walters, Fengjia Fan, Hairen Tan, Min Liu, Zhenyu Yang, Sjoerd Hoogland, and Edward H. Sargent. 10.6% certified colloidal quantum dot solar cells via solvent-polarity-engineered halide passivation. *Nano Letters*, 16(7):4630–4634, 2016.
- [225] Xinzheng Lan, Oleksandr Voznyy, Amirreza Kiani, F. Pelayo García de Arquer, Abdullah Saud Abbas, Gi-Hwan Kim, Mengxia Liu, Zhenyu Yang, Grant Walters, Jixian Xu, Mingjian Yuan, Zhijun Ning, Fengjia Fan, Pongsakorn Kanjanaboos, Illan Kramer, David Zhitomirsky, Philip Lee, Alexander Perelgut, Sjoerd Hoogland, and Edward H. Sargent. Passivation using molecular halides increases quantum dot solar cell performance. *Advanced Materials*, 28(2):299–304, 2016.
- [226] P. T. Landsberg. *Recombination in Semiconductors*. Cambridge University Press, NY, USA, 1991.
- [227] M. Lannoo, C. Delerue, and G. Allan. Nonradiative recombination on dangling bonds in silicon crystallites. *J. Lumin.*, 57(16):243 – 247, 1993.
- [228] Ka Un Lao and John M. Herbert. Energy decomposition analysis with a stable charge-transfer term for interpreting intermolecular interactions. *Journal of Chemical Theory and Computation*, 12(6):2569–2582, 2016. PMID: 27049750.
- [229] Benjamin G. Lee, Daniel Hiller, Jun-Wei Luo, Octavi E. Semonin, Matthew C. Beard, Margit Zacharias, and Paul Stradins. Strained interface defects in silicon nanocrystals. *Advanced Functional Materials*, 22(15):3223–3232, 2012.

- [230] Benjamin G. Lee, Daniel Hiller, Jun-Wei Luo, Octavi E. Semonin, Matthew C. Beard, Margit Zacharias, and Paul Stradins. Strained interface defects in silicon nanocrystals. *Advanced Functional Materials*, 22(15):3223–3232, 2012.
- [231] Kurt Lejaeghere, Gustav Bihlmayer, Torbjörn Björkman, Peter Blaha, Stefan Blügel, Volker Blum, Damien Caliste, Ivano E Castelli, Stewart J Clark, Andrea Dal Corso, Stefano de Gironcoli, Thierry Deutsch, John Kay Dewhurst, Igor Di Marco, Claudia Draxl, Marcin Dułak, Olle Eriksson, José A Flores-Livas, Kevin F Garrity, Luigi Genovese, Paolo Giannozzi, Matteo Giantomassi, Stefan Goedecker, Xavier Gonze, Oscar Grånäs, E K U Gross, Andris Gulans, François Gygi, D R Hamann, Phil J Hasnip, N A W Holzwarth, Diana Iuan, Dominik B Jochym, François Jollet, Daniel Jones, Georg Kresse, Klaus Koepernik, Emine Küçükbenli, Yaroslav O Kvashnin, Inka L M Loch, Sven Lubeck, Martijn Marsman, Nicola Marzari, Ulrike Nitzsche, Lars Nordström, Taisuke Ozaki, Lorenzo Paulatto, Chris J Pickard, Ward Poelmans, Matt I J Probert, Keith Refson, Manuel Richter, Gian-Marco Rignanese, Santanu Saha, Matthias Scheffler, Martin Schlipf, Karlheinz Schwarz, Sangeeta Sharma, Francesca Tavazza, Patrik Thunström, Alexandre Tkatchenko, Marc Torrent, David Vanderbilt, Michiel J van Setten, Veronique Van Speybroeck, John M Wills, Jonathan R Yates, Guo-Xu Zhang, and Stefaan Cottenier. Reproducibility in Density Functional Theory Calculations of Solids. *Science*, 351(6280):1415, 2016.
- [232] Kurt Lejaeghere, Gustav Bihlmayer, Torbjörn Björkman, Peter Blaha, Stefan Blügel, Volker Blum, Damien Caliste, Ivano E. Castelli, Stewart J. Clark, Andrea Dal Corso, Stefano de Gironcoli, Thierry Deutsch, John Kay Dewhurst, Igor Di Marco, Claudia Draxl, Marcin Dułak, Olle Eriksson, José A. Flores-Livas, Kevin F. Garrity, Luigi Genovese, Paolo Giannozzi, Matteo Giantomassi, Stefan Goedecker, Xavier Gonze, Oscar Grånäs, E. K. U. Gross, Andris Gulans, François Gygi, D. R. Hamann, Phil J. Hasnip, N. A. W. Holzwarth, Diana Iuşan, Dominik B. Jochym, François Jollet, Daniel Jones, Georg Kresse, Klaus Koepernik, Emine Küçükbenli, Yaroslav O. Kvashnin, Inka L. M. Loch, Sven Lubeck, Martijn Marsman, Nicola Marzari, Ulrike Nitzsche, Lars Nordström, Taisuke Ozaki, Lorenzo Paulatto, Chris J. Pickard, Ward Poelmans, Matt I. J. Probert, Keith Refson, Manuel Richter, Gian-Marco Rignanese, Santanu Saha, Matthias Scheffler, Martin Schlipf, Karlheinz Schwarz, Sangeeta Sharma, Francesca Tavazza, Patrik Thunström, Alexandre Tkatchenko, Marc Torrent, David Vanderbilt, Michiel J. van Setten, Veronique Van Speybroeck, John M. Wills, Jonathan R. Yates, Guo-Xu Zhang, and Stefaan Cottenier. Reproducibility in density functional theory calculations of solids. *Science*, 351(6280), 2016.
- [233] Huashan Li, Zhigang Wu, and Mark T Lusk. Dangling Bond Defects: The Critical Roadblock to Efficient Photoconversion in Hybrid Quantum Dot Solar Cells. *J. Phys. Chem. C*, 118(1):46–53, jan 2014.
- [234] Huashan Li, Zhigang Wu, and Mark T. Lusk. Dangling bond defects: The critical roadblock to efficient photoconversion in hybrid quantum dot solar cells. *J. Phys. Chem. C*, 118(1):46–53, 2014.

- [235] Huashan Li, Zhigang Wu, and Mark T. Lusk. Dangling bond defects: The critical roadblock to efficient photoconversion in hybrid quantum dot solar cells. *J. Phys. Chem. C*, 118(1):46–53, January 2014.
- [236] Huashan Li, Zhigang Wu, and Mark T. Lusk. Dangling bond defects: The critical roadblock to efficient photoconversion in hybrid quantum dot solar cells. *The Journal of Physical Chemistry C*, 118(1):46–53, 2014.
- [237] Huashan Li, David Zhitomirsky, Shreya Dave, and Jeffrey C. Grossman. Toward the ultimate limit of connectivity in quantum dots with high mobility and clean gaps. *ACS Nano*, 10(1):606–614, 2016.
- [238] Huashan Li, David Zhitomirsky, and Jeffrey C. Grossman. Tunable and energetically robust pbs nanoplatelets for optoelectronic applications. *Chemistry of Materials*, 28(6):1888–1896, 2016.
- [239] Tianshu Li, Francois Gygi, and Giulia Galli. Tailored nanoheterojunctions for optimized light emission. *Phys. Rev. Lett.*, 107:206805, Nov 2011.
- [240] Wu Li. Electrical transport limited by electron-phonon coupling from boltzmann transport equation: An *ab initio* study of si, al, and mos₂. *Phys. Rev. B*, 92:075405, Aug 2015.
- [241] Wun-Fan Li, Chang-Ming Fang, Marjolein Dijkstra, and Marijn A van Huis. The role of point defects in pbs, pbse and pbte: a first principles study. *Journal of Physics: Condensed Matter*, 27(35):355801, 2015.
- [242] Qianglu Lin, Nikolay S. Makarov, Weon kyu Koh, Kirill A. Velizhanin, Claudiu M. Cirloganu, Hongmei Luo, Victor I. Klimov, and Jeffrey M. Pietryga. Design and synthesis of heterostructured quantum dots with dual emission in the visible and infrared. *ACS Nano*, 9(1):539–547, 2015.
- [243] Zhibin Lin, Alberto Franceschetti, and Mark T. Lusk. Size dependence of the multiple exciton generation rate in cdse quantum dots. *ACS Nano*, 5(4):2503–2511, 2011. PMID: 21355556.
- [244] Zhibin Lin, Huashan Li, Alberto Franceschetti, and Mark T. Lusk. Efficient exciton transport between strongly quantum-confined silicon quantum dots. *ACS Nano*, 6(5):4029–4038, 2012. PMID: 22468899.
- [245] P.J. Linstrom and W.G. Mallard. Nist standard reference database number 69, 2017. [Online; accessed 2017-1-26].
- [246] Gerald Lippert, Jurg Hutter, and Michele Parrinello. A hybrid gaussian and plane wave density functional scheme. *Mol. Phys.*, 92(3):477–488, 1997.
- [247] Benkang Liu, Yanqiu Wang, and Li Wang. Experimental observations of s-p coupling in copper dimer anions. *Phys. Rev. A*, 88:033413, Sep 2013.

- [248] Jin Liu, Amanda J. Neukirch, and Oleg V. Prezhdo. Non-radiative electronhole recombination in silicon clusters: Ab initio non-adiabatic molecular dynamics. *J. Phys. Chem. C*, 118(35):20702–20709, 2014.
- [249] Mengxia Liu, F. Pelayo García de Arquer, Yiyang Li, Xinzheng Lan, Gi-Hwan Kim, Oleksandr Voznyy, Lethy Krishnan Jagadamma, Abdullah Saud Abbas, Sjoerd Hoogland, Zhenghong Lu, Jin Young Kim, Aram Amassian, and Edward H. Sargent. Double-sided junctions enable high-performance colloidal-quantum-dot photovoltaics. *Advanced Materials*, 28(21):4142–4148, 2016.
- [250] Yao Liu, Jason Tolentino, Markelle Gibbs, Rachelle Ihly, Craig L. Perkins, Yu Liu, Nathan Crawford, John C. Hemminger, and Matt Law. Pbse quantum dot field-effect transistors with air-stable electron mobilities above $7 \text{ cm}^2 \text{ v}^{-1} \text{ s}^{-1}$. *Nano Letters*, 13(4):1578–1587, 2013. PMID: 23452235.
- [251] Yao Liu, Jason Tolentino, Markelle Gibbs, Rachelle Ihly, Craig L. Perkins, Yu Liu, Nathan Crawford, John C. Hemminger, and Matt Law. Pbse quantum dot field-effect transistors with air-stable electron mobilities above $7 \text{ cm}^2 \text{ v}^{-1} \text{ s}^{-1}$. *Nano Letters*, 13(4):1578–1587, 2013.
- [252] Run Long and Oleg V. Prezhdo. Ab initio nonadiabatic molecular dynamics of the ultrafast electron injection from a pbse quantum dot into the tio2 surface. *J. Am. Chem. Soc.*, 133(47):19240–19249, 2011.
- [253] M. Lopez, B. Garrido, C. Garca, P. Pellegrino, A. Prez-Rodrguez, J. R. Morante, C. Bonafos, M. Carrada, and A. Claverie. Elucidation of the surface passivation role on the photoluminescence emission yield of silicon nanocrystals embedded in sio2. *Appl. Phys. Lett.*, 80(9):1637–1639, 2002.
- [254] PerOlov Löwdin. On the nonorthogonality problem connected with the use of atomic wave functions in the theory of molecules and crystals. *J. Chem. Phys.*, 18(3):365–375, 1950.
- [255] Jun-Wei Luo, Alberto Franceschetti, and Alex Zunger. Carrier multiplication in semiconductor nanocrystals: Theoretical screening of candidate materials based on band-structure effects. *Nano Lett.*, 8(10):3174–3181, 2008. PMID: 18729418.
- [256] Marcello Luppi and Stefano Ossicini. Ab initio study on oxidized silicon clusters and silicon nanocrystals embedded in sio₂: Beyond the quantum confinement effect. *Phys. Rev. B*, 71:035340, Jan 2005.
- [257] Antonio Luque and Antonio Martí. Increasing the efficiency of ideal solar cells by photon induced transitions at intermediate levels. *Phys. Rev. Lett.*, 78:5014–5017, Jun 1997.
- [258] Joseph M. Luther, Matt Law, Qing Song, Craig L. Perkins, Matthew C. Beard, and Arthur J. Nozik. Structural, optical, and electrical properties of self-assembled films of pbse nanocrystals treated with 1,2-ethanedithiol. *ACS Nano*, 2(2):271–280, 2008.

- [259] J. L. Lyons, A. Janotti, and C. G. Van de Walle. Effects of carbon on the electrical and optical properties of inn, gan, and aln. *Phys. Rev. B*, 89:035204, Jan 2014.
- [260] Pui-Wai Ma and S. L. Dudarev. Constrained density functional for noncollinear magnetism. *Phys. Rev. B*, 91:054420, Feb 2015.
- [261] Georg K.H. Madsen and David J. Singh. Boltztrap. a code for calculating band-structure dependent quantities. *Computer Physics Communications*, 175(1):67 – 71, 2006.
- [262] Santanu K. Maiti and Abraham Nitzan. Mobility edge phenomenon in a hubbard chain: A mean field study. *Phys. Lett. A*, 377(1617):1205 – 1209, 2013.
- [263] Adi Makmal, Stephan Kummel, and Leor Kronik. Dissociation of diatomic molecules and the exact-exchange kohn-sham potential: The case of lif. *Phys. Rev. A*, 83:062512, Jun 2011.
- [264] G. Makov and M. C. Payne. Periodic boundary conditions in ab initio calculations. *Phys. Rev. B*, 51:4014–4022, Feb 1995.
- [265] G. Makov and M. C. Payne. Periodic boundary conditions in ab initio calculations. *Phys. Rev. B*, 51:4014–4022, Feb 1995.
- [266] G. Makov and M. C. Payne. Periodic boundary conditions in ab initio calculations. *Physical Review B*, 51(7):4014–4022, February 1995.
- [267] G. Makov and M. C. Payne. Periodic boundary conditions in ψ ab initio/ ψ calculations. *Phys. Rev. B*, 51:4014, Feb 1995.
- [268] R.A. Marcus and Norman Sutin. Electron transfers in chemistry and biology. *Biochim. Biophys. Acta-Bioenergetics*, 811(3):265 – 322, 1985.
- [269] Rudolph A. Marcus. The second r. a. robinson memorial lecture. electron proton and related transfers. *Faraday Discuss. Chem. Soc.*, 74:7–15, 1982.
- [270] Rudolph A. Marcus. Electron Transfer Reactions in Chemistry. Theory and Experiment. *Rev. Mod. Phys.*, 65(3):599–610, jul 1993.
- [271] Dimitrije Markovi and Claudius Gros. Power laws and self-organized criticality in theory and nature. *Phys. Rep.*, 536(2):41 – 74, 2014.
- [272] Miguel A. L. Marques, Julien Vidal, Micael J. T. Oliveira, Lucia Reining, and Silvana Botti. Density-based mixing parameter for hybrid functionals. *Phys. Rev. B*, 83:035119, Jan 2011.
- [273] R. M. Martin, Reining L., and Ceperley D. *Interacting Electrons Theory and Computational Approaches*. Cambridge University Press, 2016.

- [274] Glenn J. Martyna and Mark E. Tuckerman. A reciprocal space based method for treating long range interactions in ab initio and force-field-based calculations in clusters. *J. Chem. Phys.*, 110(6):2810, 1999.
- [275] T. Matsuoka, L. S. Vlasenko, M. P. Vlasenko, T. Sekiguchi, and K. M. Itoh. Identification of a paramagnetic recombination center in silicon/silicon-dioxide interface. *Appl. Phys. Lett.*, 100(15):1–3, 2012.
- [276] Volkhard May and Oliver Kuhn. *Charge and Energy Transfer Dynamics in Molecular Systems*. Wiley-VCH, Weinheim, Germany, 2011.
- [277] G. McLane and J.N. Zemel. Surface interaction of h and o2 on thin pbse epitaxial films. *Thin Solid Films*, 7(3):229 – 246, 1971.
- [278] Marko Melander, Elvar Ö. Jónsson, Jens J. Mortensen, Tejs Vegge, and Juan Maria García Lastra. Implementation of constrained dft for computing charge transfer rates within the projector augmented wave method. *Journal of Chemical Theory and Computation*, 12(11):5367–5378, 2016.
- [279] Allen Miller and Elihu Abrahams. Impurity conduction at low concentrations. *Phys. Rev.*, 120:745–755, Nov 1960.
- [280] Elisa M. Miller, Daniel M. Kroupa, Jianbing Zhang, Philip Schulz, Ashley R. Marshall, Antoine Kahn, Stephan Lany, Joseph M. Luther, Matthew C. Beard, Craig L. Perkins, and Jao van de Lagemaat. Revisiting the valence and conduction band size dependence of pbs quantum dot thin films. *ACS Nano*, 10(3):3302–3311, 2016. PMID: 26895310.
- [281] Elisa M. Miller, Daniel M. Kroupa, Jianbing Zhang, Philip Schulz, Ashley R. Marshall, Antoine Kahn, Stephan Lany, Joseph M. Luther, Matthew C. Beard, Craig L. Perkins, and Jao van de Lagemaat. Revisiting the valence and conduction band size dependence of pbs quantum dot thin films. *ACS Nano*, 10(3):3302–3311, 2016.
- [282] Somak Mitra, Vladimir Vrek, Manuel Macias-Montero, Tamilselvan Velusamy, and Davide Mariotti. Temperature-dependent photoluminescence of surface-engineered silicon nanocrystals. *Sci. Rep.*, 6:27727, June 2016.
- [283] Iwan Moreels, Bernd Fritzing, Jos C. Martins, and Zeger Hens. Surface chemistry of colloidal pbse nanocrystals. *Journal of the American Chemical Society*, 130(45):15081–15086, 2008.
- [284] Iwan Moreels, Karel Lambert, David De Muynck, Frank Vanhaecke, Dirk Poelman, Jos C. Martins, Guy Allan, and Zeger Hens. Composition and size-dependent extinction coefficient of colloidal pbse quantum dots. *Chemistry of Materials*, 19(25):6101–6106, 2007.
- [285] Dirk K. Morr. Crossover from quantum to classical transport. *Contemporary Physics*, 57(1):19–45, 2016.

- [286] Jonathan E. Moussa, Peter A. Schultz, and James R. Chelikowsky. Analysis of the heyd-scuseria-ernzerhof density functional parameter space. *J. Chem. Phys.*, 136(20), 2012.
- [287] Petri Myöhänen, Adrian Stan, Gianluca Stefanucci, and Robert van Leeuwen. Kadanoff-baym approach to quantum transport through interacting nanoscale systems: From the transient to the steady-state regime. *Phys. Rev. B*, 80:115107, Sep 2009.
- [288] Prashant Nagpal and Victor I Klimov. Role of mid-gap states in charge transport and photoconductivity in semiconductor nanocrystal films. *Nature communications*, 2:486, 2011.
- [289] Gautham Nair, Liang-Yi Chang, Scott M. Geyer, and Mounqi G. Bawendi. Perspective on the prospects of a carrier multiplication nanocrystal solar cell. *Nano Letters*, 11(5):2145–2151, 2011.
- [290] J. B. Neaton, Mark S. Hybertsen, and Steven G. Louie. Renormalization of molecular electronic levels at metal-molecule interfaces. *Phys. Rev. Lett.*, 97:216405, Nov 2006.
- [291] Jörg Neugebauer and Chris G. Van de Walle. Hydrogen in gan: Novel aspects of a common impurity. *Phys. Rev. Lett.*, 75:4452–4455, Dec 1995.
- [292] R. G. Neuhauser, K. T. Shimizu, W. K. Woo, S. A. Empedocles, and M. G. Bawendi. Correlation between fluorescence intermittency and spectral diffusion in single semiconductor quantum dots. *Phys. Rev. Lett.*, 85:3301, Oct 2000.
- [293] Huy-Viet Nguyen, T. Anh Pham, Dario Rocca, and Giulia Galli. Improving accuracy and efficiency of calculations of photoemission spectra within the many-body perturbation theory. *Phys. Rev. B*, 85:081101, Feb 2012.
- [294] S. Niesar, A. R. Stegner, R. N. Pereira, M. Hoeb, H. Wiggers, M. S. Brandt, and M. Stutzmann. Defect reduction in silicon nanoparticles by low-temperature vacuum annealing. *Appl. Phys. Lett.*, 96(19):193112–193115, 2010.
- [295] Sabrina Niesar, Rui N. Pereira, Andre R. Stegner, Nadine Erhard, Marco Hoeb, Andrea Baumer, Hartmut Wiggers, Martin S. Brandt, and Martin Stutzmann. Low-cost post-growth treatments of crystalline silicon nanoparticles improving surface and electronic properties. *Adv. Funct. Mater.*, 22(6):1190–1198, 2012.
- [296] W. Von Niessen. Ionization energies of the transition metal diatomics cu₂, ag₂, cr₂, and mo₂: A greens function investigation. *The Journal of Chemical Physics*, 85(1):337–345, 1986.
- [297] Zhijun Ning, Haopeng Dong, Qiong Zhang, Oleksandr Voznyy, and Edward H. Sargent. Solar cells based on inks of n-type colloidal quantum dots. *ACS Nano*, 8(10):10321–10327, 2014. PMID: 25225786.

- [298] Zhijun Ning, Oleksandr Voznyy, Jun Pan, Sjoerd Hoogland, Valerio Adinolfi, Jixian Xu, Min Li, Ahmad R Kirmani, Jon-paul Sun, James Minor, Kyle W Kemp, Haopeng Dong, Lisa Rollny, André Labelle, Graham Carey, Brandon Sutherland, Ian Hill, Aram Amassian, Huan Liu, Jiang Tang, Osman M Bakr, and Edward H Sargent. Air-Stable N-Type Colloidal Quantum Dot Solids. *Nat. Mater.*, 13(June):4–10, 2014.
- [299] Zhijun Ning, Oleksandr Voznyy, Jun Pan, Sjoerd Hoogland, Valerio Adinolfi, Jixian Xu, Min Li, Ahmad R. Kirmani, Jon-Paul Sun, James Minor, Kyle W. Kemp, Haopeng Dong, Lisa Rollny, Andr Labelle, Graham Carey, Brandon Sutherland, Ian Hill, Aram Amassian, Huan Liu, Jiang Tang, Osman M. Bakr, and Edward H. Sargent. Air-stable n-type colloidal quantum dot solids. *Nature materials*, 13(8):822–828, 2014.
- [300] Zhijun Ning, David Zhitomirsky, Valerio Adinolfi, Brandon Sutherland, Jixian Xu, Oleksandr Voznyy, Pouya Maraghechi, Xinzheng Lan, Sjoerd Hoogland, Yuan Ren, and Edward H. Sargent. Graded doping for enhanced colloidal quantum dot photovoltaics. *Adv. Mater.*, 25(12):1719–1723, 2013.
- [301] M. Nirmal, B. O. Dabbousi, M. G. Bawendi, J. J. Macklin, J. K. Trautman, T. D. Harris, and L. E. Brus. Fluorescence intermittency in single cadmium selenide nanocrystals. *Nature*, 383(6603):802–804, October 1996.
- [302] Yoshio Nishi. Study of silicon-silicon dioxide structure by electron spin resonance i. *Jpn. J. Appl. Phys*, 10(1):52–62, 1971.
- [303] NIST. T. Shimanouchi, "Molecular Vibrational Frequencies" in NIST Chemistry Web-Book, NIST Standard Reference Database Number 69, Eds. P.J. Linstrom and W.G. Mallard, National Institute of Standards and Technology, Gaithersburg MD, 20899, <http://webbook.nist.gov>, (retrieved August 3, 2016).
- [304] NIST. Computational chemistry comparison and benchmark database, September 2015.
- [305] Francesca Nunzi, Saurabh Agrawal, Annabella Selloni, and Filippo De Angelis. Structural and electronic properties of photoexcited tio2 nanoparticles from first principles. *J. Chem. Theory Comput.*, 11(2):635–645, 2015.
- [306] Harald Oberhofer and Jochen Blumberger. Charge Constrained Density Functional Molecular Dynamics for Simulation of Condensed Phase Electron Transfer Reactions. *J. Chem. Phys.*, 131(6):064101, 2009.
- [307] Harald Oberhofer and Jochen Blumberger. Electronic Coupling Matrix Elements From Charge Constrained Density Functional Theory Calculations Using a Plane Wave Basis Set. *J. Chem. Phys.*, 133(2010):244105, 2010.
- [308] Harald Oberhofer and Jochen Blumberger. Revisiting Electronic Couplings and Incoherent Hopping Models for Electron Transport in Crystalline C60 at Ambient Temperatures. *Phys. Chem. Chem. Phys.*, 14(40):13846, 2012.

- [309] Soong Ju Oh, Nathaniel E. Berry, Ji-Hyuk Choi, E. Ashley Gaulding, Hangfei Lin, Taejong Paik, Benjamin. T. Diroll, Shin Muramoto, Christopher B. Murray, and Cherie R. Kagan. Designing high-performance pbs and pbse nanocrystal electronic devices through stepwise, post-synthesis, colloidal atomic layer deposition. *Nano Letters*, 14(3):1559–1566, 2014.
- [310] Soong Ju Oh, Nathaniel E. Berry, Ji-Hyuk Choi, E. Ashley Gaulding, Taejong Paik, Sung-Hoon Hong, Christopher B. Murray, and Cherie R. Kagan. Stoichiometric control of lead chalcogenide nanocrystal solids to enhance their electronic and optoelectronic device performance. *ACS Nano*, 7(3):2413–2421, 2013.
- [311] Jacob H. Olshansky, Tina X. Ding, Youjin V. Lee, Stephen R. Leone, and A. Paul Alivisatos. Hole transfer from photoexcited quantum dots: The relationship between driving force and rate. *Journal of the American Chemical Society*, 137(49):15567–15575, 2015. PMID: 26597761.
- [312] Giovanni Onida, Lucia Reining, and Angel Rubio. Electronic excitations: density-functional versus many-body green’s-function approaches. *Rev. Mod. Phys.*, 74:601–659, Jun 2002.
- [313] Eoin P. O’Reilly and John Robertson. Theory of defects in vitreous silicon dioxide. *Phys. Rev. B*, 27:3780, Mar 1983.
- [314] Frank Ortmann, Friedhelm Bechstedt, and Karsten Hannewald. Charge transport in organic crystals: interplay of band transport, hopping and electron-phonon scattering. *New J. Phys.*, 12:23011, 2010.
- [315] Frank Ortmann, Friedhelm Bechstedt, and Karsten Hannewald. Charge transport in organic crystals: Theory and modelling. *Phys. Status Solidi*, 248(3):511–525, 2011.
- [316] Timothy P. Osedach, Ni Zhao, Trisha L. Andrew, Patrick R. Brown, Darcy D. Wanger, David B. Strasfeld, Liang-Yi Chang, Mounqi G. Bawendi, and Vladimir Bulovi. Bias-stress effect in 1,2-ethanedithiol-treated pbs quantum dot field-effect transistors. *ACS Nano*, 6(4):3121–3127, 2012.
- [317] Jonathan Owen. The coordination chemistry of nanocrystal surfaces. *Science*, 347(6222):615–616, 2015.
- [318] Gianfranco Pacchioni, Linards Skuja, and David Griscom. *Defects in SiO₂ and Related Dielectrics: Science and Technology*. Springer Netherlands, 2000.
- [319] Lazaro A. Padilha, John T. Stewart, Richard L. Sandberg, Wan Ki Bae, Weon-Kyu Koh, Jeffrey M. Pietryga, and Victor I. Klimov. Carrier multiplication in semiconductor nanocrystals: Influence of size, shape, and composition. *Accounts of Chemical Research*, 46(6):1261–1269, 2013.
- [320] Michele Pavanello, Troy Van Voorhis, Lucas Visscher, and Johannes Neugebauer. An Accurate and Linear-Scaling Method for Calculating Charge-Transfer Excitation Energies and Diabatic Couplings. *J. Chem. Phys.*, 138(5):054101, feb 2013.

- [321] L. Pavesi and R. Turan. *Silicon Nanocrystals: Fundamentals, Synthesis and Applications*. Wiley, 2010.
- [322] Michel Pelissier. Bonding between transition metal atoms. ab initio effective potential calculations of cu2. *The Journal of Chemical Physics*, 75(2):775–780, 1981.
- [323] Timothy J. Pennycook, George Hadjisavvas, Juan C. Idrobo, Pantelis C. Kelires, and Sokrates T. Pantelides. Optical gaps of free and embedded si nanoclusters: Density functional theory calculations. *Phys. Rev. B*, 82:125310, Sep 2010.
- [324] John P. Perdew, Kieron Burke, and Matthias Ernzerhof. Generalized gradient approximation made simple. *Phys. Rev. Lett.*, 77:3865–3868, Oct 1996.
- [325] John P. Perdew, Kieron Burke, and Matthias Ernzerhof. Generalized gradient approximation made simple. *Phys. Rev. Lett.*, 77:3865–3868, Oct 1996.
- [326] John P. Perdew, Matthias Ernzerhof, and Kieron Burke. Rationale for mixing exact exchange with density functional approximations. *J. Chem. Phys.*, 105(22):9982–9985, 1996.
- [327] R. N. Pereira, S. Niesar, W. B. You, A. F. da Cunha, N. Erhard, A. R. Stegner, H. Wiggers, M. G. Willinger, M. Stutzmann, and M. S. Brandt. Solution-processed networks of silicon nanocrystals: The role of internanocrystal medium on semiconducting behavior. *J. Phys. Chem. C*, 115(41):20120–20127, 2011.
- [328] R. N. Pereira, D. J. Rowe, R. J. Anthony, and U. Kortshagen. Oxidation of freestanding silicon nanocrystals probed with electron spin resonance of interfacial dangling bonds. *Phys. Rev. B*, 83:155327, Apr 2011.
- [329] R. N. Pereira, D. J. Rowe, R. J. Anthony, and U. Kortshagen. Oxidation of freestanding silicon nanocrystals probed with electron spin resonance of interfacial dangling bonds. *Phys. Rev. B*, 83:155327, Apr 2011.
- [330] R. N. Pereira, D. J. Rowe, R. J. Anthony, and U. Kortshagen. Freestanding silicon nanocrystals with extremely low defect content. *Phys. Rev. B*, 86:085449–085454, Aug 2012.
- [331] V. Petkov, I. Moreels, Z. Hens, and Y. Ren. Pbse quantum dots: Finite, off-stoichiometric, and structurally distorted. *Phys. Rev. B*, 81:241304, Jun 2010.
- [332] Roberto Peverati and Donald G. Truhlar. Screened-exchange density functionals with broad accuracy for chemistry and solid-state physics. *Phys. Chem. Chem. Phys.*, 14:16187–16191, 2012.
- [333] T. Anh Pham, Huy Viet Nguyen, Dario Rocca, and Giulia Galli. *gw* calculations using the spectral decomposition of the dielectric matrix: Verification, validation, and comparison of methods. *Phys. Rev. B*, 87:155148, Apr 2013.

- [334] T. Anh Pham, Huy-Viet Nguyen, Dario Rocca, and Giulia Galli. *gw* calculations using the spectral decomposition of the dielectric matrix: Verification, validation, and comparison of methods. *Phys. Rev. B*, 87:155148, Apr 2013.
- [335] Yuan Ping, Dario Rocca, and Giulia Galli. Electronic excitations in light absorbers for photoelectrochemical energy conversion: first principles calculations based on many body perturbation theory. *Chem. Soc. Rev.*, 42:2437–2469, 2013.
- [336] M-E. Pistol, P. Castrillo, D. Hessman, J. A. Prieto, and L. Samuelson. Random telegraph noise in photoluminescence from individual self-assembled quantum dots. *Phys. Rev. B*, 59:10725, Apr 1999.
- [337] Giovanni Pizzi, Dmitri Volja, Boris Kozinsky, Marco Fornari, and Nicola Marzari. Boltzmann: A code for the evaluation of thermoelectric and electronic transport properties with a maximally-localized wannier functions basis. *Computer Physics Communications*, 185(1):422 – 429, 2014.
- [338] E. H. Poindexter, G. J. Gerardi, M.E. Rueckel, P. J. Caplan, N. M. Johnson, and D. K. Biegelsen. Electronic traps and pb centers at the si/sio2 interface: Bandgap energy distribution. *J. Appl. Phys*, 56(10):2844–2849, 1984.
- [339] Edward H. Poindexter and Philip J. Caplan. Characterization of si/sio2 interface defects by electron spin resonance. *Prog. Surf. Sci.*, 14(3):201 – 294, 1983.
- [340] Edward H. Poindexter, Philip J. Caplan, Bruce E. Deal, and Reda R. Razouk. Interface states and electron spin resonance centers in thermally oxidized (111) and (100) silicon wafers. *J. Appl. Phys*, 52(2):879–884, 1981.
- [341] Edward H. Poindexter, Philip J. Caplan, Bruce E. Deal, and Reda R. Razouk. Interface states and electron spin resonance centers in thermally oxidized (111) and (100) silicon wafers. *J. Appl. Phys*, 52(2):879–884, 1981.
- [342] S. Ponc, E.R. Margine, C. Verdi, and F. Giustino. Epw: Electronphonon coupling, transport and superconducting properties using maximally localized wannier functions. *Computer Physics Communications*, 209:116 – 133, 2016.
- [343] O. V. Prezhdo, J. T. Kindt, and J. C. Tully. Perturbed ground state method for electron transfer. *J. Chem. Phys.*, 111(17):7818–7827, 1999.
- [344] Francesco Priolo, Tom Gregorkiewicz, Matteo Galli, and Thomas F. Krauss. Silicon Nanostructures for Photonics and Photovoltaics. *Nat. Nanotechnol.*, 9(1):19–32, 2014.
- [345] Aaron Puzder, a. Williamson, Jeffrey Grossman, and Giulia Galli. Surface Chemistry of Silicon Nanoclusters. *Phys. Rev. Lett.*, 88(9):097401, feb 2002.
- [346] R Core Team. *R: A Language and Environment for Statistical Computing*. R Foundation for Statistical Computing, Vienna, Austria, 2015.

- [347] Pablo Ramos and Michele Pavanello. Constrained subsystem density functional theory. *Phys. Chem. Chem. Phys.*, 18:21172–21178, 2016.
- [348] Andrew M. Rappe, Karin M. Rabe, Efthimios Kaxiras, and J. D. Joannopoulos. Optimized pseudopotentials. *Phys. Rev. B*, 41:1227, Jan 1990.
- [349] Laura E. Ratcliff, Luca Grisanti, Luigi Genovese, Thierry Deutsch, Tobias Neumann, Denis Danilov, Wolfgang Wenzel, David Beljonne, and Jérôme Cornil. Toward fast and accurate evaluation of charge on-site energies and transfer integrals in supramolecular architectures using linear constrained density functional theory (cdft)-based methods. *Journal of Chemical Theory and Computation*, 11(5):2077–2086, 2015.
- [350] Sivan Refaely-Abramson, Manish Jain, Sahar Sharifzadeh, Jeffrey B. Neaton, and Leeor Kronik. Solid-state optical absorption from optimally tuned time-dependent range-separated hybrid density functional theory. *Phys. Rev. B*, 92:081204, Aug 2015.
- [351] Sivan Refaely-Abramson, Sahar Sharifzadeh, Manish Jain, Roi Baer, Jeffrey B. Neaton, and Leeor Kronik. Gap renormalization of molecular crystals from density-functional theory. *Phys. Rev. B*, 88:081204, Aug 2013.
- [352] Santiago Rigamonti, Silvana Botti, Valérie Veniard, Claudia Draxl, Lucia Reining, and Francesco Sottile. Estimating excitonic effects in the absorption spectra of solids: Problems and insight from a guided iteration scheme. *Phys. Rev. Lett.*, 114:146402, Apr 2015.
- [353] Erin A. Riley, Chris Bingham, Eric D. Bott, Bart Kahr, and Philip J. Reid. Two mechanisms for fluorescence intermittency of single violamine r molecules. *Phys. Chem. Chem. Phys.*, 13:1879–1887, 2011.
- [354] Dario Rocca, Ralph Gebauer, Yousef Saad, and Stefano Baroni. Turbo charging time-dependent density-functional theory with lanczos chains. *J. Chem. Phys.*, 128(15):154105, 2008.
- [355] Dario Rocca, Márton Vörös, Adam Gali, and Giulia Galli. Ab initio optoelectronic properties of silicon nanoparticles: Excitation energies, sum rules, and tammdancoff approximation. *J. Chem. Theory Comput.*, 10(8):3290–3298, 2014.
- [356] Dario Rocca, Márton Vörös, Adam Gali, and Giulia Galli. Ab initio optoelectronic properties of silicon nanoparticles: Excitation energies, sum rules, and tammdancoff approximation. *Journal of Chemical Theory and Computation*, 10(8):3290–3298, 2014.
- [357] Michael Rohlfing and Steven G. Louie. Electron-hole excitations and optical spectra from first principles. *Phys. Rev. B*, 62:4927–4944, Aug 2000.
- [358] Shamir Rosen, Osip Schwartz, and Dan Oron. Transient fluorescence of the off state in blinking cdse/cds/zns semiconductor nanocrystals is not governed by auger recombination. *Phys. Rev. Lett.*, 104:157404, Apr 2010.

- [359] C. Rostgaard, K. W. Jacobsen, and K. S. Thygesen. Fully self-consistent gw calculations for molecules. *Phys. Rev. B*, 81:085103, Feb 2010.
- [360] C. Rostgaard, K. W. Jacobsen, and K. S. Thygesen. Fully self-consistent gw calculations for molecules. *Phys. Rev. B*, 81:085103, Feb 2010.
- [361] Subhayan Roychoudhury, Carlo Motta, and Stefano Sanvito. Charge transfer energies of benzene physisorbed on a graphene sheet from constrained density functional theory. *Phys. Rev. B*, 93:045130, Jan 2016.
- [362] Na Sai, Paul F. Barbara, and Kevin Leung. Hole localization in molecular crystals from hybrid density functional theory. *Phys. Rev. Lett.*, 106:226403, Jun 2011.
- [363] Sang-Min Lee, Young-wook Jun, Sung-Nam Cho, , and Jinwoo Cheon*. Single-crystalline star-shaped nanocrystals and their evolution: programming the geometry of nano-building blocks. *Journal of the American Chemical Society*, 124(38):11244–11245, 2002.
- [364] Pralay K. Santra, Axel F. Palmstrom, Jukka T. Tanskanen, Nuoya Yang, and Stacey F. Bent. Improving performance in colloidal quantum dot solar cells by tuning band alignment through surface dipole moments. *The Journal of Physical Chemistry C*, 119(6):2996–3005, 2015.
- [365] Alina M. Schimpf, Kathryn E. Knowles, Gerard M. Carroll, and Daniel R. Gamelin. Electronic doping and redox-potential tuning in colloidal semiconductor nanocrystals. *Accounts of Chemical Research*, 48(7):1929–1937, 2015.
- [366] Martin Schlipf and François Gygi. Optimization Algorithm for the Generation of ONCV Pseudopotentials. *Comput. Phys. Commun.*, 196:36–44, nov 2015.
- [367] Martin Schlipf and François Gygi. Optimization algorithm for the generation of {ONCV} pseudopotentials. *Computer Physics Communications*, 196:36 – 44, 2015.
- [368] M. Schnabel, M. Canino, S. Kühnhold-Pospischil, J. López-Vidrier, T. Klugermann, C. Weiss, L. López-Conesa, M. Zschintzsch-Dias, C. Summonte, P. Löper, S. Janz, and P. R. Wilshaw. Charge transport in nanocrystalline sic with and without embedded si nanocrystals. *Phys. Rev. B*, 91:195317, May 2015.
- [369] Marko Schreiber, Mario R. Silva-Junior, Stephan P. A. Sauer, and Walter Thiel. Benchmarks for electronically excited states: Caspt2, cc2, ccsd, and cc3. *J. Chem. Phys.*, 128(13), 2008.
- [370] A. Seidl, A. Görling, P. Vogl, J. A. Majewski, and M. Levy. Generalized kohn-sham schemes and the band-gap problem. *Phys. Rev. B*, 53:3764–3774, Feb 1996.
- [371] Alex M. P. Sena, Tsuyoshi Miyazaki, and David R. Bowler. Linear scaling constrained density functional theory in conquest. *Journal of Chemical Theory and Computation*, 7(4):884–889, 2011.

- [372] Andrew Shabaev, C. Stephen Hellberg, and Alexander L. Efros. Efficiency of multiexciton generation in colloidal nanostructures. *Accounts of Chemical Research*, 46(6):1242–1251, 2013.
- [373] W. Shan, W. Walukiewicz, J. Ager, E. Haller, J. Geisz, D. Friedman, J. Olson, and S. Kurtz. Band Anticrossing in GaInNAs Alloys. *Phys. Rev. Lett.*, 82(6):1221–1224, 1999.
- [374] Shawn P. Shields, Vernal N. Richards, and William E. Buhro. Nucleation Control of Size and Dispersity in Aggregative Nanoparticle Growth. A Study of the Coarsening Kinetics of Thiolate-Capped Gold Nanocrystals. *Chem. Mater.*, 22(10):3212–3225, 2010.
- [375] Tomomi Shimazaki and Yoshihiro Asai. First principles band structure calculations based on self-consistent screened hartreefock exchange potential. *J. Chem. Phys.*, 130(16), 2009.
- [376] K. T. Shimizu, R. G. Neuhauser, C. A. Leatherdale, S. A. Empedocles, W. K. Woo, and M. G. Bawendi. Blinking statistics in single semiconductor nanocrystal quantum dots. *Phys. Rev. B*, 63:205316, May 2001.
- [377] M. Shishkin, M. Marsman, and G. Kresse. Accurate quasiparticle spectra from self-consistent gw calculations with vertex corrections. *Phys. Rev. Lett.*, 99:246403, Dec 2007.
- [378] William Shockley and Hans J. Queisser. Detailed balance limit of efficiency of p-n junction solar cells. *Journal of Applied Physics*, 32(3):510–519, 1961.
- [379] Yinan Shu and Benjamin G. Levine. Communication: Non-radiative recombination via conical intersection at a semiconductor defect. *J. Chem. Phys.*, 139(8):1–4, 2013.
- [380] Yinan Shu and Benjamin G. Levine. Communication: Non-radiative recombination via conical intersection at a semiconductor defect. *J. Chem. Phys.*, 139(8):1–4, 2013.
- [381] Yinan Shu and Benjamin G. Levine. Do excited siliconoxygen double bonds emit light? *The Journal of Physical Chemistry C*, 118(14):7669–7677, April 2014.
- [382] Yinan Shu and Benjamin G. Levine. Do excited siliconoxygen double bonds emit light? *J. Phys. Chem. C*, 118(14):7669–7677, 2014.
- [383] Yinan Shu and Benjamin G. Levine. Nonradiative recombination via conical intersections arising at defects on the oxidized silicon surface. *J. Phys. Chem. C*, 119(4):1737–1747, 2015.
- [384] Mario R. Silva-Junior, Marko Schreiber, Stephan P. A. Sauer, and Walter Thiel. Benchmarks of electronically excited states: Basis set effects on caspt2 results. *J. Chem. Phys.*, 133(17):174318, 2010.

- [385] Jonathan H. Skone, Marco Govoni, and Giulia Galli. Self-consistent hybrid functional for condensed systems. *Phys. Rev. B*, 89:195112, May 2014.
- [386] Jonathan H. Skone, Marco Govoni, and Giulia Galli. Nonempirical range-separated hybrid functionals for solids and molecules. *Phys. Rev. B*, 93:235106, Jun 2016.
- [387] Michael Sluydts, Kim De Nolf, Veronique Van Speybroeck, Stefaan Cottenier, and Zeger Hens. Ligand addition energies and the stoichiometry of colloidal nanocrystals. *ACS Nano*, 10(1):1462–1474, 2016.
- [388] A. M. Souza, I. Rungger, C. D. Pemmaraju, U. Schwingenschloegl, and S. Sanvito. Constrained-dft method for accurate energy-level alignment of metal/molecule interfaces. *Phys. Rev. B*, 88:165112, Oct 2013.
- [389] A. M. Souza, I. Rungger, C. D. Pemmaraju, U. Schwingenschloegl, and S. Sanvito. Constrained-dft method for accurate energy-level alignment of metal/molecule interfaces. *Phys. Rev. B*, 88:165112, Oct 2013.
- [390] Alexandros Stavrinadis and Gerasimos Konstantatos. Strategies for the controlled electronic doping of colloidal quantum dot solids. *ChemPhysChem*, 17(5):632–644, 2016.
- [391] A. R. Stegner, R. N. Pereira, K. Klein, R. Lechner, R. Dietmueller, M. S. Brandt, M. Stutzmann, and H. Wiggers. Physrevlett.100.026803. *Phys. Rev. Lett.*, 100:026803–026807, Jan 2008.
- [392] Tamar Stein, Helen Eisenberg, Leeor Kronik, and Roi Baer. Fundamental gaps in finite systems from eigenvalues of a generalized kohn-sham method. *Phys. Rev. Lett.*, 105:266802, Dec 2010.
- [393] P. J. Stephens, F. J. Devlin, C. F. Chabalowski, and M. J. Frisch. Ab initio calculation of vibrational absorption and circular dichroism spectra using density functional force fields. *J. Phys. Chem.*, 98(45):11623–11627, 1994.
- [394] A. Stesmans. Relationship between stress and dangling bond generation at the (111)si/sio₂ interface. *Phys. Rev. Lett.*, 70:1723, Mar 1993.
- [395] A. Stesmans, B. Nouwen, and V. V. Afanas'ev. P_{b1} . *Phys. Rev. B*, 58:15801, Dec 1998.
- [396] Kurt Stokbro, Jeremy Taylor, Mads Brandbyge, and Pablo Ordejon. Transiesta: a spice for molecular electronics. *Annals of the New York Academy of Sciences*, 1006(1):212–226, 2003.
- [397] Joseph E Subotnik, Josh Vura-Weis, Alex J Sodt, and Mark A Ratner. Predicting Accurate Electronic Excitation Transfer Rates via Marcus Theory with Boys or Edmiston-Ruedenberg Localized Diabatization. *J. Phys. Chem. A*, 114(33):8665–75, aug 2010.

- [398] Ilya Sychugov, Robert Juhasz, Jan Linnros, and Jan Valenta. Luminescence blinking of a si quantum dot in a sio₂ shell. *Phys. Rev. B*, 71:115331, Mar 2005.
- [399] Jau Tang and R. A. Marcus. Mechanisms of fluorescence blinking in semiconductor nanocrystal quantum dots. *J. Chem. Phys.*, 123(5):1–12, 2005.
- [400] Kartick Tarafder, Yogesh Surendranath, Jacob H. Olshansky, A. Paul Alivisatos, and Lin-Wang Wang. Hole transfer dynamics from a cdse/cds quantum rod to a tethered ferrocene derivative. *Journal of the American Chemical Society*, 136(13):5121–5131, 2014.
- [401] Sybren ten Cate, Yao Liu, C. S. Suchand Sandeep, Sachin Kinge, Arjan J. Houtepen, Tom J. Savenije, Juleon M. Schins, Matt Law, and Laurens D. A. Siebbeles. Activating carrier multiplication in pbse quantum dot solids by infilling with atomic layer deposition. *The Journal of Physical Chemistry Letters*, 4(11):1766–1770, 2013.
- [402] Nir Tessler, Yevgeni Preezant, Noam Rappaport, and Yohai Roichman. Charge transport in disordered organic materials and its relevance to thin-film devices: A tutorial review. *Adv. Mater.*, 21(27):2741–2761, 2009.
- [403] Nir Tessler, Yevgeni Preezant, Noam Rappaport, and Yohai Roichman. Charge transport in disordered organic materials and its relevance to thin-film devices: A tutorial review. *Adv. Mater.*, 21(27):2741–2761, 2009.
- [404] Llewellyn H. Thomas. The calculation of atomic fields. *Mathematical Proceedings of the Cambridge Philosophical Society*, 23(5):542–548, 001 1927.
- [405] Murilo L. Tiago and James R. Chelikowsky. Optical excitations in organic molecules, clusters, and defects studied by first-principles green’s function methods. *Phys. Rev. B*, 73:205334, May 2006.
- [406] Julien Toulouse, Francois Colonna, and Andreas Savin. Long-range-short-range separation of the electron-electron interaction in density-functional theory. *Phys. Rev. A*, 70:062505, Dec 2004.
- [407] Alessandro Troisi. Charge transport in high mobility molecular semiconductors: classical models and new theories. *Chem. Soc. Rev.*, 40:2347–2358, 2011.
- [408] N Troullier and JL Martins. Efficient pseudopotentials for plane-wave calculations. *Phys. Rev. B*, 43(3):1993, 1991.
- [409] Florian Uekermann, Sebastian Fiedler, and Bálint Aradi. Nanocut, May 2016.
- [410] R. T. M. Ummels, P. A. Bobbert, and W. van Haeringen. First-order corrections to random-phase approximation gw calculations in silicon and diamond. *Phys. Rev. B*, 57:11962–11973, May 1998.
- [411] Edward F. Valeev, Veaceslav Coropceanu, Demetrio A. da Silva Filho, Seyhan Salman, and Jean-Luc Brdas. Effect of electronic polarization on charge-transport parameters in molecular organic semiconductors. *J. Am. Chem. Soc.*, 128(30):9882–9886, 2006.

- [412] Jan Valenta, Anna Fucikova, Frantiek Vcha, Frantiek Adamec, Jana Humpolkov, Martin Hof, Ivan Pelant, Kateina Ksov, Kateina Dohnalov, and Jan Linnros. Light-emission performance of silicon nanocrystals deduced from single quantum dot spectroscopy. *Adv. Funct. Mater.*, 18(18):2666–2672, 2008.
- [413] Chris G. Van de Walle. Hydrogen as a cause of doping in zinc oxide. *Phys. Rev. Lett.*, 85:1012–1015, Jul 2000.
- [414] Chris G Van de Walle and Jörg Neugebauer. Universal alignment of hydrogen levels in semiconductors, insulators and solutions. *Nature*, 423(6940):626–628, 2003.
- [415] John S. Van Dyke and Dirk K. Morr. Controlling the flow of spin and charge in nanoscopic topological insulators. *Phys. Rev. B*, 93:081401, Feb 2016.
- [416] Michiel J. van Setten, Fabio Caruso, Sahar Sharifzadeh, Xinguo Ren, Matthias Scheffler, Fang Liu, Johannes Lischner, Lin Lin, Jack R. Deslippe, Steven G. Louie, Chao Yang, Florian Weigend, Jeffrey B. Neaton, Ferdinand Evers, and Patrick Rinke. Gw100: Benchmarking g0w0 for molecular systems. *Journal of Chemical Theory and Computation*, 11(12):5665–5687, 2015. PMID: 26642984.
- [417] Troy Van Voorhis, Tim Kowalczyk, Benjamin Kaduk, Lee-Ping Wang, Chiao-Lun Cheng, and Qin Wu. The Diabatic Picture of Electron Transfer, Reaction Barriers, and Molecular Dynamics. *Annu. Rev. Phys. Chem.*, 61:149–70, jan 2010.
- [418] Igor Vasiliev, James R. Chelikowsky, and Richard M. Martin. Surface Oxidation Effects on the Optical Properties of Silicon Nanocrystals. *Phys. Rev. B*, 65(12):121302, 2002.
- [419] Tamilselvan Velusamy, Somak Mitra, Manuel Macias-Montero, Vladimir Svrcek, and Davide Mariotti. Varying Surface Chemistries for P-Doped and N-Doped Silicon Nanocrystals and Impact on Photovoltaic Devices. *ACS Appl. Mater. Interfaces*, 7(51):28207–28214, 2015.
- [420] Rogier Verberk, Antoine M. van Oijen, and Michel Orrit. Simple model for the power-law blinking of single semiconductor nanocrystals. *Phys. Rev. B*, 66:233202, Dec 2002.
- [421] George H. Vineyard. Frequency factors and isotope effects in solid state rate processes. *Journal of Physics and Chemistry of Solids*, 3(1):121 – 127, 1957.
- [422] Marton Voros, Nicholas P. Brawand, and Giulia Galli. Hydrogen treatment as a detergent of electronic trap states in lead chalcogenide nanoparticles. *Chemistry of Materials*, 29(6):2485–2493, 2017.
- [423] Marton Voros, Adam Gali, Efthimios Kaxiras, Thomas Frauenheim, and Jan M. Knaup. Identification of defects at the interface between 3c-sic quantum dots and a sio2 embedding matrix. *Phys. Status Solidi B*, 249(2):360–367, 2012.
- [424] Marton Voros, Giulia Galli, and Gergely T. Zimanyi. Colloidal nanoparticles for intermediate band solar cells. *ACS Nano*, 9(7):6882–6890, 2015.

- [425] Márton Vörös, Giulia Galli, and Gergely T. Zimanyi. Colloidal nanoparticles for intermediate band solar cells. *ACS Nano*, 9(7):6882–6890, 2015.
- [426] Márton Vörös, Dario Rocca, Giulia Galli, Gergely T. Zimanyi, and Adam Gali. Increasing impact ionization rates in si nanoparticles through surface engineering: A density functional study. *Phys. Rev. B*, 87:155402, Apr 2013.
- [427] Márton Vörös, Dario Rocca, Giulia Galli, Gergely T. Zimanyi, and Adam Gali. Increasing impact ionization rates in si nanoparticles through surface engineering: A density functional study. *Phys. Rev. B*, 87:155402, Apr 2013.
- [428] Márton Vörös, Dario Rocca, Giulia Galli, Gergely T. Zimanyi, and Adam Gali. Increasing impact ionization rates in si nanoparticles through surface engineering: A density functional study. *Physical Review B*, 87(15):155402, April 2013.
- [429] Márton Vörös, Stefan Wippermann, Bálint Somogyi, Adam Gali, Dario Rocca, Giulia Galli, and Gergely T. Zimanyi. Germanium nanoparticles with non-diamond core structures for solar energy conversion. *Journal of Materials Chemistry A*, 2(25):9820, 2014.
- [430] O. Voznyy and E. H. Sargent. Atomistic model of fluorescence intermittency of colloidal quantum dots. *Phys. Rev. Lett.*, 112:157401, Apr 2014.
- [431] O. Voznyy and E. H. Sargent. Atomistic model of fluorescence intermittency of colloidal quantum dots. *Phys. Rev. Lett.*, 112:157401, Apr 2014.
- [432] O. Voznyy, S. M. Thon, A. H. Ip, and E. H. Sargent. Dynamic trap formation and elimination in colloidal quantum dots. *The Journal of Physical Chemistry Letters*, 4(6):987–992, 2013.
- [433] Oleksandr Voznyy. Mobile surface traps in cdse nanocrystals with carboxylic acid ligands. *The Journal of Physical Chemistry C*, 115(32):15927–15932, 2011.
- [434] Oleksandr Voznyy, David Zhitomirsky, Philipp Stadler, Zhijun Ning, Sjoerd Hoogland, and Edward H Sargent. A Charge-Orbital Balance Picture of Doping in Colloidal Quantum Dot Solids. *ACS Nano*, 6(9):8448–8455, sep 2012.
- [435] Oleksandr Voznyy, David Zhitomirsky, Philipp Stadler, Zhijun Ning, Sjoerd Hoogland, and Edward H. Sargent. A charge-orbital balance picture of doping in colloidal quantum dot solids. *ACS Nano*, 6(9):8448–8455, 2012.
- [436] Jan Řezáč, Bernard Lévy, Isabelle Demachy, and Aurlien de la Lande. Robust and efficient constrained dft molecular dynamics approach for biochemical modeling. *Journal of Chemical Theory and Computation*, 8(2):418–427, 2012.
- [437] Oleg A. Vydrov, Jochen Heyd, Aliaksandr V. Krukau, and Gustavo E. Scuseria. Importance of short-range versus long-range hartree-fock exchange for the performance of hybrid density functionals. *J. Chem. Phys.*, 125(7), 2006.

- [438] Lin-Wang Wang. Charge-Density Patching Method for Unconventional Semiconductor Binary Systems. *Phys. Rev. Lett.*, 88:256402, 2002.
- [439] Xiaojing Wang, Xiaohong Wan, Hui Zhou, Seiichi Takami, Momoji Kubo, and Akira Miyamoto. Electronic structures and spectroscopic properties of dimers Cu_2 , Ag_2 , and Au_2 calculated by density functional theory. *Journal of Molecular Structure: THEOCHEM*, 579(1-3):221–227, 2002.
- [440] Xuefeng Wang, , and Lester Andrews*. Infrared spectra of group 14 hydrides in solid hydrogen: Experimental observation of PbH_4 , Pb_2H_2 , and Pb_2H_4 . *Journal of the American Chemical Society*, 125(21):6581–6587, 2003.
- [441] J. R. Weber, A. Janotti, and C. G. Van de Walle. Dangling bonds and vacancies in germanium. *Phys. Rev. B*, 87:035203, Jan 2013.
- [442] Mark C. Weidman, Detlef-M Smilgies, and William A. Tisdale. Kinetics of the self-assembly of nanocrystal superlattices measured by real-time in situ x-ray scattering. *Nat Mater*, advance online publication, Mar 2016. Article.
- [443] Mark C. Weidman, Kevin G. Yager, and William A. Tisdale. Interparticle spacing and structural ordering in superlattice pbs nanocrystal solids undergoing ligand exchange. *Chemistry of Materials*, 27(2):474–482, 2015.
- [444] Elon Weintraub, Thomas M. Henderson, and Gustavo E. Scuseria. Long-range-corrected hybrids based on a new model exchange hole. *J. Chem. Theory Comput.*, 5(4):754–762, 2009.
- [445] Xiaoming Wen, Lap Van Dao, and Peter Hannaford. Temperature dependence of photoluminescence in silicon quantum dots. *J. Phys. D: Appl. Phys.*, 40(12):3573, 2007.
- [446] Frank Wilcoxon. Individual comparisons by ranking methods. *Biometrics Bull*, 1(6):80–83, 1945.
- [447] Hugh F. Wilson, François Gygi, and Giulia Galli. Efficient iterative method for calculations of dielectric matrices. *Phys. Rev. B*, 78:113303, Sep 2008.
- [448] Hugh F. Wilson, Deyu Lu, François Gygi, and Giulia Galli. Iterative calculations of dielectric eigenvalue spectra. *Phys. Rev. B*, 79:245106, Jun 2009.
- [449] Mark Winter. webelements.com, 2017. [Online; accessed 2017-1-26].
- [450] S. Wippermann, M. Vörös, D. Rocca, A. Gali, G. Zimanyi, and G. Galli. High-pressure core structures of si nanoparticles for solar energy conversion. *Phys. Rev. Lett.*, 110:046804, Jan 2013.
- [451] S. Wippermann, Márton Vörös, D. Rocca, A. Gali, G. Zimanyi, and G. Galli. High-pressure core structures of si nanoparticles for solar energy conversion. *Physical Review Letters*, 110(4):046804, January 2013.

- [452] Stefan Wippermann, Yuping He, Marton Voros, and Giulia Galli. Novel silicon phases and nanostructures for solar energy conversion. *Applied Physics Reviews*, 3(4), 2016.
- [453] Stefan Wippermann, Yuping He, Mrton Vörös, and Giulia Galli. Novel silicon phases and nanostructures for solar energy conversion. *Applied Physics Reviews*, 3(4):040807, 2016.
- [454] Jonathon Witte, Matthew B. Goldey, Jeffrey B. Neaton, and Martin Head-Gordon. Beyond energies: Geometries of nonbonded molecular complexes as metrics for assessing electronic structure approaches. *J. Chem. Theory Comput.*, 11(4):1481–1492, 2015.
- [455] M. Wolkin, J. Jorne, P. Fauchet, G. Allan, and C. Delerue. Electronic States and Luminescence in Porous Silicon Quantum Dots: The Role of Oxygen. *Phys. Rev. Lett.*, 82(August 2015):197–200, 1999.
- [456] Ju Young Woo, Jae-Hyeon Ko, Jung Hoon Song, Kyungnam Kim, Hyekyoung Choi, Yong-Hyun Kim, Doh C. Lee, and Sohee Jeong. Ultrastable pbse nanocrystal quantum dots via in situ formation of atomically thin halide adlayers on pbse(100). *Journal of the American Chemical Society*, 136(25):8883–8886, 2014.
- [457] Young wook Jun, Jae-Hyun Lee, Jin sil Choi, , and Jinwoo Cheon*. Symmetry-controlled colloidal nanocrystals: nonhydrolytic chemical synthesis and shape determining parameters. *The Journal of Physical Chemistry B*, 109(31):14795–14806, 2005.
- [458] Qin Wu and Troy Van Voorhis. Direct Optimization Method to Study Constrained Systems Within Density-Functional Theory. *Phys. Rev. A*, 72(2):7–10, 2005.
- [459] Qin Wu and Troy Van Voorhis. Constrained Density Functional Theory and Its Application in Long-Range Electron Transfer. *J. Chem. Theory Comput.*, 2(3):765–774, may 2006.
- [460] Qin Wu and Troy Van Voorhis. Direct Calculation of Electron Transfer Parameters Through Constrained Density Functional Theory. *J. Phys. Chem. A*, 110(29):9212–8, jul 2006.
- [461] Qin Wu and Troy Van Voorhis. Extracting Electron Transfer Coupling Elements From Constrained Density Functional Theory. *J. Chem. Phys.*, 125(16):1–9, oct 2006.
- [462] Takeshi Yanai, David P Tew, and Nicholas C Handy. A new hybrid exchange-correlation functional using the coulomb-attenuating method (cam-b3lyp). *Chem. Phys. Lett.*, 393(13):51 – 57, 2004.
- [463] Jun Yang and Frank W. Wise. Effects of disorder on electronic properties of nanocrystal assemblies. *The Journal of Physical Chemistry C*, 119(6):3338–3347, 2015.
- [464] Shenyan Yang, David Prendergast, and Jeffrey B. Neaton. Tuning semiconductor band edge energies for solar photocatalysis via surface ligand passivation. *Nano Letters*, 12(1):383–388, 2012. PMID: 22192078.

- [465] Zeng-hui Yang, Francesco Sottile, and Carsten A. Ullrich. Simple screened exact-exchange approach for excitonic properties in solids. *Phys. Rev. B*, 92:035202, Jul 2015.
- [466] J.J. Young and J.N. Zemel. Kinetics of the hydrogen effect on pbse epitaxial films. *Thin Solid Films*, 31(12):25 – 37, 1976.
- [467] Mingjian Yuan, Mengxia Liu, and Edward H Sargent. Colloidal quantum dot solids for solution-processed solar cells. *Nature Energy*, 1:16016, 2016.
- [468] Gary Zaiats, Diana Yanover, Roman Vaxenburg, Jenya Tilchin, Aldona Sashchiuk, and Efrat Lifshitz. Pbse-based colloidal core/shell heterostructures for optoelectronic applications. *Materials*, 7(11):7243–7275, 2014.
- [469] Clarence Zener. Non-adiabatic crossing of energy levels. *Proc. Roy. Soc. A*, 137:696, 1932.
- [470] Cui Zhang, Tuan Anh Pham, Francois Gygi, and Giulia Galli. Communication: Electronic structure of the solvated chloride anion from first principles molecular dynamics. *The Journal of Chemical Physics*, 138(18):181102, 2013.
- [471] Jianbing Zhang, Jianbo Gao, Carena P. Church, Elisa M. Miller, Joseph M. Luther, Victor I. Klimov, and Matthew C. Beard. Pbse quantum dot solar cells with more than 6% efficiency fabricated in ambient atmosphere. *Nano Letters*, 14(10):6010–6015, 2014.
- [472] Yingjie Zhang, Qian Chen, A. Paul Alivisatos, and Miquel Salmeron. Dynamic charge carrier trapping in quantum dot field effect transistors. *Nano Letters*, 15(7):4657–4663, 2015.
- [473] Yingjie Zhang, Danylo Zhrebetskyy, Noah D. Bronstein, Sara Barja, Leonid Lichtenstein, A. Paul Alivisatos, Lin-Wang Wang, and Miquel Salmeron. Molecular oxygen induced in-gap states in pbs quantum dots. *ACS Nano*, 9(10):10445–10452, 2015.
- [474] Yingjie Zhang, Danylo Zhrebetskyy, Noah D. Bronstein, Sara Barja, Leonid Lichtenstein, David Schuppisser, Lin Wang Wang, A. Paul Alivisatos, and Miquel Salmeron. Charge Percolation Pathways Guided by Defects in Quantum Dot Solids. *Nano Lett.*, 15(5):3249–3253, 2015.
- [475] Zhilong Zhang, Jianfeng Yang, Xiaoming Wen, Lin Yuan, Santosh Shrestha, John A. Stride, Gavin J. Conibeer, Robert J. Patterson, and Shujuan Huang. Effect of halide treatments on pbse quantum dot thin films: Stability, hot carrier lifetime, and application to photovoltaics. *The Journal of Physical Chemistry C*, 119(42):24149–24155, 2015.
- [476] Danylo Zhrebetskyy, Marcus Scheele, Yingjie Zhang, Noah Bronstein, Christopher Thompson, David Britt, Miquel Salmeron, Paul Alivisatos, and Lin-Wang Wang. Hydroxylation of the surface of pbs nanocrystals passivated with oleic acid. *Science*, 344(6190):1380–1384, 2014.

- [477] Danylo Zherebetsky, Yingjie Zhang, Miquel Salmeron, and Lin-Wang Wang. Tolerance of intrinsic defects in pbs quantum dots. *The Journal of Physical Chemistry Letters*, 6(23):4711–4716, 2015.
- [478] Haiming Zhu, Ye Yang, Kim Hyeon-Deuk, Marco Califano, Nianhui Song, Youwei Wang, Wenqing Zhang, Oleg V. Prezhdo, and Tianquan Lian. Auger-assisted electron transfer from photoexcited semiconductor quantum dots. *Nano Letters*, 14(3):1263–1269, 2014. PMID: 24359156.